2015

SATELLITE MICROWAVE MEASUREMENT OF LAND SURFACE PHENOLOGY: CLARIFYING VEGETATION PHENOLOGY RESPONSE TO CLIMATIC DRIVERS AND EXTREME EVENTS

Matthew Oushana Jones
The University of Montana

SATELLITE MICROWAVE MEASUREMENT OF LAND SURFACE PHENOLOGY: CLARIFYING VEGETATION PHENOLOGY RESPONSE TO CLIMATIC DRIVERS AND EXTREME EVENTS

By

Matthew Oushana Jones

M.S., University of Montana, Missoula, MT, 2006
Teacher Education Credential, San Francisco State University, San Francisco CA, 1998
B.A., Philosophy, University of California at Santa Barbara, Santa Barbara, CA, 1995

Dissertation

presented in partial fulfillment of the requirements
for the degree of

Doctor of Philosophy
in Systems Ecology

The University of Montana
Missoula, MT

May 2015

Approved by:

Sandy Ross, Dean of The Graduate School
Graduate School

Dr. John S. Kimball, Chair
Ecosystem & Conservation Sciences

Dr. Steven W. Running
Regent's Professor, Ecosystem & Conservation Sciences

Dr. Anna Sala
Division of Biological Sciences

Dr. Ashley Ballantyne
Ecosystem & Conservation Sciences

Dr. Matthew Jolly
US Forest Service, Rocky Mountain Research Station, Fire Sciences Laboratory

Jones, Matthew, Ph.D., May 2015 Systems Ecology

Satellite Microwave Measurement of Land Surface Phenology: Clarifying Vegetation Phenology Response to Climatic Drivers and Extreme Events

Chairperson: Dr. John S. Kimball

Abstract

The seasonality of terrestrial vegetation controls feedbacks to the climate system including land-atmosphere water, energy and carbon (CO_2) exchanges with cascading effects on regional-to-global weather and circulation patterns. Proper characterization of vegetation phenology is necessary to understand and quantify changes in the earth's ecosystems and biogeochemical cycles and is a key component in tracking ecological species response to climate change. The response of both functional and structural vegetation phenology to climatic drivers on a global scale is still poorly understood however, which has hindered the development of robust vegetation phenology models. In this dissertation I use satellite microwave vegetation optical depth (VOD) in conjunction with an array of satellite measures, Global Positioning System (GPS) reflectometry, field observations and flux tower data to 1) clarify vegetation phenology response to water, temperature and solar irradiance constraints, 2) demonstrate the asynchrony between changes in vegetation water content and biomass and changes in greenness and leaf area in relation to land cover type and climate constraints, 3) provide enhanced assessment of seasonal recovery of vegetation biomass following wildfire and 4) present a method to more accurately model tropical vegetation phenology. This research will establish VOD as a useful and informative parameter for regional-to-global vegetation phenology modeling, more accurately define the drivers of both structural and functional vegetation phenology, and help minimize errors in phenology simulations within earth system models. This dissertation also includes the development of Gross Primary Productivity (GPP) and Net Primary Productivity (NPP) vegetation health climate indicators as part of a NASA funded project entitled "Development and Testing of Potential Indicators for the National Climate Assessment; Translating EOS datasets into National Ecosystem Biophysical Indicators".

Table of Contents

Abstract ..... **ii**

Table of Contents ..... **iii**

List of Tables ..... **vii**

List of Figures ..... **vii**

Chapter 1. Introduction **1**

1.1 Land Surface Phenology from Satellite Optical-Infrared Data 4

1.2 Phenological Response to a Changing Climate 5

1.3 Microwave Vegetation Optical Depth and LSP Monitoring 7

1.4 Comparing Microwave and Optical-IR LSP 8

1.5 Variance and Validation of LSP Metrics 10

1.6 Dissertation Objectives and Hypothesis 13

1.7 Dissertation Structure 14

1.8 References Cited 15

Chapter 2. Satellite Passive Microwave Vegetation Optical Depth for Monitoring Land Surface Phenology **19**

2.1 Methods 20

2.1.1 Passive Microwave Remote Sensing Retrieval of Vegetation Optical Depth 20

2.1.2 AMSR-E Brightness Temperatures 27

2.1.3 MODIS EVI, NDVI, LAI and Land Cover 28

2.1.4 Growing Season Index 28

2.1.5 Global and regional correlation analysis and phenology metrics 29

2.2. Results 30

2.2.1 Algorithm Error Sensitivity Analysis 30

2.2.2 Comparison with an Independent Emissivity Database 32

2.2.3 Continuity of phenology data time series 33

2.2.4 Global phenology patterns 35

2.2.5 Regional phenology patterns 38

2.2.6 GSI, VOD and EOS timing 40

2.3. Discussion 41

2.3.1 Interpreting the global correlation maps 41

2.3.2 Interpreting regional phenology patterns 43
2.4 Summary 45
2.5 Acknowledgements 46
2.6 References Cited 46
Chapter 3. Comparing Land Surface Phenology Derived from Satellite and GPS Network Microwave Remote Sensing 52
3.1 Data and Methods 53
3.1.1 Microwave Vegetation Optical Depth 53
3.1.2 GPS Normalized Microwave Reflection Index 54
3.1.3 Correlations and Phenology Metrics 57
3.1.4 NMRI and VOD Sensitivity to Moisture Variability 58
3.1.5 Multiple Sites within a Single VOD Grid Cell 59
3.2 Results 60
3.2.1 VOD and NMRI Correlations 60
3.2.2 Start of Season Metrics 64
3.2.3 NMRI and NDVI heterogeneity within a single VOD grid cell 65
3.3 Discussion 68
3.4 Acknowledgments 71
3.5 References Cited 71
Chapter 4. Satellite Microwave Detection of Boreal Forest Recovery from the Extreme 2004 Wildfires in Alaska and Canada 75
4.1 Materials and Methods 79
4.1.1 Canadian National Fire and Alaska Fire History Databases 79
4.1.2 Burn Severity Classification 79
4.1.3 Microwave Vegetation Optical Depth 81
4.1.4 MODIS Normalized Difference Vegetation Index and Percent Tree Cover 82
4.1.5 AMSR-E VOD and MODIS NDVI Spatial Resolutions 82
4.1.6 Selection of Unburned Control Pixels 83
4.1.7 Comparison of Pre-Fire and Post-Fire VOD and NDVI Time Series 85
4.1.8 Estimation of Years to Post-Fire Recovery 85
4.1.9 Incorporating Field Data within Fire Perimeters 86

4.2 Results 86
4.2.1 VOD and NDVI Anomalies 86
4.2.2 Post-fire Changes in Canopy Maximums 88
4.2.3 Canopy Recovery to Steady State Conditions and Tree Cover Loss 91
4.2.4 Field Data Comparisons to Fire Severity and Vegetation Recovery 92
4.3 Discussion 93
4.3.1 Defining Canopy "Recovery" from Relatively Short-Term Satellite Records 93
4.3.2 Recovery Trajectory Impacts on Aboveground Carbon Stocks 94
4.3.3 Post-fire Boreal Vegetation Considerations and Recovery Trajectories 94
4.3.4 Microwave Remote Sensing of Fire Recovery – Future Considerations 95
4.4 Acknowledgements 96
4.5 References Cited 97
Chapter 5. Asynchronous Amazon forest canopy phenology indicates adaptation to both water and light availability 103
5.1 Data and Methods 106
5.1.1 GRACE terrestrial water storage 106
5.1.2 AMSR-E vegetation optical depth 106
5.1.3 MODIS leaf area index and enhanced vegetation index 107
5.1.4 CERES photosynthetically active radiation 107
5.1.5 TRMM precipitation 107
5.1.6 Terrestrial ecoregions 107
5.1.7 Plot level data and tower GEP, Pc 109
5.1.8 Sinusoidal model fits to estimate ecoregion climatology 110
5.1.9 Simplified Analysis of LAI and VOD Amazon Seasonality 110
5.2 Results 111
5.2.1 Initial Results of VOD and LAI Seasonality over the Amazon 111
5.2.2 Seasonality of Amazon forests 113
5.2.3 Dry, wet seasons and water availability in the Amazon 114
5.2.4 Seasonal phase shifts in TWS, VOD, and LAI 115
5.2.5 Estimates of canopy phenology adaptation to light and water availability 117
5.3 Discussion 117

5.3.1 The transition from light-adapted to water-adapted regions 117
5.3.2 Solar irradiance seasonality 118
5.3.3 Implications for drought tolerance 119
5.3.4 Modeling Applications 120
5.4. Conclusion 120
5.5 Acknowledgements 121
5.6 References Cited 121
Chapter 6. Development of Climate Indicators for National Climate Assessments 127
6.1 Approach and Methods 128
6.2 Carbon and Vegetation Health Indicators of Net and Gross Primary Productivity 130
6.3 Water Focused Evapotranspiration Indicator 133
6.4 Planned Production of Indicators 134
6.5 Incorporating End-User Feedback 136
6.6 Summary 137
6.7 Development of Alternative Indicator Visualizations 137
6.8 References Cited 144
7.0 Conclusions and Future Research 145
7.1 Dissertation Hypotheses 145
7.2 Future Research 148
7.3 Conclusion 150
7.4 References Cited 151
Appendix A. 152
A.1 Amazon forests show canopy structure seasonality 152
A.1.1 Data and Methods 153
A.2 References 155
A.3 Letter to Nature Editors 156
Appendix B. 159
B.1 Sinusoidal Model Results 159
Appendix C. 162
C.1 Pairwise Bispectral Analysis 162
C.2 References 163

List of Tables

Table 2.1. Summary of global VOD and LAI means, VOD coefficients of variation (CV) and pixel-wise correlations for pixels of homogeneous (>80%) land cover; significance column refers to the LAI-VOD correlations.

Table 2.2. Summary of linear correlation results for the regional mean time series (shown in Figure 8).

Table 4.1. List of 14 fire perimeter areas selected in this investigation and labeled by Fire ID with geographic coordinates of fire perimeter centers. The last four columns are the percent of dominant land cover types within fire perimeters based on the MODIS 1km (MOD12Q1) Land Cover Product: ENF – Evergreen Needleleaf Forest, MXF – Mixed Forest, SHR – Open Shrubland, WSV – Woody Savanna.

Table 5.1. Flux towers providing measures of Gross Ecosystem Productivity (GEP) and Photosynthetic Capacity (Pc), and studies with published field data used in this study. Monthly GEP (µmol CO_2 m^{-2} s^{-1}) and Pc (µmol CO_2 m^{-2} s^{-1}) from the Large-Scale Biosphere-Atmosphere (LBA) Experiment in Amazonia were acquired from the LBA flux tower integrated database (Restrepo-Coupe et al 2014). Pc is estimated as the mean of flux tower derived GEP for a fixed range of PAR (725 < PAR < 925 µmol CO2 m^{-2} s^{-1}); the methods for calculating GEP and Pc can be found in Restrepo-Coupe et al (2013).

Table 5.2. Pearson product-moment cross-correlations between monthly TRMM precipitation and GRACE TWS by ecoregion. A positive lag equates to TRMM precipitation peaking prior to GRACE TWS. *p<0.001

Table 6.1. Input products for the creation of the proposed Indicators; inclusive of planned VIIRS products that would allow for future production of the Indicator suite

List of Figures

Figure 1.1. Land Surface Phenology publications (red bars) and citations (blue line).

Figure 1.2. Interannual variations of area-averaged start (SOS), end (EOS) and length (LOS) of season of temperate vegetation in the northern hemisphere for 1982-2008 (Jeong et al., 2011)

Figure 1.3. Map of the mean annual Potential Growing Season (PGS) from 1979-2010 for North America (left). Plot of PGS and surface air temperature anomalies (as difference from the long-

term mean) for Alaska and the Contiguous U.S. for the 1979-2010 period (right). (Kim et al., 2012, 2014)

Figure 1.4. Global Mean VOD at 18.7GHz (Jones et al. 2011)

Figure 1.5. Four year (2004-2007) mean of microwave VOD SOS and MODIS-for-NACP NDVI Greenup Date by ecoregion. (Jones et al. 2012)

Figure 1.6. The range of daily maximum and minimum temperatures (gray area), precipitation accumulation (blue line) and a collection of phenology metrics from four satellite LSP products (green and red bars), phenology camera time series (triangles), and USA-NPN observed phenophases (circles) at Harvard Forest, MA, USA.

Figure 1.7. Prototype visualization of data via PhenoFrame for one region; Harvard Forest, MA, USA. Red circles on maps are in situ USA-NPN observations and white stars are established PhenoCam sites.

Figure 2.1. Simulated effect of vegetation optical depth (VOD) on the above canopy V- and H-polarization emissivity at 18.7 GHz frequency. (b) Sensitivity of the slope parameter is effectively saturated at VOD values above 1.5, with limited sensitivity up to approximately 2.0. The model simulation assumes a single scattering albedo of 0.05, surface temperature of 280 K, and dry (0.05 m^3 m^{-3} volumetric moisture content) loam soil (30% sand, 50% silt, and 20% clay).

Figure 2.2. (a) Conservative estimation of algorithm retrieval error expressed as a percentage of retrieved VOD across the global VOD range. Labeled lines represent each source of error independently considered, and then summed in quadrature to estimate total daily error and total 30-day moving mean error accounting for temporal autocovariance. The legend indicates if each error source was considered as persistent (bias) or random error. (b) Distribution of retrieved VOD means from 2003-2008 for the global vegetated land area. Approximately 66% of the vegetated land area has a mean VOD within a range of 0.5 to 1.5, corresponding to VOD mean retrieval errors ≤30%.

Figure 2.3. (a) Scatter plot of alternative VOD monthly retrievals for the the nine contiguous land cover regions (Figure 8) at 18.7 GHz derived from emissivities using the Jones et al. (2010) emissivity derivation method and an alternative, independent emissivity database (Moncet & Liang, 2009); the gray line is the least-squares linear regression relationship (r^2=0.83, p<.0001) between the two VOD series. (b) Mean monthly VOD time series for 2003 over three contiguous land cover regions with characteristic large VOD seasonality; the VOD series represent retrievals derived using the Jones et al. (2010) emissivity approach (dotted lines) and the alternative emissivity database (solid lines).

Figure 2.4. (map) Percent availability of highest QC 16-day data for AMSR-E VOD (top) and MODIS EVI (bottom) from 2003 to 2008. Stars indicate locations of time series pixel extractions

shown in plots; the VOD shows relatively complete yearly time series compared to optical-infrared based indices from available MODIS EVI and NDVI time series at these EBF sites.

Figure 2.5. Global mean VOD at 18.7 GHz for the six year (2003-2008) study period.

Figure 2.6. VOD means and variance by year for homogeneous (>80%) land cover pixels.

Figure 2.7. Pixel-wise linear correlations between AMSR-E VOD and MODIS NDVI, EVI and LAI, and GSI time series for the 6 year (2003-2008) study period. Gray areas denote barren land cover areas that were screened from the analysis. Areas in black denote full year unconstrained (GSI=1) growing seasons.

Figure 2.8. Spatially contiguous regions of relatively uniform land cover and climate were defined and nine regions were selected covering a range of biomes, latitudes and continents (maps; black and grey regions). The resulting 16-day time series of each regional mean dataset (VOD, NDVI, EVI, LAI, GSI) are plotted for the six year (2003-2008) study period.

Figure 2.9. Time series of mean open water fraction (f_w), and 16-day VOD and EVI medians for the Liuwa Plains region (see map in Figure 8). The f_w parameter is calculated following the methods of Jones et al. (2009). The effect of inundation under vertically-oriented vegetation on the polarized emissivities causes an anomalous VOD trough.

Figure 3.1. Pearson correlation coefficients ($p<0.05$) between VOD and NMRI time series for 305 GPS base station sites across the western USA. Inset map displays sites over the Alaska portion of the domain. Open circles represent non-significant ($p>0.05$) correlation sites. Stars represent 24 homogeneous land cover sites used in the SOS calculations. Inset graph displays number of NMRI sites by land cover type as designated by the PBO network (ENF-evergreen needle leaf forest, CNV-cropland/natural vegetation mosaic, CRP-cropland, TUN-tundra, SAV-savanna, WSV-woody savanna, SHR-shrubland, GRA-grassland). Background represents the MODIS IGBP land cover classification.

Figure 3.2. VOD versus NMRI correlations and temporally lagged correlations, grouped by land cover type at the individual NMRI sites. Plot displays median, quartiles, 5th and 95th percentiles and outliers. Inset graph depicts the number of sites which achieved their highest correlation coefficient at the given temporal lag.

Figure 3.3. Scatterplots and least squares linear relationship between NMRI and VOD correlations (R-values) and Shannon Diversity Index (a), Percent Tree Cover (b), and Terrain Heterogeneity (c) (calculated as the SD of elevation), within the 25km VOD pixels.

Figure 3.4. Space (y-axis) vs time (x-axis) plot of NMRI and VOD 16-day anomalies (2007 to 2011) determined as significant departures from normal and plotted over monthly vapor pressure deficit (VPD) anomalies at each of the 305 NMRI sites. Each site is represented by a

row of pixels distributed along the time (x) axis, while sites are ordered by latitude along the y-axis. Green and black pixels represent 16-day intervals when both NMRI and VOD anomalies were significantly positive or negative departures from normal; i.e. greater than or less than the SD of the full data record anomalies.

Figure 3.5. Least-squares linear regression fit between VOD and NMRI derived SOS values at the 24 homogeneous land cover sites for the 2007-2011 record. Mean Absolute Error (MAE) = 26.7 days. Each NMRI site is given a unique symbol.

Figure 3.6. (a) The spatial mean and standard deviation of 4-day median time series from nine NMRI sites located within a single VOD grid cell, the mean 16-day 250m MODIS (MOD13Q1) NDVI of the three dominant land cover types within the VOD grid cell, and the corresponding VOD time series. The nine NMRI sites represent grassland (8 sites) and shrubland (1 site) conditions; (b) the mean NDVI time series from individual dominant land cover classes representing 53% (GRA – grassland), 32% (SHR – shrubland), and 12 % (WSV - woody savanna) of the overlying VOD grid cell.

Figure 3.7. Top plot is TIMESAT estimated SOS (day of year) for the 2007-2011 record derived for the 9 NMRI sites, and MODIS NDVI and VOD time series within the single VOD grid cell; cumulative daily precipitation from a nearby weather station is also shown (grey bar); the NMRI site SOS values are labeled by PBO Site ID, and NDVI based SOS values by their respective dominant land cover classes (GRA - grassland, SHR - shrubland, WSV - woody savanna) and the overall NDVI mean (Mean). The lower graphic shows the VOD time series and three representative land cover NMRI site time series (p539 - SHR; p542 and p552 - GRA) within the single VOD grid cell.

Figure 4.1. Map of 14 fire perimeters (labeled by Fire ID numbers) in Alaska, USA and the Yukon Territory, Canada. Inset map illustrates a single fire perimeter in the Northwest Territories, Canada. The fires occurred in 2004 and were greater than 1000km^2. The fire perimeters are superimposed on the MODIS IGBP land cover classification. The white box is the sub-region represented in Figure 4.4.

Figure 4.2. Monthly pre-fire (2000-2003) NDVI time series of burned areas and their associated control areas.

Figure 4.3. Complete data records for MODIS NDVI (2000-2010) and AMSR-E VOD (2003-2010) representing mean anomaly and standard deviation (SD) time series for all fire perimeter locations; 16-day anomalies were calculated as the difference from the full VOD and NDVI data record means.

Figure 4.4. Year by year summaries of 16-day VOD and NDVI anomalies for all fire perimeters, as derived from (a) differences from pre-fire reference year (2003) conditions and (b)

differences from adjacent unburned control pixels. Boxes display median, upper and lower quartiles, and whiskers display 5th and 95th percentiles.

Figure 4.5. Yearly VOD anomalies of annual maxima relative to the 2003 pre-fire reference year. Fires from 2003 to 2010 in both databases beyond the 14 selected are also mapped to display yearly effects of all fires. In each panel, fires from the previous year are annotated (blue outline) to highlight the effect on the year's anomaly. The MODIS IGBP land cover classification is also displayed (top left).

Figure 4.6. Phenological timing of yearly VOD and NDVI maxima for individual fire perimeter areas, and overall mean and SD variability across all fire perimeters relative to the timing of 2003 (pre-burn reference) maxima. Negative (positive) values denote earlier (later) timing of annual maxima relative to the 2003 pre-burn control year. The mean timing of adjacent control pixel maxima is also plotted.

Figure 4.7. Results of an asymptotic curve fit applied to individual post-fire VOD and NDVI maximums from 2005-2010 and model fit extended to 2012, when all fires reached the defined recovery. Recovery was defined as the year when the curve reached 95% of the asymptote. Vertical black line and grey shading are mean and standard deviation of years to recovery for all fires.

Figure 4.8. Scatter plot and linear regression results comparing post-fire percent tree cover loss within fire perimeters normalized by the 2003 reference year ($PTC_{loss} = PTC_{2003} – PTC_{2005} / PTC_{2003}$) versus the years to recovery (initial steady state conditions).

Figure 5.1. Amazon study domain showing southern equatorial ecoregions (*Olson et al* 2001) with the mean number of dry months (<100mm) per year calculated from TRMM 3B43 version 7 Accumulated Rainfall at 0.25 degree resolution from 1998-2011. Flux tower locations used in this study are shown; Reserve Jaru (RJA), Tapajos K67 (K67), Tapajos K83 (K83) and Caxiuana (CAX) (Table 5.1). The green border denotes the legal Amazon boundary in Brazil.

Figure 5.2. (a) Normalized VOD seasonal amplitude for all evergreen broadleaf forest (EBF) dominant (>80%) 25km pixels calculated from the monthly time series for each grid cell [(maximum-minimum)/annual mean] for the 2003-2010 record. (b) VOD and MODIS LAI monthly climatology (normalized by annual means) and monthly average precipitation (TRMM) from 2003-2010 for all EBF dominant 25km pixels having >5% VOD seasonal amplitude and located within the southern Amazon domain investigated by Morton et al. (2013) (black box in (a)). Grey vertical bars are VOD monthly climatology standard deviation. Grey and black horizontal bars denote respective months of increasing individuals with new leaves ([11] Brando et al., 2010) and months of peak litterfall from available field studies ([11] Brando et al., 2010; [12] Rice et al., 2004; [13]Goulden et al., 2004).

Figure 5.3. Monthly climatologies (plotted as the percentage of maximum) of satellite observations for Madeira-Tapajos (a,d,g), Tapajos-Xinghu (b,e,h) and Xinghu-Tocantins-Araguaia (c,f,i) ecoregions; satellite observations include TWS and direct and total PAR (a-c); VOD, LAI and MAIAC EVI (d-f). GEP and Pc from four flux tower sites are also presented (g-i), including Reserve Jaru (RJA), Tapajos K67 (K67), Tapajos K83 (K83) and Caxiuana (CAX) sites. Horizontal lines represent interpretations (i.e. examination of plots if specific data was not provided) of reported field data within ecoregions, including increasing (blue-solid) and decreasing (blue-dotted) PAW [1-Asner et al 2004, 2-Brando et al 2010] and soil water content [3-Fisher et al 2007]; increasing woody growth (brown) [4-Goulden et al 2004, 5-Rice et al 2004, 6-Saleska et al 2003]; increasing leaf flush (green) [2-Brando et al 2010, 7-Doughty and Goulden 2008]; peaks in leaf litterfall rates (yellow) [2-Brando et al 2010, 5-Rice et al 2004, 8-Barlow et al 2007], and increasing sap flow (red) [3-Fisher et al 2007].

Figure 5.4. Sinusoidal model climatology for TWS, VOD and LAI; direct PAR monthly climatology and statistics (box plots) of dry months per year by ecoregion. TWS, VOD and LAI, are plotted as anomalies from the long-term means [mean value (y_0) subtracted from fitted values (y_t)], and the y-axis (not shown) for TWS, VOD, and LAI are relatively scaled for visual interpretation of phase shifts. Box plots display median, 25th and 75th percentiles, and 10th and 90th percentiles. Ecoregion plots are ordered from west (top left) to east (bottom right).

Figure 5.5. Least-squares linear regression relationships between mean dry season length from TRMM and associated phase shift differences (months) for TWS and VOD, VOD and LAI, and TWS and LAI by ecoregion.

Figure 5.6. Pixel-wise (0.25 degree) relative canopy phenology adaptation to light or water availability based on the linear relationship between the mean number of dry months per pixel from TRMM precipitation, and the seasonal phase shift between VOD and LAI across ecoregions. Yellow (Blue) pixels denote areas where canopy water uptake and timing of canopy development and growth have adapted predominantly to light (water) availability, with dry season generally increasing from west to east, respectively.

Figure 6.1. Yearly maps of the Net Primary Productivity Indicator for years 2000 and 2001. The NPP anomaly is calculated as the given year's difference from the full data record (2000-2013) mean.

Figure 6.2. Summary plot of the NPP Anomaly displaying the percent of area (bars) in the contiguous U.S. above or below the long-term mean, in 20gC m^{-2} increments. Included is the sum of national NPP (black line) by year.

Figure 6.3. Map of the MODIS GPP Anomaly for the July 20-27, 2004 period with year 2004 Alaska fire perimeters (black polygons). Time series (8-day) plots of GPP Anomaly means from 2000 to 2013 within the two labeled fire perimeters (1,2). Pink bar is year of fire.

Figure 6.4. North America annual ET anomalies (2001, 2002, 2003) relative to a six year (2001-2006) average.

Figure 6.5. Workflow diagram for production of Indictors. Iterative algorithm development and product creation will take place at NTSG at the University of Montana. Initial products will be distributed to end-users for feedback which will be incorporated throughout the iterative process. The operational algorithm will then be transferred to NEX for automated processing.

Figure 6.6. Yearly NPP anomalies from the long-term mean for both the total U.S. (filled areas) and by regions (bars), providing a proxy to determine regional contributions to the overall U.S. NPP anomaly.

Figure 6.7. Yearly NPP anomalies from the long-term mean for both the total U.S. and by region. The 50 gC/m^2 and -50 gC/m^2 reference lines (displayed in the U.S. plot) are maintained across each plot.

Figure 6.8 Yearly NPP anomalies from the long-term mean for both the total U.S. and by region displayed as cascade plots representing accumulation or depletion of NPP through time.

Figure 6.9. Experimental summary figure of four Climate Indicators (Global Temperature, Atmospheric CO2, Sea Ice Extent, Vegetation Productivity). The figure aims to provide a synopsis of long (large arrows) and short (small arrows) term trends, the degree of concern related to those trends (arrow color), the first and most current measures, and the time series. The condensed figure is formatted to fit in a newspaper column or on the borders of a webpage and resemble common financial indicators (e.g. stock market trends, commodity prices).

Figure 6.10 A further distillation of the information from four Climate Indicators (Global Temperature, Atmospheric CO2, Sea Ice Extent, Vegetation Productivity) provided in Figure 6.9, with an emphasis on long-term trend (first column), 5-year trend (second column), and change from the previous year (third column).

Figure 6.11. Visuals of Global Temperature Anomalies, Net Primary Productivity Anomalies, and Sea Ice Extent data records. Numbers to left and right of each bar display the minima and maxima of the data records, and year of occurrence in parentheses. Change over a recent period is shown; large white circle (current year's value) and small grey circle (past value - for NPP and Sea Ice Extent 3 years and for Temperature 5 years) and red arrow to displays direction of change. The color gradient is a histogram of the number of years within the range; i.e. dark colors represent peaks in histograms and highlights the distribution (e.g. uniform, bi-modal, skewed) of the data records.

Chapter 1. Introduction

Phenology is the study of the timing of recurring biological events, the causes of their timing, their relationship to biotic and abiotic forces, and the inter-relations among phases of the same or different species (Lieth, 1974). Seasonal changes in leaf area control terrestrial vegetation feedbacks to the climate system (e.g. albedo, surface energy balance, partitioning of latent and sensible heat fluxes) with cascading effects on regional-to-global circulation patterns. The seasonal onset of vegetation activity, including canopy growth and associated increases in land-atmosphere water, energy and carbon (CO2) exchanges influences weather and climate variability. Vegetation phenology specifically characterizes the seasonal timing of vegetation growth and senescence and is often identified through observed phenophases such as budburst, leaf unfolding, or changes in leaf color and satellite derived phenology metrics, such as the start, peak, and end of the growing season. The timing, rate and duration of these phenological events are integral components in the study of global change and the carbon cycle through direct effects on vegetation photosynthesis, carbon sequestration and land-atmosphere water and energy exchange (Peñuelas et al. 2009). The Committee on Earth Observation Satellites Land Product Validation (CEOS-LPV) subgroup has also recently established a Phenology focus area to develop validation protocols for satellite derived vegetation phenology products.

The study of phenology has historic roots dating back approximately 3000 years (Zhu, 1931). These historic references primarily relate to agricultural practices and it was not until the mid-twentieth century that phenology became an established scientific discipline. The seminal work by Lieth (1974) was the first modern synthesis to examine the interdisciplinary extent of the field and spawned the emergence of phenology as an environmental science. In the last 15 years, the study of Land Surface Phenology (LSP - recently defined by the CEOS-LPV to represent satellite-based products that are derived by summarizing an annual land surface signal) has undergone a resurgence through the application of long-term records provided by satellite sensors, the creation of citizen science networks to aid in observations, and canopy mounted cameras to record high temporal resolution changes in canopy status; all of which

have allowed for the assessment of climate change impacts on vegetation phenology. This led the U.S. Global Change Research Program to include a set of Phenology Indicators as part of a system of indicators to be included in the upcoming National Climate Assessment.

An ISI Web of Science analysis finds 876 papers published in the last 15 years (Figure 1; red bars) that have used satellite data to derive LSP, with an average 20% increase per year. The citations of these papers are even stronger, averaging over 3000 per year for the last five years (Figure 1; blue line). LSP is clearly a growing field of research in environmental and ecological applications. With approximately 35 years of continuous global data and planned new sensors, satellite remote sensing provides a unique record to quantify global land surface phenological changes and the potential impacts of climate change.

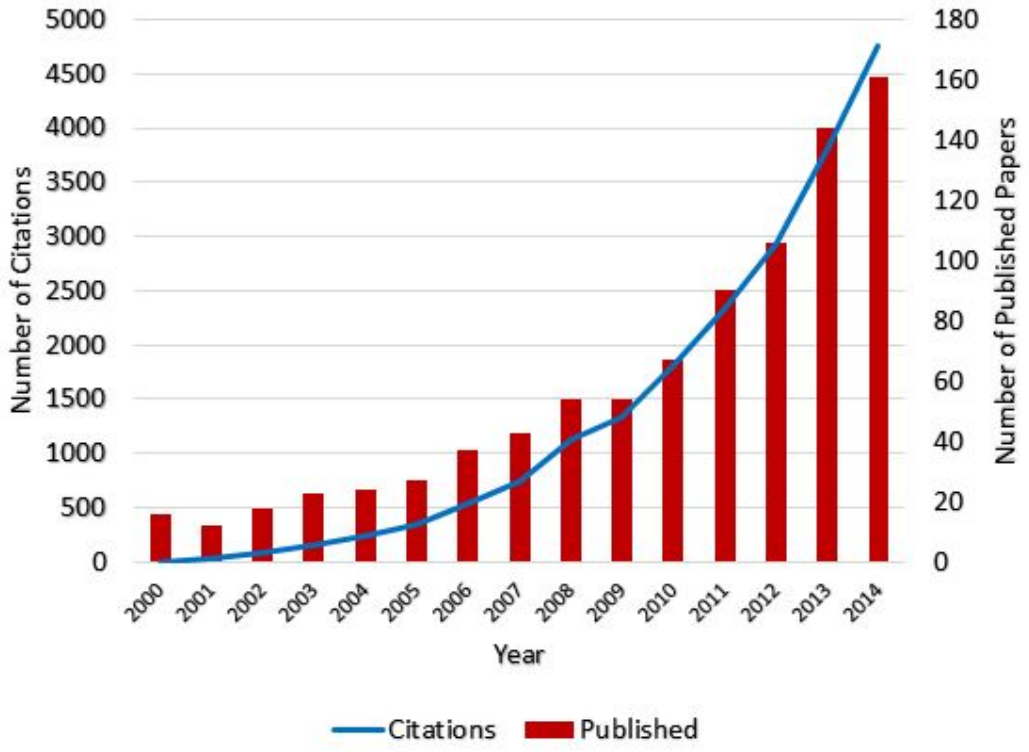

Figure 1.1. Land Surface Phenology publications (red bars) and citations (blue line).

The study of Phenology has blossomed into a cross-disciplinary science that can identify both drivers and constraints on ecological system dynamics and inform decisions relative to societal risks and benefits from a changing climate. As with most rising scientific disciplines a

wide range of data collection methods and protocols have been established across individual government agencies and research initiatives. These data collections have been running along parallel tracks, but due to their system specific temporal and spatial resolutions, merging these data to conduct integrative cross-disciplinary research has been a challenge. Land surface phenology observations from satellite remote sensing provide yearly vegetation phenology metrics (e.g. start, peak and end of season) at 250m to ~5km resolution on national to global scales. Canopy and understory automated cameras (e.g. The PhenoCam Network) provide high temporal resolution (daily to sub-daily) stand level observations of vegetation status. Species level in situ observations are also available via research and citizen science networks (e.g. USA-NPN) and while highly valuable, collected following a precise protocol, and covering a wide geographic range, they are geographically disparate and not observed at a systematic sampling frequency.

The disparity in spatial and temporal frequency across observations has hindered efforts to validate the satellite remote sensing scale phenology metrics and to better inform global circulation models. Community members have highlighted the need to improve understanding of environmental controls and land cover heterogeneity on vegetation phenology and incorporate this knowledge to better inform phenological components of biophysical models (Richardson et al., 2012). The Center on Earth Observations Land Product Validation (CEOS-LPV) Phenology subgroup has identified the need to synergize phenology datasets as a vital first step in validating derived phenology metrics. Past efforts to compare and validate these metrics have highlighted the difficulty in overcoming not only the temporal and spatial discrepancies between satellite and near-surface (PhenoCam) remote sensing (Hufkens et al., 2011) but also the wide array of methods used to define phenology metrics (White et al., 2009). Incorporating high-resolution spatial and temporal in situ vegetation phenology information can aid in overcoming these discrepancies and in particular better inform dynamic global vegetation models and carbon budgets (Jeong et al., 2013) and better attribute variation in carbon assimilation to local climate regimes (Schwartz et al., 2013). Combining the three levels of phenology data will also help to answer emerging questions such as the extent to which

regional and species diversity will exert critical controls on phenological events and how interspecies competition may affect phenology (Jeong et al., 2013).

1.1 Land Surface Phenology from Satellite Optical-Infrared Data

In situ phenological measures are often focused on species, population or community level events (e.g. budburst, leaf unfolding, leaf senescence) while satellite derived metrics are based on the aggregate vegetation phenology within a pixel footprint. The pixel may be composed of a variety of species or multiple land cover types which may exhibit differences in timing of growth onset and senescence. The specificity of satellite derived measures is therefore reduced leading to the extraction of more general metrics (i.e. the start, peak and end of the growing season). Satellite derived measures do however present distinct advantages such as global coverage, high temporal frequency, and objectivity in measurement. Spectral vegetation indices (VIs), including the Normalized Difference Vegetation Index (NDVI) and Enhanced Vegetation Index (EVI), exploit differences in the reflectance of green vegetation between red and near-infrared wavelengths and are sensitive to photosynthetic canopy cover and associated metrics including leaf area index (LAI). A variety of global VI and LAI products are currently available from operational satellite sensors including MODIS and AVHRR. These data provide a means for LSP monitoring, but retrievals are constrained over many areas and periods by signal degradation from low solar illumination and atmospheric clouds, smoke and aerosol contamination. These constraints require spatial and temporal compositing of the data to reduce noise, which can create data gaps, reduce temporal fidelity and degrade the LSP signal for many parts of the globe.

To mitigate for time series gaps and noisy retrievals, the majority of LSP metric algorithms first apply a gap-filling or smoothing technique. The smoothed time series are then analyzed using threshold-based approaches which use a pre-defined or relative reference value for determining the start and end of season (Lloyd 1990, Reed et al. 1994, Jonsson & Eklundh 2004) or curve derivative approaches which use local maximums or minimums of derivative functions fit to the vegetation index time series (Zhang et al. 2006, Tan et al. 2010). These methods have been shown to be effective estimators of vegetation dynamics and phenology

events, but validation of these metrics in terms of their relation to species, population, or community level events has only been minimally assessed (Polgar et al. 2013, Liang et al 2011, Schwartz & Hanes 2009). Even with such limitations the optical-infrared (IR) wavelengths have long been used with considerable success (Reed et al. 2009) and until recently have been the primary means for global LSP monitoring.

1.2 Phenological Response to a Changing Climate

The effect of climate change on phenology patterns and trends has been observed through a generally earlier spring onset and delayed end of the growing season (e.g. Delbart et al. 2008, Piao et al. 2008, Parmesan 2007). The temporal variation in the seasonal onset of vegetation growth has been documented across multiple scales from in situ measures of species specific first leaf and first flower events (Wolfe et al. 2005) to continental and global scale assessments of canopy leaf onset (Zhang et al. 2007) and growing season length (Piao et al. 2007). The rise in mean annual temperatures from climate change has resulted in the earlier onset of optimum spring temperatures for vegetation growth (Xu et al. 2013) and optical-IR satellite remote sensing studies have demonstrated a trend toward earlier spring onset, particularly at northern latitudes. Implementing satellite derived NDVI retrievals Jeong et al. (2011) found that the northern hemisphere start of season advanced by 5.4 days from 1982 – 2008 (Figure 1.2). Vegetation growth was estimated to increase by up to 10% per decade in certain regions from this earlier onset and extension of the growing season.

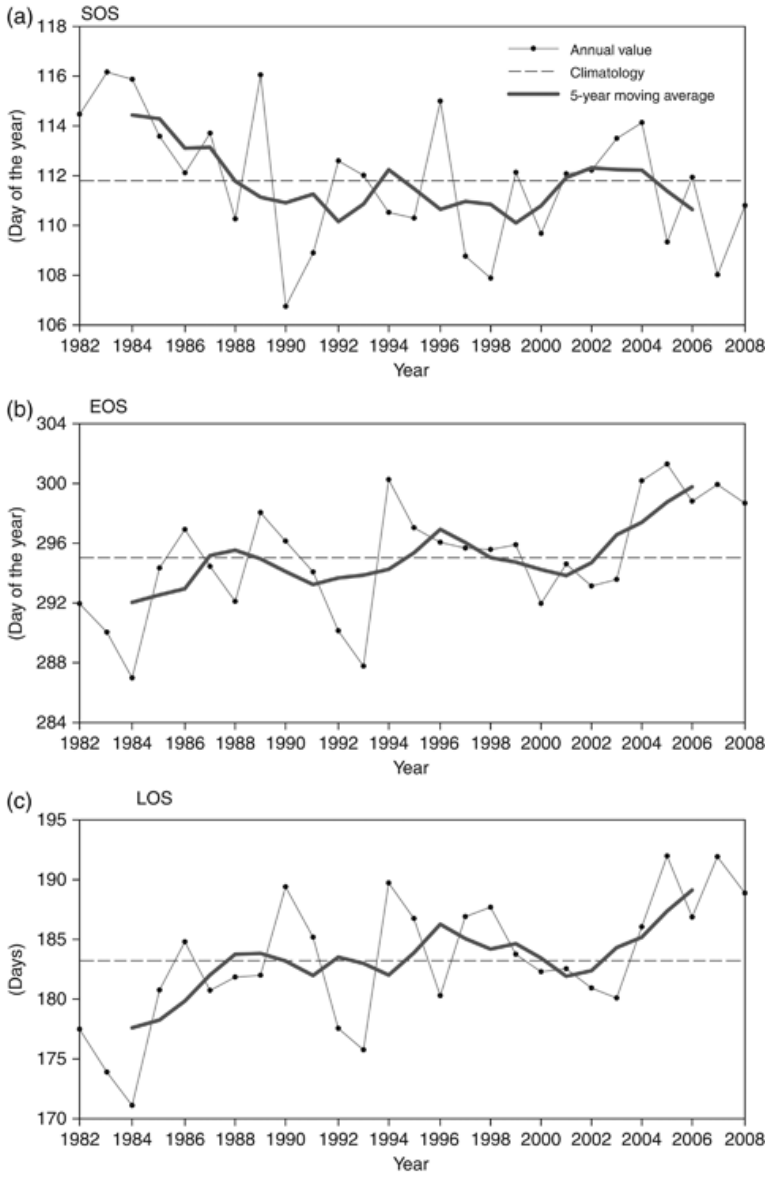

Figure 1.2. Interannual variations of area-averaged start (SOS), end (EOS) and length (LOS) of season of temperate vegetation in the northern hemisphere for 1982-2008 (Jeong et al., 2011)

Although there is widespread evidence supporting these phenological responses, conflicting results regarding satellite derived phenology trends and the methods used to define phenology metrics have been under examination (White et al. 2009). This is due to the challenge of equating LSP metrics to in situ phenology measurements (Schwartz & Hanes 2009, Wang et al. 2005), the lack of widely available field level measures of vegetation phenology, and the reliance on optical-IR measures for deriving LSP metrics.

1.3 Microwave Vegetation Optical Depth and LSP Monitoring

An alternative data source for global LSP monitoring involves the use of satellite microwave remote sensing, which is sensitive to changes in frozen/non-frozen land surface conditions, and vegetation biomass and canopy water content while being relatively insensitive to signal degradation from solar illumination and atmospheric effects, and providing near daily global coverage. Previous studies have applied satellite passive and active (radar) microwave remote sensing data records for vegetation phenology assessment (Shi et al. 2008, Frolking et al. 2006, Jones et al. 2011, Jones et al. 2012), vegetation drought response (Frolking et al. 2005, 2011), potential growing season variability or length of the non-frozen season (Figure 1.3) (Kimball et al. 2004, 2006; Kim et al., 2012, 2014), and seasonal changes in evapotranspiration and canopy CO_2 exchange (Min & Lin 2006).

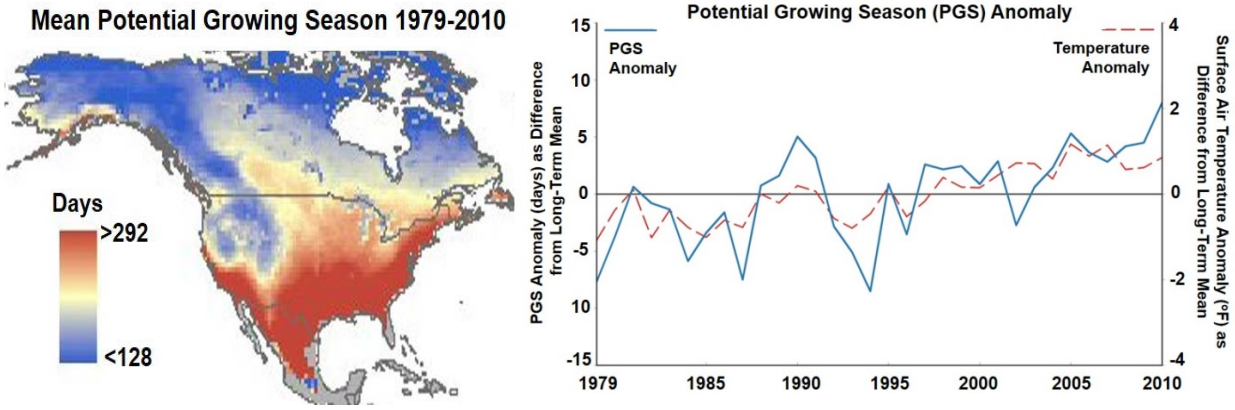

Figure 1.3. Map of the mean annual Potential Growing Season (PGS) from 1979-2010 for North America (left). Plot of PGS and surface air temperature anomalies (as difference from the long-term mean) for Alaska and the Contiguous U.S. for the 1979-2010 period (right). (Kim et al., 2012, 2014)

Microwave LSP monitoring is also subject to constraints and limitations; retrievals are generally coarse (~25km) and sensitive to inundation, soil moisture, and landscape freeze-thaw dynamics that may vary independent of vegetation changes, as well as possible saturation effects over high biomass levels (Frolking et al. 2006).

The microwave Vegetation Optical Depth (VOD) parameter defines the frequency dependent extinction of land surface microwave emissions by the intervening vegetation layer (Jackson & Schmugge 1991, Van de Griend & Wigneron 2004). VOD is sensitive to changes in

vegetation water content and biomass (inclusive of photosynthetic and non-photosynthetic components), and provides a measure of vegetation phenology that is complementary to the optical-IR response to chlorophyll content or "greenness". A consistent global VOD record (Figure 1.4) was developed from 18.7, 10.7 and 6.9 GHz frequency brightness temperature (T_b) measurements from the AMSR-E (Advanced Microwave Scanning Radiometer for EOS) sensor on the NASA EOS Aqua satellite and provides global coverage and near daily temporal fidelity under classified non-frozen conditions from 2002 to 2012 (Jones & Kimball 2011). The VOD retrieval algorithm minimizes potential noise effects from dynamic atmosphere precipitable water vapor, temperature, surface inundation and soil moisture, resulting in global consistency and relatively high accuracy (Jones et al. 2009). A comprehensive review and analysis of AMSR-E VOD is provided in Chapter 2.

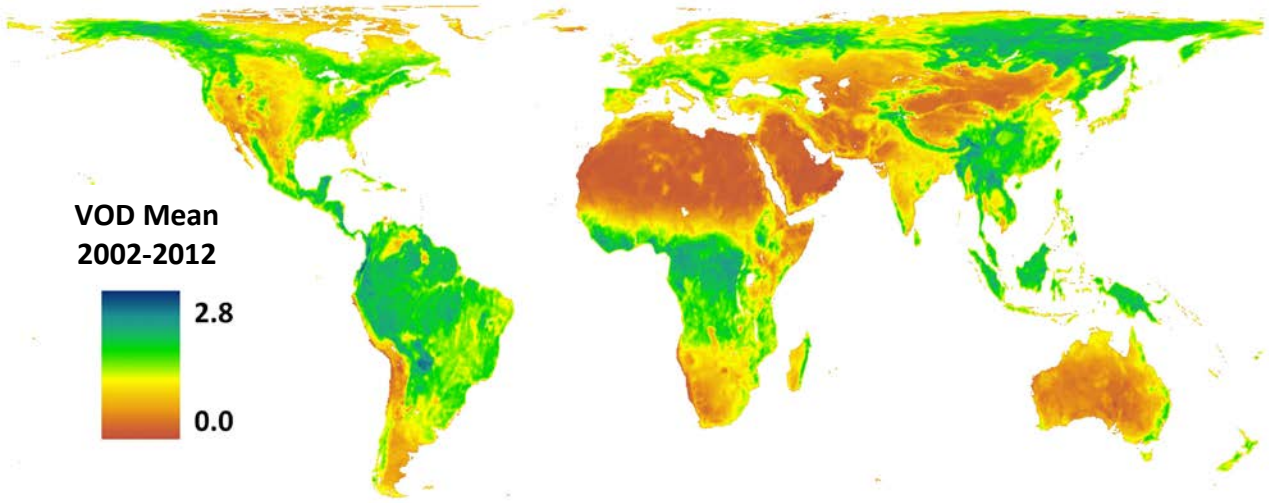

Figure 1.4. Global Mean VOD at 18.7GHz (Jones et al. 2011)

1.4 Comparing Microwave and Optical-IR LSP

Both VOD and optical-IR measures will respond to the onset of vegetation respiration and growth. Phase differences in the seasonal patterns of these two measures are expected however due to variation in physiological mechanisms, the canopy structure of biomes being measured, and the climatic constraints imposed on those biomes which limit physiological function; in particular temperature extremes and water supply. An initial global analysis (Jones et al. 2011) comparing VOD to optical-IR vegetation indices (NDVI, EVI, LAI) and a bioclimatic

Growing Season Index (GSI; Jolly et al. 2005) showed strong temporal correspondence (see Chapter 2). Phase shifts were evident in the VOD time series which displayed a delayed seasonal onset in regions where water availability is a primary constraint to growth; grasslands, savannas, woody savannas, and shrublands. The VOD also displayed a prolonged senescence period over deciduous broadleaf and mixed forest regions. As leaves senesce the optical-IR indices decrease in response to diminished photosynthetic capacity yet leaf biomass persists until abscission and will continue to attenuate the microwave signal. A comprehensive review and analysis of AMSR-E VOD and it comparison to optical-infrared satellite data is provided in Chapter 2.

The VOD was also used to derive start of season (SOS) estimates for the contiguous United States at an ecoregion scale and then compared to MODIS derived NDVI Greenup (Figure 1.5) and flux tower based SOS estimates (Jones et al. 2012). Temporal offsets between these SOS estimates generally followed underlying physiological response characteristics related to regional climate constraints on vegetation productivity, canopy structure dynamics in the form of woody vegetation cover, and underlying vegetation water and carbon allocation processes. The VOD SOS generally preceded NDVI Greenup in cold temperature constrained ecoregions and followed Greenup in warmer, water limited ecoregions, with delays increasing for areas with greater woody vegetation cover.

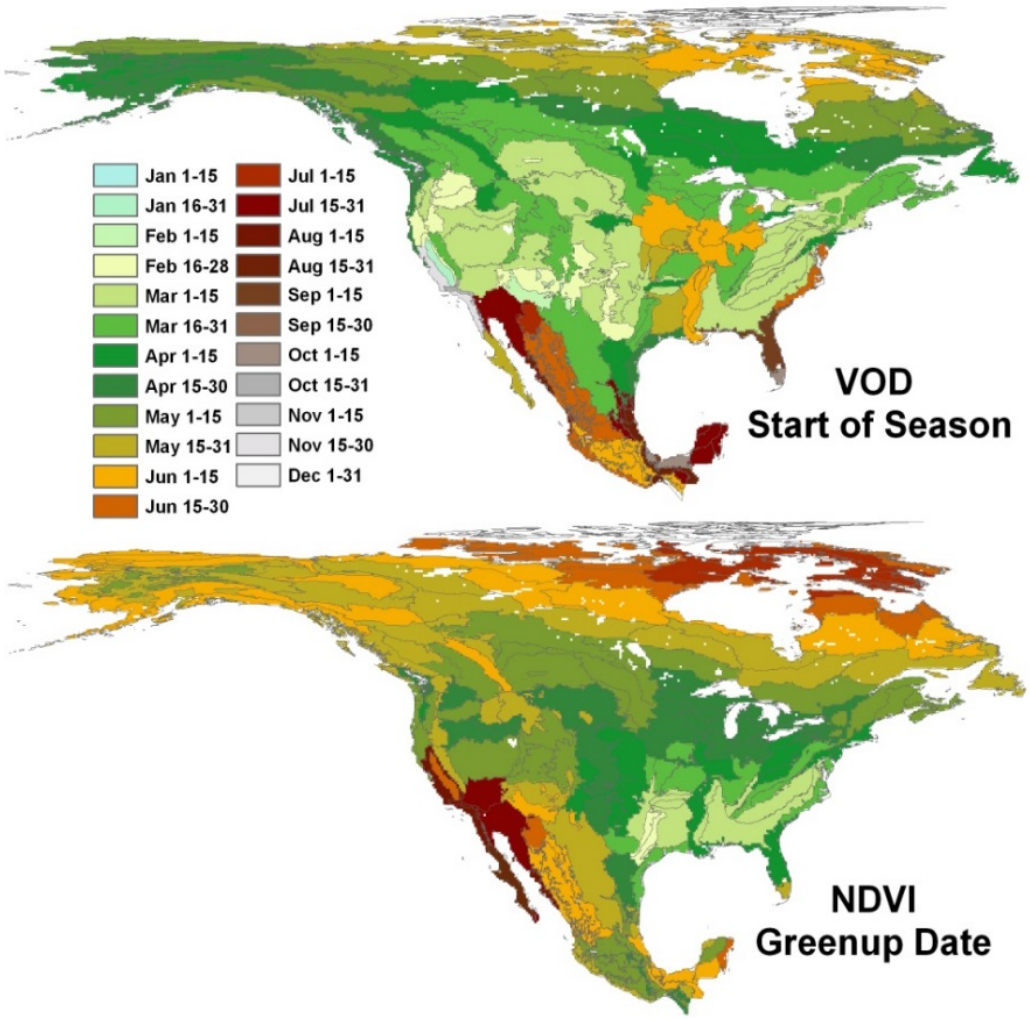

Figure 1.5. Four year (2004-2007) mean of microwave VOD SOS and MODIS-for-NACP NDVI Greenup Date by ecoregion. (Jones et al. 2012)

1.5 Variance and Validation of LSP Metrics

Satellite derived phenology metrics represent an aggregate pixel level response which is difficult to equate to species or population specific phenological events. This is particularly difficult due to the spatial and temporal disparity between LSP and in situ metrics (Liang et al. 2011). LSP metrics are provided from 250m to 0.05 degree resolution while in situ measures tend to be measures of individual species with sparse geographic distribution and limited in time. Temporal variation in optical-IR and microwave LSP metrics are also dependent on the spatial resolution and frequency (i.e. wavelength) of the data implemented and on the methods

employed. Also, there is no widespread agreement within the LSP science community on the best methodology for computing LSP metrics. White et al. (2009) conducted an intercomparison of start of season methods and concluded that independent of interpretive and assessment data there is no rational basis for selecting one method over another. Figure 1.6 is an example of the temporal range of start and end of season phenology metrics derived over a single site at Harvard Forest, Massachusetts, USA. The four satellite optical-IR Season Onset and End of Season metrics each range across approximately 40 days.

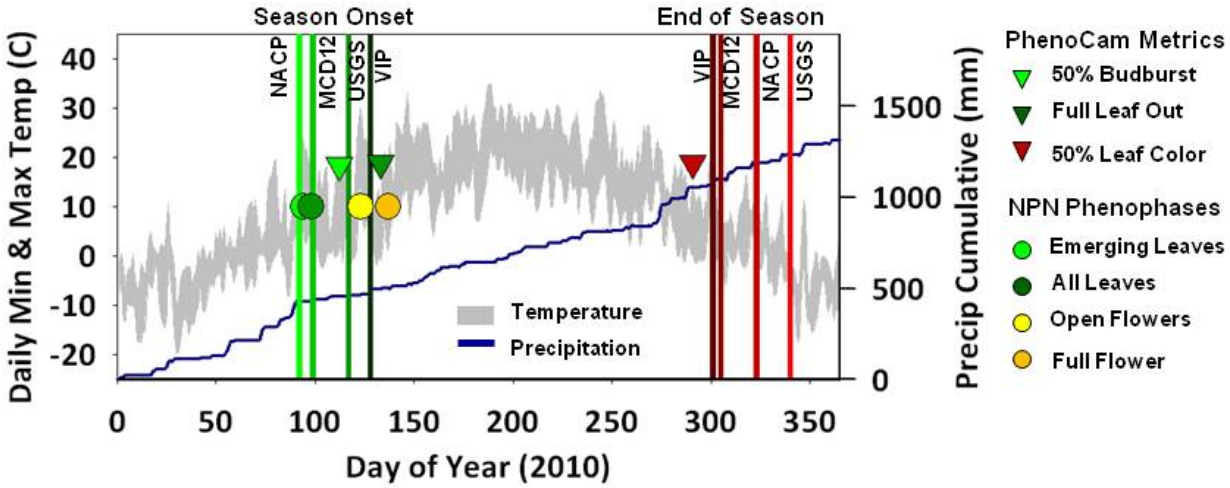

Figure 1.6. The range of daily maximum and minimum temperatures (gray area), precipitation accumulation (blue line) and a collection of phenology metrics from four satellite LSP products (green and red bars), phenology camera time series (triangles), and USA-NPN observed phenophases (circles) at Harvard Forest, MA, USA.

Two Season Onset estimates (NACP, MCD12Q2) are well aligned with National Phenology Network (NPN) observed phenophases and the remaining two (USGS, VIP) are comparable to phenology camera (PhenoCam) metrics of budburst and leaf out.

In an effort to validate optical-IR LSP metrics, the CEOS-LPV Phenology focus group has made progress in identifying the initial steps for LSP validation. They have pinpointed a clear need to synergize phenological datasets that exist across disparate spatial and temporal scales. The group aims to provide packaged collections of phenology products to initiate and support phenology validation efforts. The Phenology Focus Group is working in conjunction with USGS Remote Sensing Phenology, NASA phenology product providers (Boston University, MODIS-for-

NACP, University of Arizona VIP lab), USA National Phenology Network, PhenoCam, and Oak Ridge National Laboratory Distributed Active Archive Center to develop a web-based interface allowing users to define a geographic area of interest and access all available phenology data (satellite products, phenology camera time series, in-situ observations) within that area. The interface, named PhenoFrame, will also provide a host of ancillary data products (meteorology, land cover, digital elevation models, fire perimeters and others), to aid in assessing the role of climatic and biophysical drivers on vegetation phenology (Figure 1.7).

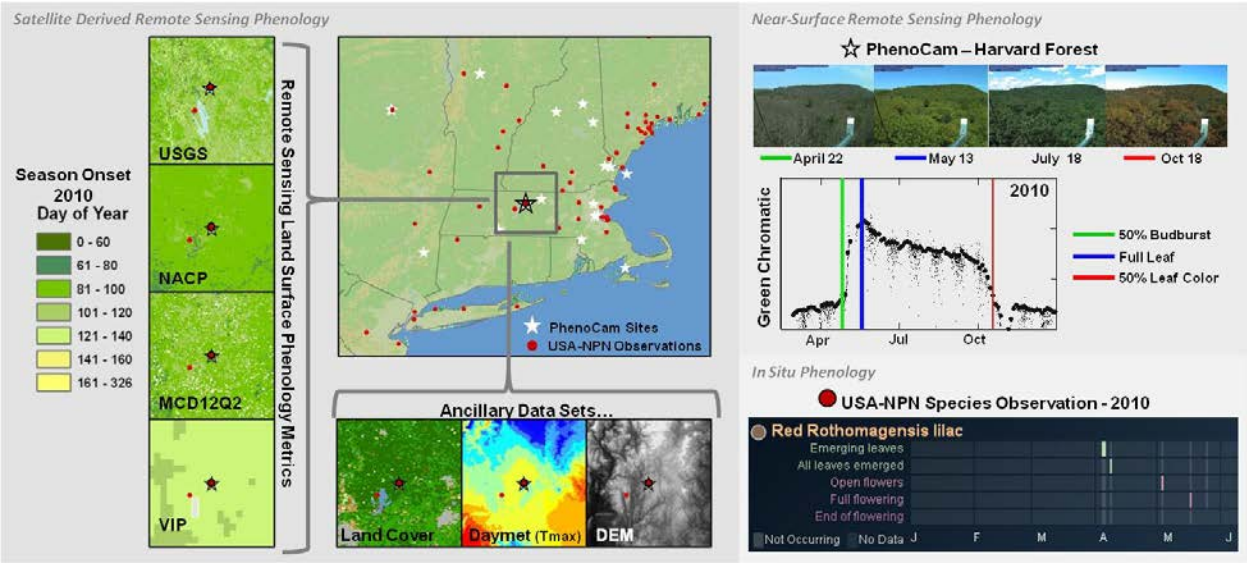

Figure 1.7. Prototype visualization of data via PhenoFrame for one region; Harvard Forest, MA, USA. Red circles on maps are in situ USA-NPN observations and white stars are established PhenoCam sites.

It is clear that validation of these LSP metrics and an assessment of the variance across products and methods are the next critical steps that need to be addressed within the LSP scientific community. The needed validation and variance assessment (and the steps integral to that process) will also help better inform terrestrial biosphere models. Desai (2010) showed that if the net uptake of CO_2 is to be correctly predicted in these models, an accurate representation of vegetation phenology interannual variability is critical. Recently, Richardson et al., (2012) evaluated the representation of phenology in 14 terrestrial biosphere models participating in the North America Carbon Program (NACP) Site Synthesis. The authors found that for deciduous forests, an early SOS bias of two weeks or more was typical across all models

which resulted in a 13% over prediction of gross ecosystem productivity. Such misrepresentation of phenology has consequences beyond modeling ecosystem productivity. For example, Levis and Bonan (2004) demonstrated that when phenology was prescribed on a regional scale, the coupling of the Community Land Model and the Community Atmosphere Model could not reproduce observations of reductions in temperature associated with the onset of leaf emergence and associated increases in transpiration. Insufficient coupling of the land surface to the atmosphere during critical phenological stages could lead to large errors in the modeled seasonal evolution of weather patterns (Richardson et al. 2012) and thus present cascade effects on other model components. LSP science applications would highly benefit from an improved understanding of environmental controls on phenology and an assessment of the variation and uncertainty across LSP metrics.

1.6 Dissertation Objectives and Hypothesis

In this dissertation I implement satellite microwave vegetation optical depth (VOD) in conjunction with an array of satellite measures, GPS reflectometry, field observations and flux tower data to achieve the following objectives: 1) clarify vegetation phenology response to water, temperature and solar irradiance constraints at local, regional, continental, and global scales, 2) demonstrate the asynchrony between changes in vegetation water content and biomass and changes in greenness and leaf area in relation to land cover type and climate constraints, 3) provide enhanced assessment of seasonal recovery of vegetation biomass and phenology following wildfire and 4) present a method to more accurately model tropical vegetation phenology using VOD. The fifth objective is to develop a set of potential climate indicators using NASA MODIS data products for use in sustained National Climate Assessments.

This effort is based on four primary hypotheses:

1. Through its sensitivity to changes in vegetation water content and biomass, the seasonality of microwave VOD and associated phenology metrics will lag or lead optical-infrared derived phenology metrics based on specific land cover responses to climatic constraints on vegetation growth.

2. Vegetation water content changes inferred from GPS Normalized Microwave Reflection Index data provide validation of VOD response to changes in vegetation water content over the western continental USA and Alaska.

3. The satellite microwave VOD signature will display an alternate vegetation recovery response related to canopy foliar and woody biomass regeneration following large scale fire events versus the canopy greenness recovery inferred from the optical-infrared satellite record. The variation in response will be dependent on the proportion of woody vegetation loss within fire perimeters.

4. Equatorial Amazon forests exhibit a distinctive seasonal signal whereby the seasonal timing of water availability, canopy biomass growth, and net leaf flush are responsive to seasonal disparities in both water and solar radiation availability.

1.7 Dissertation Structure

This Dissertation consists of six chapters. Chapter 2 provides a broad overview and analysis of satellite AMSR-E Microwave Vegetation Optical Depth (VOD), its implementation for monitoring global land surface phenology, and a comparison to satellite optical-infrared data and phenology metrics. Chapter 3 presents a comparison of VOD to a novel GPS derived vegetation water content measure (the Normalized Microwave Reflection Index - NMRI) and associated phenology metrics to test whether the high spatial resolution NMRI can aid in VOD validation. Chapters 4 and 5 present direct applications of VOD for phenology monitoring and modeling. Chapter 4 implements VOD to monitor vegetation phenology and biomass recovery following a year of extreme wildfires in Alaska, USA and Canada. Chapter 5 uses VOD to monitor and model tropical vegetation phenology over Amazon forests which can inform and enhance the Community Land Model that operates within the Community Earth System Model. Chapter 6 presents the development of Gross Primary Productivity (GPP) and Net Primary Productivity (NPP) vegetation health climate indicators as part of a NASA funded project entitled "Development and Testing of Potential Indicators for the National Climate Assessment; Translating EOS datasets into National Ecosystem Biophysical Indicators".

1.8 References Cited

Delbart N, Picard G, Le Toans T, Kergoat L, Quegan S, Woodward I, Dye D, Fedotova V (2008) Spring phenology in boreal Eurasia over a nearly century time scale. Global Change Biology, 14, 603-614

Frolking S, Fahnestock M, Milliman T, McDonald K, Kimball J (2005) Interannual variability in North American grassland biomass/productivity detected by SeaWinds scatterometer backscatter. Geophysical Research Letters, 32, 1–5.

Frolking S, Milliman T, McDonald K, Kimball J, Zhao M, Fahnestock M (2006) Evaluation of the SeaWinds scatterometer for regional monitoring of vegetation phenology. Journal of Geophysical Research, 111.

Frolking S, Milliman T, Palace M, Wisser D, Lammers R, Fahnestock M (2011) Tropical forest backscatter anomaly evident in SeaWinds scatterometer morning overpass data during 2005 drought in Amazonia. Remote Sensing of Environment, 115, 897–907.

Hufkens K, Friedl M, Sonnentag O, Braswell BH, Milliman T, Richardson AD (2011) Linking near-surface and satellite remote sensing measurements of deciduous broadleaf forest phenology. Remote Sensing of Environment, 117, 307-321.

Jackson TJ, Schmugge TJ (1991) Vegetation Effects On The Microwave Emission Of Soils. Remote Sensing Of Environment, 36, 203-212

Jeong SJ, Ho CH, Gim HJ, Brown ME (2011) Phenology shifts at start vs. end of growing season in temperate vegetation over the Northern Hemisphere for the period 1982-2008. Global Change Biology, 17, 2385–2399.

Jeong SJ, Medvigy D, Shevliakova E, Malyshev S (2013) Predicting changes in temperate forest budburst using continental-scale observations and models. Geophysical Research Letters, 40, 359–364.

Jolly WM, Nemani R, Running SW (2005) A generalized, bioclimatic index to predict foliar phenology in response to climate. Global Change Biology, 11, 619-632

Jones LA, Kimball JS (2011) Daily Global Land Surface Parameters Derived from AMSR-E. Boulder, Colorado USA: National Snow and Ice Data Center. Digital media.

Jones LA, Kimball JS, McDonald KC, Chan SK, Njoku EG (2009) A method for deriving northern hemisphere vegetation phenology, land surface wetness, and open water fraction from AMSR-E. In, IGARSS Symposium. Cape Town, South Africa

Jones MO, Jones LA, Kimball JS, McDonald KC (2011) Satellite passive microwave remote sensing for monitoring global land surface phenology. Remote Sensing of Environment, 115, 1102–1114.

Jones MO, Kimball JS, Jones LA, McDonald KC (2012) Satellite passive microwave detection of North America start of season. Remote Sensing of Environment, 123, 324–333.

Jonsson P, Eklundh L (2004) TIMESAT - a program for analyzing time-series of satellite sensor data. Computers & Geosciences, 30, 833–845.

Kim Y, Kimball JS, Didan K, and Henebry GM, 2014. Response of vegetation growth and productivity to spring climate indicators in the conterminous United States derived from satellite remote sensing data fusion. Agricultural and Forest Meteorology, 194, 132-143.

Kim Y, Kimball JS, Zhang K, and McDonald KC, 2012. Satellite detection of increasing northern hemisphere non-frozen seasons from 1979 to 2008: Implications for regional vegetation growth. Remote Sensing of Environment 121, 472-487.

Kimball JS, McDonald KC, Running SW, Frolking SE (2004) Satellite radar remote sensing of seasonal growing seasons for boreal and subalpine evergreen forests. Remote Sensing of Environment, 90, 243–258.

Levis S, Bonan GB (2004) Simulating springtime temperature patterns in the community atmosphere model coupled to the community land model using prognostic leaf area. Journal of Climate, 17, 4531–4540.

Liang L, Schwartz MD, Fei S (2011) Validating satellite phenology through intensive ground observation and landscape scaling in a mixed seasonal forest. Remote Sensing of Environment, 115, 143–157.

Lieth H (1974) Phenology and Seasonality Modeling, Springer-Verlag, New York 444 pp.

Lloyd D (1990) A phenological classification of terrestrial vegetation cover using shortwave vegetation index imagery. International Journal of Remote Sensing, 11, 2269–2279.

Min Q, Lin B (2006) Remote sensing of evapotranspiration and carbon uptake at Harvard Forest. Remote Sensing of Environment, 100, 379–387.

Parmesan C (2007) Influences of species, latitudes and methodologies on estimates of phenological response to global warming. Global Change Biology, 13, 1860–1872.

Penuelas J, Rutishauser T, Filella I. (2009) Phenology Feedbacks on Climate Change. Science, 324, 887-888

Piao S, Ciais P, Friedlingstein P, Peylin P, Reichstein M, Luyssaert S, Margolis H, Fang J, Barr A, Chen A, Grelle A, Hollinger DY, Laurila T, Lindroth A, Richardson AD, Vesala T (2008) Net carbon dioxide losses of northern ecosystems in response to autumn warming. Nature, 451, 49

Piao S, Friedlingstein P, Ciais P, Viovy N, Demarty J (2007) Growing season extension and its impact on terrestrial carbon cycle in the Northern Hemisphere over the past 2 decades. Global Biogeochemical Cycles, 21

Polgar CA, Primack RB, Dukes JS, Schaaf C, Wang Z, Hoeppner SS (2013) Tree leaf out response to temperature: comparing field observations, remote sensing, and a warming experiment. International Journal of Biometeorology

Reed B, White M, Brown J (2003) Remote Sensing Phenology. In: Phenology: An Integrative Environmental Science. pp. 365-381 (Ed. M. Schwartz) Springer, Netherlands.

Reed BC, Brown JF, Vanderzee D, Loveland TR, Merchant JW, Ohlen DO (1994) Measuring Phenological Variability From Satellite Imagery. Journal Of Vegetation Science, 5, 703-714

Richardson AD, Anderson RS, Arain MA, et al. (2012) Terrestrial biosphere models need better representation of vegetation phenology: results from the North American Carbon Program Site Synthesis. Global Change Biology, 18, 566–584.

Schwartz M, Hanes J (2009) Intercomparing multiple measures of the onset of spring in eastern North America. International Journal of Climatology

Schwartz M, Hanes J, Liang L (2013) Comparing carbon flux and high-resolution spring phenological measurements in a northern mixed forest. Agricultural and Forest Meteorology.

Shi J, Jackson T, Tao J, Du J, Bindlish R, Lu L, Chen K (2008) Microwave vegetation indices for short vegetation covers from satellite passive microwave sensor AMSR-E. Remote Sensing of Environment, 112, 4285–4300.

Tan B, Morisette JT, Wolfe RE, Gao F, Ederer GA, Nightingale J, Pedelty JA (2010). An Enhanced TIMESAT Algorithm for Estimating Vegetation Phenology Metrics From MODIS Data. IEEE Journal of Selected Topics in Applied Earth Observations and Remote Sensing, 4, 361

Van De Griend A, Wigneron J (2004) On the Measurement of Microwave Vegetation Properties: Some Guidelines for a Protocol. IEEE Transactions on Geosciences and Remote Sensing, 42, 2277–2289.

Wang Q, Tenhunen J, Dinh N, Reichstein M, Otieno D, Granier A, Pilegarrd K (2005) Evaluation of seasonal variation of MODIS derived leaf area index at two European deciduous broadleaf forest sites. Remote Sensing of Environment, 96, 475–484.

White MA, de Beurs KM, Didan K, et al. (2009) Intercomparison, interpretation, and assessment of spring phenology in North America estimated from remote sensing for 1982-2006. Global Change Biology, 15, 2335–2359.

Wolfe DW, Schwartz MD, Lakso AN, Otsuki Y, Pool RM, Shaulis NJ (2005) Climate change and shifts in spring phenology of three horticultural woody perennials in northeastern USA. International Journal of Biometeorology, 49, 303–9.

Xu L, Myneni RB, Chapin III FS, et al. (2013) Temperature and vegetation seasonality diminishment over northern lands. Nature Climate Change

Zhang X, Tarpley D, Sullivan JT (2007) Diverse responses of vegetation phenology to a warming climate. Geophysical Research Letters, 34, L19405.

Zhang XY, Friedl MA, Schaaf CB (2006) Global vegetation phenology from Moderate Resolution Imaging Spectroradiometer (MODIS): Evaluation of global patterns and comparison with

in situ measurements. Journal Of Geophysical Research-Biogeosciences, 111(G4), G04017.

Zhu K (1931) New Monthly Calendar, Bulletin of the Chinese Meteorological Society, 6, 1-14

Chapter 2. Satellite Passive Microwave Vegetation Optical Depth for Monitoring Land Surface Phenology

The sensitivity of optical and near-infrared wavelengths to photosynthetic canopy cover has long been used for global LSP monitoring (Reed et al., 2009). Spectral vegetation indices (VIs), including the Normalized Difference Vegetation Index (NDVI) and Enhanced Vegetation Index (EVI), exploit differences in the reflectance of green vegetation between red and near-infrared wavelengths and are sensitive to photosynthetic canopy cover and associated metrics including the leaf area index (LAI). A variety of global VI and LAI products are currently available from operational satellite sensors including MODIS and AVHRR. These data provide a means for LSP monitoring, but retrievals are confounded by the above constraints. An alternative data source for global LSP monitoring involves the use of satellite microwave remote sensing, which is sensitive to vegetation biomass and relatively insensitive to signal degradation from solar illumination and atmospheric effects, while providing near daily global coverage. Satellite active microwave sensors such as SeaWinds-on-QuikSCAT have been applied for mapping regional phenological variables associated with seasonal changes in canopy freeze/thaw status (Kimball et al. 2004b), canopy roughness and biomass water content (Frolking et al., 2005; 2006). Satellite microwave radiometers, such as AMSR-E on Aqua, are also sensitive to seasonal changes in landscape freeze/thaw status, canopy water content, and vegetation biomass but application to LSP detection and monitoring has been limited.

Past research has shown that the microwave polarization difference index (MPDI), defined as the difference of the first two Stokes parameters (H- and V- polarization) divided by their sum, corresponds with seasonal changes in vegetation water content and LAI (Becker & Choudury, 1988; Choudury & Tucker, 1987; Jackson & Schmugge, 1991; Paloscia & Pampaloni, 1992). The MPDI is sensitive to the NDVI (Becker & Choudury, 1988; Choudury et al., 1987), but is also sensitive to open water, soil moisture and surface roughness (Njoku & Chan, 2006). Recent advances in algorithm retrievals have focused on separating the multiple dependencies of the MPDI on soil moisture and surface roughness to obtain more robust measures of vegetation water content and canopy attenuation (Njoku & Chan 2006; Owe et al., 2001). Other advances have been made in the use of passive and active (i.e. radar) satellite microwave

remote sensing related to vegetation phenology (Shi, et al. 2008; Min & Lin, 2006a; Frolking et al., 2006; Kimball et al. 2004b), evapotranspiration and canopy CO_2 exchange (Min & Lin, 2006b), but there have been relatively few studies involving multi-year datasets (De Jue & Owe, 2003) and no direct application to LSP assessment over multiple years and a global domain.

In this study we evaluate the utility of satellite passive microwave remote sensing for LSP monitoring. We quantify global patterns and seasonal variability in vegetation optical depth (VOD) over a 6 year record (2003-2008). The VOD data are derived at moderate (~25 km) spatial resolution from AMSR-E 18.7 GHz frequency daily brightness temperature (T_b) measurements with input ancillary data also derived from AMSR-E and compared with alternative results derived using an entirely independent monthly emissivity database (Moncet & Liang, 2009). An algorithm sensitivity analysis is conducted to estimate VOD retrieval accuracy over a global range of vegetation biomass given algorithm assumptions. Temporal correlations are assessed between the VOD record and coincident VI and LAI measurements from satellite optical-infrared (MODIS) remote sensing and an independent, surface meteorology driven bioclimatic growing season index (GSI). The correspondence between VOD seasonal signals and coincident VI, LAI and GSI time series is examined on a global basis using pixel-wise correlation analysis to assess regional variations in these relationships with respect to land cover and climate characteristics. Land cover specific regional phenology signals and relative agreement among the different data records are also examined over nine spatially contiguous global biomes spanning a range of latitudes and climate conditions.

2.1 Methods

2.1.1 Passive Microwave Remote Sensing Retrieval of Vegetation Optical Depth

2.1.1.1 Vegetation Radiative Transfer

A target's thermal radiance at microwave wavelengths linearly increases with temperature and is expressed as a brightness temperature at a given polarization ($T_{b,p}$) equivalent to the physical temperature (T_s) of an ideal blackbody (emissivity = 1). The target's actual emissivity (e_p, usually <1) is determined by its refractive electrical properties and the polarization (subscript p) describing the preferred orientation of its electric field vector.

Current satellite microwave radiometers have generally coarse spatial resolution (>20 km for lower frequencies). As a result, the satellite observed radiance represents the aggregate microwave emissions of landscape elements (e.g. soil, vegetation, open water and atmosphere elements represented by subscripts *s*, *l*, *w*, and *a*, respectively) within the sensor field-of-view. Vegetation stems and leaves emit microwave radiation, absorb and scatter radiance from the soil and reflected emissions from the atmosphere. Water vapor and cloud liquid water in various atmospheric layers also absorb and emit scattered radiation (cloud liquid water and ice crystals also scatter radiation for higher frequencies >18.7 GHz). The well-known tau-omega (τ-ω) model was developed as a relatively simple method to describe upwelling radiation from the land surface as observed above a canopy (Ulaby et al., 1982; Mo et al., 1982):

$$T_b = T_s e_r \Gamma + (1-\omega) T_s (1-\Gamma) + (1-e_r)(1-\omega) T_s (1-\Gamma)\Gamma \quad (1)$$

$$\Gamma = \exp(-VOD) = \exp(-\tau/\cos\mu) \quad (2)$$

The emissivity of vegetation covered land is the sum of microwave emissions of the underlying soil with emissivity e_r (eqn. (1) first term) attenuated by the overlying vegetation with transmissivity Γ, direct canopy emission with single scattering albedo, ω, (eqn. (1) second term), and the downwelling canopy emission reflected by the soil and attenuated by the canopy (eqn. (1) third term). The effective physical temperature of the soil-vegetation continuum is given by T_s. The soil emissivity depends on soil dielectric properties given by the Fresnel coefficients modified for surface roughness (Wang & Choudhury, 1981). The soil bulk dielectric properties are determined by soil conditions (e.g. sand, silt and clay content) and estimated from a dielectric mixing model (e.g. Dobson et al., 1985). Canopy transmissivity is determined by the slant path optical depth, VOD, which is a function of nadir optical depth, τ, and incidence angle, μ, in radians (eqn. 2). The τ-ω model is properly classified as a zero-order model because it accounts only for single-scattering in the forward direction, neglecting higher-order scattering terms. It is a scalar model because the H- and V- polarizations are functionally

de-coupled from one another. These considerations limit application at higher frequencies where higher-order scattering and polarimetric effects are significant.

The presence of vegetation generally de-polarizes underlying soil specular emissions and dampens the T_b sensitivity to soil dielectric properties. There is a semi-empirical relationship between the VOD parameter and canopy water content that varies with both wavelength and canopy structure (Jackson & Schmugge, 1991), while V- and H- polarization emissivity differences and corresponding algorithm VOD sensitivity decreases at higher canopy biomass levels (Figure 2.1a). This limits capabilities for accurate VOD retrievals at higher biomass levels (Section 2.1.1.3). The relationship between VOD and canopy biomass and associated water content follows a general power-law response that varies with microwave frequency (Njoku & Chan, 2006; Kirdyashev et al., 1979; Jackson et al., 1982). VOD retrievals at lower (e.g. 10.7 and 6.9 GHz) microwave frequencies increase potential VOD sensitivity at higher biomass levels; however, AMSR-E T_b retrievals at these frequencies are reported to have significant RFI contamination and are more sensitive to surface soil moisture at lower VOD levels (Njoku et al., 2005), while higher frequencies are increasingly sensitive to atmosphere effects. Alternatively, the 18.7 GHz frequency has relatively low RFI and reduced atmosphere and soil moisture sensitivity relative to other AMSR-E channels (Njoku & Li, 1999). Evidence suggests that VOD and ω are typically polarization-independent for coarse-scale observations over natural vegetation (Owe et al., 2001); however, some studies note that vegetation with preferential orientation (e.g. maize, grains and other croplands) can cause polarization-dependent extinction for specific vegetation types and associated deviations in the expected VOD response (e.g. Figure 2.1a) depending on the underlying surface emissions (e.g. soil vs. open water; Wigneron et al., 1995).

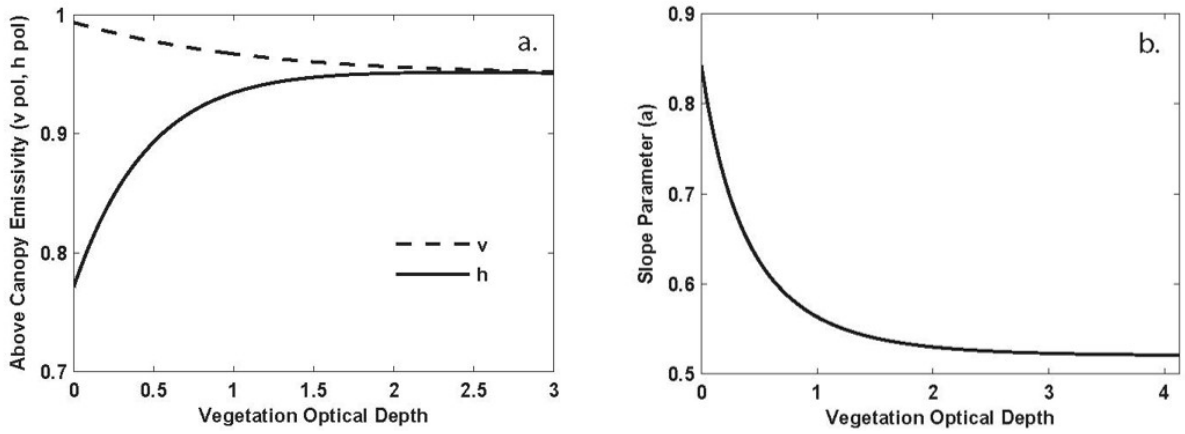

Figure 2.1. Simulated effect of vegetation optical depth (VOD) on the above canopy V- and H-polarization emissivity at 18.7 GHz frequency. (b) Sensitivity of the slope parameter is effectively saturated at VOD values above 1.5, with limited sensitivity up to approximately 2.0. The model simulation assumes a single scattering albedo of 0.05, surface temperature of 280 K, and dry (0.05 m^3 m^{-3} volumetric moisture content) loam soil (30% sand, 50% silt, and 20% clay).

2.1.1.2 Vegetation Optical Depth Retrievals

We developed an algorithm for global VOD retrievals using H- and V- polarized $T_{b,p}$ values for a single frequency (18.7 GHz) with ancillary surface temperature and atmospheric water vapor information (Jones et al., 2009). The resulting VOD information integrates canopy attenuation related to vegetation biomass and water content and limits the effects of open water pixel fraction and soil moisture that impact the MPDI. As with any global application and semi-empirical algorithm, our method requires several simplifying assumptions that are examined in a subsequent error sensitivity analysis (Section 2.1.1.3).

The algorithm assumes that a given grid cell is composed of a mixture of open water and vegetated land, but does not specifically account for inundated pixels with overlying vegetation (Section 2.3.1) . Open water emissivity can vary with changes in waves, foam or salinity, but can be considered constant for inland water bodies at lower microwave frequencies (≤ 18.7 GHz). Vegetated land is treated as a two-layer surface with soil (semi-infinite lower layer) covered by a continuous vegetation canopy (translucent upper layer). Each grid cell is

composed of a fractional mix of open water (f_w) with emissivity $e_{w,p}$ and vegetated land with emissivity $e_{l,p}$ with polarization p:

$$e_p = e_{l,p} * (1 - f_w) + e_{w,p} * f_w \quad (3)$$

It follows from (3) that the points (e_h, e_v), ($e_{l,h}$, $e_{l,v}$), and ($e_{h,w}$, $e_{v,w}$) are collinear with slope (a; Figure 2.1b):

$$a = \frac{e_v - e_{w,v}}{e_h - e_{w,h}} \quad (4)$$

The slope parameter a is therefore independent of f_w variability. Additionally, soil moisture tends to be spatially heterogeneous depending on topography and soil type unless the soil is extremely dry or extremely wet. The microwave emissivity of a given grid cell typically represents the aggregate conditions for a wide range of soil moisture levels, causing a linear empirical dependence on soil moisture in contrast to that of an entirely homogenous surface expected from the non-linear Fresnel coefficients. Therefore, the ratio in (4) greatly reduces soil moisture dependence because soil moisture varies principally along the f_w principle axis. Soil moisture dependence is not entirely eliminated. The slope of the principle axis of soil moisture variability is less than a because the dielectric of wet soil is less than that of open water.

The a parameter can be calculated from the effective emissivity given satellite observed $T_{b,p}$ and ancillary surface temperature (T_s) and atmospheric water vapor (V) information. The effective surface emissivity can be estimated as:

$$e_p = \frac{T_{b,p}/T_s - (1 - t_a(V))\Delta T}{t_a(V)} \quad (5)$$

The atmospheric transmissivity (t_a) is a function of V, oxygen absorption, and cloud liquid water path (assumed negligible for ≤ 18.7 GHz), and ΔT is the ratio of atmospheric to

surface temperature. Eqn. (5) is simplified and linearized from its usual quadratic form by ignoring atmospheric emissions reflected by the surface (see Jones et al., 2010 for further information). In this investigation we use ancillary T_s and V retrievals from AMSR-E obtained separately, from a similar algorithm (Jones et al., 2010), although other data sources, including satellite or reanalysis data can alternatively provide this information as demonstrated by the use of an independent emissivity database (Section 2.2.2). The simplified form of the atmospheric radiative transfer equation (5) was adopted for consistency with the AMSR-E T_s retrieval algorithm, although the standard quadratic form could also be used (e.g. Prigent et al., 1997).

The τ-ω model (eqns. 1-2) is combined with the slope equation (4) and inverted to solve for the VOD of the land fraction of a given grid cell:

$$A = (1-\omega)\left(r_{s,v} - a * r_{s,h}\right) \tag{6}$$

$$B = a * e_{s,h} - e_{s,v} + (1-\omega)\left(a * r_{s,h} - r_{s,v} + 1 - a\right) \tag{7}$$

$$C = (1-\omega)(a-1) + e_{w,v} - a * e_{w,h} \tag{8}$$

$$VOD = -\log\left(\frac{-B-\sqrt{B^2-4AC}}{2A}\right) \tag{9}$$

To solve for VOD using H- and V- polarized T_b at a single frequency (eqns. 5-9), the parameters ω and $r_{s,v}$ and $r_{s,h}$ (single scattering and Fresnel reflectivities of the soil ($r_{s,p}$ = 1-$e_{s,p}$), respectively) are treated as constants that define the bounds of minimum and maximum VOD. Surface soil roughness has a similar impact on microwave emission and the VOD retrieval therefore incorporates surface roughness information (Njoku & Chan, 2006). Surface (soil) roughness is assumed temporally static relative to seasonal changes in vegetation canopy biomass (Njoku & Chan, 2006). We find that $e_{l,h}$ and $e_{l,v}$ typically converge to 0.95 for high biomass vegetation cover, which is also consistent with previous studies (Prigent et al., 1997;

Peterson et. al., 2000; English, 2008); therefore the ω parameter is set to 0.05. Soil moisture determines $r_{s,v}$ and $r_{s,h}$, but an assumed constant 0.05 m^3 m^{-3} volumetric soil moisture and loam soil (30% sand, 50% silt, and 20% clay) is adopted for determining the bare soil endpoint consistent with arid, sparsely vegetated regions. Random error in VOD is expected to increase for higher canopy biomass levels (VOD>1.5 for 18.7 GHz) because of the inverse exponential dependence of VOD on a (Figure 2.1b). The V- and H- polarization emissivity difference and associated slope parameter sensitivity effectively saturate for the 18.7 GHz retrievals at VOD levels above a threshold of approximately 1.5-2.0. Since we are primarily interested in determining VOD seasonal patterns, a 30-day moving median time-domain filter is applied to the slope parameter (result of (4)) prior to the VOD calculation (Eqns. (6-9)) to reduce daily VOD random error effects.

2.1.1.3 Error Sensitivity Analysis

An error sensitivity analysis was conducted to assess the impact of algorithm assumptions on expected VOD retrieval accuracy. The VOD algorithm retrievals are composed of two primary error sources: 1) Random error from input $T_{b,p}$, T_s and V information, the assumption of negligible cloud liquid water path, and the dense vegetation ω endpoint constant, which are potentially variable in time and space; 2) Bias error from assuming constant values for the bare soil and simplified treatment of atmospheric effects in (6). For the sensitivity analysis, error is considered independent among sources and summed in quadrature to yield a total daily error (E_{day}) estimate. A smoothed (30-day moving window mean) VOD time series error (E_{30day}) was estimated from the E_{day} series by assuming an autoregressive (AR) covariance matrix (**C**, 30 × 30) with an AR (lag 1) coefficient of 0.7 and applying the 30 × 1 mean operator matrix ($A = \left\{\frac{1}{N}\right\}_i \; \forall \; i$, for a N-day window):

$$E_{30day} = E_{day} * \sqrt{\mathbf{A}' * \mathbf{C} * \mathbf{A}} \tag{10}$$

Random errors were propagated by taking the absolute value of the partial derivative of the VOD algorithm (Eqns. 4-9) with respect to each variable of interest and multiplying by a

defined error level for the respective parameter. The error in the slope parameter, a, is sensitive to inputs $T_{b,p}$, T_s and V. $T_{b,p}$ was perturbed with Gaussian radiometer noise with standard deviation of 0.5 K. T_s and V were fixed at 280 K and 10 mm and perturbed with Gaussian errors having standard deviations of 2 K and 1.5 mm, respectively. The ω parameter was assumed to have a Gaussian error with standard deviation of 0.02. These error levels reflect typical conditions expected for the global land area.

Bias errors were computed using the VOD algorithm to invert simulated $T_{b,p}$ values from a more detailed forward model with specified VOD ('truth'), and then differences between inverted and 'truth' VOD values were calculated. Details of the forward model depend on the parameter of interest. For soil moisture, the $e_{s,p}$ and $r_{s,p}$ parameters (Eqns. 6-9) were assigned a value corresponding to 0.30 $m^3 m^{-3}$ volumetric soil moisture for which maximum bias in the proposed algorithm occurs. A more detailed forward model was adopted from Wentz (2000) to evaluate potential atmospheric effects on VOD retrievals, including the influences of cloud liquid water and use of a simplified radiative transfer equation (5); using this model, V and cloud liquid water were assigned representative values of 10 mm and 0.3 mm, respectively.

2.1.2 AMSR-E Brightness Temperatures

The Advanced Microwave Scanning Radiometer on the Earth Observing System (AMSR-E) is a microwave radiometer deployed on the polar-orbiting Aqua satellite platform with UTC 1:30 A.M. (descending)/P.M. (ascending) orbit equatorial crossings. The AMSR-E sensor measures vertically (V) and horizontally (H) polarized T_b at six frequencies (6.9, 10.7, 18.7, 23.8, 36.5, 89.0 GHz) at a constant Earth incidence angle of 55° from nadir. In this study we employ the daily 25 km resolution global Equal Area Scalable Earth (EASE) Grid brightness temperatures provided by the National Snow and Ice Data Center for years 2003 to 2008 (Knowles et al., 2009). The resulting VOD daily retrievals were temporally composited into 16-day and 8-day median values to coincide with MODIS (Collection 5) NDVI/EVI and LAI products (see section 2.3), respectively. The global land domain was defined as pixels with <50% permanent ice and open water cover identified from a MODIS global land cover classification (see section 2.1.3). The retrieval algorithm is only valid for non-precipitating and snow-free conditions. Masks for

precipitation and snow were adopted from Ferraro et al. (1996), as described by Jones et al. (2010). Additionally, lower frequency (≤18.7 GHz) AMSR-E brightness temperatures are susceptible to radio frequency interference (RFI) mainly from surface and space-based telecommunications and were masked (Jones et al., 2010) by employing frequency and polarization thresholds (Njoku et al., 2005).

2.1.3 MODIS EVI, NDVI, LAI and Land Cover

The MODIS EVI and NDVI (MOD13C1 16-Day) vegetation indices (VIs), and LAI (MOD15A2 8-Day) global data series were spatially resampled to the 25km global EASE-grid format of the AMSR-E VOD data series. The MOD13C1 product is gap filled using historical MODIS time series data to provide cloud-free global coverage. Means and standard deviations of the 1-km resolution MODIS pixels within each 25-km EASE-Grid pixel were calculated using only the highest quality pixels (QC = 0), while avoiding lower quality or gap filled data; this was done to facilitate direct comparisons between AMSR-E and MODIS retrievals acquired at the same time period while minimizing the influence of atmospheric contamination. MODIS Land Cover data (MOD12Q1) acquired from the National Snow and Ice Data Center were used as ancillary information. The original 1 km resolution MODIS Land Cover data were resampled to the global EASE Grid projection by spatially aggregating to 25 km pixels, while retaining sub-grid scale information on the relative proportions (%) of dominant and sub-dominant IGBP land cover classes (Knowles, 2004; see Table 2.1 for definitions of land cover acronyms). Dominant land cover is defined as the class with the highest percent cover. Pixels were further classified as either homogeneous (dominant land cover ≥80%) or heterogeneous (<80%).

2.1.4 Growing Season Index

The Growing Season Index (GSI) is a simple bioclimatic phenology model that uses daily air temperature (*T*), atmospheric vapor pressure deficit (*VPD*) and photoperiod as the primary constraints to vegetation growth (Jolly et al., 2005). This simple index accounts for much of the global variation in seasonal phenology. Threshold limits for each variable are used to create a linear index of growing season activity ranging from inactive (0) to unconstrained (1). Inactivity (0) is set for each variable if: $T \leq -2$°C, photoperiod ≤ 10hours or $VPD \geq 4100$Pa. Unconstrained

activity (1) is set if: $T \geq 5$°C, photoperiod ≥ 11.5 hours or $VPD \leq 900$Pa. Values for each variable between the minimums and maximums are fit to a linear function returning a dimensionless 0 to 1 index. The daily product of these individual indices forms the bioclimatic index:

$$GSI_{daily} = T_{index} * VPD_{index} * Photo_{index} \quad (11)$$

where GSI_{daily} is the dimensionless (0 to 1) daily value of the GSI, and T_{index}, VPD_{index} and $Photo_{index}$ are the respective dimensionless (0 to 1) constraints for daily air temperature, VPD and photoperiod. Daily surface meteorology inputs to the GSI model were obtained from the NCEP/NCAR Reanalysis (NNR) project (Kalnay et al., 1996). The NNR is available at approximately 2.0 degree spatial resolution with 6-hour temporal fidelity. The NNR surface daily *T* (minimum, maximum, average) and air vapor pressure (*AVP*) data were spatially resampled to match the 25km EASE Grid projection format using bilinear interpolation. Daily *VPD* was calculated as the difference between *AVP* and the saturated vapor pressure following Waring and Running (1998). The GSI_{daily} values were temporally composited into 16-day and 8-day median values consistent with the MODIS and VOD time series. The GSI provides an independent, model-based phenology metric based on biological response to environmental constraints.

2.1.5 Global and regional correlation analysis and phenology metrics

We computed global pixel-wise linear correlations between the AMSR-E VOD, GSI and MODIS EVI, NDVI and LAI time series over the 6 year (2003-2008) study period. The satellite optical-infrared indices are relatively common LSP measures and were used as a standard to assess VOD correlations and phenology signal correspondence. To assess and compare regional phenology signals over relatively homogeneous land areas, contiguous areas of common land cover were defined from the MODIS land cover data. Contiguous land cover areas were defined using a 6250 km^2 minimum polygon size threshold where all adjacent pixels had the same dominant land cover class. From the resulting global map, nine representative regions were selected spanning a range of biomes, latitudes and continents. These methods were used

to mitigate the effects of gaps in the optical-infrared remote sensing data series and analyze biome specific signals and correspondence through correlation analysis and inspection of a common set of LSP metrics. The LSP metrics are similar to curve derivative terms used by the USGS/EROS Remote Sensing Phenology effort to describe and compare the resulting aggregate seasonal time series. The terms include: start-of-season (SOS), the first significant upward trend of the yearly cycle; end-of-season (EOS), the end of a consistent downward trend; and peak-of-season, the maximum point between the SOS and EOS. The SOS and EOS slopes are also referenced and refer to the slope of the time series between the SOS and the peak-of-season (or start of a mid-season plateau if no definitive peak is present) and the slope between the peak (or end of plateau) and the EOS. A temporal phase shift is also referenced in the comparisons and refers to a later SOS, peak and EOS. In many cases an EOS lag is referenced and refers to a later EOS.

2.2. Results

2.2.1 Algorithm Error Sensitivity Analysis

The algorithm error sensitivity analysis indicates that the lowest retrieval error (i.e. relative error ≤ 30%) occurs in the 0.5 to 1.5 VOD range, which represents approximately 66% of the global vegetated area (Figure 2.2).

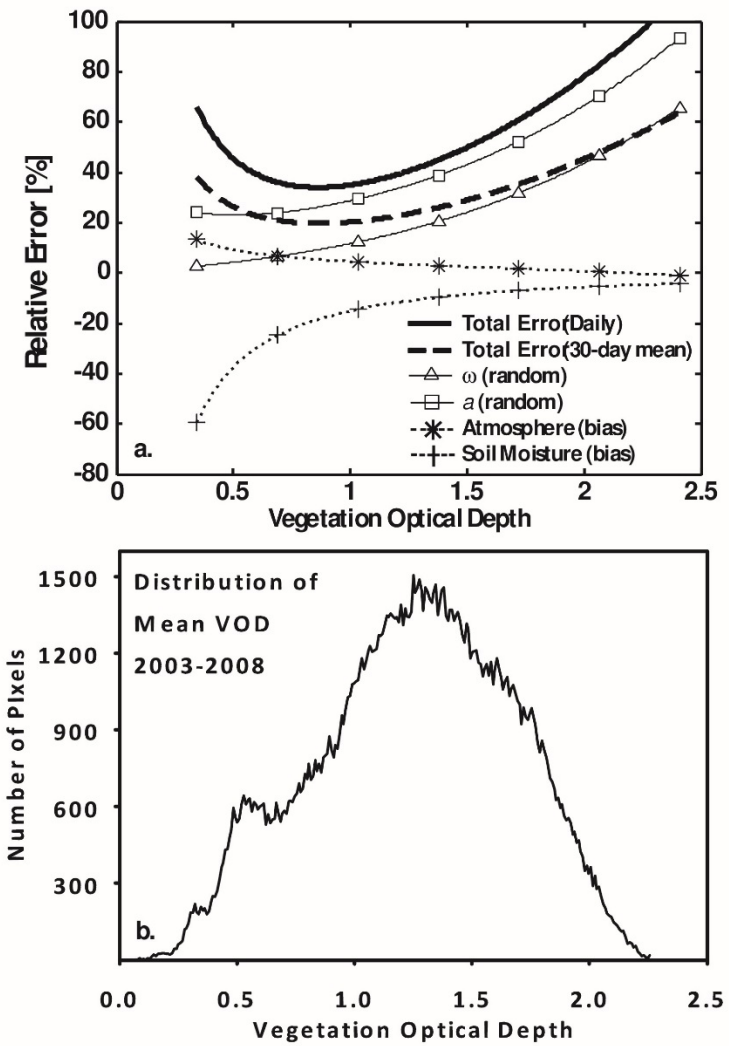

Figure 2.2. (a) Conservative estimation of algorithm retrieval error expressed as a percentage of retrieved VOD across the global VOD range. Labeled lines represent each source of error independently considered, and then summed in quadrature to estimate total daily error and total 30-day moving mean error accounting for temporal autocovariance. The legend indicates if each error source was considered as persistent (bias) or random error. (b) Distribution of retrieved VOD means from 2003-2008 for the global vegetated land area. Approximately 66% of the vegetated land area has a mean VOD within a range of 0.5 to 1.5, corresponding to VOD mean retrieval errors ≤30%.

These results are considered a conservative estimate of potential VOD retrieval error due to the conservative selection of algorithm parameters and assumptions; these results are therefore likely to represent the upper bounds of actual VOD retrieval errors. Atmospheric biases represent less than 10% relative error for VOD>0.5, indicating that this is a relatively

minor error source at longer (≤18.7 GHz) microwave frequencies. Total retrieval error is dominated by soil moisture bias for VOD levels below 0.5 and by a combination of random error sources at VOD levels above 1.5. Soil moisture always causes negative VOD bias because a dry algorithm endpoint was chosen (Section 2.1.1.2). Estimated soil moisture bias is especially conservative because over real soils the microwave penetration depth is very shallow (<1 cm) and surface soil roughness is significant. As a result, previous studies indicate very modest soil moisture sensitivity at the 18.7 GHz frequency (Prigent et al., 2005; Crow et al., 2010). Increasing dominance of random error at higher VOD results from increasing sensitivity of the exponential terms in (1) and will be present in any similar inversion method. Random error in this region of the response curve is caused by radiometer noise, error in input T_s and V parameters, and variability in canopy scattering extinction (indicated by ω). The temporal smoothing procedure reduces VOD retrieval error particularly at higher VOD levels, representing a 14 % improvement at VOD = 0.8 and more than 30% improvement for VOD>1.9. Despite these improvements, the expected VOD retrieval error still increases at higher biomass levels due to increasing convergence of canopy V- and H- polarization emissivity at the 18.7 GHz frequency as shown in Figure 2.1a. Although temporal smoothing improves potential retrieval accuracy at higher biomass levels (VOD>1.5), caution should be taken when interpreting these results because of increased algorithm sensitivity to other potential error sources in this region of the response curve.

2.2.2 Comparison with an Independent Emissivity Database

An alternative set of VOD retrievals was derived using an independent monthly 2003 emissivity database (Moncet et al., 2010) as a substitute for e_p derived from ancillary T_s and V inputs in (5). Figure 2.3a compares the resulting mean monthly VOD retrievals from the two approaches for each of the nine contiguous land cover regions (Figure 2.8). These results show strong correspondence (r^2=0.83, p<.0001) across all global land cover classes, but with larger deviations between the two approaches at larger (>1.5) VOD levels due to increasing sensitivity of VOD to small differences in emissivity error at higher biomass levels. Monthly VOD time series (Figure 2.3b) for three representative land cover classes (GRA, SAV, MXF) with large

characteristic VOD seasonality depict similar VOD magnitudes and seasonal patterns, while discrepancies between the two retrieval sets are within the expected algorithm uncertainty (Section 2.2.1).

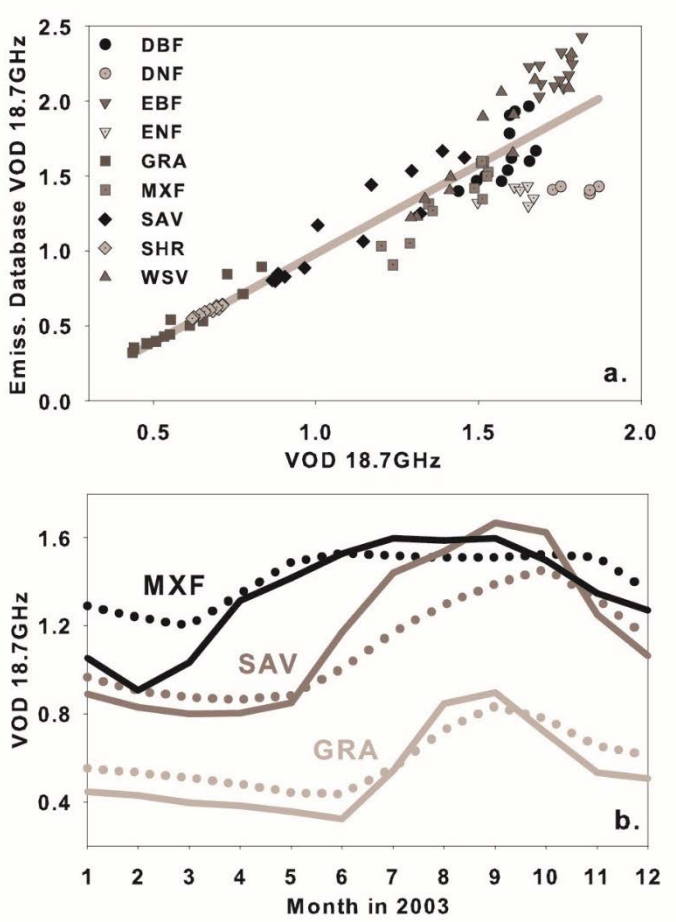

Figure 2.3. (a) Scatter plot of alternative VOD monthly retrievals for the the nine contiguous land cover regions (Figure 8) at 18.7 GHz derived from emissivities using the Jones et al. (2010) emissivity derivation method and an alternative, independent emissivity database (Moncet & Liang, 2009); the gray line is the least-squares linear regression relationship (r^2=0.83, p<.0001) between the two VOD series. (b) Mean monthly VOD time series for 2003 over three contiguous land cover regions with characteristic large VOD seasonality; the VOD series represent retrievals derived using the Jones et al. (2010) emissivity approach (dotted lines) and the alternative emissivity database (solid lines).

2.2.3 Continuity of phenology data time series

The MODIS VI and LAI retrievals are constrained by signal degradation and data loss from solar illumination effects, clouds, smoke and other atmospheric effects over much of the

globe, even at relatively coarse 16-day time intervals. The AMSR-E VOD retrievals are less constrained by these effects, resulting in a large improvement in non-gap-filled, 16-day data time series (Figure 2.4).

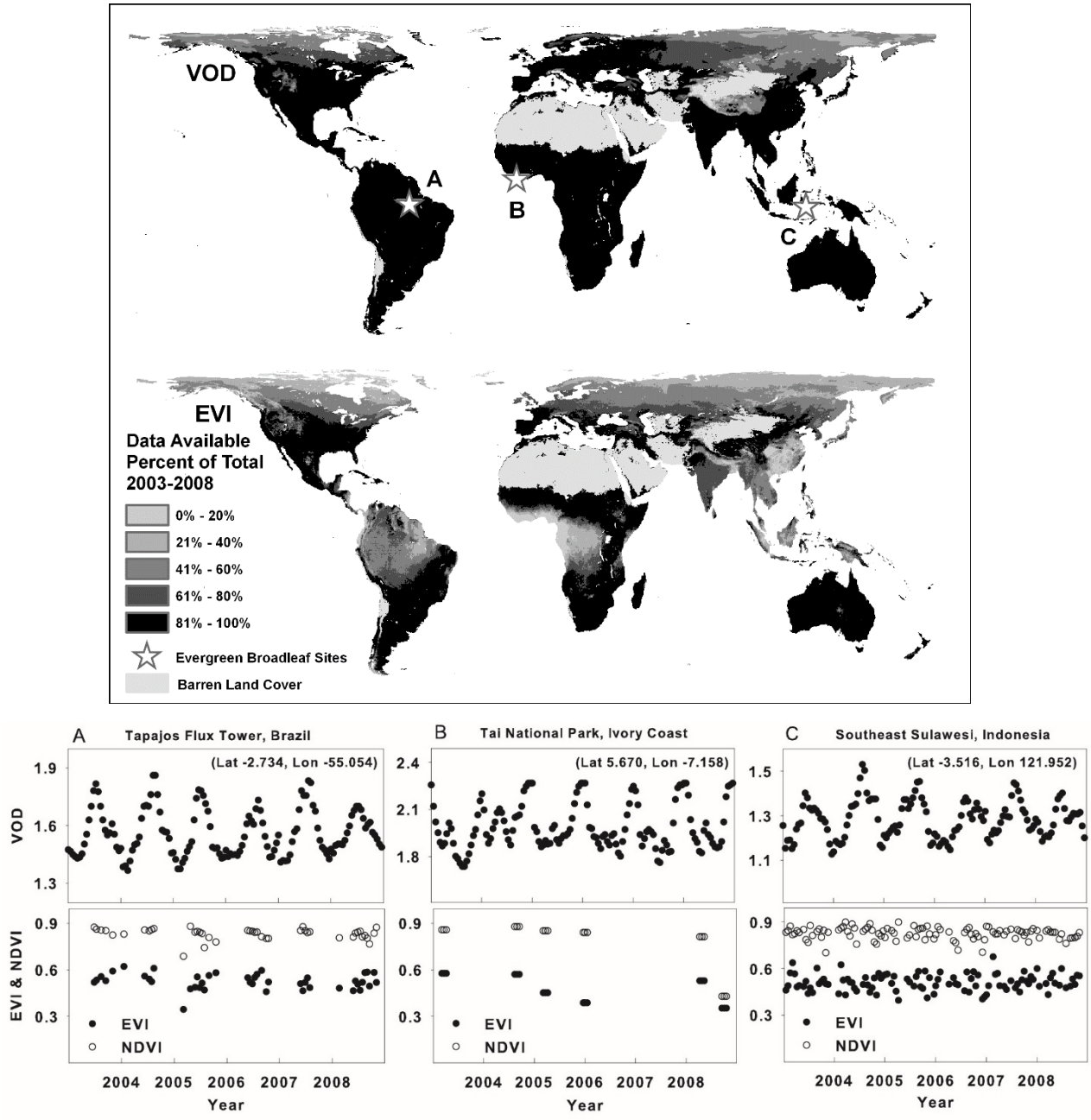

Figure 2.4. (map) Percent availability of highest QC 16-day data for AMSR-E VOD (top) and MODIS EVI (bottom) from 2003 to 2008. Stars indicate locations of time series pixel extractions shown in plots; the VOD shows relatively complete yearly time series compared to optical-infrared based indices from available MODIS EVI and NDVI time series at these EBF sites.

Tropical EBF regions are susceptible to frequent cloud cover and show considerable increases in microwave data availability relative to 16-day best QC MODIS EVI data. Of the 132 possible 16-day retrievals from 2003-2008, the VOD series provides an average of 45% more data retrievals per pixel for the Amazon region, 75% more for EBF regions in Africa and 42% more for Indonesia and surrounding EBF areas. The high VOD retrieval rate allows for relatively continuous pixel-wise, non-gap filled data time series over these regions for improved resolution of vegetation changes and LSP signals. Representative sites (pixels) from Amazon, Africa and Indonesia EBF regions are presented (Figure 2.4) and illustrate the relatively enhanced VOD temporal fidelity for these regions. Site A is over the Ameriflux LBA Tapajos flux tower and is characterized as a moist tropical forest (87% EBF) with a 7 month wet season extending from January to June. Site B is over Tai National Park in the Ivory Coast region, a designated UNESCO Biosphere Reserve and within the largest remaining mature tropical forest (93% EBF) in West Africa. Site C in Sulawesi Tenggara was selected as a representative homogeneous (99% EBF) pixel without visible deforestation patterns or anthropogenic impacts indicated by visual inspection of high-resolution satellite imagery. Seasonal snow cover and frozen conditions limit the VOD retrievals over northern latitudes and higher elevations, while snow and seasonal reductions in solar illumination also reduce the reliability and completeness of VI and LAI time series for these regions.

2.2.4 Global phenology patterns

The observed spatial pattern of AMSR-E derived VOD follows global vegetation biomass distributions (Figure 2.5) and an expected gradient of VOD means in relation to land cover type (Figure 2.6). VOD 16-day median values for homogeneous land cover pixels range from 0.14 (SHR) to 2.27 (EBF). Approximately 30% of the global vegetated land area shows a mean VOD over the composite 6 year period above the expected (Figure 2.1) approximate saturation point of 1.5 and comprised primarily of high biomass land cover classes (EBF, DBF, DNF, MXF, WSV, ENF). The coefficient of variation (CV) within individual land cover classes ranges from 5.7% (EBF and DNF) to 17.6% (CRP) (Table 2.1). Generally, CV values are inversely proportional to the

VOD mean, which follows emissivity model expectations showing decreased algorithm sensitivity to VOD at higher biomass (VOD) levels.

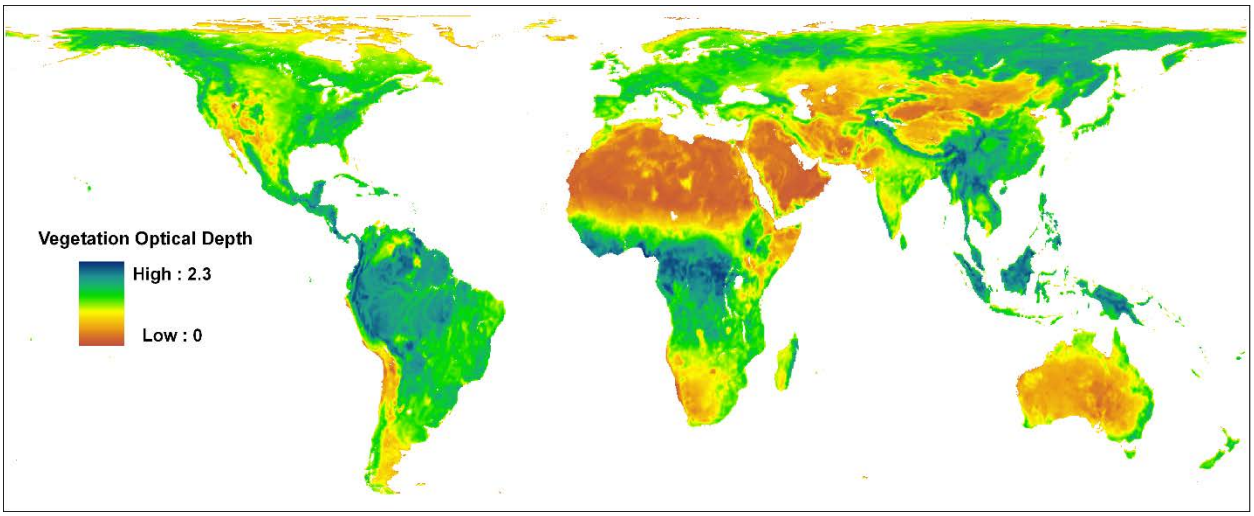

Figure 2.5. Global mean VOD at 18.7 GHz for the six year (2003-2008) study period.

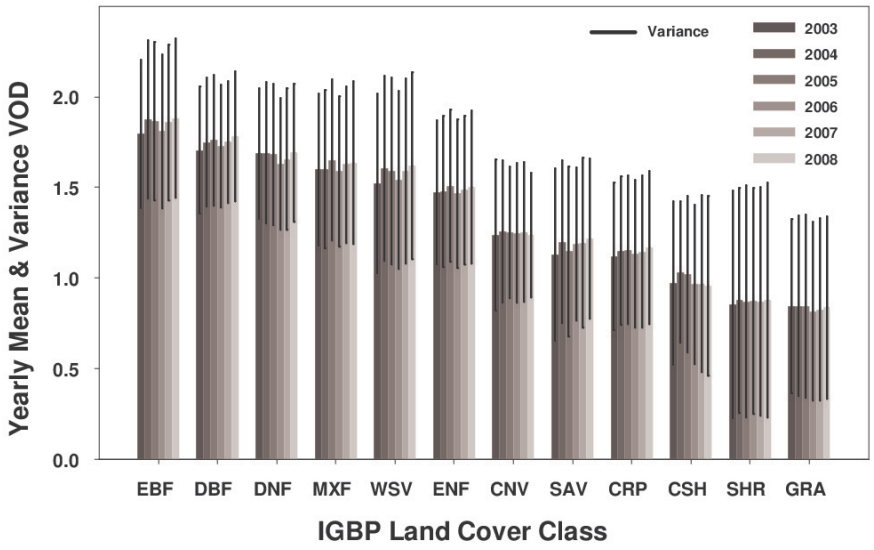

Figure 2.6. VOD means and variance by year for homogeneous (>80%) land cover pixels.

Pixel-wise linear correlations between VOD and VI, LAI and GSI time series are summarized by land cover type for homogeneous pixels in Table 2.1, while global maps of these correlations are presented in Figure 2.7. Land cover classes with characteristically low biomass levels (e.g. savannas) show the highest correlations, with decreasing correspondence for land cover classes with characteristically higher canopy density and biomass. When summarized by

land cover class, the VOD-EVI and VOD-NDVI correlations were similar, while the VOD-LAI correlations showed the best results (Table 2.1). In some regions correlations are negative implying inverse seasonality between the datasets. The GSI correlation coefficients cover a similar range as the VI-LAI correlations. However, in certain regions the GSI shows full-year unconstrained growing seasons (GSI=1; e.g. NW Amazonia), resulting in a yearly variance of zero which does not allow for correlation analysis (i.e. black areas in Figure 2.7).

Table 2.1. Summary of global VOD and LAI means, VOD coefficients of variation (CV) and pixel-wise correlations for pixels of homogeneous (>80%) land cover; significance column refers to the LAI-VOD correlations.

Land Cover ID	Land Cover Name	VOD Mean	LAI Mean	VOD CV	LAI-VOD Mean R	NDVI-VOD Mean R	EVI-VOD Mean R	GSI-VOD Mean R	Percent of pixels significant (p<0.10)
EBF	Evergreen Broadleaf Forest	1.85	2.93	5.7%	0.07	0.03	-0.07	-0.14	30%
DBF	Deciduous Broadleaf Forest	1.74	1.41	6.1%	0.03	0.11	0.05	0.12	57%
DNF	Deciduous Needleleaf Forest	1.67	1.22	5.7%	0.43	0.23	0.25	0.61	53%
MXF	Mixed Forests	1.62	1.43	10.0%	0.39	0.35	0.31	0.48	86%
WSV	Woody Savannas	1.58	1.73	12.5%	0.34	0.37	0.25	0.37	82%
ENF	Evergreen Needleleaf Forest	1.48	1.33	10.1%	0.51	0.45	0.40	0.57	88%
CNV	Cropland/Natural Vegetation	1.25	0.91	15.5%	0.66	0.60	0.54	0.59	100%
SAV	Savannas	1.18	1.20	16.2%	0.65	0.66	0.54	0.55	98%
CRP	Croplands	1.14	0.82	17.6%	0.51	0.47	0.44	0.34	92%
CSH	Closed Shrublands	0.99	0.43	10.0%	0.27	0.48	0.41	-0.23	93%
SHR	Open Shrublands	0.87	0.45	13.5%	0.49	0.51	0.45	0.35	87%
GRA	Grasslands	0.83	0.37	14.3%	0.64	0.59	0.56	0.41	98%

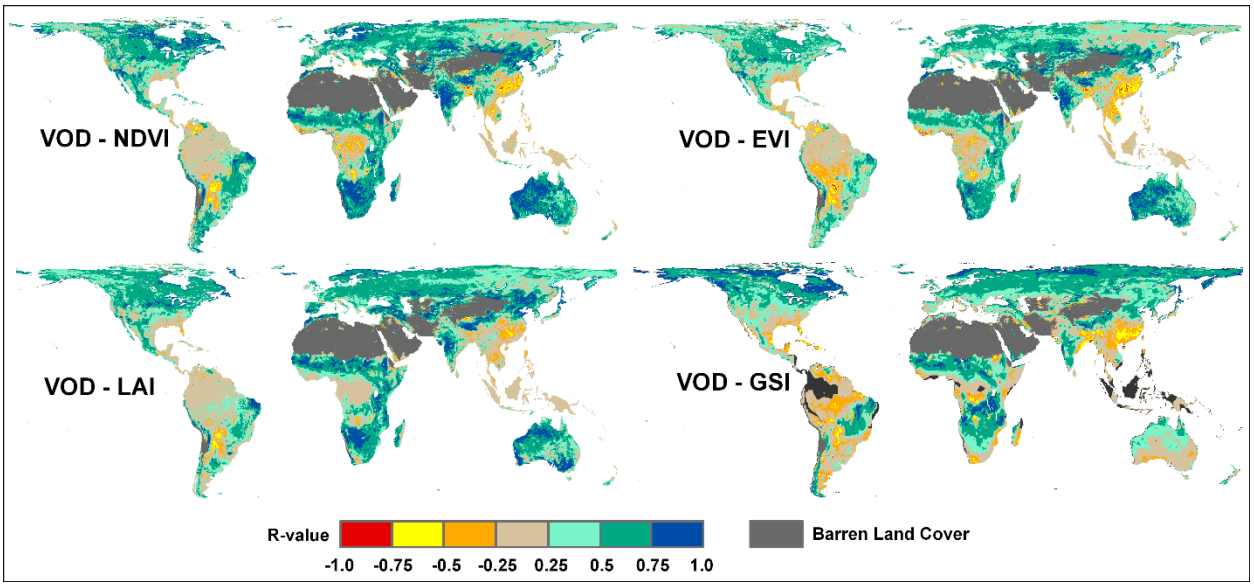

Figure 2.7. Pixel-wise linear correlations between AMSR-E VOD and MODIS NDVI, EVI and LAI, and GSI time series for the 6 year (2003-2008) study period. Gray areas denote barren land cover areas that were screened from the analysis. Areas in black denote full year unconstrained (GSI=1) growing seasons.

2.2.5 Regional phenology patterns

The 16-day time series of each regional mean dataset (VOD, NDVI, EVI, LAI, GSI) is plotted in Figure 2.8 for the six year (2003 to 2008) study period.

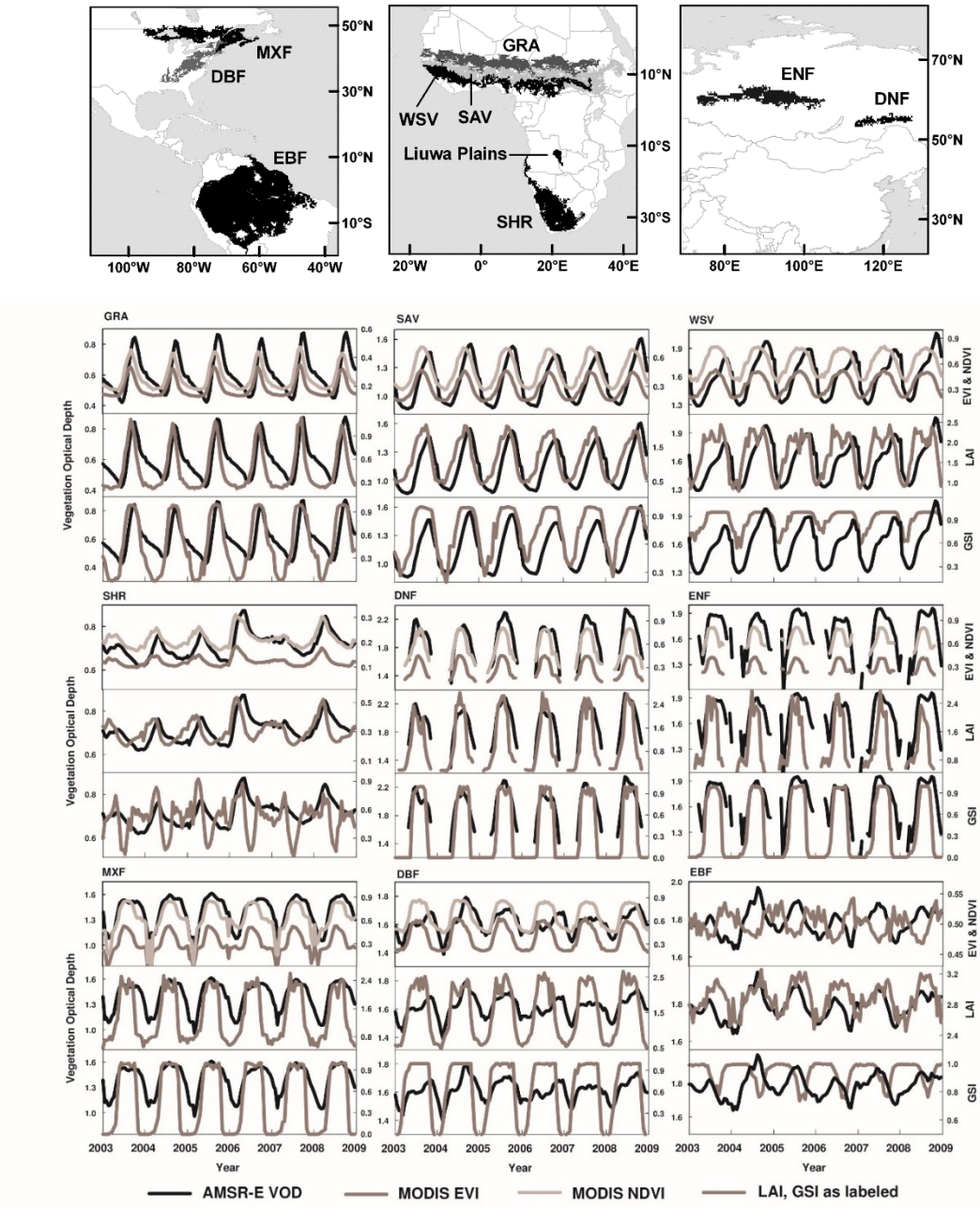

Figure 2.8. Spatially contiguous regions of relatively uniform land cover and climate were defined and nine regions were selected covering a range of biomes, latitudes and continents (maps; black and grey regions). The resulting 16-day time series of each regional mean dataset (VOD, NDVI, EVI, LAI, GSI) are plotted for the six year (2003-2008) study period.

These time series were evaluated by correlation analysis (Table 2.2) and visual inspection of phenology metrics between the aggregate VOD time series and corresponding VI, LAI and GSI results. A prominent feature of these results is an apparent VOD phase shift or EOS lag relative to the other indices. The four land cover regions (GRA, SAV, WSV, SHR) in Africa span a large latitudinal land cover and biomass gradient. The observed GRA VOD of the African Sahel shows well defined seasonal cycles and strong correspondence across all datasets ($0.58<R<0.71$; $p<.01$), as well as a unique EOS slope. Moving south across the SAV region a VOD phase shift is present, but correlation values remain high ($0.60<R<0.77$, $p<.01$). The VOD phase shift is greater in the WSV region which is manifested in lower correlation values ($0.36<R<0.71$, $p<.01$). During the WSV growing season the VOD SOS slope decreases and then exhibits a secondary rise. The decrease in slope occurs during the approximate time span of the first LAI peak and mid-season trough. The slope then increases corresponding to the secondary rise in LAI and peaks very close to the second LAI peak. The VOD of the southern African SHR region exhibits good seasonal correspondence with all indices ($0.46<R<0.76$; $p<.01$) except the GSI ($R=0.18$; $p<.05$) and shows the negative impact of a severe regional drought in 2007 (USDA-FAS, 2007). A phase shift is also apparent in the SHR VOD signal compared to the EVI, NDVI and LAI time series.

Table 2.2. Summary of linear correlation results for the regional mean time series (shown in Figure 8).

Land Cover ID	Land Cover Name	LAI-VOD R	NDVI-VOD R	EVI-VOD R	GSI-VOD R
EBF	Evergreen Broadleaf Forest	0.54*	-0.27*	-0.56*	-0.33*
DBF	Deciduous Broadleaf Forest	0.54*	0.60*	0.47*	0.46*
DNF	Deciduous Needleleaf Forest	0.77*	0.81*	0.77*	0.86*
MXF	Mixed Forests	0.71*	0.83*	0.75*	0.77*
WSV	Woody Savannas	0.41*	0.50*	0.36*	0.71*
ENF	Evergreen Needleleaf Forest	0.56*	0.61*	0.47*	0.76*
SAV	Savannas	0.66*	0.69*	0.60*	0.77*
SHR	Open Shrublands	0.46*	0.76*	0.63*	0.18**
GRA	Grasslands	0.68*	0.65*	0.58*	0.71*

*p<.01; **p<.05

Strong correlations are seen for DNF ($0.77<R<0.86$; $p<.01$) and ENF ($0.47<R<0.76$; $p<.01$) regions. Over the ENF region a dual VOD peak or plateau is present in some years, with the initial peak coinciding with VI and LAI peaks, and the final peak coinciding with the approximate end of the GSI plateau. Identification of SOS and EOS periods for the DNF and ENF time series is

constrained by the lack of winter data in all remote sensing indices and increasing noise in the VOD retrieval during seasonal freeze-thaw transitions; VOD noise during these periods may be due to pixels within the aggregate region that were not effectively screened by the snow flag, but may still be affected by frozen conditions.

The MXF region shows strong VOD correlations ($0.71<R<0.83$; $p<.01$), but with a general EOS lag compared to the VIs and LAI. The Deciduous Broadleaf Forest (DBF) region shows generally good correspondence ($0.46<R<0.60$; $p<.01$). The SOS and initial SOS slope of the VOD correspond well with the other indices but in 5 of the 6 years the VOD seasonal curve levels off above approximately 1.6 and in some years shows a mid-season trough. In most years the VOD peaks are delayed relative to the other indices, with considerable delays in 2003 (96 days) and 2006 (128 days), the two years with the most apparent mid-season trough.

For the aggregate EBF region of the Amazon, the VOD signal never drops below the expected saturation level (1.5) of the 18.7 GHz frequency, but still shows strong seasonality ranging between seasonal minima (~1.65) in January and maximum (~1.96) values in July. The VOD seasonal signal for the EBF region is inverse to the EVI and GSI temporal patterns, but is strongly and positively correlated with LAI ($R=0.54$; $p<.01$).

2.2.6 GSI, VOD and EOS timing

The GSI seasonality is generally defined by a consistent seasonal rise and fall, with a mid-season plateau representing the extent of prime growing season conditions for a specific climatic zone. For the majority of land cover classes, this plateau generally extends beyond seasonal peaks of the VIs and LAI, implying that the photosynthetic properties (vegetation greenness, photosynthetic leaf area) measured by these indices begin a downward trend while the bioclimatic indicators are still under optimal conditions. This is not true for the VOD however. In the regional analysis, the primary discrepancy between the VOD and optical-infrared indices is the delayed peak (due to a phase shift) or delayed EOS of the VOD signal. In all regions, except for EBF and two years of the DBF time series, the VOD peak and the initiation of its downward trend coincides with the end of the GSI seasonal plateau. The consistency of this GSI-VOD pattern indicates potential VOD sensitivity to the timing of vegetation biomass

depletion (e.g. abscission) and associated changes in vegetation water content (e.g. dormancy preparation) in response to specific bioclimatic triggers**.**

2.3. Discussion

2.3.1 Interpreting the global correlation maps

The global correlation maps (Figure 2.7) provide a general indication of agreement between the VOD parameter and the VIs, LAI and GSI. The VOD parameter is a measure of canopy density and vegetation water content, while the optical-infrared based VIs and LAI provide relative measures of photosynthetic canopy cover. These metrics are potentially complementary and together provide a more comprehensive LSP assessment. While we might expect a favorable, positive correlation between VOD and VI (NDVI and EVI) time series, stronger correspondence should occur between VOD and LAI time series because LAI is a more explicit measure of canopy biomass as the MOD15 algorithm accounts for biome specific leaf and canopy structure (Knyazikhin et al., 1999). For example, chemical changes in leaves during senescence can reduce NDVI (Di Bella et al., 2004) prior to a reduction in leaf area (Butterfield & Malmstrom, 2009; Jenkins et al., 2007). The GSI provides a general baseline of growing season timing, extent and duration. However, limitations of phenological process understanding constrain GSI utility for some biomes, including arid desert and EBF regions (Jolly et al., 2005). Unique regions where correlations were strong, but negative, were analyzed for this unexpected outcome.

Relatively weak correlations between the phenology time series can be attributed to four general scenarios: 1) The LAI and/or VIs do not contain a definitive seasonal signal; 2) The VOD does not contain a definitive seasonal signal; 3) Definitive seasonality is present, but a limited sample size (data availability) and low temporal variation limits correlation results; 4) Definitive seasonality is present for LAI, VIs and VOD but a phase shift exists between the signals.

Scenario one may result from cloud cover or atmospheric effects limiting data availability, signal saturation over dense canopies, or the presence of underlying bare soil or snow cover confounding the retrieval (Huete et al., 1999). Scenario two may result from

seasonal snow cover or frozen conditions restricting VOD retrievals and data continuity, or saturation of the microwave signal over dense vegetation (Figures 2.1a,b). Scenarios one and two can occur simultaneously and are the dominant causes of low correlations in the equatorial tropics, lands bordering the Gulf of Mexico and southeastern Asia. Scenario three predominantly occurs in northern latitude snow dominated regions where a well-defined seasonality is present but within a narrow seasonal window. Scenario four is unique from the other three scenarios because it is does not reflect a measurement limitation, but a biophysical difference in the phenology parameters measured by two independent methods. Correlations in the high biomass regions of southeastern Asia, lands bordering the Gulf of Mexico, and some areas of the equatorial tropics reflect this scenario.

Regions with strong, negative correlations (R<-0.5) cover approximately 2% (~2.1 million km^2) of the global vegetated land area and show inverse seasonality between the VOD and EVI, NDVI and GSI. The negative correlations in areas of dense vegetation (EBF, DBF, MXF) coincide with apparent VOD saturation near the peak of the growing season, as seen in the VOD troughs in the aggregated regional DBF time series (Figure 2.8). The inverse VOD phenology pattern over other land cover classes include areas subjected to frequent inundation, either naturally (wetlands, riverine flood plains) or from cultivation (e.g. rice paddies). Specific examples include the Liuwa Plains of the Zambezi River Basin of Angola and Zambia (Figure 2.8), the Pantanal flood plain in South America, the Ganges River flood plain, and the Mekong Basin. The VIs, LAI and VOD appear to respond to initial vegetation growth as shown by the VIs and LAI, but early in the growing season, inundation indicated by the AMSR-E f_w parameter dampens the VOD signal response (Figure 2.9). Even though the VOD algorithm should be independent of f_w, an anomalous VOD decline occurs with increasing f_w for seasonally inundated wetland regions. The anomalous declines in VOD are caused by a sharp decline in e_h during inundation that occurs without a concomitant decline in e_v as expected in response to increasing f_w and soil moisture. We suspect this is due to seasonal emergence of low reflectivity, vertically-oriented vegetation (grasses, reeds, etc.) over a highly reflective horizontal water surface. This follows experimental and modeling evidence that the VOD is polarization dependent over vegetation with preferential orientation, including crops (grains, corn) and grasses (Wigneron et al., 1995;

Wegmuller et al., 1995). This situation violates the algorithm assumption that the VOD over natural vegetation is polarization independent. We therefore observe a mid-season VOD drop while vegetation is present above an open water background, resulting in an inverse growing season signal compared to VI, LAI and GSI time series. Further study is needed to confirm this hypothesis and is beyond the scope of this exploratory analysis.

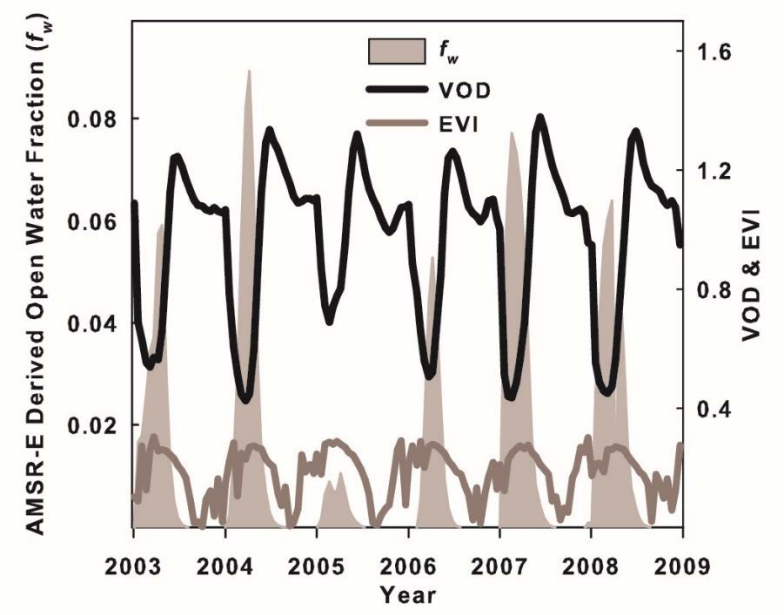

Figure 2.9. Time series of mean open water fraction (f_w), and 16-day VOD and EVI medians for the Liuwa Plains region (see map in Figure 8). The f_w parameter is calculated following the methods of Jones et al. (2009). The effect of inundation under vertically-oriented vegetation on the polarized emissivities causes an anomalous VOD trough.

2.3.2 Interpreting regional phenology patterns

A prominent feature in the regional time series is a VOD phase shift or EOS lag relative to the optical-infrared indices. In GRA areas of the African Sahel there is a VOD EOS lag, and the EOS slope decreases at the approximate point of LAI, EVI and NDVI minimums. At this point the grasses have most likely entered dormancy, though biomass is still present as both standing non-photosynthetic grasses and thatch layers from previous years. The relative decrease in VOD slope over this period is attributed to the presence of standing biomass following the growing season and associated attenuation of microwave emissions dependent on the amount of residual moisture remaining in the vegetation and thatch layers (Saatchi et al., 1994; Jackson

& Schmugge, 1991; Schmugge et al., 1988). Owe et al. (2001) found that the VOD remained noticeably higher than NDVI throughout the non-growing season over sites dominated by croplands mixed with grasses and woodlands. A more substantial VOD EOS lag is found in SAV and WSV regions of Africa. Grasses are prolific within these land cover classes and the stronger temporal lag may be due to the reasons above, as well as additional microwave attenuation from woody biomass, the presence of senescent leaves prior to abscission and associated leaf litter.

An even greater VOD EOS lag is present in MXF areas of the northeastern U.S. and Canada and DBF areas of the eastern U.S. These biomes highlight the major difference in canopy measures between optical-infrared and microwave remote sensing. As leaves senesce, the VIs drop in response to diminished photosynthetic capacity. Leaf biomass persists until abscission however, and will continue to attenuate the microwave signal causing a VOD EOS lag. A comprehensive review of phenology metrics for three deciduous species over the Hubbard Brook Experimental Forest in New Hampshire, USA (located within the MXF region) from 1989 to 2002 (Richardson et al., 2006) shows that senescence begins approximately at the end of September (day of year 270) with 50% of leaf fall reached between days 280 and 300. The initiation of the VOD downward trend over the MXF region shown here occurs consistently (5 of 6 years) between days 273 and 289. Similar abscission patterns may account for the slight temporal lag in the initiation of the DNF VOD downward trend as well. The VOD downward trend occurs approximately 16 to 32 days after that of the VIs and LAI, which may account for the period between needle senescence and abscission.

The Amazon and surrounding EBF region presents contradictory temporal signals. The VOD and LAI are strongly correlated in this region and generally coincide with an initial rise in the wet season and peak during the dry season. Myneni et al. (2007) showed a similar Amazon LAI seasonal peak during the dry season. However, the VOD (and LAI) series is inversely proportional to the EVI and GSI series. The EVI begins its rise at the initiation of the dry season, which is in accordance with the findings of Huete et al. (2006). The GSI shows some seasonality in these regions but is generally above 0.80, indicating a relatively unconstrained year-long growing season. The large number of contributing and confounding factors (e.g. atmospheric

contamination, land cover heterogeneity, high biomass levels and potential signal saturation) in this region currently limits the signal analysis for all indices and further research is needed to explain the phenology signals seen here, including regional comparisons using more explicit maps of vegetation biomass and land cover.

2.4 Summary

Our global analysis of the AMSR-E based VOD time series indicates strong utility of the VOD parameter for LSP assessment and synergy with other existing phenology metrics. The results of a conservative algorithm sensitivity analysis indicate relatively accurate VOD retrievals over a majority of the global vegetated land area using AMSR-E 18.7 GHz frequency T_b series (Figure 2.2). The resulting global VOD distribution follows general gradients in climate, land cover and canopy biomass conditions (Figure 2.5), with characteristic seasonal variability among the major land cover classes (Figure 2.6). Pixel-wise correlations between VOD and NDVI, EVI, LAI and GSI time series were generally strong on a global basis (Figure 2.7), with the exception of EBF areas that were primarily constrained by reduced availability of optical-infrared remote sensing indices and minimal GSI seasonal variation; some northern latitude areas where seasonal reductions in solar illumination, snow cover and frozen temperatures limit remote sensing data availability, and seasonally inundated regions where VOD retrievals show an inverse phenology signal relative to the other indices. Finally, aggregate regional analysis of the VOD and VI, LAI and GSI time series show strong temporal and LSP correspondence for the major global land cover categories (Figure 2.8). With the exception of phase shifts and EOS lags, the VOD time series and LSP metrics generally coincide with NDVI, EVI, and LAI time series results. The consistency of the temporal phase shifts and lags follows the different biophysical parameters that the microwave and optical-infrared instruments are sensitive to. These differences highlight potentially new and complimentary LSP information, including metrics sensitive to temporal shifts in canopy biomass and water content in addition to changes in canopy greenness. The VOD time series for this investigation were aggregated to relatively coarse 16-day temporal composites consistent with the availability of the MODIS EVI time series. However, continuous global VOD series from AMSR-E are available with higher (~4-

day or better) temporal fidelity, enabling potentially greater precision in LSP monitoring. The results of this study indicate that the satellite passive microwave remote sensing based VOD parameter may expand the breadth of phenology information, overcome many of the limitations affecting satellite optical-infrared remote sensing and advance global LSP monitoring capabilities.

2.5 Acknowledgements

This portion of the dissertation was carried out with funding from the NASA Terrestrial Ecology program. The AMSR-E T_b data and MODIS land cover in EASE grid format were provided by the National Snow and Ice Data Center (NSIDC). Other MODIS data were provided by the EOS data gateway, and NNR meteorological data were provided by the NOAA/OAR/ESRL PSD, Boulder, Colorado, USA (http://www.cdc.noaa.gov). The independent emissivity database was provided by Jean-Luc Moncet and Pan Liang of Atmospheric and Environmental Research, Inc., (http://www.aer.com/scienceResearch/mwrs/emis.html). The AMSR-E global VOD database and associated biophysical retrievals from this study are available through the UMT online data archives (ftp://ftp.ntsg.umt.edu/pub/data) and the NSIDC (http://nsidc.org/data/nsidc-0451.html). This work was performed at the University of Montana (UMT) and at the Jet Propulsion Laboratory, California Institute of Technology, under contract to the National Aeronautics and Space Administration.

2.6 References Cited

Becker, F., & Choudhury, B.J. (1988). Relative Sensitivity of Normalized Difference Vegetation Index (NDVI) and Microwave Polarization Difference Index (MPDI) For Vegetation and Desertification Monitoring. *Remote Sensing Of Environment, 24*, 297-311

Butterfield, H.S., & Malmstrom, C.M. (2009). The effects of phenology on indirect measures of aboveground biomass in annual grasses. *International Journal of Remote Sensing, 30*, 3133-3146

Choudhury, B.J., & Tucker, C.J. (1987). Monitoring global vegetation using Nimbus-7 37 GHz Data Some empirical relations. *International Journal of Remote Sensing, 8*, 1085 - 1090

Choudhury, B.J., Tucker, C.J., Golus, R.E., & Newcomb, W.W. (1987). Monitoring vegetation using Nimbus-7 scanning multichannel microwave radiometer's data. *International Journal of Remote Sensing, 8*, 533 – 538

Crow, W. T., Miralles, D. G., & Cosh, M. H. (2010). A quasi-global evaluation system from satellite-based surface soil moisture retrievals. *IEEE Trans. Geosci. Rem. Sens.* 48(6) 2516-2527.

De Jeu, R.A.M., & Owe, M. (2003). Further validation of a new methodology for surface moisture and vegetation optical depth retrieval. *International Journal of Remote Sensing, 24*, 4559-4578

Delbart, N., Picard, G., Le Toans, T., Kergoat, L., Quegan, S., Woodward, I., Dye, D., & Fedotova, V. (2008). Spring phenology in boreal Eurasia over a nearly century time scale. *Global Change Biology, 14*, 603-614

Di Bella, C.M., Paruelo, J.M., Becerra, J.E., Bacour, C., & Baret, F. (2004). Effect of senescent leaves on NDVI-based estimates of fAPAR: experimental and modeling evidences. *International Journal of Remote Sensing, 25*, 5415-5427

Dobson, M. C., Ulaby, F. T., Hallikainen, M. T., & El-Rayes, M. A. (1985). Microwave dielectric behavior of wet soil-Part II: Dielectric mixing models. *IEEE Trans. Geosci. Rem. Sens.* GE-23: 35-46.

English, S. J. (2008). The importance of accurate skin temperature in assimilating radiances from satellite sounding instruments. *IEEE Trans. Geosci. Rem. Sens.*, 46(2), 403-408.

Ferraro, R.R., Weng, F., Grody, N.C., & Basist, A. (1996). An eight-year (1987-1994) timeseries of rainfall, clouds, water vapor, snow cover and sea ice derived from SSM/I measurements. *Bulletin of the American Meteorological Society, 77*, 891-905

Frolking, S., Fahnestock, M., Milliman, T., McDonald, K., & Kimball, J. (2005). Interannual variability in North American grassland biomass/productivity detected by SeaWinds scatterometer backscatter. *Geophysical Research Letters*, 32

Frolking, S., Milliman, T., McDonald, K., Kimball, J., Zhao, M.S., & Fahnestock, M. (2006). Evaluation of the SeaWinds scatterometer for regional monitoring of vegetation phenology. *Journal Of Geophysical Research-Atmospheres, 111*

Huete, A.R., Didan, K., Shimabukuro, Y.E., Ratana, P., Saleska, S.R., Hutyra, L.R., Yang, W.Z., Nemani, R.R., & Myneni, R. (2006). Amazon rainforests green-up with sunlight in dry season. *Geophysical Research Letters, 33*

Huete, A.R., Justice, C., & van Leeuwen, W. (1999). MODIS Vegetation Index (MOD 13) Algorithm Theoretical Basis Document, Version 3, http://modis.gsfc.nasa.gov/data/atbd/atbd_mod13.pdf. In

Jackson, T.J., & Schmugge, T.J. (1991). Vegetation Effects On The Microwave Emission Of Soils. *Remote Sensing Of Environment, 36*, 203-212

Jackson, T.J., Schmugge, T.J., & Wang, J.R. (1982). Passive Microwave Sensing Of Soil-Moisture Under Vegetation Canopies. *Water Resources Research, 18*, 1137-1142

Jenkins, J.P., Richardson, A.D., Braswell, B.H., Ollinger, S.V., Hollinger, D.Y., & Smith, M.L. (2007). Refining light-use efficiency calculations for a deciduous forest canopy using

simultaneous tower-based carbon flux and radiometric measurements. *Agricultural and Forest Meteorology, 143*, 64

Jolly, W.M., Nemani, R., & Running, S.W. (2005). A generalized, bioclimatic index to predict foliar phenology in response to climate. *Global Change Biology, 11*, 619-632

Jones, L.A., Ferguson, C.R., Kimball, J.S., Zhang, K., Chan, S.K., McDonald, K.C., Njoku, E.G., & Wood, E.F. (2010). Satellite Microwave Remote Sensing of Daily Land Surface Air Temperature Minima and Maxima from AMSR-E. *IEEE J. Selected Topics. App. Earth Obs. Rem. Sens.,* 3(1), 111-123.

Jones, L. A, Kimball, J. S.. Podest, E., McDonald, K. C., Chan, S. K., & Njoku, E. G. (2009). A method for deriving land surface moisture, vegetation optical depth, and open water fraction from AMSR-E. *Proc. IEEE Int. Geosci. Rem. Sens. Symp. (IGARSS '09)*, Cape Town, South Africa, DOI: 10.1109/IGARSS.2009.5417921

Kalnay, E., Kanamitsu, M., Kistler, R., Collins, W., Deaven, D., Gandin, L., Iredell, M., Saha, S., White, G., Woollen, J., Zhu, Y., Leetmaa, A., Reynolds, R., Chelliah, M., Ebisuzaki, W., Higgins, W., Janowiak, J., Mo, K.C., Ropelewski, C., Wang, J., Jenne, R., & Joseph, D. (1996). The NCEP NCAR 40-Year Reanalysis Project. *Bulletin of the American Meteorological Society, 77*, 437-471

Kimball, J.S., McDonald, K.C., Frolking, S., & Running, S.W. (2004). Radar remote sensing of the spring thaw transition across a boreal landscape. *Remote Sensing Of Environment, 89*, 163

Kirdyashev, K.P., Chukhlantsev, A.A., & Shutko, A.M. (1979). Microwave Radiation of the Earth's Surface in the Presence of a Vegetation Cover. *Radio Engineering and Electronic Physics, 24*, 256-264

Knowles, K.W. (2004). EASE-Grid Land Cover Data Resampled from Boston University Version of Global 1 km Land Cover from MODIS 2001. In. Boulder, Colorado USA: National Snow and Ice Data Center

Knowles, K.W., Savoie, R.L., Armstrong, R.L., & Brodzik, M.J. (2009). AMSR-E/Aqua daily EASE-Grid brightness temperatures 2003-2008. In. Boulder, Colorado USA: National Snow and Ice Data Center

Knyazikhin, Y., Glassy, J., Privette, J.L., Tian, Y., Lotsch, A., Zhang, Y., Wang, Y., Morisette, J.T., Votava, P., Myneni, R.B., Nemani, R.R., & Running, S.W. (1999). MODIS Leaf Area Index (LAI) And Fraction Of Photosynthetically Active Radiation Absorbed By Vegetation (FPAR) Product (MOD15) Algorithm Theoretical Basis Document, http: //eospso.gsfc.nasa.gov/atbd/modistables.html. In

Min, Q.L., & Lin, B. (2006a). Determination of spring onset and growing season leaf development using satellite measurements. *Remote Sensing Of Environment, 104*, 96-102

Min, Q.L., & Lin, B. (2006b). Remote sensing of evapotranspiration and carbon uptake at Harvard Forest. *Remote Sensing Of Environment, 100*, 379-387

Mo, T., Choudhury, B.J., Schmugge, T.J., Wang, J.R., & Jackson, T.J. (1982). A Model for Microwave Emission From Vegetation-Covered Fields. *Journal Of Geophysical Research, 87*, 11229-11237

Moncet, J., Liang, P., Galantowicz, J., Lipton, A., Uymin, G., Prigent, C., & Grassotti, C. (2010). Land Surface Microwave Emissivities from AMSR-E and MODIS Measurements with Advanced Quality Control. *Journal of Geophysical Research*, in submission.

Myneni, R.B., Yang, W.Z., Nemani, R.R., Huete, A.R., Dickinson, R.E., Knyazikhin, Y., Didan, K., Fu, R., Juarez, R.I.N., Saatchi, S.S., Hashimoto, H., Ichii, K., Shabanov, N.V., Tan, B., Ratana, P., Privette, J.L., Morisette, J.T., Vermote, E.F., Roy, D.P., Wolfe, R.E., Friedl, M.A., Running, S.W., Votava, P., El-Saleous, N., Devadiga, S., Su, Y., & Salomonson, V.V. (2007). Large seasonal swings in leaf area of Amazon rainforests. *Proceedings of the National Academy of Sciences of the United States of America, 104*, 4820-4823

Njoku, E.G., & Li., L. (1999). Retrieval of land surface parameters using passive microwave measurements at 6-18 GHz. *IEEE Trans. Geosci. Rem. Sens.* 37(1): 79-93.

Njoku, E.G., Ashcroft, P., Chan, T.K., & Li, L. (2005). Global survey and statistics of radio-frequency interference in AMSR-E land observations. *IEEE Transactions On Geoscience And Remote Sensing, 43*, 938-947

Njoku, E.G., & Chan, S.K. (2006). Vegetation and surface roughness effects on AMSR-E land observations. *Rem. Sens. Environ.* 100: 190-99.Owe, M., de Jeu, R., & Walker, J. (2001). A methodology for surface soil moisture and vegetation optical depth retrieval using the microwave polarization difference index. *IEEE Transactions On Geoscience And Remote Sensing, 39*, 1643-1654

Owe, M., de Jeu, R., & Walker, J. (2001). A methodology for surface soil moisture and vegetation optical depth retrieval using the microwave polarization difference index. *IEEE Transactions On Geoscience And Remote Sensing, 39*, 1643-1654

Paloscia, S., & Pampaloni, P. (1992). Microwave Vegetation Indexes For Detecting Biomass And Water Conditions Of Agricultural Crops. *Remote Sensing Of Environment, 40*, 15-26

Parmesan, C. (2007). Influences of species, latitudes and methodologies on estimates of phenological response to global warming. *Global Change Biology, 13*, 1860-1872

Penuelas, J., Rutishauser, T., & Filella, I. (2009). Phenology Feedbacks on Climate Change. *Science, 324*, 887-888

Peterson, T. C., Bassist, A. N., Williams, C. N., & Grody, N. C. (2000). A blended satellite-in situ near-global surface temperature dataset. *Bull. Am. Met. Soc.*, 81(9), 2157-2164.

Piao, S., Ciais, P., Friedlingstein, P., Peylin, P., Reichstein, M., Luyssaert, S., Margolis, H., Fang, J., Barr, A., Chen, A., Grelle, A., Hollinger, D.Y., Laurila, T., Lindroth, A., Richardson, A.D., & Vesala, T. (2008). Net carbon dioxide losses of northern ecosystems in response to autumn warming. *Nature, 451*, 49

Piao, S., P. Friedlingstein, P. Ciais, N. Viovy, & J. Demarty (2007). Growing season extension and its impact on terrestrial carbon cycle in the Northern Hemisphere over the past 2 decades. *Global Biogeochemical Cycles, 21*

Prigent, C., Rossow, W. B., & Matthews, E. (1997). Microwave land surface emissivities estimated from SSM/I observations. *J. Geophys. Res.* 102(D18), 21867-90.

Prigent, C., Aires, F., Rossow, W. B., & Robock, A. (2005). Sensitivity of satellite microwave and infrared observations to soil moisture at a global scale: Relationship of satellite observations to *in situ* soil moisture measurements. *J. Geophys. Res.* 110(D07)

Reed, B.C., Schwartz, M.D., & Xiao, X. (2009). Remote Sensing Phenology: Status and the Way Forward. *Phenology of Ecosystem Processes: Applications in Global Change Research* (pp. 231-246): Springer

Richardson, A.D., Bailey, A.S., Denny, E.G., Martin, C.W., & O'Keefe, J. (2006). Phenology of a northern hardwood forest canopy. *Global Change Biology, 12*, 1174-1188

Saatchi, S.S., Levine, D.M., & Lang, R.H. (1994). Microwave Backscattering And Emission Model For Grass Canopies. *IEEE Transactions On Geoscience And Remote Sensing, 32*, 177-186

Schmugge, T.J., Wang, J.R., & Asrar, G. (1988). Results From The Push Broom Microwave Radiometer Flights Over The Konza Prairie In 1985. *IEEE Transactions On Geoscience And Remote Sensing, 26*, 590-597

Schwartz, M.D., & Hanes, J.M. (2009). Intercomparing multiple measures of the onset of spring in eastern North America. *International Journal Of Climatology, 20*, 929-932

USDA, Foreign Agricultural Service, (2007). Severe El Niño Drought Wilts Summer Grain Crops in Southern Africa, http://www.pecad.fas.usda.gov/highlights/2007/05/southern_africa_corn_may07

Shi, J., Jackson, T., Tao, J., Du, J., Bindlish, R., Lu, L., & Chen, K.S. (2008). Microwave vegetation indices for short vegetation covers from satellite passive microwave sensor AMSR-E. *Remote Sensing Of Environment, 112*, 4285

Ulaby, F.T., Moore, R.K., & Fung, A.K. (1982). *Microwave remote sensing: Active and passive, 2, Radar remote sensing and surface scattering and emission theory.* Reading, MA: Addison-Wesley

Wang, J. R., & Choudhury, B. J. (1981). Remote sensing of soil moisture content over bare fields at 1.4 GHz frequency. *J. Geophy. Res.,* 86, 5277-5282.

Wang, Q., Tenhunen, J., Dinh, N.Q., Reichstein, M., Otieno, D., Granier, A., & Pilegarrd, K. (2005). Evaluation of seasonal variation of MODIS derived leaf area index at two European deciduous broadleaf forest sites. *Remote Sensing Of Environment, 96*, 475-484

Waring, R.H., & Running, S.W. (1998). *Forest Ecosystems; Analysis at Multiple Scales*. (2 ed.). San Diego, CA: Academic Press

Wegmuller, U., Matzler, C., & Njoku, E.G. (1995). Canopy opacity models. In B.J. Choudhury, Y.H. Kerr, E.G. Njoku, & P. Pampaloni (Eds.), *Passive Microwave Remote Sensing of Land Atmosphere Interactions* (pp. 375-387). Utrecht, The Netherlands: VSP

Wentz, F. J. (2000). AMSR-E Ocean Algorithm ATBD, version 2. Remote Sensing Systems, Santa Rosa, CA. http://www.remss.com/papers/amsr/AMSR_Ocean_Algorithm_Version_2.pdf.

White, M.A., Beurs, K.M.d., Didan, K., Inouye, D.W., Richardson, A.D., Jensen, O.P., O'Keefe, J., Zhang, G., Nemani, R.R., LEEUWEN, W.J.D.v., Brown, J.F., WIT, A.d., Schaepman, M., Lin, X., Dettinger, M., Bailey, A.S., Kimball, J., Schwartz, M.D., Baldocchi, D.D., Lee, J.T., & Lauenroth, W.K. (2009). Intercomparison, interpretation, and assessment of spring phenology in North America estimated from remote sensing for 1982-2006. *Global Change Biology, 15*, 2335-2359

Wigneron, J.P., Chanzy, A., Calvet, J.C., & Bruguier, W. (1995). A Simple Algorithm To Retrieve Soil-Moisture And Vegetation Biomass Using Passive Microwave Measurements Over Crop Fields. *Remote Sensing Of Environment, 51*, 331-341

Chapter 3. Comparing Land Surface Phenology Derived from Satellite and GPS Network Microwave Remote Sensing

The relatively common use of satellite optical-IR remote sensing for vegetation studies has allowed for extensive development of validation protocols based on these data, including recent efforts by the Committee on Earth Observation Satellites Land Product Validation (CEOS-LPV) subgroup. These protocols generally involve the use of coordinated in situ measurements including tower-mounted radiometers and long-term field data collections. Other regional efforts are underway to validate satellite optical-IR based LSP metrics using stand level phenology cameras (e.g. the PhenoCam Network, Richardson et al. 2009) and more extensive citizen science based data collections including the USA National Phenology Network (USA-NPN) (Schwartz et al. 2012). Optical-IR vegetation indices are sensitive to canopy greenness, or chlorophyll content, and have the advantage of being directly comparable to easily observed changes in the state of vegetation such as bud burst, leaf unfolding or changes in leaf color.

Direct measurements of related changes in canopy water content and biomass structure suitable for satellite microwave VOD and LSP validation require more labor-intensive field measurements. Site level microwave measurements have been made by microwave radiometers, but these data are of limited scope in both space and time, and the focus of such efforts has primarily been to validate satellite soil moisture measures and not the state of vegetation through time or across a range of vegetation types. Few field level microwave datasets are currently available, which has limited the application of these data for satellite VOD and LSP validation. Recent studies however, have revealed that permanent Global Positioning System (GPS) stations installed to measure tectonic plate motions, can be used to detect ecosystem relevant biophysical parameters, including surface soil moisture (Larson et al. 2008) and vegetation water content variability (Small et al. 2010).

GPS satellites transmit L-band (1.2 and 1.5 GHz frequency) microwave signals. These signals interact strongly with water in the environment (including vegetation), and thus are suitable for monitoring temporal variations in biophysical parameters. GPS stations are designed for determining spatial location. They measure the distance between the local station antenna and the orbital constellation of GPS satellites. A secondary signal, and noise source for

positioning applications, measures signal reflectance within a local footprint of approximately 1000m^2 (~0.001 km^2) surrounding the GPS antenna. The NMRI (Normalized Microwave Reflection Index) metric is derived from these GPS reflections; it can be measured on a daily basis and is insensitive to cloud cover (Larson and Small 2013). This study uses an initial compilation of NMRI records from GPS sites distributed across the western United States.

The objective of this investigation was to quantify spatial and temporal correspondence between satellite (AMSR-E) derived VOD and in situ NMRI network observations to assess the potential of the NMRI data for satellite microwave LSP validation. We compared vegetation water content changes inferred from GPS NMRI site network data with collocated satellite VOD records over the western continental USA and Alaska. The NMRI and VOD observations were compared at 305 GPS site locations over a multi-year observation record from January 2007 to September 2011. The NMRI and VOD time series were processed to determine the vegetation SOS for a subset of 24 GPS sites determined to have regionally homogeneous land cover conditions within the overlying (25km resolution) VOD grid cell; the resulting SOS metrics were then compared to evaluate NMRI and VOD consistency in determining this critical LSP metric. Spatial heterogeneity of LSP, which potentially could affect VOD and NMRI correspondence, was examined for a single AMSR-E VOD grid cell containing multiple NMRI sites; for this location, the VOD record was evaluated against NMRI observations from nine GPS antennas and 250m resolution satellite (MODIS) NDVI records representing different land cover types within the overlying VOD grid cell to analyze the effect of mixed land cover contributions on the aggregate regional SOS metric.

3.1 Data and Methods

3.1.1 Microwave Vegetation Optical Depth

The Advanced Microwave Scanning Radiometer for EOS (AMSR-E) is deployed on the polar-orbiting Aqua satellite platform with UTC 1:30 A.M. (descending)/P.M. (ascending) orbit equatorial crossings. The AMSR-E sensor measures vertical and horizontal polarized brightness temperatures at six frequencies (6.9, 10.7, 18.7, 23.8, 36.5, 89.0 GHz), and at a constant Earth incidence angle of 55° from nadir. The daily 25km resolution global Equal Area Scalable Earth

(EASE) Grid brightness temperatures provided by the NASA data archive facility at the National Snow and Ice Data Center (Knowles et al. 2009) were used to derive an AMSR-E global land parameter database for ecosystem studies (Jones and Kimball, 2011). The database includes VOD retrievals at 6.9, 10.7 and 18.7 GHz frequencies; the VOD series derived from the 18.7 GHz T_b record was employed for this investigation due to greater radio frequency interference (RFI) and associated retrieval gaps in the 6.9 and 10.7 GHz frequency data (Njoku et al. 2005). The VOD record extends from January 2003 to September 2011 and encompasses all grid cells with <50% permanent ice or open water cover, as defined from a 1km resolution MODIS (MOD12Q1) IGBP global land cover classification aggregated to 25km resolution, while retaining relative land cover class proportions (Knowles, 2004). The VOD retrieval algorithms minimize potential noise effects from dynamic atmosphere precipitable water vapor, temperature, surface inundation and soil moisture, resulting in global consistency and relatively high accuracy (Jones et al. 2009). A detailed description of the AMSR-E VOD record, including algorithm development and sensitivity, is provided elsewhere (Jones et al. 2009; Jones et al. 2011).

In this study the daily VOD record from January, 2007 to September, 2011 was temporally composited to a 4-day median time step. This compositing mitigates signal noise and allows for the creation of a continuous time series, overcoming missing data due to observation swath coverage gaps from the polar orbiting AMSR-E sensor at mid- to lower latitudes. At higher latitudes without gaps the 4-day median is defined as the larger of the two middle values.

3.1.2 GPS Normalized Microwave Reflection Index

The GPS is a constellation of over 30 L-band (1.5 and 1.2 GHz) transmitting satellites that is best known for real-time navigation and positioning applications. Earth scientists have exploited GPS signals to measure slow tectonic variations (mm/yr) by installing and maintaining regional base station networks that operate continuously. Recently the National Science Foundation installed over 1000 GPS base stations in the western United States to measure deformation of the Pacific-North America plate boundary as part of the EarthScope Plate Boundary Observatory (PBO) initiative (http://www.earthscope.org). Most sites were installed

by 2007 and operate with nearly identical instrumentation (receivers and antennas). GPS sites are generally located in low vegetation biomass areas to minimize off nadir reflectance contamination of the GPS signal. The resulting NMRI (Small et al. 2010) site records largely reflect grassland and shrubland conditions with limited coverage of higher biomass (e.g. forest) vegetation types (Figure 3.1, inset graph).

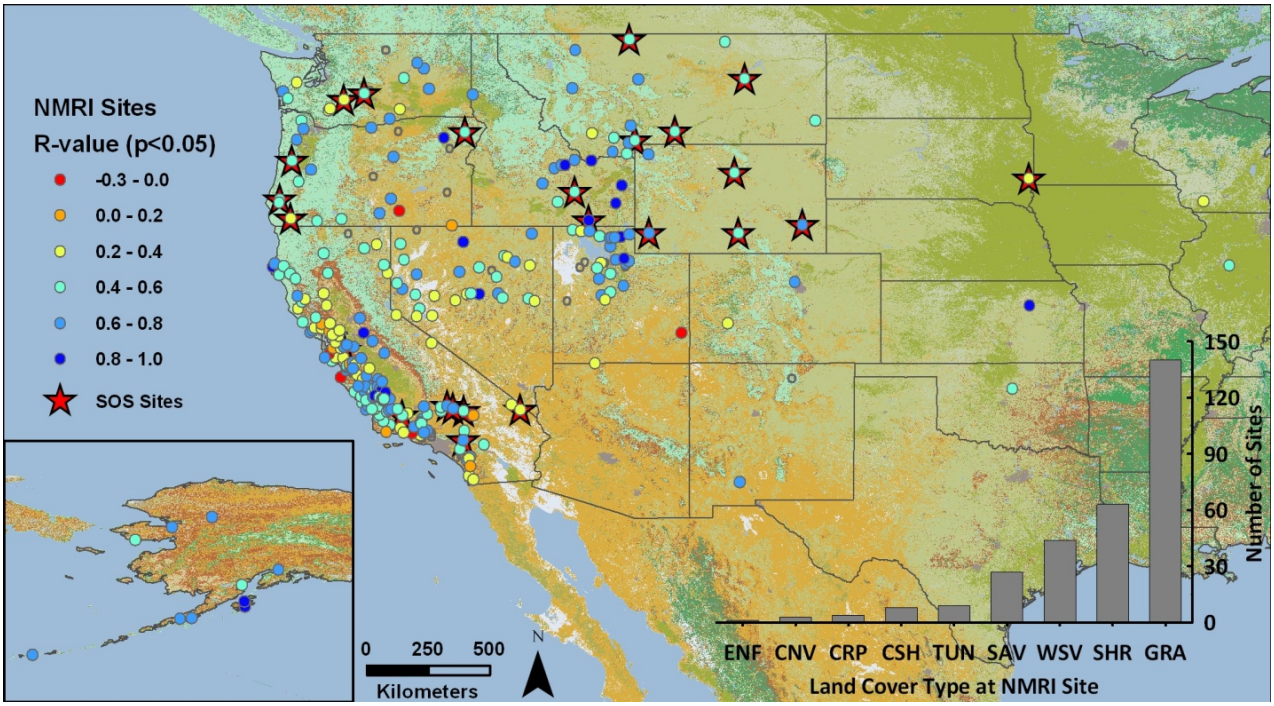

Figure 3.1. Pearson correlation coefficients (p<0.05) between VOD and NMRI time series for 305 GPS base station sites across the western USA. Inset map displays sites over the Alaska portion of the domain. Open circles represent non-significant (p>0.05) correlation sites. Stars represent 24 homogeneous land cover sites used in the SOS calculations. Inset graph displays number of NMRI sites by land cover type as designated by the PBO network (ENF-evergreen needle leaf forest, CNV-cropland/natural vegetation mosaic, CRP-cropland, TUN-tundra, SAV-savanna, WSV-woody savanna, SHR-shrubland, GRA-grassland). Background represents the MODIS IGBP land cover classification.

The NMRI vegetation metric is based on reflected GPS signals (multipath) observed in the L1 GPS ranging data, or MP1 (MultiPath on the L1 frequency) from the PBO network. The reflections are quantified by calculating the mean of the daily observation scatter (RMS) for all satellites, or MP1rms (Estey and Meertens 1999). While the MP1rms statistics are routinely calculated by GPS base station networks, GPS station operators primarily use them to evaluate

hardware performance. Small et al. (2010) was the first to show that these variations in MP1rms are strongly correlated with the NDVI ($0.60<r^2<0.80$) in the western United States (Idaho, Colorado, Montana, Utah, Nevada, Oregon). The GPS base station sites examined represented a range of land cover types, including grassland, cropland and shrubland. Amplitudes of the reflected signals are strongest when vegetation biomass within the local (~0.001 km^2) sampling footprint is relatively low, and decrease as vegetation biomass and associated water content increases. The RMS of the observation scatter captures these reflection amplitude variations.

Building on that initial study, the PBO H_2O group has compiled normalized MP1rms statistics (NMRI) for more than 300 GPS stations from the PBO network and extended it in time to 2012 (http://xenon.colorado.edu/portal). The data are screened for snow presence and recent precipitation as these adversely affect the signal and resulting NMRI value. Because reflected GPS signals are also influenced by terrain (a reflected GPS range signal depends directly on the extra path length), the MP1rms metrics have been normalized to remove this first-order effect. The bare vegetation state is determined empirically by estimating the maximum MP1rms over the entire observation record (MP1max). Dividing the variation in MP1rms by this maximum removes the extra path length term. The NMRI thus measures variation in the GPS microwave (L-band) reflection power:

$$NMRI = - (MP1rms – MP1max)/MP1max \quad (1)$$

The negative sign in Eqn. (1) is introduced to allow the NMRI to increase or decrease as vegetation grows or senesces. Further information on the NMRI database and validation with field measurements is available from Larson and Small (2013) and Small et al. (2013). In this study NMRI data from January, 2007 to December, 2011 for 305 sites within the western continental United States and Alaska were composited to the same 4-day median time step as the VOD to allow for direct comparison and to minimize potential effects from day-to-day variability on the phenology signal.

3.1.3 Correlations and Phenology Metrics

Pearson correlation coefficients and significance values were calculated between 305 NMRI 4-day time series and corresponding VOD 25km resolution grid cell time series for the full data record and for each calendar year. Full data record lagged correlations were also evaluated between the VOD and NMRI series by systematically offsetting the VOD series by up to +/- 48 days (twelve 4-day time steps). To assess the influence of land surface heterogeneity on the NMRI and VOD correlations, full data record R-values for each NMRI location were compared to a land cover heterogeneity index (Shannon Diversity Index - SDI) (Shannon 1948), MODIS derived percent tree cover (Hansen et al. 2003) and terrain heterogeneity (SD of elevation) within the overlying 25km VOD grid cell.

NMRI sites that contained the full 5 year data record and were within homogeneous VOD grid cells (>80% common land cover) were selected for SOS phenology metric calculations; this resulted in 24 sites well distributed across the western USA (Figure 3.1). The homogeneous VOD grid cells were identified using the 1 km resolution MODIS (MOD12Q1) IGBP global land cover classification (Knowles, 2004). Many of the 24 homogeneous land cover sites are located in regions where winter snow cover is common. The NMRI and VOD temporal series are degraded and screened during these periods, resulting in winter gaps in the data records that must be filled in order to apply fitting algorithms and calculate LSP metrics. Winter gaps were filled on a site or grid cell-wise basis for each year using the median of the first three NMRI or VOD values of the following spring. This approach assumes that vegetation will degrade or reach a minimum stasis and remain relatively constant (dormant) through the frozen winter period, and that the first successful retrievals of the following spring effectively represent the winter base vegetation state.

The 4-day median filled NMRI and VOD time series were input into TIMESAT (Jönnson & Eklundh, 2004), a commonly used tool for analyzing time series data (Nightingale et al. 2009, Tan et al. 2010) that provides curve fitting methods for defining phenology metrics and allows for the detection of dual (biannual) seasons. A double logistic fit was applied to the time series data and the SOS was defined as the 20% threshold of seasonal amplitude. TIMESAT requires previous and subsequent season data to classify the current (middle) season SOS metric.

Therefore, the five year (2007-2011) NMRI and VOD records produced 3 to 4 annual (or 6 to 8 biannual) SOS metrics per site. Linear regression analysis and root mean squared error (RMSE), mean absolute error (MAE), and mean residual error (MRE) statistics were then used to compare the NMRI and VOD SOS metrics.

3.1.4 NMRI and VOD Sensitivity to Moisture Variability

As the NMRI and VOD are responsive to changes in vegetation water content, climatic variations (in particular those associated with water availability), at the local and regional scale may affect seasonal and interannual variation in both data records, and their correspondence. To assess these effects, NMRI and VOD correlations for each calendar year were compared to a yearly Palmer Drought Severity Index (PDSI) (Palmer 1965, Dai et al. 2004) and the number of precipitation days per year (Harris et al. 2013) within the VOD 25km footprint for each site. Variation in the two data records was further assessed in relation to monthly changes in the atmosphere vapor pressure deficit (VPD).

The VPD term is a measure of the evaporative demand of the atmosphere and has been shown to be an effective indicator of water limitation to vegetation growth (Huffaker 1942). High VPD values are representative of water stress and if consistent over time, can significantly limit photosynthesis and growth (White 2000). The NMRI and VOD time series were composited to 16-day intervals and temporal anomalies were calculated for each data record in relation to their long-term means. These results were then plotted in relation to corresponding 0.5 degree resolution monthly VPD anomalies derived from the NASA MERRA (Modern-Era Retrospective Analysis for Research and Application) global reanalysis daily surface meteorology (Rienecker et al. 2008). Anomalies (X_i^*) were calculated as:

$$X_i^* = X_i - \mu X_i \quad (2)$$

where X_i is the 16-day (NMRI, VOD) or monthly (VPD) value and μX_i is the mean 16-day or monthly value for all years (2007-2011). The standard deviation of the anomalies was calculated for the NMRI and VOD, and 16-day anomalies were considered significant departures

from normal if they positively or negatively exceeded one standard deviation. The 16-day intervals were then flagged if NMRI and VOD anomalies were both positive or negative departures from normal.

3.1.5 Multiple Sites within a Single VOD Grid Cell

As the NMRI is calculated at over 300 GPS base stations in the western USA, there are multiple VOD grid cells containing more than one NMRI site. The AMSR-E 25km resolution VOD retrievals often represent a mix of underlying land cover types and environmental conditions, especially over complex terrain, while the NMRI represents a finer scale (~0.001 km^2) footprint surrounding the GPS antenna and often represents a single land cover type. To evaluate potential effects of NMRI heterogeneity, the VOD grid cell with the most NMRI sites (nine) was identified. The selected VOD grid cell area also contained a mix of herbaceous and woody biomass components; 53% grassland, 32% shrubland, and 12% woody savanna. The grid cell (center coordinates: Lat. 35.7544°, Lon. -120.2603°) is located in south central California and encompasses a topographic range from ~300 to 700 m with an approximate mean annual temperature of 18.3 deg C and mean annual precipitation of 21.0 cm. The initiation of vegetation growth in this relatively warm region is driven by fall or early winter (October-January) precipitation onset. Daily precipitation data (Klein 2002) were acquired from the National Climate Data Center for the Coalinga, California station (GHCND:USC00041864), approximately 28km north of the VOD grid cell. As recent precipitation and soil moisture variation adversely affect the NMRI values, days with precipitation (and the following day) were further screened using the local precipitation data. Eight of the nine NMRI sites are located in grassland and the remaining site in shrubland (note: data availability began in 2008 for sites p542, p552 and p578). We compared the single VOD time series to the nine NMRI time series and MODIS NDVI (MOD13Q1) 250m time series spatial means of the three dominant land cover types and overall NDVI spatial means within the overlying VOD grid cell. The SOS metrics were calculated using the double logistic fit and 20% of seasonal amplitude in TIMESAT for all time series.

3.2 Results

3.2.1 VOD and NMRI Correlations

Pearson correlation coefficients between 4-day VOD and NMRI time series at the 305 GPS site locations are displayed in Figure 3.1. Of the 305 sites, 276 (90.5%) showed significant ($p<0.05$) positive correlations between the VOD and NMRI time series, while twelve sites displayed negative correlations, five of which were significant ($p<0.05$). The mean of significant correlation coefficients was R=0.53 (SD = 0.21). Using temporally lagged VOD series improved the VOD-NMRI correlations at 250 sites, improving the mean of significant correlation coefficients; R=0.61 (SD=0.17). The non-lagged and lagged correlation results, grouped by local NMRI land cover type, are summarized in Figure 3.2. A majority (75%) of sites achieved the best correspondence with a VOD lag from -4 to 32 days relative to the NMRI (Figure 3.2, inset); a positive (negative) lag implies that the VOD season onset begins earlier (later) than the NMRI season onset.

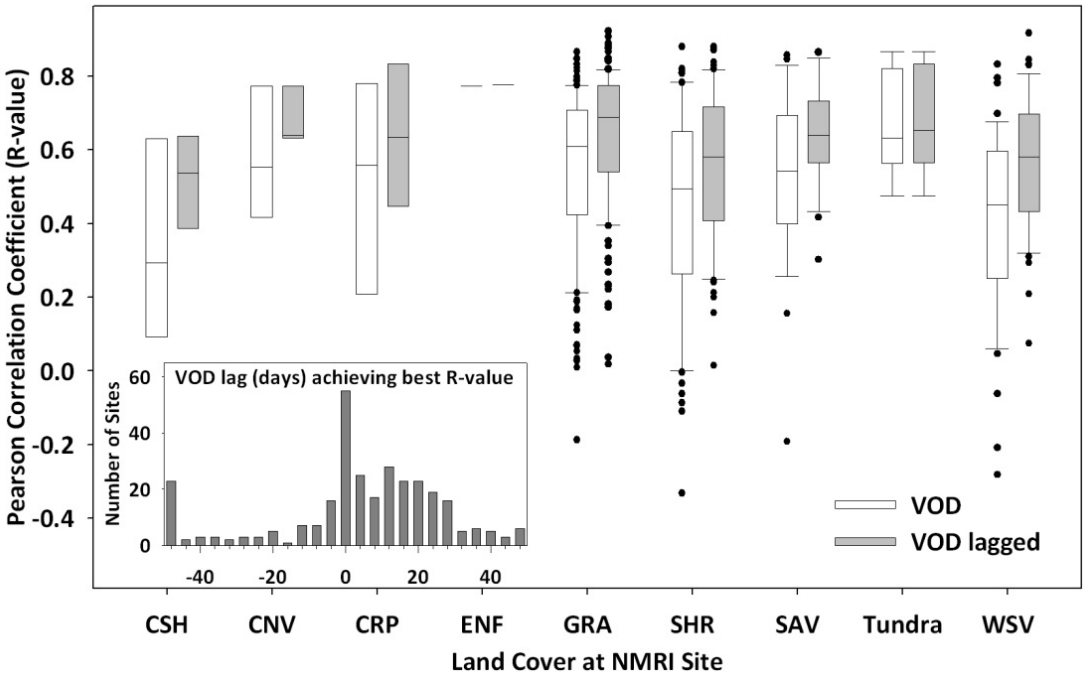

Figure 3.2. VOD versus NMRI correlations and temporally lagged correlations, grouped by land cover type at the individual NMRI sites. Plot displays median, quartiles, 5th and 95th percentiles and outliers. Inset graph depicts the number of sites which achieved their highest correlation coefficient at the given temporal lag.

The VOD and NMRI correlations were highly variable within land cover types (Figure 3.2) and examination of the individual calendar year correlations revealed a logistic relationship between each site's coefficient of variation (CV) and its mean R-value for all four years of record; sites with lower R-values generally displayed a higher CV. Although some site years displayed strong correlations, other site years showed weak correspondence, adversely affecting the full data record R-values shown in Figure 3.2. No significant relationships were found between VOD and NMRI correspondence for the full-data record and terrain heterogeneity (SD of elevation), MODIS percent tree cover, or land cover heterogeneity (SDI) (Figure 3.3).

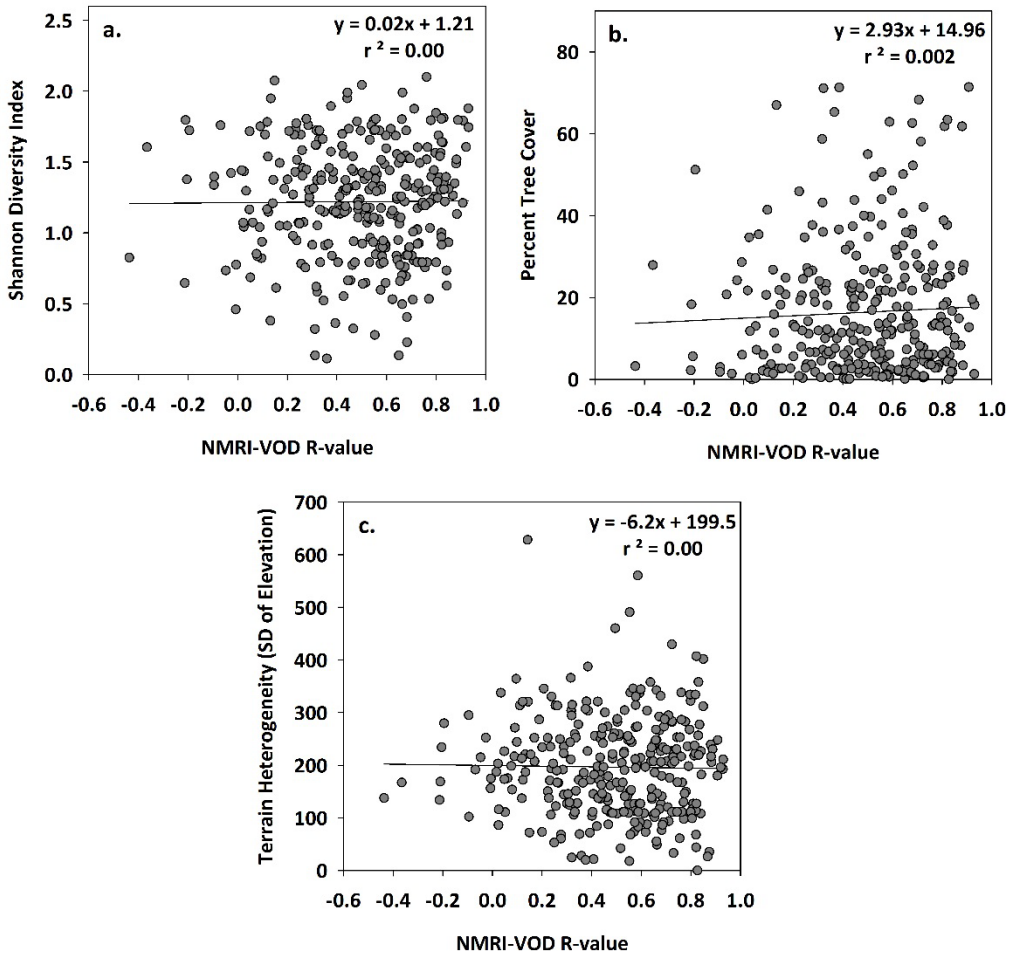

Figure 3.3. Scatterplots and least squares linear relationship between NMRI and VOD correlations (R-values) and Shannon Diversity Index (a), Percent Tree Cover (b), and Terrain Heterogeneity (c) (calculated as the SD of elevation), within the 25km VOD pixels.

The NMRI and VOD 16-day anomalies displayed widespread favorable agreement in their departures from normal across a large latitudinal range (32.6° N to 67.0° N) that were generally congruent with monthly VPD anomalies (Figure 3.4). High VPD anomalies were observed across the full latitudinal range in 2007 and both the NMRI and VOD displayed coincident negative anomalies at a majority of the sites. The opposite response is seen in years 2010 and 2011, with lower than normal VPD and higher than normal NMRI and VOD, particularly at more southerly latitudes of the western USA domain where water availability is a primary control on vegetation activity. Despite this favorable agreement with VPD, no significant relationship was found between the degree of VOD and NMRI correspondence and yearly PDSI or precipitation days per year.

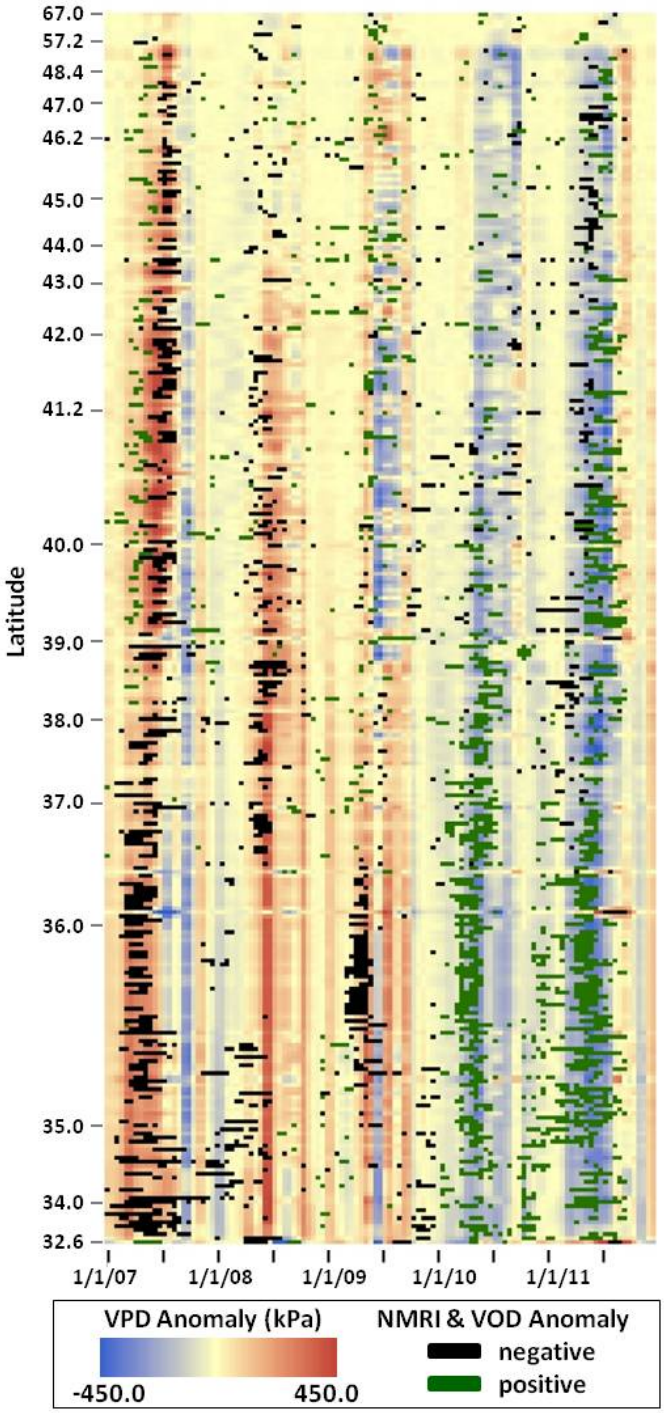

Figure 3.4. Space (y-axis) vs time (x-axis) plot of NMRI and VOD 16-day anomalies (2007 to 2011) determined as significant departures from normal and plotted over monthly vapor pressure deficit (VPD) anomalies at each of the 305 NMRI sites. Each site is represented by a row of pixels distributed along the time (x) axis, while sites are ordered by latitude along the y-axis. Green and black pixels represent 16-day intervals when both NMRI and VOD anomalies were significantly positive or negative departures from normal; i.e. greater than or less than the SD of the full data record anomalies.

3.2.2 Start of Season Metrics

A linear regression of the VOD versus NMRI derived SOS (day of year) values for the 24 homogenous land cover sites resulted in a coefficient of determination (r^2) of 0.73 ($p<0.001$), RMSE of 36.8 days and MAE of 26.7 days (Figure 3.5). The MRE in SOS values (VOD SOS – NMRI SOS) was -36.2 days for all sites with 95% of VOD seasons starting earlier than NMRI seasons. In some cases the SOS begins near the end of a calendar year for one dataset (e.g. day of year = 355, year = 2009) and at the beginning of the calendar year for the second dataset (e.g. day of year = 20, year = 2010). In order to properly plot these values and perform a linear regression analysis, the day of year values must be adjusted. For the example given, the 2009 SOS is classified as a 2010 SOS and adjusted to day of year -10 to properly account for the 30 day difference; this accounts for the negative day of year values in Figure 3.4.

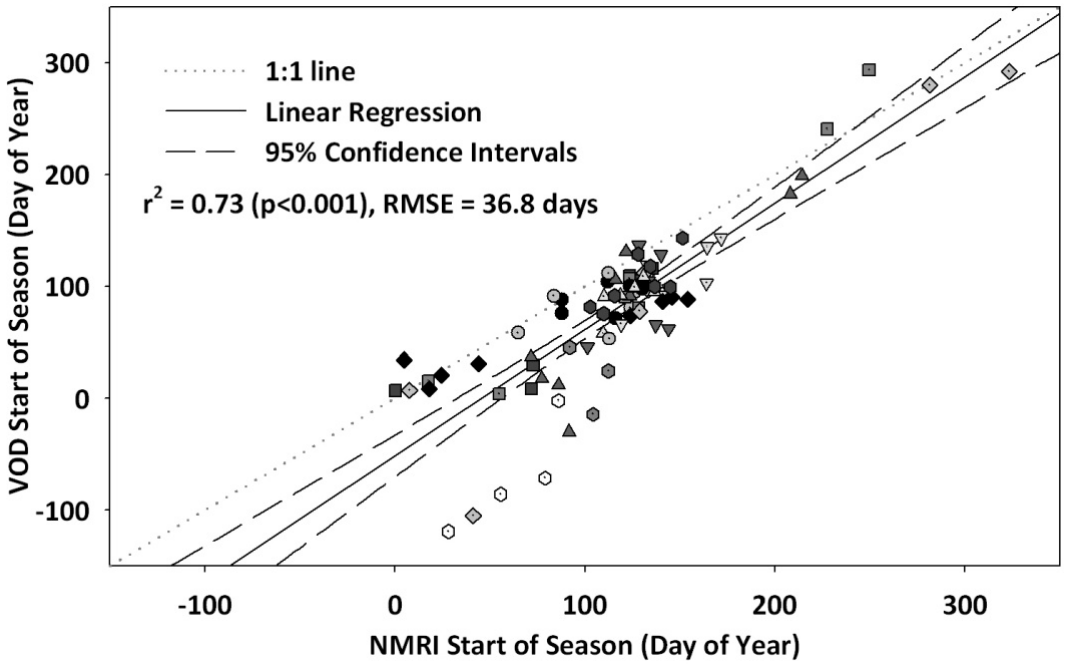

Figure 3.5. Least-squares linear regression fit between VOD and NMRI derived SOS values at the 24 homogeneous land cover sites for the 2007-2011 record. Mean Absolute Error (MAE) = 26.7 days. Each NMRI site is given a unique symbol.

Eight sites displayed one or more seasons with differences greater than 60 days and a single site displayed a consistent offset greater than 90 days (Figure 3.5, open symbol). Full data record correlation coefficients at these sites ranged from 0.21 to 0.81, indicating that the

local NMRI response for some sites may not be representative of the homogeneous land cover conditions of the larger (25km resolution) VOD grid cell, resulting in a large offset in the associated SOS metrics. This is also apparent in the lack of significant correspondence between the VOD and NMRI time series correlations, and land cover heterogeneity (SDI). A lower SDI represents low variability in land cover and therefore an inverse relationship is expected; pixels with low SDI values are expected to have stronger NMRI-VOD correlations, but this relationship was not apparent in the analysis. Examination of multiple NMRI sites within a single VOD grid cell partially explains these discrepancies.

3.2.3 NMRI and NDVI heterogeneity within a single VOD grid cell

The mean and standard deviation of the nine NMRI site records located within the single VOD grid cell are plotted in Figure 3.6a along with the VOD time series and overall NDVI mean of the three dominant land cover classes, which comprise 97% of the overlying VOD grid cell. These results display a fall (~September) VOD increase that then decreases with winter onset (December-January) in 2008 and 2010, but is relatively stable through the other winters of record (2009, 2011). The mean NDVI time series of each dominant land cover class (Figure 3.6b) within the VOD cell displays a response in the fall of some years similar to the VOD record, particularly for woody savanna. There is good agreement ($0.40<R<0.82$, $p<0.01$) between all of the time series displayed in Figure 3.6, including similar interannual variation in seasonal amplitudes, with years 2008, 2010 and 2011 all displaying high amplitudes and 2007 and 2009 displaying lower than normal amplitudes for the record.

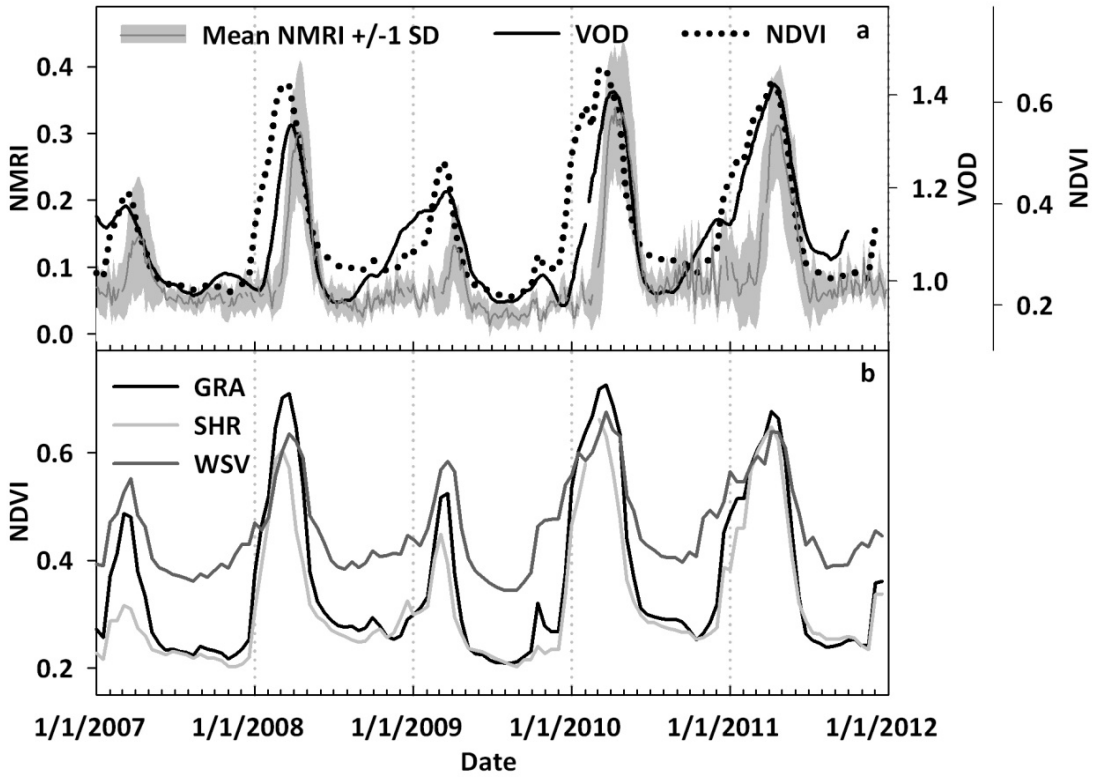

Figure 3.6. (a) The spatial mean and standard deviation of 4-day median time series from nine NMRI sites located within a single VOD grid cell, the mean 16-day 250m MODIS (MOD13Q1) NDVI of the three dominant land cover types within the VOD grid cell, and the corresponding VOD time series. The nine NMRI sites represent grassland (8 sites) and shrubland (1 site) conditions; (b) the mean NDVI time series from individual dominant land cover classes representing 53% (GRA – grassland), 32% (SHR – shrubland), and 12 % (WSV - woody savanna) of the overlying VOD grid cell.

The SOS metrics for all of the time series, including individual metrics for each NMRI site and seasonal precipitation accumulation from July 1 to June 30, are displayed in Figure 3.7a. These results demonstrate the wide variation that can occur in calculating phenology metrics even though the time series are relatively similar. The SOS values for the NMRI sites occur within approximately one month except for a single site (p542) in 2010-2011 and the drought year (2008-2009) when two of the five available sites displayed no SOS and the remaining sites displayed a SOS range of 113 days; an effect of the minimal variation in NMRI values for that season (Figure 3.6a). The VOD SOS displays large interannual variation, which is dependent on

whether a winter (November to January) VOD trough is present following the initial VOD rise in September.

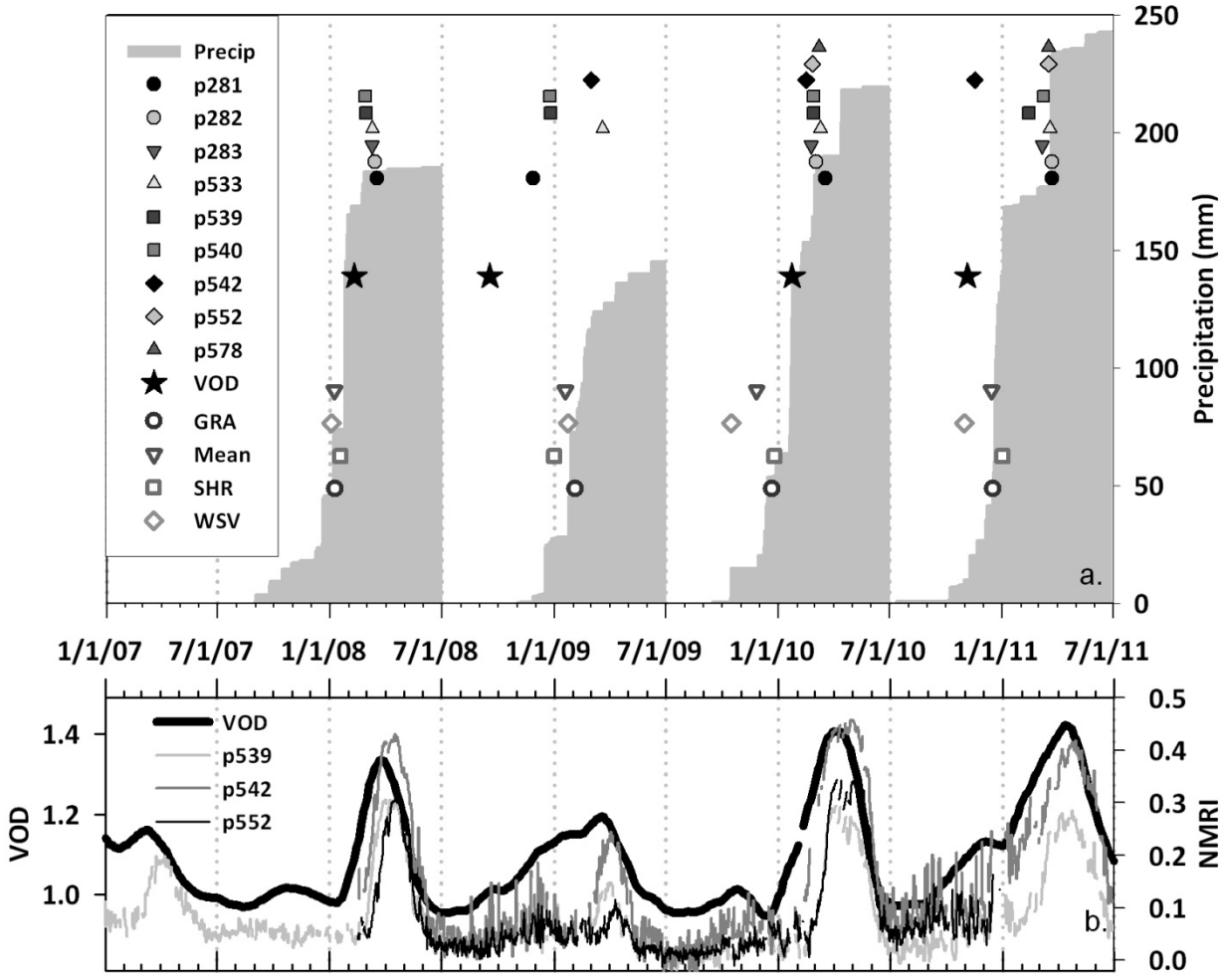

Figure 3.7. Top plot is TIMESAT estimated SOS (day of year) for the 2007-2011 record derived for the 9 NMRI sites, and MODIS NDVI and VOD time series within the single VOD grid cell; cumulative daily precipitation from a nearby weather station is also shown (grey bar); the NMRI site SOS values are labeled by PBO Site ID, and NDVI based SOS values by their respective dominant land cover classes (GRA - grassland, SHR - shrubland, WSV - woody savanna) and the overall NDVI mean (Mean). The lower graphic shows the VOD time series and three representative land cover NMRI site time series (p539 - SHR; p542 and p552 - GRA) within the single VOD grid cell.

Full data record correlations between the NMRI series for the individual sites and the overlying grid cell VOD time series ranged from 0.56 to 0.87 ($p<0.01$ all cases). Three sites (p539, p542, p552) with high correlations ($R=0.87$, 0.83 and 0.76, respectively) displayed

increasing NMRI values in the fall (September to December) of years 2008 and 2011, similar to the VOD record (Figure 3.7b). These three sites are located within 10km of each other in the southern portion of the VOD grid cell and at the highest elevations (>600m) within the cell; elevations at the nine sites ranged from 384 to 612m. Although the fall NMRI increases at these sites were not significant enough to trigger a SOS designation, except for the 2010 SOS for p542, they appear to be the best representation of the pixel-wide VOD signal.

3.3 Discussion

The large number of significant temporal correlations (276 of 305 sites) between the satellite derived VOD and in situ NMRI records indicate broad regional agreement between the two microwave vegetation metrics, despite the large difference in relative footprint size between the ~0.001 km^2 NMRI retrievals and the 625km^2 VOD grid cells. The sign and magnitude of NMRI and VOD temporal (16-day) anomalies was generally coincident with variability in the monthly VPD used as a surrogate indicator of plant-available moisture controls on vegetation activity; positive (negative) NMRI and VOD anomalies generally coincided with below (above) average VPD levels relative to the long-term record. These results indicate similar climate sensitivity of both vegetation water content metrics despite relative differences in the microwave frequency and spatial scale of the retrievals.

The lagged correlation results indicate that VOD seasonality generally precedes NMRI seasonality by approximately 0 to 30 days. This temporal lag was confirmed by the SOS results at the 24 homogeneous land cover sites and the analysis of sub-grid scale heterogeneity within a single VOD grid cell. The observed spatial heterogeneity and interannual variation of sub-grid NMRI and NDVI time series within the single VOD grid cell help to explain the variation in correlation values within and across land cover categories (Figure 3.2) and highlight the difficulty in calculating consistent LSP metrics from datasets measuring different land surface properties, and with large differences in spatial resolution (Figures 3.4 and 3.6a). Sites with relatively weak temporal NMRI and VOD correlations for the full data record generally displayed higher variability (CV) in their yearly correlations; this was often a result of one or two years displaying poor correlations and adversely affecting the full data record R-value for a

given site. The VOD grid cell coinciding with multiple NMRI sites used for the land cover heterogeneity analysis is characteristic of this pattern, as one NMRI site displayed a negative NMRI-VOD correlation one year (R=-0.47) and a strong positive correlation the following year (R=0.68, $p<0.01$), while two nearby sites had variable yearly R-values ranging from 0.11 and 0.24 to 0.57 and 0.63, respectively.

Although both the NMRI and VOD showed similar sensitivity to regional VPD changes, other climatic (PDSI, precipitation days per year) and landscape variability (SD of elevation, SDI, percent tree cover) indicators were unable to explain the NMRI-VOD correlation patterns. The observed range of full data record correlation coefficients (R=0.56 to 0.87) between the nine NMRI sites and the single VOD grid cell indicate that spatial scale discrepancies between the relatively coarse VOD retrievals and local scale NMRI measurements likely influence the VOD-NMRI correlation patterns and associated SOS metrics.

Large spatial heterogeneity in vegetation phenology may occur within a single vegetation class and may not be effectively represented by a single NMRI site even when located within the regionally dominant land cover class. For example, a subset of the MCD12Q2 500m MODIS Land Cover Dynamics Product from 2007 to 2010 within this VOD grid cell displays within season greenup dates ranging across ~51 days for grassland areas, ~53 days for shrubland areas, and ~40 days for woody savanna areas. Both herbaceous and woody vegetation components within this single VOD grid cell contribute to the aggregate microwave attenuation. If these vegetation components exhibit variations in seasonal onset, the VOD and NMRI SOS values may display significant variation dependent on which component is the primary contributor to the aggregate VOD signal and where the NMRI site is located within the VOD grid cell. For example, in a field study conducted in a similar mixed grassland and woody savanna system as the VOD multi-site pixel, Ma et al. (2007) found a mean SOS difference of 110 days between a grassland site and woody savanna site located approximately 2 km apart.

The SOS discrepancy between the NMRI and VOD data may also be partially explained by the different microwave frequencies of the two retrievals; the GPS network operates at a lower L-band (1.5 and 1.2 GHz) frequency, while the AMSR-E VOD retrievals used in this study are derived from K-band (18.65 GHz) frequency T_b series. The higher frequency (shorter

wavelength) AMSR-E retrievals exhibit greater attenuation and scattering from surface vegetation cover, particularly smaller leaf and branch elements. The VOD is therefore expected to exhibit greater sensitivity to changes in vegetation canopy water content, particularly under lower biomass (e.g. grassland) conditions representative of most NMRI sites; this may account for the generally earlier VOD SOS relative to the NMRI results. The difference between NDVI SOS dates and those of VOD or NMRI can also be partially explained by the difference in sensor wavelengths. Optical-IR remote sensing metrics respond to changes in vegetation greenness, or chlorophyll content, and the timing of greenup may not mirror changes in canopy biomass water content (Guan et al 2012). A previous study (Jones et al. 2012) demonstrated that VOD LSP metrics can lag satellite optical-IR based LSP metrics in regions where water is a primary constraint on vegetation growth, with the temporal lag increasing with the proportion of woody vegetation cover due to microwave sensitivity to both photosynthetic and non-photosynthetic vegetation components. The difference between optical-IR and microwave LSP metrics can therefore provide critical information on the timing of water uptake and allocation versus the creation of new photosynthetic biomass.

This study is the first intercomparison of satellite microwave phenology metrics and a GPS network derived reflectance index; it highlights both promising initial results and limitations to be addressed in future research. The global extent and current design of GPS base stations provide a comprehensive set of daily stand or patch scale (~0.001 km^2) microwave vegetation measures, but there are large discrepancies between the local NMRI footprint and the regional scale satellite VOD retrievals that hinder direct comparisons and interpretations for global scale microwave LSP validation. Alternative validation sites designed to overcome these discrepancies are needed in order to advance LSP understanding. To overcome spatial scale differences between local observations and overlying satellite retrievals, and limited landscape representation of the NMRI data, GPS stations spanning a full range of land cover variability within a collection of VOD grid cells could be installed. This design would include sites with raised (or top-of-canopy) GPS antennas to provide a larger sampling footprint approaching the scale of the satellite retrievals and allow for retrieval of the NMRI metric in more densely vegetated areas. Potential LSP validation sites incorporating NMRI measurements can be

integrated with current phenology observation networks at relatively low cost. These networks provide potentially synergistic observations including phenology cameras (e.g. the PhenoCam network), targeted phenophase observations (e.g. USA-NPN), tower eddy covariance carbon and water flux measurements (e.g. AmeriFlux), and other supporting biophysical measurements (e.g. temperature, snow and soil moisture data). A more comprehensive design of phenology validation sites is currently being developed by the CEOS-LPV Phenology subgroup, which will provide subsets of remote sensing LSP metrics over PhenoCam sites and bundled with USA-NPN observations. The National Ecological Observatory Network (NEON) is also developing an extensive array of similar phenology relevant observations. Including GPS instruments and the calculation of NMRI time series at these locations would provide critical information to both advance microwave LSP validation and broaden our understanding of vegetation phenology.

3.4 Acknowledgments

This portion of the dissertation was carried out with funding from the NASA Terrestrial Ecology program. The AMSR-E global VOD database and associated biophysical retrievals from this study are available through the NASA NSIDC DAAC (http://nsidc.org/data/nsidc-0451.html). This work was performed at the University of Montana under contract to the National Aeronautics and Space Administration. PBO-H2O is supported by NSF EAR-1144221. NMRI data may be downloaded from http://xenon.colorado.edu/portal.

3.5 References Cited

Dai A, Trenberth KE, Qian T (2004) A global data set of Palmer Drought Severity Index for 1870-2002: Relationship with soil moisture and effects of surface warming. J*ournal of* Hydrometeorology, 5, 1117-1130.

Estey L, Meertens C (1999) TEQC: The multi-purpose toolkit for GPS/GLONASS data, GPS Solutions, **3**(1), 42–49

Frolking S, Milliman T, McDonald K, Kimball J, Zhao MS, Fahnestock M (2006) Evaluation of the SeaWinds scatterometer for regional monitoring of vegetation phenology. *Journal Of Geophysical Research-Atmospheres*, **111**.

Guan K,Wood EF, Caylor KK (2012) Multi-sensor derivation of regional vegetation fractional cover in Africa, *Remote Sensing of Environment* **124**, 653-665.

Hansen M, DeFries RS, Townshend JRG, Carroll M, Dimiceli C, Sohlberg RA (2003) Global Percent Tree Cover at a Spatial Resolution of 500 Meters: First Results of the MODIS Vegetation Continuous Fields Algorithm, *Earth Interactions*, **7**, 1-15.

Harris I, Jones PD, Osborn TJ, Lister DH (2013) Updated high-resolution grids of monthly climatic observations – the CRU TS3.10 Dataset. *International Journal of Climatology,* doi: 10.1002/joc.3711

Huffaker CB (1942) Vegetational correlations with vapor pressure deficit and relative humidity. *American Midland Naturalist*, **28**, 486–500.

Jackson TJ, Schmugge TJ (1991) Vegetation Effects On The Microwave Emission Of Soils. *Remote Sensing Of Environment,* **36**, 203-212

Jones LA, Kimball JS, McDonald KC, Chan SK, Njoku EG (2009) A method for deriving northern hemisphere vegetation phenology, land surface wetness, and open water fraction from AMSR-E. In, IGARSS Symposium. Cape Town, South Africa

Jones LA, Kimball JS (2011) Daily Global Land Surface Parameters Derived from AMSR-E. Boulder, Colorado USA: National Snow and Ice Data Center. Digital media (http://nsidc.org/data/nsidc-0451.html).

Jones MO, Jones LA, Kimball JS, McDonald KC (2011) Satellite passive microwave remote sensing for monitoring global land surface phenology. *Remote Sensing of Environment*, **115**, 1102–1114.

Jones MO, Kimball JS, Jones LA, McDonald KC (2012) Satellite passive microwave detection of North America start of season. *Remote Sensing of Environment*, **123**, 324–333.

Jönsson P, Eklundh L (2004) TIMESAT - a program for analyzing time-series of satellite sensor data. *Computers & Geosciences*, **30**, 833–845.

Kimball JS, McDonald KC, Running SW, Frolking SE (2004) Satellite radar remote sensing of seasonal growing seasons for boreal and subalpine evergreen forests. *Remote Sensing of Environment*, **90**, 243–258.

Klein Tank, AMG et al. (2002) Daily dataset of 20th-century surface air temperature and precipitation series for the European Climate Assessment. *International Journal of Climatology*, **22**, 1441-1453.

Knowles KW (2004) EASE-Grid Land Cover Data Resampled from Boston University Version of Global 1 km Land Cover from MODIS 2001. In. Boulder, Colorado USA: National Snow and Ice Data Center

Knowles KW, Savoie RL, Armstrong RL, Brodzik MJ. (2009) AMSR-E/Aqua daily EASE-Grid brightness temperatures 2003-2008. In. Boulder, Colorado USA: National Snow and Ice Data Center

Larson KM, Small EE, Gutmann E, Bilich A, Braun J, Zavorotny V. (2008) Use of GPS receivers as a soil moisture network for water cycle studies, *Geophysical Research Letters*, **35**, L24405

Larson KM, Small EE, (*in review*) Normalized Microwave Reflection Index, part 1: A Vegetation Measurement Derived from GPS Networks. *IEEE Journal of Selected Topics in Applied Earth Observations and Remote Sensing.*

Ma S, Baldocchi D, Xu L, Hehn T (2007) Inter-annual variability in carbon dioxide exchange of an oak/grass savanna and open grassland in California. *Agricultural and Forest Meteorology*, **147**, 157–171.

Morisette JT, Richardson AD, Knapp AK, *et al.* (2009) Tracking the rhythm of the seasons in the face of global change: phenological research in the 21st century. *Frontiers in Ecology and the Environment*, **7**, 253–260.

Nightingale JM, Morisette JT, Wolfe RE, Tan B, Gao F, Ederer G, Collatz GJ, Turner DP (2009) Temporally smoothed and gap-filled MODIS land products for carbon modeling: application of the fPAR product. *International Journal Of Remote Sensing,* **30**, 1083-1090

Njoku E, Ashcroft P (2005) Global survey and statistics of radio-frequency interference in AMSR-E land observations. *IEEE Transactions on Geoscience and Remote Sensing*, **43**, 938–947.

Palmer, WC, (1965) Meteorological Drought. Res. Paper No.45, 58pp., Dept. of Commerce, Washington, D.C.

Peñuelas J, Rutishauser T, Filella I (2009) Phenology feedbacks on climate change. *Science*, **294**, 64–65.

Piao S, Friedlingstein P, Ciais P, Viovy N, Demarty J (2007) Growing season extension and its impact on terrestrial carbon cycle in the Northern Hemisphere over the past 2 decades. *Global Biogeochemical Cycles,* **21**, GB3018.

Rienecker MM, Suarez MJ, Gelaro R, Todling R, Bacmeister J, Liu E, Bosilovich MG, Schubert SD, Takacs L, Kim GK, Bloom S, Chen J, Collins D, Conaty A, da Silva A, et al. (2011) MERRA: NASA's Modern-Era Retrospective Analysis for Research and Applications. *J. Climate*, **24**, 3624-3648

Richardson AD, Braswell BH, Hollinger DY, Jenkins JP, Ollinger SV (2009) Near-surface remote sensing of spatial and temporal variation in canopy phenology. *Ecological applications,* **19**, 1417–28.

Running SW, Nemani RR (1988) Relating Seasonal Patterns Of The AVHRR Vegetation Index To Simulated Photosynthesis And Transpiration Of Forests In Different Climates. *Remote Sensing Of Environment*, **24**, 347–367.

Schwartz MD, Betancourt JL, Weltzin JF (2012) From Caprio's lilacs to the USA National Phenology Network. *Frontiers in Ecology and the Environment*, **10**, 324.

Shannon CE (1948) A mathematical theory of communication. *The Bell System Technical Journal*, **27**, 379-423 and 623-656.

Small EE, Larson KM, and Smith W (in review) Normalized Microwave Reflection Index, part 2: Validation of Vegetation Water Content Estimates at Montana Grasslands, *IEEE Journal of Selected Topics in Applied Earth Observations and Remote Sensing.*

Small EE, Larson KM, Braun JJ (2010) Sensing Vegetation Growth with GPS Reflections, *Geophysical Research Letters*, **37**, L12401

Tan B, Morisette J, Wolfe R (2011) An enhanced TIMESAT algorithm for estimating vegetation phenology metrics from MODIS data. *IEEE Journal of Selected Topics in Applied Earth Observations and Remote Sensing*, **4**, 1-11

Tarpley J, Schneider SR, Money RL (1984) Global vegetation indices from the NOAA-7 meteorological satellite. *Journal of Climate and Applied Meteorology*, **23**, 491–4.

Ulaby FT, Moore RK, Fung AK (1981) Microwave remote sensing – Active and passive, Vol. I: Microwave remote sensing Fundamentals and Radiometry, Artech house, Norwood MA.

Griend AA Van De, Wigneron J, Member S (2004) On the Measurement of Microwave Vegetation Properties: Some Guidelines for a Protocol. *IEEE Transactions on Geoscience and Remote Sensing*, **42**, 2277–2289.

White MA, Thornton PE, Running SW, Nemani RR (2000) Parameterization and sensitivity analysis of the BIOME–BGC terrestrial ecosystem model: net primary production controls. *Earth Interactions*, **4**, 1–85.

Wolfe DW, Schwartz MD, Lakso AN, Otsuki Y, Pool RM, Shaulis NJ (2005) Climate change and shifts in spring phenology of three horticultural woody perennials in northeastern USA. *International Journal of Biometeorology*, **49**, 303–9.

Zhang X, Tarpley D, Sullivan JT (2007) Diverse responses of vegetation phenology to a warming climate. *Geophysical Research Letters*, **34**, L19405.

Chapter 4. Satellite Microwave Detection of Boreal Forest Recovery from the Extreme 2004 Wildfires in Alaska and Canada

Current and projected warming in the northern latitudes is expected to have large scale impacts on ecosystem services and land-atmosphere water, energy and carbon exchange. Northern latitude warming has been linked with earlier and longer potential growing seasons (Kim et al., 2012), vegetation productivity (Myneni et al., 1997; Nemani et al., 2003; Kimball et al., 2007) and evapotranspiration increases (Zhang et al., 2011), and a continuing terrestrial carbon (CO_2) sink (Liski et al., 2003; Sarmiento et al., 2010). However, a continuing northern carbon sink is uncertain due in part to the effects of increasing boreal wildfire disturbance (Soja et al., 2007; IPCC, 2007). Fire is the dominant disturbance agent in the circumboreal region and there has been an increasing trend in burned area over recent decades (Gillett et al., 2004; Kasischke et al., 2006). Large-scale wildfires can be sources of rapid carbon emissions to the atmosphere (Soja et al., 2004; Amiro et al., 2006) and can cause temporary reductions in ecosystem carbon sequestration and storage (Kurz & Apps, 1999). Fire disturbance can enhance litter decomposition due to fire-induced mortality (Auclair & Carter, 1993), and alter ecosystem structure and function and therefore the long-term carbon balance of the landscape (Hicke et al., 2003; Field et al., 2007). Disturbance can reorganize or alter species composition within plant communities (Law & Morton, 1993) and fire severity, particularly soil burn severity, can affect seedling recruitment and vegetation succession (Johnstone & Kasischke, 2005). Previous studies have documented increased recruitment of boreal deciduous species relative to pre-fire dominant evergreen coniferous species at severely burned sites following the intense 2004 fire year in Alaska (Johnstone et al., 2010). These events can lead to marked changes in the terrestrial carbon budget, including vegetation productivity, carbon sequestration and associated climate feedbacks (Harden et al., 2002; Randerson et al., 2006; Goulden et al., 2011). A better understanding of post-fire vegetation response and recovery is needed to improve regional assessments and predictions of northern carbon cycle variability and associated climate feedbacks.

Post-fire vegetation recovery assessments are often derived from short-term plot level measurements across sparse chronosequences of varying stand age and disturbance history

that attempt to infer long-term vegetation recovery trajectories by trading space for time (Goulden et al., 2006; Goulden et al., 2011). Satellite remote sensing offers a relatively low-cost, rapid, and repeatable method to measure post-fire vegetation recovery over large regions. Kasischke and French (1997) used Advanced Very High Resolution Radiometer (AVHRR) Normalized Difference Vegetation Index (NDVI) data over the boreal forest of interior Alaska and found that pre-fire vegetation composition, area burn extent and seasonal timing of fire all affect patterns of regrowth. Goetz et al. (2006) also used AVHRR data records to examine post-fire NDVI variability and recovery rates from three episodic fire years across Canada, and concluded that post-fire NDVI variability was distinct from unburned reference sites, with approximate five year recovery times to pre-burn levels. A similar study used AVHRR NDVI records to drive a post-fire boreal forest NPP (net primary production) model and defined a recovery period of approximately 9 years, but with substantial variance among fires (Hicke et al., 2003). Variability in the estimated fire recovery periods may reflect uncertainties among regional fire databases, a general lack of information on fire severity, and associated patterns of vegetation species recruitment (Sofronov & Volokitina, 2009; Turner, 2010).

Satellite regional assessments of post-fire vegetation recovery have been largely dominated by the use of optical-infrared (IR) sensors and associated vegetation indices including the NDVI; these indices are responsive to changes in canopy greenness but are constrained at higher latitudes by signal degradation from low solar elevations and illumination, clouds, smoke and other atmosphere aerosol contamination. Post-fire assessments have also been conducted utilizing satellite and airborne Light Detecting and Ranging (LiDAR) with promising results. Airborne LiDAR was proven useful in characterizing post-fire conditions and burn induced structural change (Wulder et al., 2009) as well as estimating years to canopy height recovery following fire (Magnussen & Wulder, 2012). Using the satellite Geoscience Laser Altimeter System (GLAS) sensor on ICESat, Goetz et al., (2010) demonstrated the utility of large footprint LiDAR in assessing vegetation height properties in fire disturbed areas that was useful for inferring regrowth properties when coupled with other remotely sensed imagery. Although LiDAR can play an important role in post-fire assessment, airborne campaigns have limited sampling frequency and geographic extent due to high costs of acquisition. GLAS

operated from 2003 to 2010 and provided relatively high temporal frequency observations useful for post-fire monitoring, but neither the sensor nor its sampling strategy were designed for vegetation monitoring, resulting in limited sensitivity to vegetation vertical structure at lower height (0-5m) levels of particular importance for tracking vegetation regrowth following stand replacing fires.

Alternatively, satellite microwave remote sensing can detect changes in canopy structure, biomass and water content, and provides a means for monitoring post-fire vegetation recovery independent of many of the constraints on optical-IR remote sensing (Frolking et al., 2009; Jones et al., 2011), with near daily repeat observations over boreal regions. Previous studies have applied satellite passive and active (radar) microwave remote sensing for regional assessment of vegetation phenology (Frolking et al., 2006; Min & Lin, 2006a; Shi et al., 2008; Jones et al., 2012), vegetation drought response (Frolking et al., 2005, 2011), potential growing season variability (Kimball et al., 2004, 2006) and seasonal changes in evapotranspiration (Zhang et al., 2011) and canopy CO_2 exchange (Min & Lin, 2006b; Jones et al., 2012).

Satellite passive microwave remote sensing of the land surface detects the aggregate microwave emissions of individual landscape elements (e.g. soil, vegetation, open water, atmosphere elements) within the sensor field-of-view and algorithms have been developed to distinguish and extract higher order land parameter retrievals. The well-known tau-omega model was developed as a relatively simple method to describe upwelling radiation from the land surface as observed above an intervening vegetation layer (Ulaby et al., 1982; Mo et al., 1982). The tau portion of the model describes the transmissivity of the intervening vegetation layer to land surface microwave emissions and is often termed Vegetation Optical Depth (VOD), which can be expressed as a linear function of vegetation water content (Jackson et al., 1982; Wigneron et al., 1993). Jackson and Schmugge (1991) demonstrated a semi-empirical relationship between VOD and vegetation water content that varies with both microwave frequency and vegetation structure. The relationship between VOD, canopy biomass and associated water content was shown to follow a general power-law response that varies with microwave frequency (Njoku & Chan, 2006; Kirdyashev et al., 1979; Jackson et al., 1982).

Building on these previous studies and incorporating the tau-omega model, a VOD retrieval algorithm was developed that defines the frequency dependent extinction of land surface microwave emissions by the intervening vegetation layer and integrates canopy attenuation related to vegetation biomass structure and water content, while mitigating the potential influence of landscape freeze-thaw state transitions, open water inundation and soil moisture on the VOD retrieval (Jones et al., 2011).

Here, we applied measures of canopy greenness and biomass changes inferred from satellite NDVI and VOD records to evaluate recent post-fire vegetation recovery following the severe 2004 fire year across boreal North America. We utilized synergistic observations from both optical-IR and passive microwave remote sensing to provide a more comprehensive view of vegetation recovery that includes both photosynthetic and non-photosynthetic canopy biomass elements to improve understanding of boreal ecosystem recovery. We hypothesized that the satellite microwave VOD signature will display an alternate vegetation recovery response related to canopy foliar and woody biomass regeneration following large scale fire events relative to canopy greenness recovery inferred from the NDVI record, while the variation in response will be dependent on the proportion of woody vegetation loss within fire perimeters.

The summer of 2004 was one of the hottest and driest on record for interior Alaska since 1940 (Alaska Climate Research Center, 2009), resulting in a panoply of large-scale boreal fires across Alaska and Canada. In Alaska alone, 2.7 million hectares of forest burned, the largest in the 58-year record (Todd & Jewkes, 2006). We identified large scale boreal fires in 2004 and extracted MODIS NDVI and AMSR-E VOD time series from the pre- and post-fire records within fire perimeters and associated unburned (control) pixels. Anomalies were calculated for each grid cell from the full VOD and NDVI data record means as well as relative to the pre-fire reference year (2003) to examine the direct effect of the 2004 fires on the vegetation indices. An asymptotic curve was fit to the post-fire NDVI and VOD yearly maximums to estimate the recovery trajectory to an initial steady-state for each fire (Olsen, 1963; Mackey et al., 2002). The estimated number of years to steady-state was then compared

to independent satellite based estimates of proportional tree cover loss within each burn perimeter to clarify differences in NDVI and VOD recovery relative to estimated fire severity.

4.1 Materials and Methods

4.1.1 Canadian National Fire and Alaska Fire History Databases

The Canadian National Fire Database (CNFDB) is a collection of forest fire locations and fire perimeters from 1980 to 2009 (Canadian Forest Service, 2011). Only fire extents exceeding 2km^2 are included in the database, but these fires account for 97% of the total burned area (Stocks et al., 2002). Fire perimeters used in this study were limited to those greater than 1000km^2 that occurred in 2004, to correspond with the 2003 to 2010 AMSR-E VOD data record; this allowed for a pre-fire benchmark (or reference year) and maximized the number of post-fire years analyzed. From these criteria, 4 CNFDB fire perimeters were selected within the Yukon and Northwest Territories.

The Alaska Interagency Coordination (AIC) Center Fire History Database (AKFDB) is a collection of fire perimeters (Bureau of Land Management, 2011). The AKFDB is derived from multiple sources and methods, and is consistently updated and revised based on the latest information and available satellite imagery. The database includes large fire perimeters from 1942 through 2009. The same selection criteria were applied (>1000km^2, year=2004), resulting in 10 AK fire perimeters selected for this investigation. Overall, the above criteria resulted in 14 boreal North American fire perimeters selected from the two databases (Figure 4.1 and Table 4.1).

4.1.2 Burn Severity Classification

The Monitoring Trends in Burn Severity (MTBS) project has mapped burn severity across all fires in the United States from 1984 to 2010 utilizing Landsat imagery (Eidenshink et al., 2007). We employed thematic burn severity maps, derived from the difference Normalized Burn Ratio (dNBR) (Cocke et al., 2005; Brewer et al., 2005), over each of the 10 fires located in the Alaska domain to determine the extent of burned area within the fire perimeters and proportion of burn severity class (unburned/low, low, moderate, high) for each fire.

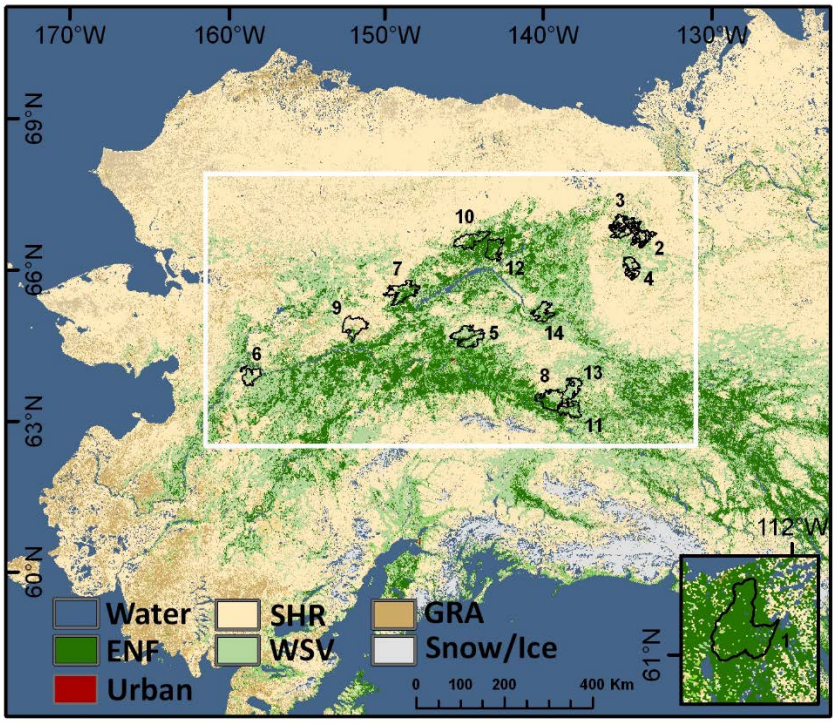

Figure 4.1. Map of 14 fire perimeters (labeled by Fire ID numbers) in Alaska, USA and the Yukon Territory, Canada. Inset map illustrates a single fire perimeter in the Northwest Territories, Canada. The fires occurred in 2004 and were greater than 1000km^2. The fire perimeters are superimposed on the MODIS IGBP land cover classification. The white box is the sub-region represented in Figure 4.4.

Table 4.1. List of 14 fire perimeter areas selected in this investigation and labeled by Fire ID with geographic coordinates of fire perimeter centers. The last four columns are the percent of dominant land cover types within fire perimeters based on the MODIS 1km (MOD12Q1) Land Cover Product: ENF – Evergreen Needleleaf Forest, MXF – Mixed Forest, SHR – Open Shrubland, WSV – Woody Savanna.

Fire ID	Latitude	Longitude	Area (km^2)	Location	ENF	MXF	SHR	WSV
1	61.201	-112.338	1,561.1	NWT, CAN	85%	0%	7%	4%
2	66.675	-137.514	1,287.4	Yukon, CAN	5%	1%	43%	43%
3	66.954	-138.379	1,759.9	Yukon, CAN	4%	0%	43%	50%
4	66.122	-138.408	1,117.7	Yukon, CAN	5%	0%	40%	56%
5	65.267	-146.883	2,171.2	Alaska, USA	11%	4%	14%	70%
6	64.468	-157.691	1,076.1	Alaska, USA	4%	2%	34%	58%
7	66.303	-149.882	1,955.8	Alaska, USA	16%	2%	18%	43%
8	63.817	-143.817	1,877.7	Alaska, USA	41%	3%	15%	40%
9	65.747	-152.229	1,699.2	Alaska, USA	5%	4%	47%	35%
10	67.208	-146.368	1,634.9	Alaska, USA	26%	8%	15%	49%
11	63.450	-142.667	1,151.7	Alaska, USA	19%	1%	7%	72%
12	66.960	-145.343	1,343.9	Alaska, USA	48%	2%	2%	44%
13	64.017	-142.000	1,295.6	Alaska, USA	3%	2%	15%	80%
14	65.517	-143.170	1,125.5	Alaska, USA	18%	3%	17%	58%

4.1.3 Microwave Vegetation Optical Depth

The Advanced Microwave Scanning Radiometer for EOS (AMSR-E) is a microwave radiometer deployed on the polar-orbiting Aqua satellite platform with UTC 1:30 A.M. (descending)/P.M. (ascending) orbit equatorial crossings. The AMSR-E sensor measures vertical and horizontal polarized brightness temperature at six frequencies (6.9, 10.7, 18.7, 23.8, 36.5, 89.0 GHz) and constant Earth incidence angle of 55° from nadir. We employed near daily 10.7 GHz frequency VOD retrievals from an existing AMSR-E global land parameter database for ecosystem studies (Jones & Kimball, 2011). The database is derived from daily 25km resolution global Equal Area Scalable Earth (EASE) Grid brightness temperatures provided by the NASA data archive facility at the National Snow and Ice Data Center for years 2003 to 2010 (Knowles et al., 2009). The database encompasses all pixels with <50% permanent ice or open water cover, as defined from a 1-km resolution MODIS (MOD12Q1) IGBP global land cover classification aggregated to 25 km resolution while retaining relative land cover class proportions (Knowles, 2004). The VOD parameter is a frequency dependent measure of canopy attenuation of microwave emissions related to changes in vegetation biomass and water content (Ulaby et al., 1982). The retrieval algorithm minimizes the effects of dynamic atmosphere precipitable water vapor, temperature, surface inundation and soil moisture variability on the VOD retrievals (Jones et al., 2009). A detailed description of the AMSR-E VOD record, including algorithm development and sensitivity, is provided in Chapter 2 and elsewhere (Jones et al., 2010; Jones et al., 2011).

In this study, the daily VOD record from 2003 to 2010 for each grid cell was temporally composited to the coarser 16-day median time step of the MODIS (MOD13A2) NDVI data record. A satellite passive microwave remote sensing derived record of daily landscape freeze/thaw (FT) status (Kim et al., 2011) was used to screen out snow covered and frozen land surface conditions, resulting in winter data gaps in the VOD record. The 2003 to 2010 spatial average primary thaw and freeze dates within each fire perimeter were extracted from the FT classification record. The earliest thaw and latest freeze dates from the FT record were used as a surrogate for the potential vegetation growing season (Kimball et al., 2004) to constrain the 16-day VOD time series to this period, resulting in 12 retrievals per year from April 24 to

November 1. Some sites displayed year-to-year variability in potential growing season length, resulting in 9 to 11 retrievals in particular years.

4.1.4 MODIS Normalized Difference Vegetation Index and Percent Tree Cover

The 16-day, 2000 to 2010 MODIS NDVI (MOD13A2 1km resolution) tiles over Canada and Alaska were reprojected to match the CNFDB and the AKFDB product formats. We used only the highest quality MODIS pixels (Pixel Reliability=0), avoiding lower quality and cloud contaminated retrievals, and extracted the same April 24 to November 1 time series based on the satellite FT record defined primary thaw and freeze dates. Similar to the VOD time series, some sites displayed yearly variability in potential growing season length, resulting in 9 to 11 retrievals in particular years.

The MODIS (MOD44B) Vegetation Continuous Fields product (Hansen et al., 2003) contains proportional (%) woody vegetation cover information at 500m spatial resolution at yearly intervals from 2003-2010. Yearly proportional vegetation cover means were calculated within each fire perimeter. As an approximation of fire severity, percent tree cover (PTC) loss from fire disturbance was estimated as the normalized difference between MODIS proportional (%) tree cover estimates between 2003 and 2005 ($PTC_{loss} = PTC_{2003} – PTC_{2005} / PTC_{2003}$). The PTC_{loss} metric was then compared to dNBR categorical assessments of burn severity for each fire to evaluate correspondence between PTC_{loss} and estimated fire severity. A linear regression between mean tree cover loss within the fire perimeter and years to recovery was run for both NDVI and VOD records. The relative (%) loss of woody vegetation cover due to fire is expected to influence the VOD response through the loss of canopy photosynthetic and non-photosynthetic biomass that attenuates the microwave signal.

4.1.5 AMSR-E VOD and MODIS NDVI Spatial Resolutions

The relatively coarse (25km) resolution VOD record results in a limited number of VOD pixels within fire perimeters. Therefore, VOD pixels associated with each fire were selected if at least 50% of the pixel area was within the fire perimeter (resulting in one to three VOD pixels per fire); the mean and standard deviation of the contributing pixels were then calculated at each 16-day interval. The 1km resolution NDVI pixels within the full extent of the fire

perimeters were selected and ranged from approximately 400 to 1000 pixels per fire; the mean and standard deviation of the contributing NDVI pixels were then calculated at each 16-day interval.

4.1.6 Selection of Unburned Control Pixels

Climate variability including temperature, freeze-thaw cycles, growing season length and precipitation or snow cover dynamics can contribute to interannual variation in vegetation growth and can therefore confound the attribution of observed canopy changes to fire disturbance. We selected control pixels unaffected by recent fire disturbance as a baseline for comparing against adjacent burned areas to distinguish fire recovery effects from other environmental factors influencing vegetation growth changes. First, using both fire databases, all pixels within fire perimeters after 1993 were excluded from selection based on reports that a 5 to 10 year period is sufficient for post-fire vegetation canopy recovery (Hicke et al., 2003; Goetz et al., 2006; Beck & Goetz, 2011). However, the fire databases do not include all fires and therefore selection of unburned pixels cannot be dependent on the absence of fire perimeters alone. Pixel-wise VOD and NDVI coefficients of variation (CV) were therefore calculated for the 8 year (2003-2010) study period. Low CV values correspond to low variability in each time series, allowing selection of pixels less likely to be influenced by unmapped or sub-pixel scale fires or other types of disturbance such as insect outbreaks or land-use change (Goetz et al., 2006). Based on the Jenks, or natural breaks, method (Jenks, 1967) of weighting, low CV pixels were identified. A random sample of low CV VOD and NDVI control pixels were selected in close proximity to each fire perimeter. For the coarse resolution VOD record, we selected an equal number of control pixels as that of the adjacent burned area pixels. For the higher resolution NDVI pixels approximately 300 control pixels were selected for each fire perimeter. Land cover classes were extracted from the MODIS land cover product (MOD12C1) to verify a similar distribution of land cover as those found within each neighboring fire perimeter. The assumption is made that close proximity pixels having a consistent land cover type will experience similar climate conditions and vegetation phenology (Goetz et al., 2006; Jones et al., 2012) absent of fire or other disturbances. To test this assumption we created pre-fire (2000-

2003) NDVI time series plots of the burn areas and their control areas (Figure 4.2). The burned and control areas display very similar intra- and interannual variation. From a remote sensing perspective the control areas can be considered equitable representations of the burn areas.

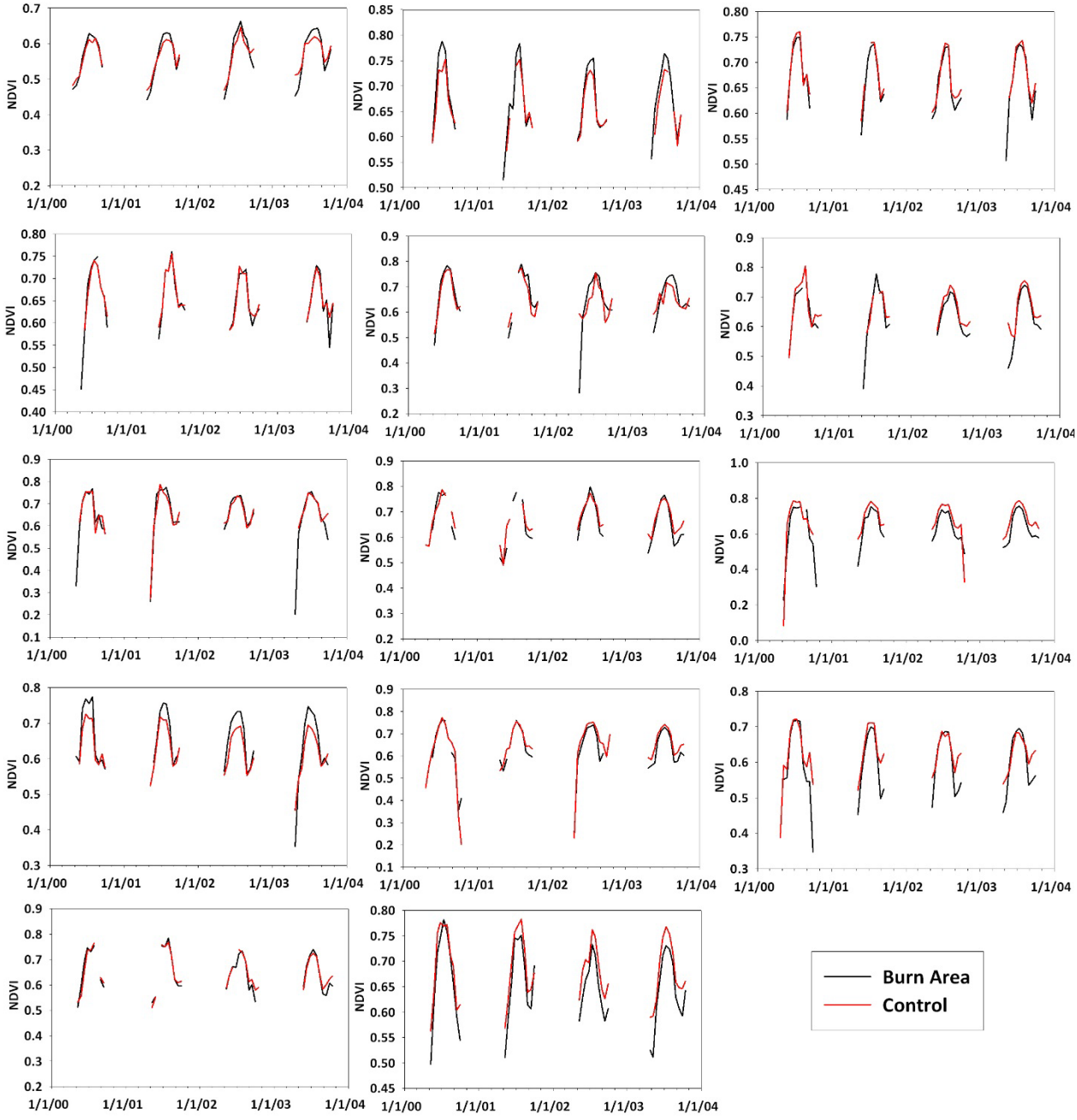

Figure 4.2. Monthly pre-fire (2000-2003) NDVI time series of burned areas and their associated control areas.

4.1.7 Comparison of Pre-Fire and Post-Fire VOD and NDVI Time Series

Spatial VOD and NDVI burned area means and standard deviations were calculated at each 16-day interval. For each fire, 16-day anomalies were derived relative to the mean of the complete data records for NDVI (2000-2010) and VOD (2003-2010). A second set of anomalies were also calculated relative to the pre-fire reference year (2003) by subtracting each burned area's 16-day post-fire mean from the corresponding 16-day mean of the pre-fire year. All anomalies and summary statistics were also calculated on the associated control (unburned) pixels. Annual maximum NDVI and VOD values, the timing (specific 16-day interval) of each annual maximum, and temporal anomalies relative to the pre-fire (2003) annual maximums were extracted for each burned area. The timing of each VOD and NDVI maximum was used to assess potential changes in canopy phenology under post-fire vegetation succession relative to the adjacent control pixels. Pixel-wise yearly VOD maximums were also extracted from a regional extent around the burned area perimeters to distinguish associated VOD responses from fire and other climate factors.

4.1.8 Estimation of Years to Post-Fire Recovery

To identify the approximate year of canopy recovery we fit an asymptotic curve to the post-fire annual VOD and NDVI maximums for each burned area using methods similar to those used to model biomass accumulation and fuel recovery (Olson 1963):

$$f(x) = y_0 + a/(1+\exp(-(x-x_0)/b)) \quad (1)$$

where f(x) is the estimated VOD or NDVI maximum value at each yearly interval (x), y_0 is the base (or initial) VOD or NDVI fitted value, *a* is the difference between the base value and the maximum of the fitted model, x_0 is the inflection point of the curve (the first derivative maximum of the function), and *b* describes the slope of the curve. The sigmoid model (Equation 1) allows for a moderate initial recovery trajectory as species establish post-disturbance, followed by a rapid exponential growth rate that eventually approaches an asymptotic steady-state. We define recovery as the year in which the fitted model reaches 95%

of the asymptote and equate recovery to this initial steady state. It is important to note that vegetation succession following fire disturbance is complex and may have multiple periods of relative stability as recovery moves through different seral stages toward maturity (Goulden et al., 2011). As a result, post-disturbance steady state values distinguished by the satellite record may be lower than pre-fire conditions and may not represent a complete greenness or biomass recovery to pre-fire levels.

4.1.9 Incorporating Field Data within Fire Perimeters

We acquired post-fire field data from the Bonanza Creek Long-Term Ecological Research Project (Johnstone, 2009; Johnstone and Hollingsworth, 2013) collected within four of the fire perimeters. Two datasets were acquired. The first, collected from 2005-2007, contains site level descriptions of environmental data, pre-fire stand characteristics, and fire conditions from the 2004 fires. The second, collected in 2008 in the same four fire perimeters, contains seedling density measures. Three fire severity measures (percent mortality, percent of canopy consumption by fire, and ranks of stand-level canopy fire severity) and three post-fire stem density measures of Spruce, Aspen and Birch, were compared to pre- and post-fire differences in NDVI and VOD measures. We tested whether the field measures of fire severity were correlated with the difference in pre-to-post fire NDVI and VOD measures, and whether post-fire stem density measures were correlated to NDVI and VOD recovery estimates.

4.2 Results

4.2.1 VOD and NDVI Anomalies

The mean and standard deviation of the VOD and NDVI 16-day anomalies for all fires, relative to complete data record means, is shown in Figure 4.3. The effect of the 2004 fires is apparent, with higher than normal variance within the growing season of 2004 and lower than normal means in 2005. The plots also provide a general indication of canopy recovery as NDVI values stabilize approximately 3 years after the fires, while the VOD values show a continual post-fire increase through the end of the data record (2010).

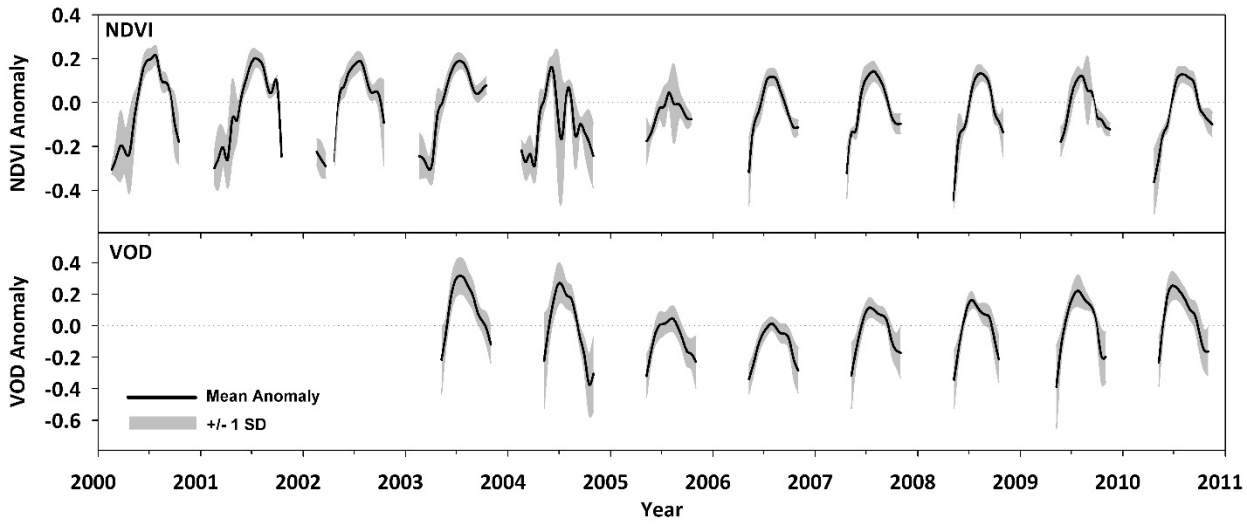

Figure 4.3. Complete data records for MODIS NDVI (2000-2010) and AMSR-E VOD (2003-2010) representing mean anomaly and standard deviation (SD) time series for all fire perimeter locations; 16-day anomalies were calculated as the difference from the full VOD and NDVI data record means.

The box and whisker plot in Figure 4.4a displays the yearly summary statistics of the 16-day anomalies for all fires relative to the 2003 reference year. The 2004 anomalies display a wide range associated with mid to late season fire disturbance and the fire effects are apparent in the low 2005 post-fire medians. The NDVI anomalies display a post-fire recovery trajectory that stabilizes in approximately 2007 and median values remain below the 2003 reference year conditions. The VOD anomalies display a continuous recovery trajectory and the median values also do not reach reference year values by the end of the data record.

The 16-day anomalies of the burned areas relative to their adjacent unburned control pixels are shown in Figure 4.4b. The resulting VOD and NDVI recovery trajectories are similar to those derived relative to pre-disturbance (2003) conditions (Figure 4.4a), indicating that fire disturbance recovery is a primary driver of post-fire NDVI and VOD changes.

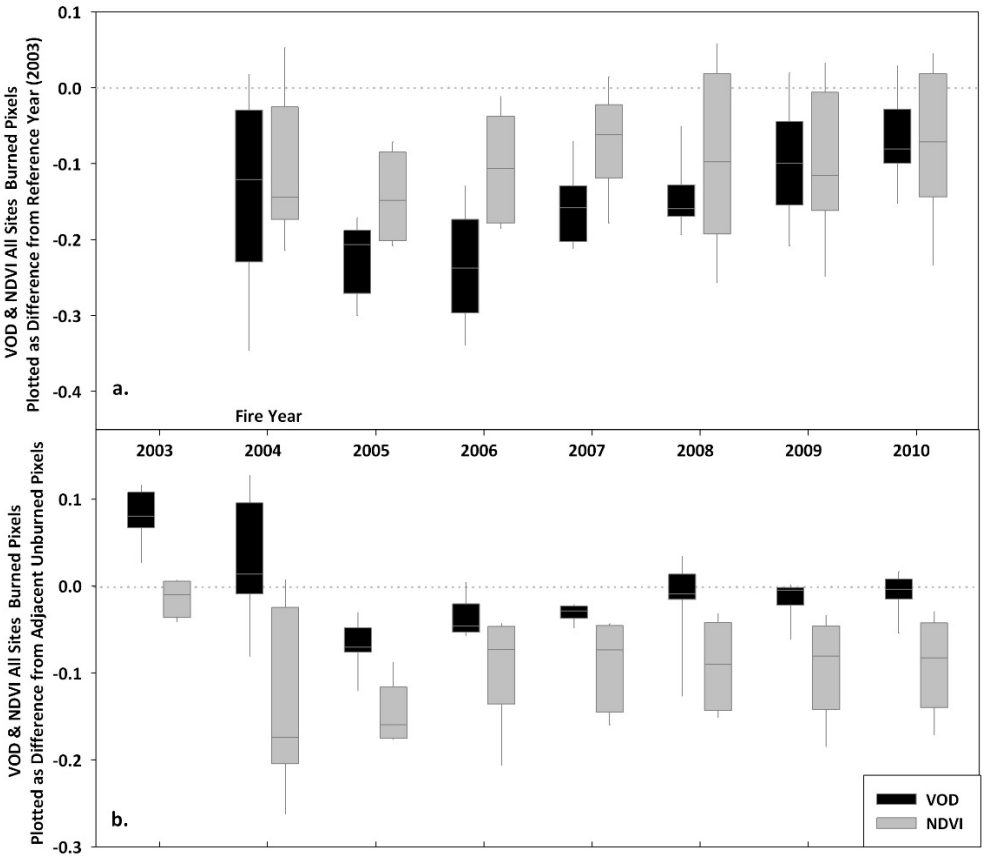

Figure 4.4. Year by year summaries of 16-day VOD and NDVI anomalies for all fire perimeters, as derived from (a) differences from pre-fire reference year (2003) conditions and (b) differences from adjacent unburned control pixels. Boxes display median, upper and lower quartiles, and whiskers display 5th and 95th percentiles.

4.2.2 Post-fire Changes in Canopy Maximums

The pixel-wise yearly differences between annual VOD maxima and 2003 pre-fire control year values (2003_{max} - $YEAR_{max}$) is shown in Figure 4.5. All documented burned areas within the region regardless of size or year are presented to illustrate the regional effects of all fires through the 2003-2010 data record.

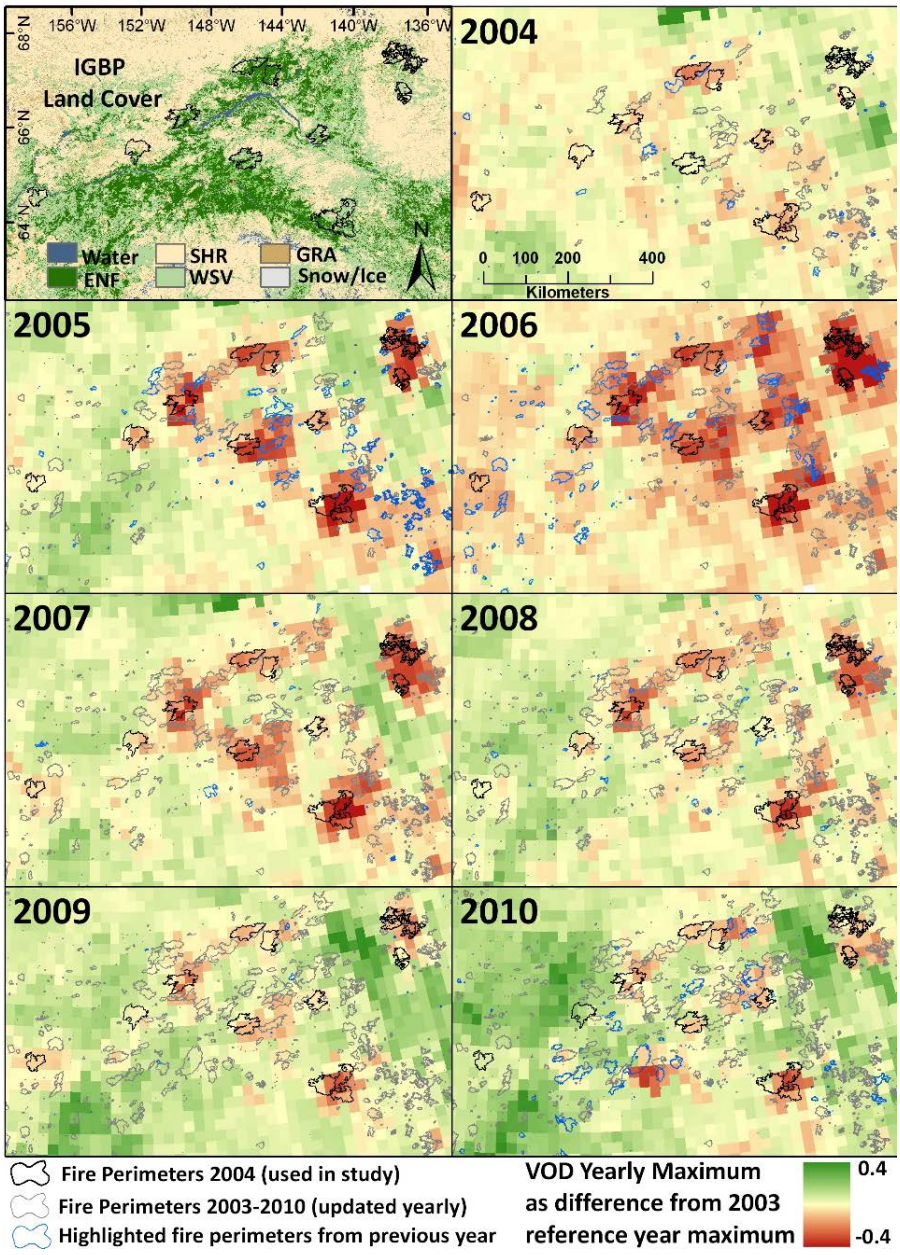

Figure 4.5. Yearly VOD anomalies of annual maxima relative to the 2003 pre-fire reference year. Fires from 2003 to 2010 in both databases beyond the 14 selected are also mapped to display yearly effects of all fires. In each panel, fires from the previous year are annotated (blue outline) to highlight the effect on the year's anomaly. The MODIS IGBP land cover classification is also displayed (top left).

These results show large VOD spatial and temporal heterogeneity, with anomalous and persistent VOD decreases over fire perimeters associated with the extreme 2004 fire year as well as other documented fire events. The negative VOD anomalies within these perimeters

are reduced in subsequent years consistent with expected canopy recovery. These results also display more spatially extensive, year-to-year VOD changes that may reflect regional climate variability.

The timing of yearly VOD and NDVI maximums for each burned area relative to the 2003 reference year and the mean timing of annual maximums for adjacent control pixels is displayed in Figure 4.6.

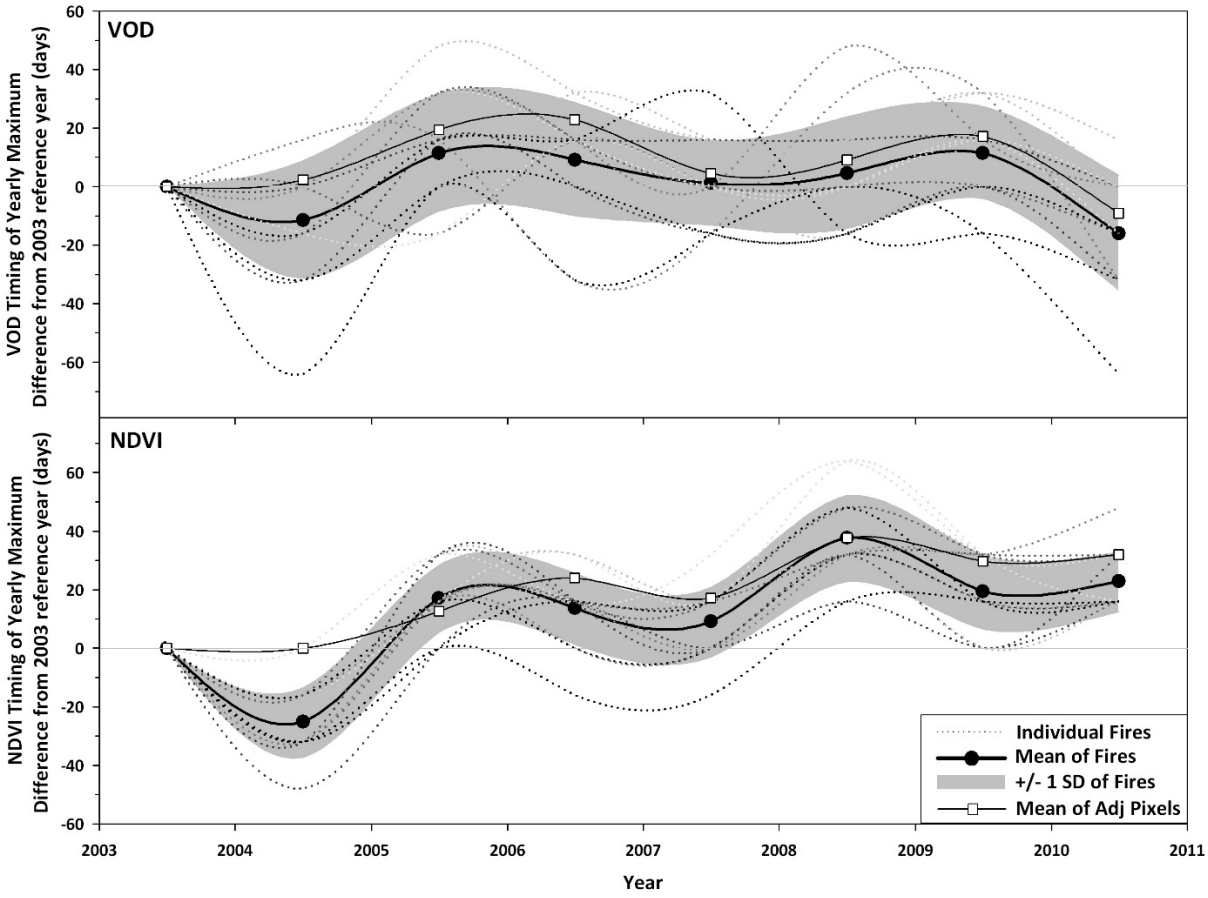

Figure 4.6. Phenological timing of yearly VOD and NDVI maxima for individual fire perimeter areas, and overall mean and SD variability across all fire perimeters relative to the timing of 2003 (pre-burn reference) maxima. Negative (positive) values denote earlier (later) timing of annual maxima relative to the 2003 pre-burn control year. The mean timing of adjacent control pixel maxima is also plotted.

The timing of VOD annual maximums varies across the fire affected areas and the mean post-fire timing relative to 2003 is only slightly later (1 to 10 days) for all years except 2010, indicating no large post-fire changes in the timing of annual canopy maximums. The NDVI post-

fire response displays incrementally later seasonal maximums with the mean ranging from 9 to 37 days later relative to the 2003 reference year. The timing of NDVI and VOD maximums for adjacent control pixels follows a similar trend, indicating that regional climate variability is likely a larger driver of this phenology metric than fire disturbance.

4.2.3 Canopy Recovery to Steady State Conditions and Tree Cover Loss

Results of the asymptotic curve fit applied to each fire are displayed in Figure 4.7. Post-fire steady state conditions were attained within 1 to 3 years (mean=2.14) for NDVI and within 3 to 7 years (mean = 4.64) for VOD, with a mean 2.5 year difference in steady state recovery between the two parameters.

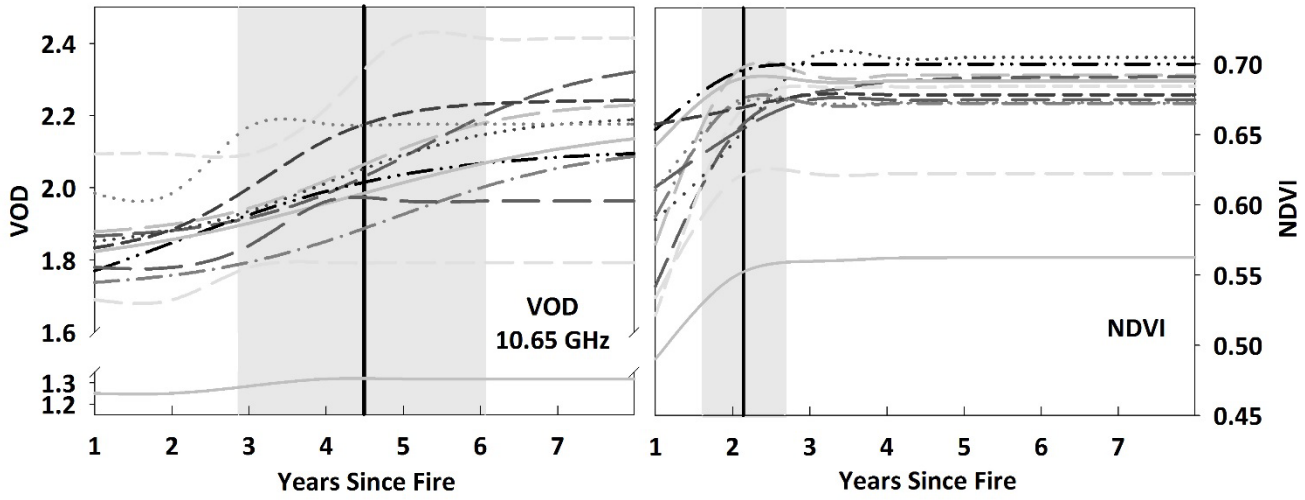

Figure 4.7. Results of an asymptotic curve fit applied to individual post-fire VOD and NDVI maximums from 2005-2010 and model fit extended to 2012, when all fires reached the defined recovery. Recovery was defined as the year when the curve reached 95% of the asymptote. Vertical black line and grey shading are mean and standard deviation of years to recovery for all fires.

The estimated number of years to post-fire VOD steady state conditions corresponded directly with proportional tree cover loss (PTC_{loss}) within fire perimeters used as a metric of fire severity ($r^2 = 0.48$, $p<0.01$) (Figure 4.8); thus greater tree cover loss and associated fire severity coincides with longer VOD recovery. PTC_{loss} was also well correlated ($r=0.70$, $p<0.05$) with the percent of high severity burn area categorized from the MTBS maps. In contrast, the estimated number of years to post-fire NDVI recovery showed relatively weak correspondence to PTC_{loss}

(r^2 = 0.13, p=0.21). The non-significant relationship between NDVI recovery and PTC_{loss} reflects the more rapid NDVI recovery to steady state conditions, with 11 of 14 fires recovering in a two year time span. The VOD recovery lag relative to NDVI reflects VOD sensitivity to both photosynthetic and non-photosynthetic vegetation, and expected slower woody biomass regeneration relative to green foliar biomass alone.

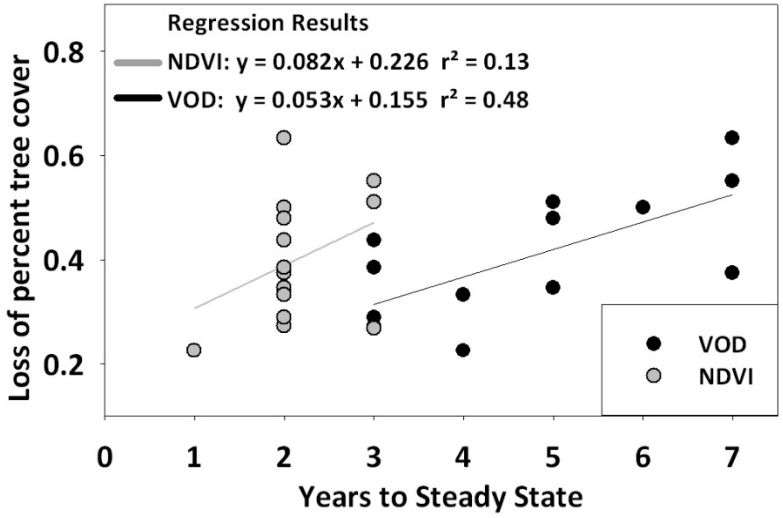

Figure 4.8. Scatter plot and linear regression results comparing post-fire percent tree cover loss within fire perimeters normalized by the 2003 reference year ($PTC_{loss} = PTC_{2003} – PTC_{2005} / PTC_{2003}$) versus the years to recovery (initial steady state conditions).

4.2.4 Field Data Comparisons to Fire Severity and Vegetation Recovery

The results of these tests provided no significant statistical relationship between the field data and estimates of fire severity or NDVI and VOD recovery estimates. The results were inconclusive for two primary reasons. First, the number of data points was limited. The field data was conducted within only 4 fire perimeters used in this study and therefore the statistical analysis lacked power. While Dr. Johnstone found significant differences in many of the stem density parameters across plots within a single fire perimeter, there was a lack of significant difference across fire perimeters which hindered our analysis capabilities. Pair-wise comparisons (t-tests) of the fire severity variables (n=3) and stem density variables (n=3) by fire (n=4) found that 28 of the 36 pairs were not significantly different. Second, the scale of the field measurements (30m x 30m plots) vs. the 25km VOD resolution limits attribution of VOD

measures to plot level data. Even considering the range of 12 to 35 plots per fire, the area measured is orders of magnitude less that even a single VOD pixel.

4.3 Discussion

4.3.1 Defining Canopy "Recovery" from Relatively Short-Term Satellite Records

The relatively short six year post-fire recovery period analyzed here constrained more comprehensive analyses of canopy recovery and associated vegetation succession dynamics. The prognostic ability of the asymptotic curve fit method allows for estimates of recovery beyond the data record, but the recovery projections are limited to an initial steady state defined by the asymptote of the model fit. Hence we calculate a relatively rapid (within 1 to 3 years) boreal NDVI recovery though the steady state values range from 83% to 95% (mean = 88%) of the pre-fire maximums and therefore do not imply canopy greenness recovery to pre-fire levels. This accounts for the difference in NDVI recovery from this investigation relative to previous reports of longer (5 to 10 year) boreal fire recovery periods that have been defined relative to pre-fire conditions (Goetz et al., 2006; Hicke et al., 2003). Post-fire NDVI recovery characteristics reported from those studies are generally consistent with the current results (Figure 4.7), where the initial year following disturbance displays the minimum of the post-fire record, followed by a strong NDVI increase the following year, and much slower NDVI recovery in subsequent years. The NDVI recovery rate remains positive after approximately five years post-fire, indicating continuing recovery to pre-fire conditions that is not captured by the asymptotic curve fit approach.

Assessments of VOD recovery are also constrained by the relatively short satellite data record, with initial steady-state values ranging from 87% to 102% (mean = 94%) of the pre-fire maximums, and incomplete canopy biomass recovery to pre-fire levels for some fires. The relatively slow VOD post-fire recovery is consistent with the expected slower growth response of photosynthetic and non-photosynthetic (woody) biomass relative to the more rapid recovery in vegetation greenness captured by the NDVI record. These results are reinforced by the significant positive relationship between estimated VOD recovery period and proportional tree

cover loss, indicating that the VOD parameter provides an effective metric of canopy biomass recovery and relative burn severity.

4.3.2 Recovery Trajectory Impacts on Aboveground Carbon Stocks

Vegetation response trajectories following fire have been used to estimate the regeneration of aboveground carbon stocks and net primary productivity (NPP). In a study examining 26 boreal forest fires from 1980-1982, post-fire NDVI driven NPP estimates showed generally rapid post-fire recovery in the first few years following fire; in some cases predicting approximately 30% greater NPP recovery rates than other independent NPP estimates (Hicke et al., 2003). The rapid recovery of NDVI (as seen in Figure 4.7) may result in overestimation of initial post-fire NPP and resulting carbon stocks, particularly as NDVI can be strongly correlated with regeneration of non-woody herbaceous vegetation cover and poorly correlated with tree seedling density in some cases (Buma, 2011). The slower VOD recovery trajectory in the first years following fire may be more representative of initial NPP recovery and regeneration of aboveground carbon stocks (Hicke et al., 2003; Goulden et al., 2011).

Difference in NDVI and VOD recovery rates in these initial years can translate to large-scale differences in regional and global terrestrial carbon (CO_2) sequestration, especially given the large regional and global extent of fire affected areas, including 3.0×10^6 ha of fire affected area within the interior Alaska boreal zone estimated from 2004 to 2008 (Kasischke & Hoy, 2012), and 3.3×10^8 to 4.3×10^8 ha of global annual burned area estimated from 1997 to 2008 (Giglio et al., 2010). The integrated use of NDVI and VOD information may provide a more effective means for estimating post-fire productivity and carbon stock recovery, utilizing NDVI as a measure of photosynthetic potential and the VOD as a measure of biomass resulting from that potential. The integrated use of these data may lead to better understanding of carbon use efficiency, carbon allocation (foliar vs. woody), respiration partitioning (autotrophic vs. heterotrophic) and net ecosystem productivity in the initial years following fire (Yi et al., 2013).

4.3.3 Post-fire Boreal Vegetation Considerations and Recovery Trajectories

Post-fire boreal vegetation recovery is influenced by many factors including fire duration and intensity, crown versus understory burn characteristics, and topographic and edaphic

conditions. These factors can result in a wide range of post-fire species recruitment, stem density patterns and recovery trajectories across fires. For example, post-fire surveys within 4 fire perimeters used in this study found that fire eliminated half of the understory species; 25% of the post-fire flora represented new species, while high burn severity sites showed significantly greater change in community composition than low severity sites (Bernhardt et al., 2011). Within the same perimeters, Johnstone et al., (2010) found inconsistent stem density recovery across fires, with post-fire evergreen spruce densities ranging from 0 to 22 stems m^{-2} and new recruitment of deciduous densities ranging from 0 to 230 stems m^{-2}.

We therefore expect spatial variation in post-fire vegetation recovery trajectories and associated remote sensing metrics due to spatial differences in fire severity, species recruitment and abundance. Yet for the 14 fires measured, NDVI recovery trajectories displayed minimal spatial variation within the first 6 years post-fire. The relatively rapid and consistent vegetation greenness recovery may reflect NDVI sensitivity to initial vegetation re-establishment and the development of a simple foliar canopy layer. In contrast, the VOD fire recovery trajectories displayed considerable spatial heterogeneity (e.g. Figure 4.7) that may reflect wider variation in fire severity impacts on vegetation biomass recovery and species composition, particularly the establishment of deciduous versus evergreen species. These results highlight the need for more specific studies on NDVI and VOD responses to understory versus overstory vegetation (e.g. Suzuki et al., 2011), species composition and biomass distributions.

4.3.4 Microwave Remote Sensing of Fire Recovery – Future Considerations

The VOD record confirms generally rapid boreal vegetation canopy biomass recovery that is similar to previous studies derived from NDVI and tower CO_2 eddy covariance measurements (Hicke et al., 2003; Goetz et al., 2006; Goulden et al., 2011). However, the VOD response lagged NDVI recovery of canopy greenness by approximately two years which meets expectations of slower recovery of non-photosynthetic canopy biomass elements. The duration of VOD recovery was directly proportional ($p<0.01$) to independent estimates of post-fire woody vegetation cover loss from MODIS, indicating that the VOD recovery is sensitive to fire

severity. Microwave VOD sensitivity to canopy biomass is also frequency dependent. This investigation examined a satellite microwave VOD record derived from only a single frequency (10.7 GHz), while alternative VOD records are available that have been derived from other (6.9 and 18.7 GHz) microwave frequencies (Jones & Kimball, 2011). Lower frequency VOD retrievals may be sensitive to a greater volume of canopy biomass and therefore exhibit a different recovery trajectory than higher frequency retrievals. The potential exists for more comprehensive studies of canopy recovery not only from combined NDVI and VOD studies, but also by including VOD retrievals at different frequencies to better distinguish responses from different canopy layers.

While the satellite microwave VOD record provides near-daily temporal fidelity, the relatively coarse (25-km) resolution of the retrievals constrains capabilities for examining sub-grid scale heterogeneity and linking to stand level processes. The NDVI and VOD together provide a more comprehensive view of relations between both photosynthetic leaf-area and aggregate canopy biomass recovery that includes both foliar and woody vegetation components. Additional research and information is needed, however, to attribute the observed changes to different vegetation successional stages and species compositions, and distinguish overstory and understory processes. Synergistic use of these data potentially allow for effective upscaling of stand level processes and regional monitoring of disturbance recovery to inform carbon models and advance understanding of boreal vegetation succession following wildfire.

4.4 Acknowledgements

This portion of the dissertation was carried out with funding from the NASA Terrestrial Ecology program. We thank the Canadian Wildland Fire Information System and the Alaska Interagency Coordination Center for making the fire perimeter data freely available. The AMSR-E global VOD database and associated biophysical retrievals from this study are available through the NASA NSIDC DAAC (http://nsidc.org/data/nsidc-0451.html). This work was performed at the University of Montana (UMT) under contract to the National Aeronautics and Space Administration.

4.5 References Cited

Alaska Climate Research Center (2009) Alaska climate data. Available at http://climate.gi.alaska.edu/index.html. Geophysical Institute, University of Alaska Fairbanks. (Accessed 8 August 2012).

Amiro BD, Barr AG, Black TA, *et al.* (2006) Carbon, energy and water fluxes at mature and disturbed forest sites, Saskatchewan, Canada. *Agricultural and Forest Meteorology*, **136**, 237–251.

Auclair AND, Carter TB (1993) Forest Wildfires as a Recent Source of CO2 at Northern Latitudes. *Canadian Journal of Forest Research*, **23**, 1528–1536.

Beck P, Goetz S (2011) Satellite observations of high northern latitude vegetation productivity changes between 1982 and 2008: ecological variability and regional differences. *Environmental Research Letters*, **6**.

Bernhardt EL, Hollingsworth TN, Chapin FS (2011) Fire severity mediates climate-driven shifts in understorey community composition of black spruce stands of interior Alaska. *Journal of Vegetation Science*, **22**, 32–44.

Brewer KC, Winne JC, Redmond RL, Opitz DW, Mangrich MV (2005) Classifying and mapping wildfire severity: A comparison of methods. *Photogrammetric Engineering and Remote Sensing*, **71,** 1311–1320

Buma B (2012) Evaluating the utility and seasonality of NDVI values for assessing post-disturbance recovery in a subalpine forest. *Environmental monitoring and assessment*, **184**, 3849–60.

Bureau of Land Management (2011) Alaska Fire Service, AFS GIS Specialists. http://afsmaps.blm.gov/imf_fire/imf.jsp?site=fire (accessed 28 August, 2012)

Canadian Forest Service (2011) National Fire Database - Agency Fire Data. Natural Resources Canada, Canadian Forest Service, Northern Forestry Centre, Edmonton, Alberta. http://cwfis.cfs.nrcan.gc.ca/en_CA/nfdb. (accessed 28 August, 2012)

Cocke AE, Fulé PZ, Crouse JE (2005) Comparison of burn severity assessments using Differenced Normalized Burn Ratio and ground data. *International Journal of Wildland Fire*, **14**, 189–198

Eidenshink J, Schwind B, Brewer K, Zhu Z-L, Quayle B, Howard S (2007) A project for monitoring trends in burn severity. *Fire Ecology*, **3**, 3–21.

Field CB, Lobell DB, Peters HA, Chiariello NR. (2007) Feedbacks of terrestrial ecosystems to climate change. *Annual Review of Environment and Resources* pp.1-29. Palo Alto: Annual Reviews

Frolking S, Milliman T, Palace M, Wisser D, Lammers R, Fahnestock M (2011) Tropical forest backscatter anomaly evident in SeaWinds scatterometer morning overpass data during 2005 drought in Amazonia. *Remote Sensing of Environment*, **115**, 897–907.

Frolking S, Palace MW, Clark DB, Chambers JQ, Shugart HH, Hurtt GC (2009) Forest disturbance and recovery: A general review in the context of spaceborne remote sensing of impacts on aboveground biomass and canopy structure. *Journal of Geophysical Research*, **114**.

Frolking S, Milliman T, McDonald K, Kimball J, Zhao M, Fahnestock M (2006) Evaluation of the SeaWinds scatterometer for regional monitoring of vegetation phenology. *Journal of Geophysical Research*, **111**.

Frolking S, Fahnestock M, Milliman T, McDonald K, Kimball J (2005) Interannual variability in North American grassland biomass/productivity detected by SeaWinds scatterometer backscatter. *Geophysical Research Letters*, **32**, 1–5.

Gillett NP (2004) Detecting the effect of climate change on Canadian forest fires. *Geophysical Research Letters*, **31**.

Giglio L, Randerson J, van der Werf GR, Kasibhatla PS, Collatz GJ, Morton DC, DeFries RS (2010) Assessing variability and long-term trends in burned area by merging multiple satellite fire products. *Biogeosciences*, **7**, 1171–1186.

Goetz SJ, Fiske GJ, Bunn AG (2006) Using satellite time-series data sets to analyze fire disturbance and forest recovery across Canada. *Remote Sensing of Environment*, **101**, 352–365.

Goetz SJ, Sun M, Baccini a., Beck PS a. (2010) Synergistic use of spaceborne lidar and optical imagery for assessing forest disturbance: An Alaska case study. *Journal of Geophysical Research*, **115**, G00E07.

Goulden ML, McMillan MS, Winston GC, Rocha AV, Manies KL, Harden JW, Bond-Lamberty BP (2011) Patterns of NPP, GPP, respiration, and NEP during boreal forest succession. *Global Change Biology*, **17**, 855–871.

Goulden ML, Winston GC, McMillan AMS, Litvak ME, Read EL, Rocha AV, Elliot JR (2006) An eddy covariance mesonet to measure the effect of forest age on land?atmosphere exchange. *Global Change Biology*, **12**, 2146–2162.

Hansen M, DeFries RS, Townshend JRG, Carroll M, Dimiceli C, Sohlberg RA (2003) Global Percent Tree Cover at a Spatial Resolution of 500 Meters: First Results of the MODIS Vegetation Continuous Fields Algorithm, *Earth Interactions*, **7**, 1-15.

Harden JW, Mack M, Veldhuis H, Gower ST (2002) Fire dynamics and implications for nitrogen cycling in boreal forests. *Journal of Geophysical Research*, **108**, 8223.

Hicke JA, Asner G, Kasischke E (2003) Postfire response of North American boreal forest net primary productivity analyzed with satellite observations. *Global Change Biology*, **9**, 1145–1157.

IPCC. Climate Change 2007: The Physical Science Basis. Contribution of Working Group I to the Fourth Assessment Report of the Intergovernmental Panel on Climate Change. Cambridge, UK: Cambridge University Press, 2007.

Jackson TJ, Schmugge TJ (1991) Vegetation Effects on The Microwave Emission Of Soils. *Remote Sensing Of Environment*, **36**, 203-212

Jackson TJ, Schmugge TJ, Wang JR (1982) Passive Microwave Sensing Of Soil-Moisture Under Vegetation Canopies. *Water Resources Research*, **18**, 1137-1142

Jenks GF (1967) The data model concept in statistical mapping. International Yearbook of Cartography, **7**, 186−190.

Johnstone JF (2009) Post-fire recovery in the 2004 burns of interior Alaska: Densities of tree seedlings measured in 2008 by Joint Fire Science Program, Bonanza Creek LTER University of Alaska Fairbanks. BNZ:398

Johnstone JF, Hollingsworth TN, and Bonanza Creek LTER (2013) Environmental and stand data for sites located in the 2004 burns off the Steese, Taylor, and Dalton Highways, collected in 2005-2007. knb-lter-bnz.342.17

Johnstone JF, Hollingsworth TN, Chapin FS, Mack MC (2010) Changes in fire regime break the legacy lock on successional trajectories in Alaskan boreal forest. *Global Change Biology*, **16**, 1281–1295.

Johnstone J, Kasischke E (2005) Stand-level effects of soil burn severity on postfire regeneration in a recently burned black spruce forest. *Canadian Journal of Forestry,* **2163**, 2151–2163.

Jones LA, Kimball JS (2011) Daily Global Land Surface Parameters Derived from AMSR-E. Boulder, Colorado USA: National Snow and Ice Data Center. Digital media.

Jones LA, Ferguson CR, Kimball JS, Zhang K, Chan SK, McDonald KC, Njoku EG, Wood EF (2010) Satellite Microwave Remote Sensing of Daily Land Surface Air Temperature Minima and Maxima from AMSR-E. IEEE Journal of Selected Topics in Applied Earth Observations and Remote Sensing. **3**, 111-123.

Jones MO, Jones LA, Kimball JS, McDonald KC (2011) Satellite passive microwave remote sensing for monitoring global land surface phenology. *Remote Sensing of Environment*, **115**, 1102–1114.

Jones MO, Kimball JS, Jones LA, McDonald KC (2012) Satellite passive microwave detection of North America start of season. *Remote Sensing of Environment*, **123**, 324–333.

Kasischke ES, French NHF (1997) Constraints on using AVHRR composite index imagery to study patterns of vegetation cover in boreal forests. *International Journal Of Remote Sensing*, **18**, 2403-2426.

Kasischke ES, Hoy EE (2012) Controls on carbon consumption during Alaskan wildland fires. *Global Change Biology*, **18**, 685–699.

Kasischke ES, Rupp TS, Verbyla DL (2006) Fire trends in the Alaskan boreal forest region. In: Alaska's Changing Boreal Forest (Eds. Chapin III FS, Oswood M, Cleve KV, Viereck LA, Verbyla DL), Oxford University Press, Oxford, pp. 285–301.

Kim Y, Kimball JS, Zhang K, McDonald KC (2012) Satellite detection of increasing Northern Hemisphere non-frozen seasons from 1979 to 2008: Implications for regional vegetation growth. *Remote Sensing of Environment*, **121**, 472–487.

Kim Y, Kimball JS, McDonald KC, Glassy J (2011) Developing a Global Data Record of Daily Landscape Freeze / Thaw Status Using Satellite Passive Microwave Remote Sensing. *IEEE Transactions on Geoscience and Remote Sensing*, **49**, 949–960.

Kimball JS, McDonald KC, Running SW, Frolking SE (2004) Satellite radar remote sensing of seasonal growing seasons for boreal and subalpine evergreen forests. *Remote Sensing of Environment*, **90**, 243–258.

Kimball JS, McDonald KC, Zhao M, (2006) Spring thaw and its effect on terrestrial vegetation productivity in the western Arctic observed from satellite microwave and optical remote sensing. *Earth Interactions* **10**, 1-22.

Kimball JS, Zhao M, McGuire AD, Heinsch FA, Clein J, Calef M., Jolly, WM, Kang S, Euskirchen SE, McDonald KC, Running SW (2007) Recent Climate-Driven Increases in Vegetation Productivity for the Western Arctic: Evidence of an Acceleration of the Northern Terrestrial Carbon Cycle. *Earth Interactions*, **11**, 1-30.

Kirdyashev KP, Chukhlantsev AA, Shutko AM (1979) Microwave Radiation of the Earth's Surface in the Presence of a Vegetation Cover. *Radio Engineering and Electronic Physics*, **24**, 256-264

Knowles KW (2004) EASE-Grid Land Cover Data Resampled from Boston University Version of Global 1 km Land Cover from MODIS 2001. In. Boulder, Colorado USA: National Snow and Ice Data Center

Knowles KW, Savoie RL, Armstrong RL, Brodzik MJ. (2009) AMSR-E/Aqua daily EASE-Grid brightness temperatures 2003-2008. In. Boulder, Colorado USA: National Snow and Ice Data Center

Kurz WA, Apps MJ (1999) A 70-year retrospective analysis of carbon fluxes in the Canadian forest sector. Ecological Applications, **9**, 526–547.

Law R, Morton, RD (1993) Alternative permanent states of ecological communities. *Ecology*, **74**, 1347–1361.

Liski J, Korotkov AV, Prins CFL, Karjalainen T, Victor DG, Kauppi PE (2003) Increased carbon sink in temperate and boreal forests. *Climatic Change,* **1**, 89–99.

Mackey BG, Lindenmayer DB, Gill M, McCarthy MA, Lindesay J (2002). Wildfire, fire and future climate. Collingwood: CSIRO Publishing.

Magnussen S, Wulder MA (2012) Post-Fire Canopy Height Recovery in Canada's Boreal Forests Using Airborne Laser Scanner (ALS). *Remote Sensing*, **4**, 1600–1616.

Min Q, Lin B (2006a) Remote sensing of evapotranspiration and carbon uptake at Harvard Forest. *Remote Sensing of Environment*, **100**, 379–387.

Min Q, Lin B (2006b) Determination of spring onset and growing season leaf development using satellite measurements. *Remote Sensing of Environment*, **104**, 96–102.

Mo T, Choudhury BJ, Schmugge TJ, Wang JR, Jackson TJ (1982). A Model for Microwave Emission From Vegetation-Covered Fields. Journal Of Geophysical Research, **87**, 11229-11237

Myneni RB, Keeling CD, Tucker CJ, Asrar G, Nemani, RR. (1997) Increased plant growth in the northern high latitudes from 1981 to 1991. *Nature*, **386**, 698

Nemani RR, Keeling CD, Hashimoto H, *et al.* (2003) Climate-driven increases in global terrestrial net primary production from 1982 to 1999. *Science*, **300**, 1560–1563.

Njoku EG, Chan SK (2006). Vegetation and surface roughness effects on AMSR-E land observations. *Remote Sensing of Environment*, **100**, 190-99.

Olson J (1963) Energy storage and the balance of producers and decomposers in ecological systems. *Ecology*, **44**, 322–331.

Randerson JT, Masiello CA, Still CJ, Rahn T, Poorter H, Field CB (2006) Is carbon within the global terrestrial biosphere becoming more oxidized? Implications for trends in atmospheric O2. *Global Change Biology*, **12**, 260–271.

Sarmiento JL, Gloor M, Gruber N, *et al.* (2010) Trends and regional distributions of land and ocean carbon sinks. *Biogeosciences*, **7**, 2351–2367.

Shi J, Jackson T, Tao J, Du J, Bindlish R, Lu L, Chen K (2008) Microwave vegetation indices for short vegetation covers from satellite passive microwave sensor AMSR-E. *Remote Sensing of Environment*, **112**, 4285–4300.

Sofronov MA, Volokitina AV (2009) Wildfire ecology in continuous permafrost zone Permafrost Ecosystems: Siberian Larch Forests, (Eds.) Osawa A, Zyryanova OA, Matsuura Y, Kajimoto T, Wein RW (Dordrecht: Springer) pp. 59–82.

Soja AJ, Cofer WR, Shugart HH, *et al.* (2004) Estimating fire emissions and disparities in boreal Siberia (1998–2002). *Journal of Geophysical Research*, **109**, D14S06.

Soja AJ, Tchebakova NM, French NHF, *et al.* (2007) Climate-induced boreal forest change: Predictions versus current observations. *Global and Planetary Change*, **56**, 274–296.

Stocks BJ, Mason JA, Todd JB, Bosch EM, Wotton BM, Amiro BD (2002) Large forest fires in Canada, 1959–1997. *Journal of Geophysical Research*, **107**

Suzuki R, Kobayashi H, Delbart N, Asanuma J,= Hiyama T (2011) NDVI responses to the forest canopy and floor from spring to summer observed by airborne spectrometer in eastern Siberia. *Remote Sensing of Environment*, **115**, 3615–3624.

Todd SK, Jewkes HA (2006) Wildland fire in Alaska: a history of organized fire suppression and management in the last frontier. Agricultural and Forestry Experiment Station Bulletin No 114. Fairbanks, AK: University of Alaska Fairbanks, School of Natural Resources and Agriculture, Agricultural and Forestry Experiment Station.

Turner M (2010) Disturbance and landscape dynamics in a changing world. *Ecology*, **91**, 2833–2849.

Ulaby FT, Moore RK, Fung AK. (1982) Microwave remote sensing: Active and passive, 2, Radar remote sensing and surface scattering and emission theory. Reading, MA. (Addison-Wesley)

Wigneron JP, Kerr Y, Chanzy A, Jin Y (1993) Inversion of surface parameters from passive microwave measurements over a soybean field. *Remote Sensing of Environment*, **46**, 61-72

Wulder MA, White JC, Alvarez F, Han T, Rogan J, Hawkes B (2009) Characterizing boreal forest wildfire with multi-temporal Landsat and LIDAR data. *Remote Sensing of Environment*, **113**, 1540–1555.

Yi Y, Kimball JS, Jones LA, Reichle RH, Nemani R, Margolis HA (2013) Recent climate and fire disturbance impacts on boreal and arctic ecosystem productivity estimated using a satellite-based terrestrial carbon flux model. *Journal of Geophysical Research: Biogeosciences*, doi: 10.1002/jgrg.20053

Zhang K, Kimball JS, Kim Y, McDonald KC (2011) Changing freeze-thaw seasons in northern high latitudes and associated influences on evapotranspiration. *Hydrological Processes*, **25**, 4142–4151.

Chapter 5. Asynchronous Amazon forest canopy phenology indicates adaptation to both water and light availability

Amazon forests are a major component of the global carbon (C) cycle, processing ~18 Pg C annually through photosynthetic uptake and respiration of atmospheric CO_2 (Christiansen et al 2007), and representing nearly half of all tropical vegetation biomass (Saatchi et al 2011). Projected drying from climate change (Salazar et al 2007, Cox et al 2008) may alter the regional C balance and the critical role of these forests in the global C cycle (Cox et al 2013). For example, widespread drought in 2005 and 2010 and subsequent effects on forest mortality (Phillips et al 2009, Lewis et al 2011) and canopy greenness (Xu et al 2011) may become more typical future scenarios (Li et al 2008, Lee et al 2011). Predicting long-term vegetation responses to a changing climate is complex (Cox et al 2013), but understanding how Amazon forest canopy phenology has adapted to seasonal changes in water and light availability may provide insight into forest behavior under future climate conditions (Malhi et al 2008).

The climatic constraints of water and light availability on forest growth in the Amazon are small when compared to more temperate systems with clear active and dormant seasons, yet the majority of the region experiences peaks in solar irradiance out of phase with precipitation due to cloud cover seasonality (Restrepo-Coupe et al 2013). The extent to which seasonal fluctuations of these constraints control Amazon canopy phenology is still poorly understood. This is due in part to the wide species diversity and variety of phenological patterns in tropical forests where leaf flush and senescence are continuous processes. Satellite remote sensing however provides a spatially integrated measure of canopy scale net leaf flush (i.e. the majority of species exhibiting new leaf growth). Satellite and field observations have demonstrated that net leaf flush is often asynchronous with peaks in water availability, woody growth, canopy greenness, photosynthetic capacity (Pc), and gross ecosystem productivity (GEP) (Myneni et al 2007, Samanta et al 2012, Restrepo-Coupe et al 2013, Lee et al 2013, Rowland et al 2014), which has further confounded an integrated understanding of light and water availability effects on Amazon canopy phenology.

Reliable satellite optical-infrared remote sensing observations are hindered in the Amazon by persistent clouds, smoke and atmosphere aerosol contamination, and signal

saturation over dense broadleaf forests. These measurement difficulties spurred a contrary report claiming Amazon forests display no seasonality in canopy greenness and structure (Morton et al 2013), yet the majority of data from in situ to basin wide scales confirm forest canopy seasonality (Saleska et al 2003, Asner et al 2004, Goulden et al 2004, Rice et al 2004, Barlow et al 2007, Fisher et al 2007, Doughty and Goulden 2008, Brando et al 2010, Lee et al 2013, Parazoo et al 2013, Frankenberg et al 2014). Also, a relatively long historical satellite record and sophisticated data processing has allowed for identification of Amazon canopy seasonality (Myneni et al 2007, Samanta et al 2012, Silva et al 2013), including observed seasonal changes in canopy biomass from satellite active and passive microwave sensors (Frolking et al 2011, Jones et al 2011) that are insensitive to solar illumination, cloud and atmospheric effects. Amazon canopies are also vertically and spatially complex, and remote sensing observations over intact forests primarily represent upper canopy conditions. These observations cannot be readily extrapolated to the lower canopy and understory, which may display different phenological processes responsive to a far more variable light regime dependent on canopy architecture. Proper characterization therefore requires the use of multiple satellite measures across a range of frequencies and coupled with ground based observations to measure and compare multiple aspects of Amazon phenology. This coupled strategy builds confidence in satellite retrievals by reducing dependency on any single observation source.

To better characterize Amazon canopy phenology we use six remotely sensed data sets spanning nine years (2003-2011), in context with reported field and flux tower data. This study aims to elucidate Amazon forest canopy phenology and provide a methodology for pixel-wise mapping of the extent to which canopy phenology has adapted to light and/or water availability across a longitudinal moisture gradient. We address the following questions. First, are canopy net leaf flush and increases in vegetation canopy biomass water content asynchronous across the Amazon? Second, if asynchrony is present, does the degree of asynchrony show a dependence on water availability and photosynthetically active radiation (PAR)?

The observed asynchronous behavior of these forests and severe constraints on remote sensing observations has posed a challenge to improving understanding and model predictions

of Amazon canopy phenology, primary productivity and vegetation-atmosphere interactions. Early models (e.g. Moorcroft et al. 2001) implemented a drought-deciduous phenology (leaf abscission occurs when plant available water drops below a critical threshold), which failed to represent observed canopy phenology over tropical systems where plant available water is often abundant, and leaf growth is synchronous with light availability. Recent terrestrial biosphere and land surface models implemented a satellite derived enhanced vegetation index (EVI) to capture leaf photosynthetic capacity (Xiao et al 2005) and parameters for root water uptake and hydraulic redistribution (Lee et al 2005, Baker et al 2008) to allow for dry season evapotranspiration increases. These models showed improved GEP accuracy against tower observations, but still lacked proper characterization of canopy leafing phenology. To better capture canopy phenology, Kim et al (2012) developed a light-controlled phenology sub-model which improved model simulation of seasonal carbon fluxes over a flux tower footprint, and indicated that light-controlled phenology may act as a source of resilience to climate variability.

The light-controlled phenology sub-model (Kim et al 2012) supports the theory that in the absence of water deficits tree phenologies have been selected to coincide with peaks in solar irradiance (Wright 1996) and subsequently that tropical forest canopy net leaf flushing is responsive to irradiance seasonality. Seasonal changes in water availability, irradiance and insect activity (e.g. herbivory) are expected to have consistent effects across the majority of tropical forest species (Wright 1996). When water deficits are absent, selection will favor net leaf production during periods of low herbivory and high irradiance. In contrast, when seasonal water deficits are sufficient to detrimentally affect plant cell expansion and growth, trees must produce leaves during periods of adequate water availability. Data compiled from 53 worldwide studies of tropical plant phenology (van Schaik et al 1993) and an experiment over four evergreen tropical forests (Wright and van Schaik 1994) demonstrated that canopy net leaf flushing coincides with seasonal solar maxima. More recently, a study of Amazon tower flux data across multiple years and sites (Restrepo-Coupe et al 2013) implemented two leaf-flush models and found a consistent positive correlation between leaf flush and light availability. The work presented here provides further support that leaf growth is responsive to irradiance seasonality in the Amazon, examining this hypothesis beyond the scale of plot level data and

flux tower footprints by incorporating a suite of remote sensing data and taking account of the longitudinal gradient in water versus light availability across the Amazon.

5.1 Data and Methods

5.1.1 GRACE terrestrial water storage

The GRACE mission provides measurements of spatio-temporal changes in Earth's gravity field which can be used to derive changes in terrestrial water storage (TWS), and has been implemented in previous studies over the Amazon (Chen et al 2010, Frappart et al 2013, Thomas et al 2014). We use the GRACE GRCTellus Monthly Mass Grids-Land product (Landerer and Swenson 2012, Swenson and Wahr 2006) at 1.0 degree resolution from January 2003 to December 2011 provided by the Jet Propulsion Laboratory. Monthly grids represent the mass deviation relative to the January 2004 to December 2009 baseline and are implemented here as a proxy for water availability to vegetation. Four missing months of data were filled by taking the mean of the previous and subsequent months.

5.1.2 AMSR-E vegetation optical depth

The Advanced Microwave Scanning Radiometer - EOS (AMSR-E) is a microwave radiometer deployed on the polar-orbiting Aqua satellite. The vegetation optical depth (VOD) parameter derived from AMSR-E brightness temperatures, defines the frequency dependent extinction of land surface microwave emissions by the intervening vegetation layer (Jackson and Schmugge 1991, Van de Griend and Wigneron 2004, Jones and Kimball 2012). VOD is sensitive to changes in canopy biomass and water content, including both photosynthetic and woody elements (hereafter referred to as canopy biomass), and has been used to track both Amazon (Jones et al 2011) and African (Guan et al 2012) forest phenology. The VOD retrieval algorithm minimizes the potential influence of atmosphere precipitable water vapor, temperature, surface water inundation and soil moisture effects, providing near-daily global observations posted to a 25km resolution global EASE grid projection (Jones et al. 2011, Jones and Kimball 2012). For this application, the 10.7 GHz, descending orbit (UTC 1:30 A.M. equatorial crossings) VOD record from January 2003 to September 2011 was composited to a monthly mean time series consistent with the GRACE TWS record.

5.1.3 MODIS leaf area index and enhanced vegetation index

The Moderate Resolution Imaging Spectroradiometer (MODIS) MOD15A2 8-day L4 Collection 5 leaf area index (LAI) and an enhanced vegetation index (EVI) (Huete et al 2002) derived from MODIS Multiangle Implementation of Atmospheric Correction (MAIAC) data (Lyapustin et al 2011a, 2011b, 2012) are used to track canopy leaf area and greenness, respectively, from January 2003 to December 2011 at 1 km resolution. The LAI product was spatially resampled to match the VOD 25km EASE grid format by taking the mean of all highest quality LAI pixels with pixel centers in the spatial extent of each 25km pixel. The 8-day LAI record was then temporally resampled to monthly means.

5.1.4 CERES photosynthetically active radiation

Gridded monthly 1.0 degree resolution diffuse and direct PAR data (CERES_SYN1deg_Ed3A) was used from the Clouds and the Earth's Radiant Energy System (CERES) (Wielicki et al 1996) record from January 2003 to December 2011. Total PAR was calculated as the sum of direct and diffuse PAR.

5.1.5 TRMM precipitation

Tropical Rainfall Monitoring Mission (TRMM) 3B43 version 7 Accumulated Rain monthly (cm/month) gridded data at 0.25 degree resolution from January 1998 to December 2011 was acquired from the Goddard Earth Sciences Data and Information Services Center. The pixel-wise number of months per year with less than 100mm precipitation (dry months) were calculated and summarized by ecoregion (Figure 5.1). Pearson product-moment cross-correlations between TRMM precipitation and GRACE TWS were calculated to examine the temporal offset between precipitation inputs and water availability.

5.1.6 Terrestrial ecoregions

We used the World Wildlife Fund (WWF) Terrestrial Ecoregions of the World data set (Olson et al 2001) to distinguish ecoregion level changes in canopy seasonality. The WWF data contains 867 global ecoregions, each representing distinct assemblages of natural communities sharing a large majority of species, dynamics and environmental conditions. Nine terrestrial

ecoregions spanning the west-to-east regional moisture gradient encompassing southern equatorial Amazon evergreen broadleaf forest were used in the analysis (Figure 5.1). Monthly ecoregion means of the remotely sensed datasets were used to calculate monthly climatology and as inputs to a 4-parameter sinusoidal model (detailed in section 5.1.8) for estimating ecoregion scale phase shift differences between water availability (TWS), vegetation canopy biomass (VOD) and canopy leaf area (LAI) phenology.

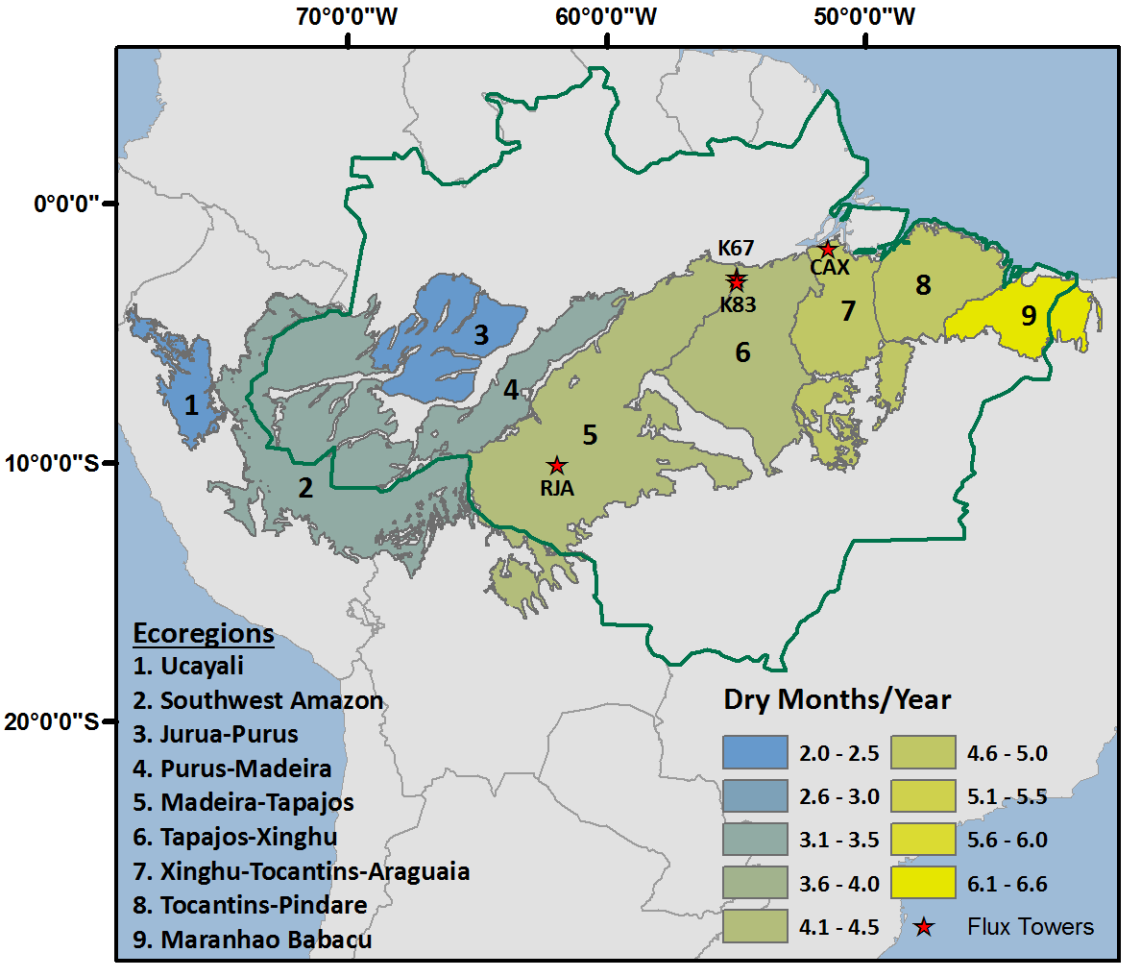

Figure 5.1. Amazon study domain showing southern equatorial ecoregions (*Olson et al* 2001) with the mean number of dry months (<100mm) per year calculated from TRMM 3B43 version 7 Accumulated Rainfall at 0.25 degree resolution from 1998-2011. Flux tower locations used in this study are shown; Reserve Jaru (RJA), Tapajos K67 (K67), Tapajos K83 (K83) and Caxiuana (CAX) (Table 5.1). The green border denotes the legal Amazon boundary in Brazil.

5.1.7 Plot level data and tower GEP, Pc

An extensive literature review located vegetation phenology field data within the ecoregions and general period of this study. Site specific field measurements within intact forests and without experimental manipulation (Table 5.1) were found in two ecoregions (Tapajos-Xinghu, Xinghu-Tocantins-Araguaia). Although the temporal span of the field data was incomplete relative to the remote sensing record, with some data collected in prior years (1999-2002), these data constituted the only publicly available field observation record. Tower flux data of aggregated monthly GEP and Pc (Table 5.1) from the Large-Scale Biosphere-Atmosphere (LBA) Experiment in Amazonia was acquired from the LBA flux tower integrated database (Restrepo-Coupe et al 2013).

Table 5.1. Flux towers providing measures of Gross Ecosystem Productivity (GEP) and Photosynthetic Capacity (Pc), and studies with published field data used in this study. Monthly GEP (µmol CO_2 m^{-2} s^{-1}) and Pc (µmol CO_2 m^{-2} s^{-1}) from the Large-Scale Biosphere-Atmosphere (LBA) Experiment in Amazonia were acquired from the LBA flux tower integrated database (Restrepo-Coupe et al 2014). Pc is estimated as the mean of flux tower derived GEP for a fixed range of PAR (725 < PAR < 925 µmol CO2 m^{-2} s^{-1}); the methods for calculating GEP and Pc can be found in Restrepo-Coupe et al (2013).

Reference	Data	Period	Reported Location
Restrepo-Coupe et al 2013	Reserve Jaru Flux Tower (RJA) GEP, Pc	1999-2002	10.08° S, 61.93° W
	Tapajos K67 Flux Tower (K67) GEP, Pc	2002-2006	2.85° S, 54.97° W
	Tapajos K83 Flux Tower (K83) GEP, Pc	2000-2004	3.01° S, 54.58° W
	Caxiuana Flux Tower (CAX) GEP, Pc	1999-2003	1.72° S, 51.53° W
Asner et al 2004	Plant available water	2000-2001	2.897°S, 54.952°W
Barlow et al 2007	Litterfall rates	2004-2005	0° 27' 00" - 1° 30' 00" S, 51° 40' 00" - 53° 20' 00" W
Brando et al 2010	Plant available water	2000-2004	2.897°S, 54.952°W
	Individuals with new leaves	1999-2004	2.897°S, 54.952°W
	Litterfall rates	2000-2005	2.897°S, 54.952°W
Doughty and Goulden 2008	Increasing leaf flush	2001-2004	3.020833 S, 54.972221W
Fisher et al 2007	Soil Moisture	2001-2003	1° 43' 3.5" S, 51° 27' 36" W
	Sap flow	2002-2003	1° 43' 3.5" S, 51° 27' 36" W
Goulden et al 2004	Woody growth increments	2000-2001	3.0103° S, 54.5815° W
Rice et al 2004	Litterfall Rates	2000-2002	2° 51' S, 54° 58' W
	Woody growth increments	2000-2002	2° 51' S, 54° 58' W
Saleska et al 2003	Woody growth increments	2000-2002	2°51' S, 54°58' W

The GEP data was calculated as the difference between day and night tower estimates of Net Ecosystem Exchange of CO_2 (NEE), assuming no temperature effect on ecosystem respiration as no within-month correlation was observed between nighttime NEE and nighttime temperature at any sites studied. Pc (photosynthetic capacity not constrained by light) was calculated as GEP for a fixed range of PAR (725 < PAR < 925 µmol CO_2 m^{-2} s^{-1}). In this study, Monthly GEP and Pc climatologies were calculated at four sites (RJA, K67, K83, CAX) within three ecoregions (Figure 5.1). The field and flux tower observations are not implemented in the formal analysis, but are presented for comparison and interpretation of the satellite record.

5.1.8 Sinusoidal model fits to estimate ecoregion climatology

Monthly climatologies were calculated over the 2003-2011 record for TWS, VOD, LAI, EVI, and both total and direct PAR by ecoregion. We also implemented a 4-parameter sinusoidal fit (1) to the full TWS, VOD and LAI data records,

$$y_t = y_0 + a\sin\left(\frac{2\pi x}{b} + \mathrm{c}\right) \quad (1)$$

where y_t is the fitted monthly climatology value, y_0 is the mean value, a is the amplitude of the sinusoidal curve, x is the monthly increment, b is the frequency, and c is the phase shift. Although this method gives a generalized monthly climatology interpretation, it provides a phase shift parameter (c) quantifying the temporal offset between the three data sets within each ecoregion. The temporal offset in months was calculated as the phase shift difference divided by $2\pi/b$; b in all cases was equivalent to 12 months (Appendix B), confirming a yearly cycle. Model results, specifically the temporal offset between the three data sets, was confirmed by a more robust pairwise bispectral analysis (Appendix C).

5.1.9 Simplified Analysis of LAI and VOD Amazon Seasonality

As a preliminary analysis of Amazon seasonality, the VOD and LAI records from 2003-2010 were aggregated to a monthly mean climatology over evergreen broadleaf forest (EBF) dominant (>80%) 25km pixels in the Amazon region. The normalized VOD and LAI seasonal amplitudes were calculated from the monthly time series for each grid cell [(maximum-minimum)/annual mean] across the 8-year record. The VOD and MODIS LAI monthly

climatology (normalized by annual means) and monthly average precipitation (TRMM) from 2003-2010 were calculated for all EBF dominant 25km pixels having >5% VOD seasonal amplitude and located within the southern Amazon domain investigated by Morton et al. (2013) (black box Figure 5.2a).

5.2 Results

5.2.1 Initial Results of VOD and LAI Seasonality over the Amazon

While this portion of the dissertation was being conducted a contrary report was published claiming Amazon forests display no seasonality in canopy greenness and structure (Morton et al. 2013). In response to these findings we conducted a simplified analysis of MODIS LAI and AMSR-E VOD seasonality (see section 6.9), including field data of net leaf flush (Brando et al., 2010) and peaks in litterfall rates (Brando et al., 2010; Rice et al., 2004; Goulden et al., 2004), over the same Amazon region (black box, Figure 6.2a) used by Morton et al. (2013). The results of this simplified analysis show that VOD and LAI both exhibit seasonality. The apparent temporal phase difference in VOD and LAI seasonality (Figure 6.2b) follows current theories on tropical forest phenology, well demonstrated physiological mechanisms, and field level studies of canopy seasonality, as will be clarified in the results of the more specific analysis that follows. The results of this preliminary analysis were submitted (but rejected) as a Brief Communications Arising response to the journal *Nature.* The complete submittal can be found in Appendix A.

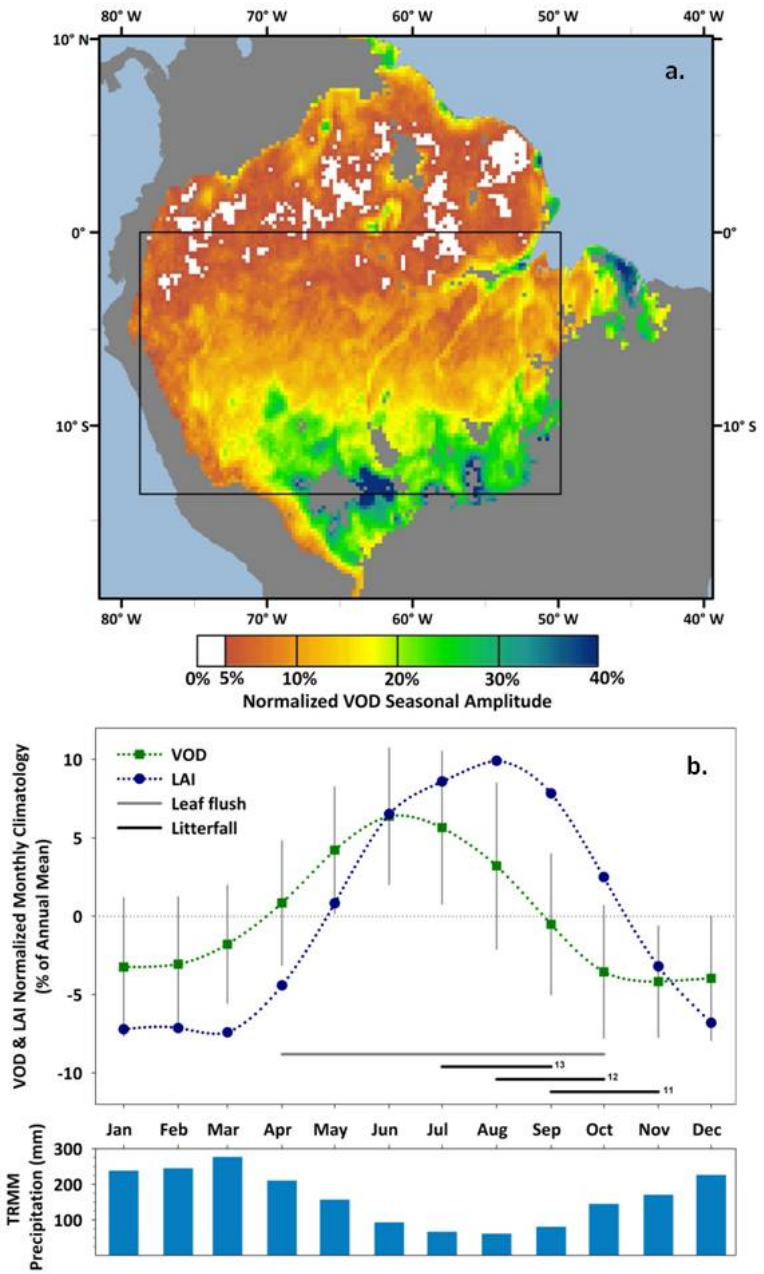

Figure 5.2. (a) Normalized VOD seasonal amplitude for all evergreen broadleaf forest (EBF) dominant (>80%) 25km pixels calculated from the monthly time series for each grid cell [(maximum-minimum)/annual mean] for the 2003-2010 record. (b) VOD and MODIS LAI monthly climatology (normalized by annual means) and monthly average precipitation (TRMM) from 2003-2010 for all EBF dominant 25km pixels having >5% VOD seasonal amplitude and located within the southern Amazon domain investigated by Morton et al. (2013) (black box in (a)). Grey vertical bars are VOD monthly climatology standard deviation. Grey and black horizontal bars denote respective months of increasing individuals with new leaves ([11] Brando et al., 2010) and months of peak litterfall from available field studies ([11] Brando et al., 2010; [12] Rice et al., 2004; [13]Goulden et al., 2004).

5.2.2 Seasonality of Amazon forests

The satellite observations, when examined over ecoregions and supported by available field and flux tower data, confirm that Amazon forest canopies exhibit seasonality (Figure 5.3).

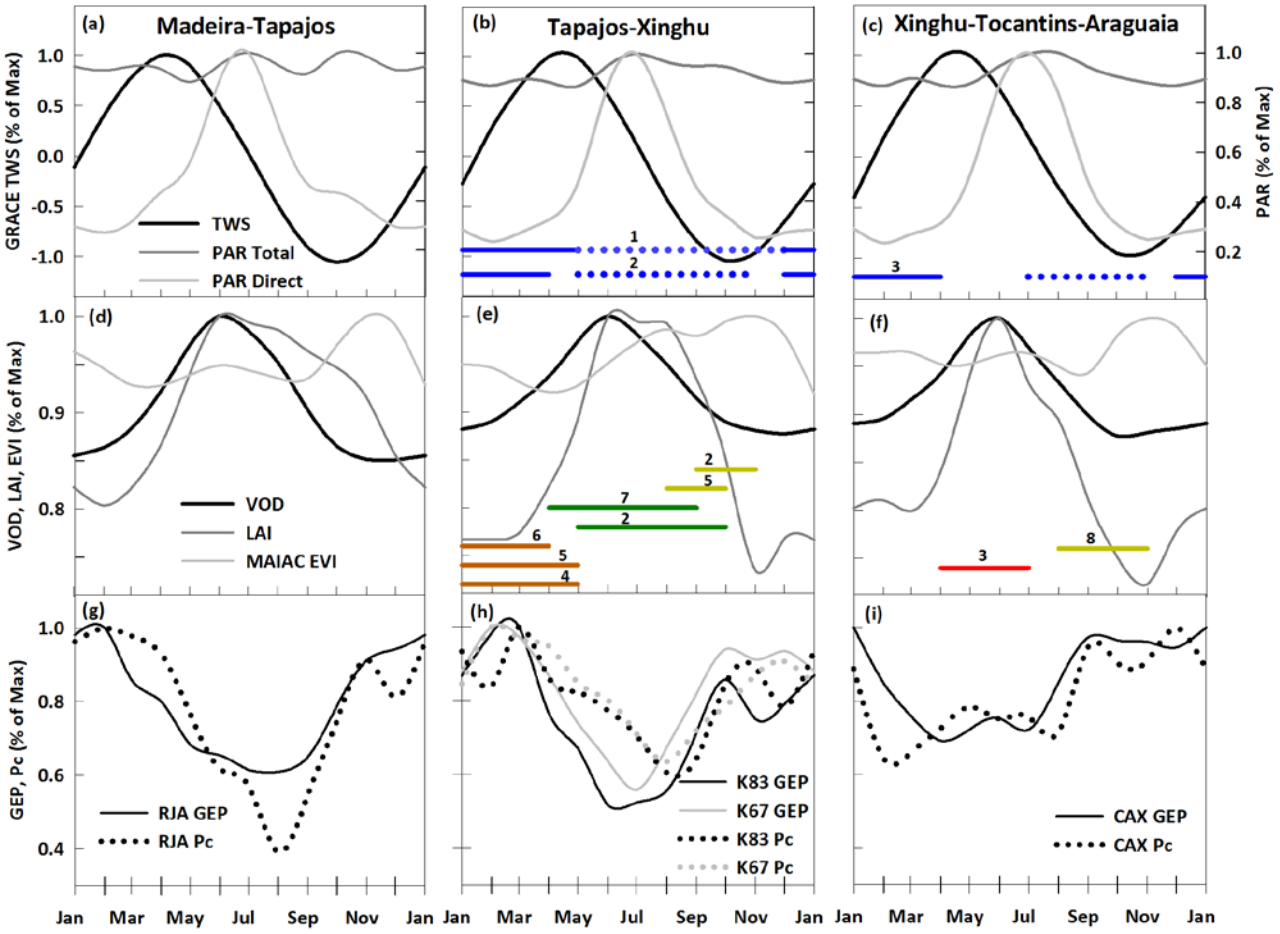

Figure 5.3. Monthly climatologies (plotted as the percentage of maximum) of satellite observations for Madeira-Tapajos (a,d,g), Tapajos-Xinghu (b,e,h) and Xinghu-Tocantins-Araguaia (c,f,i) ecoregions; satellite observations include TWS and direct and total PAR (a-c); VOD, LAI and MAIAC EVI (d-f). GEP and Pc from four flux tower sites are also presented (g-i), including Reserve Jaru (RJA), Tapajos K67 (K67), Tapajos K83 (K83) and Caxiuana (CAX) sites. Horizontal lines represent interpretations (i.e. examination of plots if specific data was not provided) of reported field data within ecoregions, including increasing (blue-solid) and decreasing (blue-dotted) PAW [1-Asner et al 2004, 2-Brando et al 2010] and soil water content [3-Fisher et al 2007]; increasing woody growth (brown) [4-Goulden et al 2004, 5-Rice et al 2004, 6-Saleska et al 2003]; increasing leaf flush (green) [2-Brando et al 2010, 7-Doughty and Goulden 2008]; peaks in leaf litterfall rates (yellow) [2-Brando et al 2010, 5-Rice et al 2004, 8-Barlow et al 2007], and increasing sap flow (red) [3-Fisher et al 2007].

The observed TWS seasonality is consistent with basin-wide model and field measurement based observations of plant available water (PAW) (Brando et al 2010, Asner et al 2004) and soil moisture (Fisher et al 2007). The observed VOD seasonality is synchronous with woody biomass increment growth (Goulden et al 2004, Rice et al 2004, Saleska et al 2003) and sap flow (Fisher et al 2007) from available field measurements. Observed LAI and VOD seasonality is well aligned with field-level leaf production increases and peaks in litterfall rates (Rice et al 2004, Barlow et al 2007, Doughty and Goulden, 2008, Brando et al 2010), while peaks in MAIAC EVI, a well-established proxy for photosynthetic C fixation, are temporally aligned with Pc and GEP from regional flux tower observations.

5.2.3 Dry, wet seasons and water availability in the Amazon

Pearson product-moment cross-correlations between TRMM precipitation and GRACE TWS at the ecoregion scale were greatest at a 2 month lag ($0.78 < R < 0.91$) for seven ecoregions and a 3 month lag ($0.89 < R < 0.91$) for two ecoregions (Table 5.2). These results confirm a reported 2 month lag between precipitation inputs and TWS across eight Amazon sub-basins (Frappart et al 2013) and a 2-3 month lag between peak precipitation and river level and stream flow observations (Marengo et al 2008).

Table 5.2. Pearson product-moment cross-correlations between monthly TRMM precipitation and GRACE TWS by ecoregion. A positive lag equates to TRMM precipitation peaking prior to GRACE TWS. *p<0.001

Ecoregion	R-value	lag (months)
Ucayali	0.78*	2
Southwest	0.91*	3
Jurua-Purus	0.87*	2
Purus-Madeira	0.89*	3
Madeira-Tapajos	0.91*	2
Tapajos-Xingu	0.88*	2
Xingu-Tocantins-Araguaia	0.87*	2
Tocantins/Pindare	0.85*	2
Maranhao Babacu	0.82*	2

Thus, seasonal minima in plant-available moisture indicated from bulk TWS changes occur months after the initial dry season (precipitation < 100mm/month) onset, which is also

confirmed by estimates and measures of plant-available water at variable soil depths (Asner et al 2004, Fisher et al 2007, Brando et al 2010). Therefore, equating dry months to periods of minimum water availability represents an oversimplification of ecosystem water dynamics and neglects hydraulic transport processes and water residence times, which can be considerable in the Amazon basin.

5.2.4 Seasonal phase shifts in TWS, VOD, and LAI

The resulting coefficients and statistics from the sinusoidal model fits are displayed in Appendix A. The sinusoidal model ecoregion climatology of TWS, VOD, and LAI each displayed seasonal phase shifts along the west-to-east moisture gradient (Figure 5.4). GRACE TWS displayed a 2 month shift in seasonal peak over the Amazon, ranging from March in the west to May in the east. VOD displayed a 1 month shift, peaking in June in the west and July in the east; LAI displayed the greatest shift of 2.5 months, with western peaks occurring in August and eastern peaks in mid-May.

The ecoregion phase shift difference between the three datasets decreased with increasing dry season across the west-to-east moisture gradient (Figure 5.4). VOD seasonality lagged TWS by a maximum of 2.8 months to a minimum of 1 month. LAI seasonality lagged TWS by 4.9 to 0.7 months. LAI seasonality lagged VOD for 5 of 9 ecoregions by 2.1 to 0.8 months, was equivalent (no lag) for one ecoregion, and preceded VOD by 0.3 to 0.8 months for the remaining two ecoregions. The phase shift differences all displayed significant negative linear relationships ($0.67 < r^2 < 0.73$; $p<0.01$) with dry season length by ecoregion (Figure 5.5), where VOD, LAI and TWS seasonal patterns are more synchronous for ecoregions with longer dry seasons.

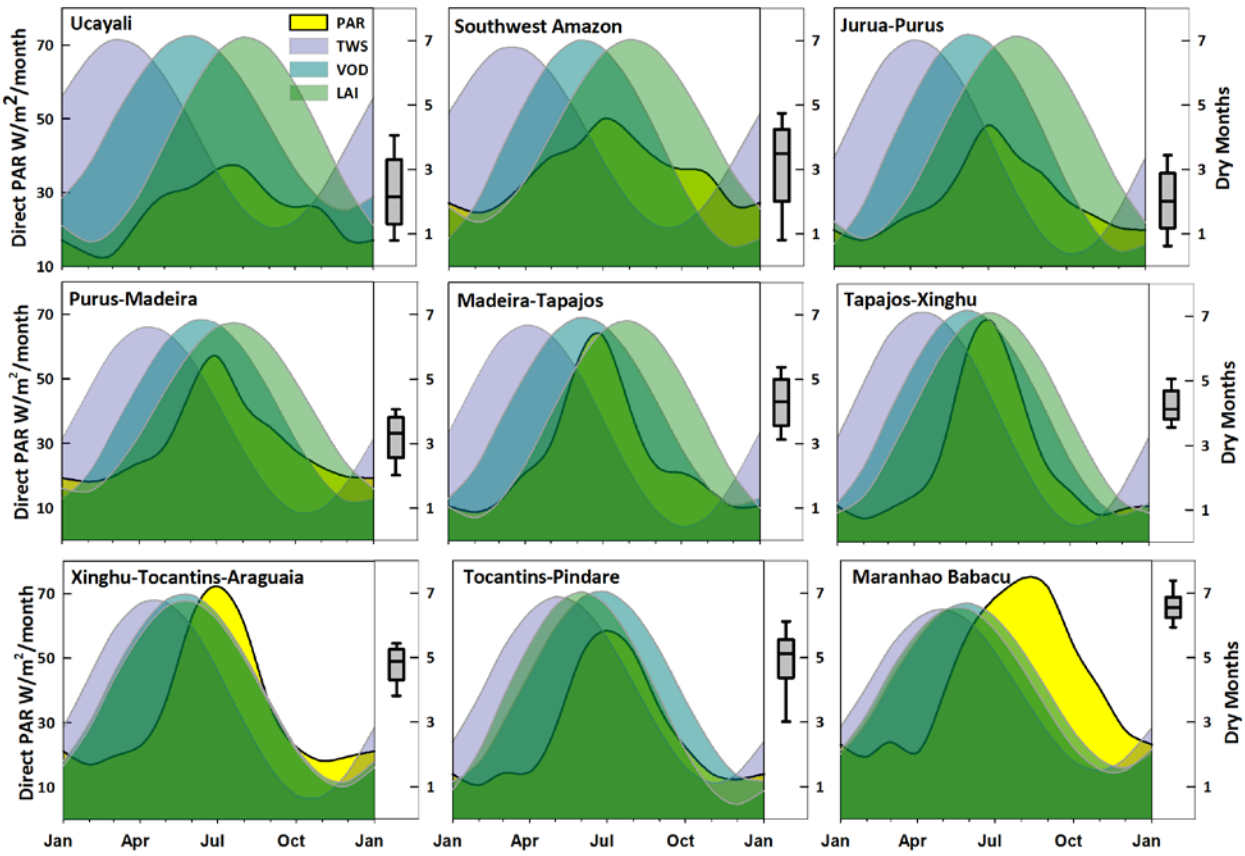

Figure 5.4. Sinusoidal model climatology for TWS, VOD and LAI; direct PAR monthly climatology and statistics (box plots) of dry months per year by ecoregion. TWS, VOD and LAI, are plotted as anomalies from the long-term means [mean value (y_0) subtracted from fitted values (y_t)], and the y-axis (not shown) for TWS, VOD, and LAI are relatively scaled for visual interpretation of phase shifts. Box plots display median, 25th and 75th percentiles, and 10th and 90th percentiles. Ecoregion plots are ordered from west (top left) to east (bottom right).

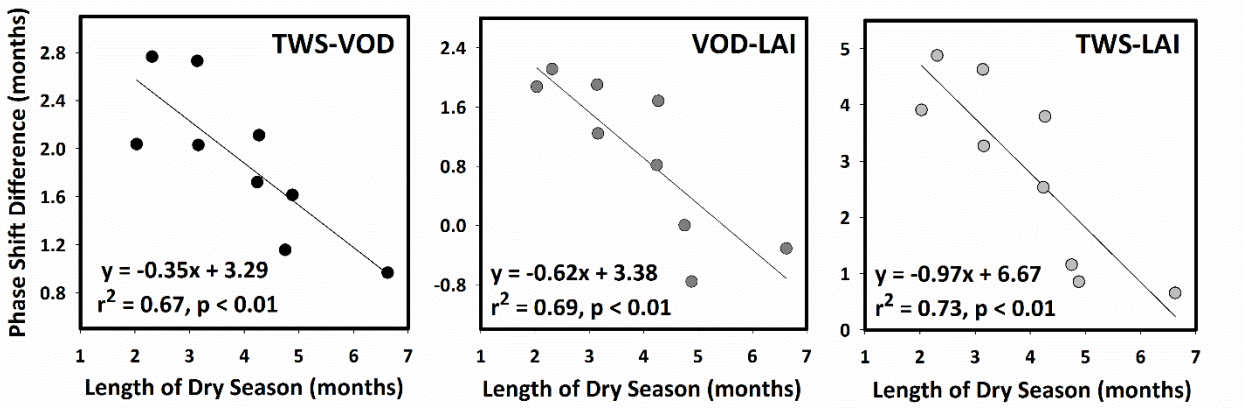

Figure 5.5. Least-squares linear regression relationships between mean dry season length from TRMM and associated phase shift differences (months) for TWS and VOD, VOD and LAI, and TWS and LAI by ecoregion.

5.2.5 Estimates of canopy phenology adaptation to light and water availability

The linear relationship between dry season length and the phase shift difference between VOD and LAI (Figure 5.5) was used to estimate relative canopy phenology adaptations to light and water availability. The mean number of dry months per pixel from the 0.25 degree TRMM data was input to the linear model to estimate expected pixel-wise phase shifts between VOD and LAI. The resulting phase shifts provide a proxy for the degree to which the timing of canopy growth and development has adapted primarily to light (maximal phase shift) or water (minimal phase shift) availability (Figure 5.6).

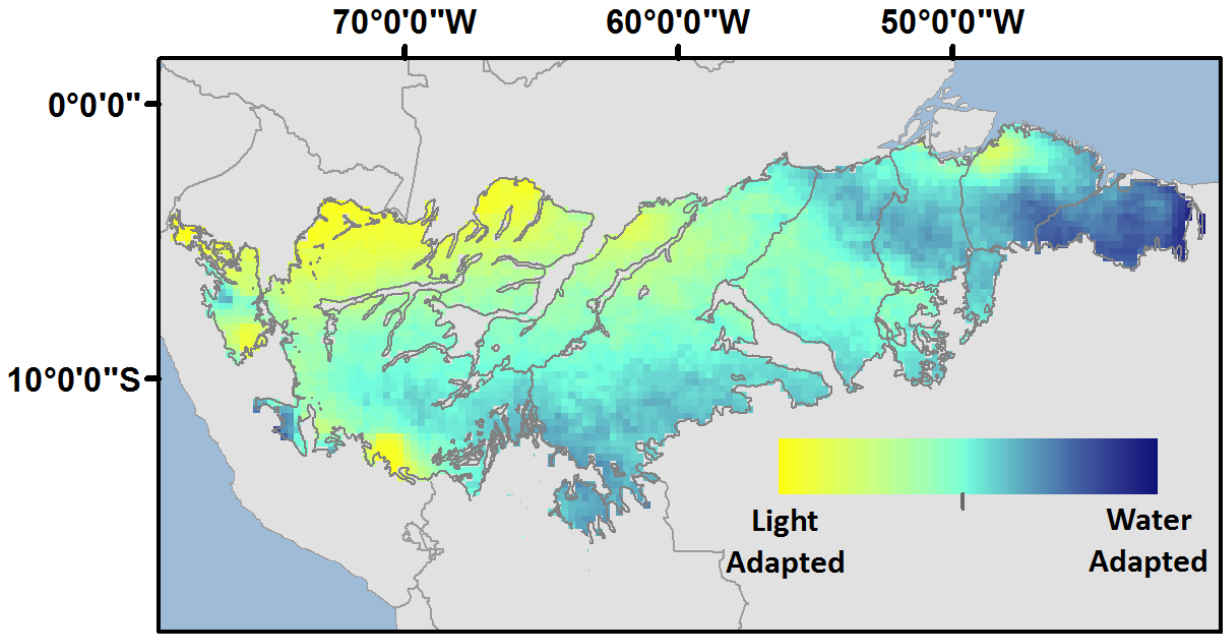

Figure 5.6. Pixel-wise (0.25 degree) relative canopy phenology adaptation to light or water availability based on the linear relationship between the mean number of dry months per pixel from TRMM precipitation, and the seasonal phase shift between VOD and LAI across ecoregions. Yellow (Blue) pixels denote areas where canopy water uptake and timing of canopy development and growth have adapted predominantly to light (water) availability, with dry season generally increasing from west to east, respectively.

5.3 Discussion

5.3.1 The transition from light-adapted to water-adapted regions

The southern equatorial Amazon ecoregions represent a west-to-east transition from predominantly light-adapted to water-adapted canopy phenology (Figure 5.6). The observed

canopy behavior supports current theories that net leaf flush is responsive to solar irradiance, but also demonstrates an adaptive response to limit drought susceptibility, even in relatively precipitation rich regions, for efficient temporal allocation of resources for wood or leaf growth. In more light-adapted western ecoregions (Figure 5.4, row 1), available water (TWS) reaches maximum levels during seasonal lows in direct PAR and allocation of resources to non-photosynthetic canopy elements is prioritized, displayed as a rise in VOD and confirmed by field measures of wet season woody growth (Goulden et al 2004, Rice et al 2004, Saleska et al 2003). The VOD rise is also consistent with canopy water content increases required for cellular expansion and new leaf formation (Pantin et al 2012). Increases in LAI (i.e. the net flush of new leaves) coincides with seasonal increases in direct PAR, representing a shift in resource allocation from woody to leaf growth. Decreasing LAI (i.e. peaks in net leaf senescence and abscission) is then observed as available water (TWS) reaches seasonal lows and canopy biomass (VOD) declines. Canopy greenness (EVI) and productivity (Pc and GEP) then rise as the new cohort of leaves reach photosynthetic maturity, which has been reported to occur up to approximately 40 days following full leaf expansion for tropical species (Niinemets et al 2012).

As dry season length increases, a general transition from light-adapted to water-adapted canopy phenology becomes apparent (Figure 5.6). For longer dry seasons (Figure 5.4, row 2), seasonal net leaf flush (LAI) becomes more synchronous with canopy biomass (VOD) increases, yet maintains comparable seasonality with direct PAR and remains somewhat decoupled from water availability (TWS). As dry season increases further (Figure 5.4, row 3) and water becomes more limiting, net leaf flush (LAI) and canopy biomass (VOD) become tightly coupled to water availability (TWS) and begin to lag direct PAR seasonality, characteristics attributable to drought-tolerant systems where water deficits, increasing temperatures and inhibitory atmosphere vapor pressure deficits coincide with seasonal peaks in direct solar irradiance.

5.3.2 Solar irradiance seasonality

Top-of-atmosphere irradiance seasonality varies with latitude and solar azimuth angle, but total PAR seasonality at the ecoregion scale displays relatively small seasonal increases, on

the order of 11-18% (Figure 5.3), due to cloud cover seasonality. The low PAR seasonality perhaps counters the theory that leaf growth is responsive to increases in irradiance, which is not obvious when examining the climatology of total PAR and LAI (Figure 5.3). However, the amount of quanta, which ultimately drives photosynthesis, can vary with no change in total PAR. Diffuse solar irradiance, enriched by blue quanta with higher energy, contains less quanta than direct irradiance with a more uniform spectral distribution (Valladares et al 2012); the photosynthetically active photon-flux density (PPFD) of diffuse irradiance will be lower than direct irradiance at equal PAR. The endogenous response that drives synchronous net leaf flush with increases in direct PAR in light-adapted systems (Figure 5.4) may be responsive to increases in PPFD associated with the transition from diffuse-dominated to direct-dominated PAR.

5.3.3 Implications for drought tolerance

In ecoregions that experience short dry seasons, net leaf flush is synchronized with direct PAR resulting in canopy leaf area peaks during periods of lowest water availability. If water availability were to decline below critical thresholds following leaf flush (i.e. drought years) would ecoregions that exhibit asynchrony between net leaf flush and water availability display greater detrimental canopy effects (e.g. lack of available water to support a new cohort of leaves) than ecoregions that exhibit net leaf flush synchronous with water availability? A study of the 2005 and 2010 Amazon droughts (Xu et al 2011), which spanned approximately 2.5 and 3.2 million km^2, respectively (Lewis et al 2011, Xu et al 2011), and were among the driest years of record based on river observations dating to 1902 (Xu et al 2011), provides context for addressing this question. Of the vegetated area that experienced significant declines in precipitation in 2010, 51% displayed significant declines in satellite observed greenness (NDVI) during July, August, September (JAS) and October, November, December (OND) composite periods. The areas affected in 2010 were located in all ecoregions used in this study, indicating that even eastern ecoregions with drought tolerant phenology (net leaf flush synchronous with available water) could not withstand the extreme water limitations. In contrast, of the vegetated area that experienced significant declines in precipitation in 2005, 14% displayed

significant declines in greenness during the JAS composite period. However, during the OND composite period western ecoregions displayed an increase in area of significant greenness decline while eastern ecoregions displayed some recovery to normal greenness. Although further research is needed, western ecoregions displaying light-adapted canopy phenology (net leaf flush asynchronous with water availability) may be more sensitive to detrimental drought effects.

5.3.4 Modeling Applications

Seasonal phase differences between canopy phenology and light and water availability indicators documented in this study may improve understanding, and parameterizations and representations, of canopy processes in regional carbon and climate models. Regions that display light-adapted canopy phenology can be weighted for greater sensitivity to solar irradiance seasonality, while regions displaying water-adapted canopy phenology can be driven primarily by water availability and estimates of rooting depth (Nepstad et al 1994) and hydraulic redistribution (da Rocha et al 2004). Investigating these phase differences at moderate spatial scales may allow for a classification scheme, whereby the driving factor of canopy phenology (whether it be water or light, or a combination thereof) is based on the phase difference between satellite derived water availability, canopy biomass, and leaf flush, as displayed in Figure 5. Such an effort would allow for more specific modeling of canopy phenology across contiguous tropical forests.

5.4. Conclusion

This study provides evidence from six independent satellite data records, and available ground observations and reported field studies, that southern equatorial Amazon forests have a distinctive canopy phenology that is responsive to seasonal changes in both water availability and solar radiation. Our results support the hypothesis that net leaf flush in tropical forests is responsive to solar irradiance seasonality, but is also responsive to variations in dry season length and associated water availability supporting vegetation growth. The timing of water availability, canopy biomass growth and net leaf flush are asynchronous in regions with short dry seasons and become more synchronous across a west-to-east longitudinal moisture

gradient of increasing dry season length. These results have important implications for modeling efforts by providing insight into the abiotic cues that influence tropical forest phenology and the temporal allocation of resources to woody versus foliar growth. They also provide a means to estimate region specific sensitivity to drought and anticipated drying under projected future climate conditions.

5.5 Acknowledgements

We thank the flux tower Principal Investigators, S. Wofsy, V. Kirchhoff, M. Goulden, H. da Rocha, M. Waterloo, A. Manzi, and L. Sa of the Large Scale Biosphere-Atmosphere Experiment in Amazonia (LBA) for making their data freely available and Alexei Lyapustin for creating the MODIS MAIAC data. We also thank S. Saleska, H. da Rocha, N. Restrepo-Coupe, A. Huete, A. Nobre, P. Artaxo, and Y. Shimabukuro for creating the publicly available LBA flux tower integrated database, Dr. Cory Cleveland for his valuable input, and the anonymous reviewers for their valuable input and suggestions which improved this manuscript. The GRACE land data (available at http://grace.jpl.nasa.gov) processing algorithms were provided by Sean Swenson, and supported by the NASA MEaSUREs Program. This portion of the dissertation was performed at the University of Montana, and the Ames Research Center with funding provided by the NASA Science of Terra and Aqua program (NNX11AD46G).

5.6 References Cited

Asner G P, Nepstad D, Cardinot G and Ray D (2004) Drought stress and carbon uptake in an Amazon forest measured with spaceborne imaging spectroscopy. *Proc. Natl. Acad. Sci. U. S. A.* **101** 6039–44 Online:

Baker I T, Prihodko L, Denning A S, Goulden M, Miller S and da Rocha H R (2008) Seasonal drought stress in the Amazon: Reconciling models and observations *J. Geophys. Res.* **113** G00B01

Barlow J, Gardner T A, Ferreira L V and Peres C A (2007) Litter fall and decomposition in primary, secondary and plantation forests in the Brazilian Amazon *For. Ecol. Manage.* **247** 91–7

Brando P M, Goetz S J, Baccini A, Nepstad D C, Beck P S and Christman M C (2010) Seasonal and interannual variability of climate and vegetation indices across the Amazon. *Proc. Natl. Acad. Sci. U. S. A.* **107** 14685–90

Chen J L, Wilson C R and Tapley B D (20100 The 2009 exceptional Amazon flood and interannual terrestrial water storage change observed by GRACE *Water Resour. Res.* **46**

Christensen J H , Hewitson B, Busuioc A, Chen A, Gao X, Held I, Jones R, Kolli R K, Kwon W-T, Laprise R, Magaña Rueda V, Mearns L, Menéndez C G, Räisänen J,Rinke A, Sarr A and Whetton P 2007. Regional Climate Projections. In: Climate Change 2007: The Physical Science Basis. Contribution of Working Group I to the Fourth Assessment Report of the Intergovernmental Panel on Climate Change [Solomon S, Qin D, Manning M, Chen Z, Marquis M, Averyt K B, Tignor M and Miller H L (eds)]. Cambridge University Press. Cambridge, United Kingdom and New York, NY, USA.

Cox P M, Harris P P, Huntingford C, Betts R A, Collins M, Jones C D, Jupp T E, Marengo J A and Nobre C A (2008) Increasing risk of Amazonian drought due to decreasing aerosol pollution. *Nature* **453** 212–5

Cox P M, Pearson D, Booth B B, Friedlingstein P, Huntingford C, Jones C D and Luke C M (2013) Sensitivity of tropical carbon to climate change constrained by carbon dioxide variability. *Nature* **494** 341–4

Doughty C E and Goulden M L (2008) Seasonal patterns of tropical forest leaf area index and CO2 exchange *J. Geophys. Res.* **113** 1–12

Fisher R A, Williams M, da COSTA A L, Malhi Y, da COSTA R F, Almeida S and Meir P (2007) The response of an Eastern Amazonian rain forest to drought stress: results and modelling analyses from a throughfall exclusion experiment *Glob. Chang. Biol.* **13** 2361–78

Frankenberg C, O'Dell C, Berry J, Guanter L, Joiner J, Köhler P, Pollock R and Taylor T E (2014) Prospects for chlorophyll fluorescence remote sensing from the Orbiting Carbon Observatory-2 *Remote Sens. Environ.* **147** 1–12

Frappart F, Ramillien G and Ronchail J (2013) Changes in terrestrial water storage versus rainfall and discharges in the Amazon basin *Int. J. Climatol.* **33** 3029–46

Frolking S, Milliman T, Palace M, Wisser D, Lammers R and Fahnestock M (2011) Tropical forest backscatter anomaly evident in SeaWinds scatterometer morning overpass data during 2005 drought in Amazonia *Remote Sens. Environ.* **115** 897–907

Goulden M and Miller S (2004) Diel and seasonal patterns of tropical forest CO2 exchange *Ecol. Appl.* **14** 42–54

Griend A A Van De, Wigneron J and Member S (2004) On the Measurement of Microwave Vegetation Properties : Some Guidelines for a Protocol *IEEE Trans. Geosci. Remote Sens.* **42** 2277–89

Guan K, Wood E F and Caylor K K (2012) Multi-sensor derivation of regional vegetation fractional cover in Africa *Remote Sens. Environ.* **124** 653–65 Online:

Huete A, Didan K, Miura T, Rodriguez E P, Gao X and Ferreira L G (2002) Overview of the radiometric and biophysical performance of the MODIS vegetation indices *Remote Sens. Environ*. 83 195–213

Jackson T J and Schmugge T J (1991) Vegetation effects on the microwave emission of soils *Remote Sens. Environ.* **36** 203–12

Jones M O, Jones L A, Kimball J S and McDonald K C (2011) Satellite passive microwave remote sensing for monitoring global land surface phenology *Remote Sens. Environ.* **115** 1102–14

Jones L A and Kimball J S (2012) Daily Global Land Surface Parameters Derived from AMSR-E. Boulder, Colorado USA: NASA DAAC at the National Snow and Ice Data Center. (http://nsidc.org/data/nsidc-0451.html)

Kim Y, Knox R G, Longo M, Medvigy D, Hutyra L R, Pyle E H, Wofsy S C, Bras R L and Moorcroft P R (2012) Seasonal carbon dynamics and water fluxes in an Amazon rainforest *Glob. Chang. Biol.* **18** 1322–34

Krinner G, Viovy N, de Noblet-Ducoudré N, Ogée J, Polcher J, Friedlingstein P, Ciais P, Sitch S and Prentice I C (2005) A dynamic global vegetation model for studies of the coupled atmosphere-biosphere system *Global Biogeochem. Cycles* **19**

Landerer F W and Swenson S C (2012) Accuracy of scaled GRACE terrestrial water storage estimates. *Water Resources Research*, **48**, W04531, 11 PP

Lee J-E, Frankenberg C, van der Tol C, Berry J A, Guanter L, Boyce C K, Fisher J B, Morrow E, Worden J R, Asefi S, Badgley G and Saatchi S (2013) Forest productivity and water stress in Amazonia: observations from GOSAT chlorophyll fluorescence *Proc. R. Soc. B-BIOLOGICAL Sci*. 280

Lee J-E, Lintner B R, Boyce C K and Lawrence P J (2011) Land use change exacerbates tropical South American drought by sea surface temperature variability *Geophys. Res. Lett.* **38**

Lee J and Oliveira R (2005) Root functioning modifies seasonal climate *Proc. Natl. Acad. Sci. U. S. A*. 102 17576–81

Lewis S L, Brando P M, Phillips O L, van der Heijden G M F and Nepstad D (2011) The 2010 Amazon drought. *Science* **331** 554

Li W, Fu R, Juárez R I N and Fernandes K (2008) Observed change of the standardized precipitation index, its potential cause and implications to future climate change in the Amazon region. *Philos. Trans. R. Soc. Lond. B. Biol. Sci.* **363** 1767–72

Lyapustin A, Wang Y, Laszlo I, Hilker T, Hall F, Sellers P, Tucker J, Korkin S (2012) Multi-Angle Implementation of Atmospheric Correction for MODIS (MAIAC). 3: Atmospheric Correction. *Rem. Sens. Environ*.

Lyapustin A, Martonchik J, Wang Y, Laszlo I, Korkin S (2011a) Multi-Angle Implementation of Atmospheric Correction (MAIAC): Part 1. Radiative Transfer Basis and Look-Up Tables, *J. Geophys. Res*., 116, D03210.

Lyapustin A, Wang Y, Laszlo I, Kahn R, Korkin S, Remer L, Levy R, Reid JS (2011b) Multi-Angle Implementation of Atmospheric Correction (MAIAC): Part 2. Aerosol Algorithm, *J. Geophys. Res*., 116, D03211.

Malhi Y, Aragão L E O C, Galbraith D, Huntingford C, Fisher R, Zelazowski P, Sitch S, McSweeney C and Meir P (2009) Exploring the likelihood and mechanism of a climate-change-induced dieback of the Amazon rainforest *Proc. Natl. Acad. Sci.* **106** 20610–5

Marengo J A, Nobre C A, Tomasella J, Oyama M D, Sampaio de Oliveira G, de Oliveira R, Camargo H, Alves L M and Brown I F (2008) The Drought of Amazonia in 2005 *J. Clim.* **21** 495–516

Moorcroft P, Hurtt G and Pacala S (2001) A method for scaling vegetation dynamics: the ecosystem demography model (ED) *Ecol. Monogr*. 71 557–85

Morton D C, Nagol J, Carabajal C C, Rosette J, Palace M, Cook B D, Vermote E F, Harding D J and North P R J (2014) Amazon forests maintain consistent canopy structure and greenness during the dry season. *Nature* 506 221–4

Myneni R B, Yang W, Nemani R R, Huete A R, Dickinson R E, Knyazikhin Y, Didan K, Fu R, Negrón Juárez R I, Saatchi S S, Hashimoto H, Ichii K, Shabanov N V, Tan B, Ratana P, Privette J L, Morisette J T, Vermote E F, Roy D P, Wolfe R E, Friedl M A, Running S W, Votava P, El-Saleous N, Devadiga S, Su Y and Salomonson V V (2007) Large seasonal swings in leaf area of Amazon rainforests. *Proc. Natl. Acad. Sci. U. S. A.* **104** 4820–3

Nepstad D C, de Carvalho C R, Davidson E A, Jipp P H, Lefebvre P A, Negreiros G H, da Silva E D, Stone T A, Trumbore S E and Vieira S (1994) The role of deep roots in the hydrological and carbon cycles of Amazonian forests and pastures *Nature* **372** 666–9

Niinemets U, Garcıa-Plazaola J I, Tosens T (2012) Photosynthesis during leaf development and ageing, In: Flexas J, Loreto F, Medrano H (eds) Terrestrial photosynthesis in a changing environment. A molecular, physiological, and ecological approach. Cambridge University Press, Cambridge, pp 353-372

Olson D M, Dinerstein E, Wikramanayake E D, Burgess N D, Powell G V N, Underwood E C, D'amico J A, Itoua I, Strand H E, Morrison J C, Loucks C J, Allnutt T F, Ricketts T H, Kura Y, Lamoreux J F, Wettengel W W, Hedao P and Kassem K R (2001) Terrestrial Ecoregions of the World: A New Map of Life on Earth *Bioscience* **51** 933

Pantin F, Simonneau T and Muller B (2012) Coming of leaf age: control of growth by hydraulics and metabolics during leaf ontogeny *New Phytol.* 349–66 Online:

Parazoo N C, Bowman K, Frankenberg C, Lee J-E, Fisher J B, Worden J, Jones D B a., Berry J, Collatz G J, Baker I T, Jung M, Liu J, Osterman G, O'Dell C, Sparks A, Butz A, Guerlet S, Yoshida Y, Chen H and Gerbig C (2013) Interpreting seasonal changes in the carbon balance of southern Amazonia using measurements of XCO 2 and chlorophyll fluorescence from GOSAT *Geophys. Res. Lett.* **40** 2829–33

Phillips O L, Aragão L E O C, Lewis S L, Fisher J B, Lloyd J, López-González G, Malhi Y, Monteagudo A, Peacock J, Quesada C a, van der Heijden G, Almeida S, Amaral I, Arroyo L, Aymard G, Baker T R, Bánki O, Blanc L, Bonal D, Brando P, Chave J, de Oliveira A C A, Cardozo N D, Czimczik C I, Feldpausch T R, Freitas M A, Gloor E, Higuchi N, Jiménez E, Lloyd G, Meir P, Mendoza C, Morel A, Neill D a, Nepstad D, Patiño S, Peñuela M C, Prieto

A, Ramírez F, Schwarz M, Silva J, Silveira M, Thomas A S, Steege H Ter, Stropp J, Vásquez R, Zelazowski P, Alvarez Dávila E, Andelman S, Andrade A, Chao K-J, Erwin T, Di Fiore A, Honorio C E, Keeling H, Killeen T J, Laurance W F, Peña Cruz A, Pitman N C a, Núñez Vargas P, Ramírez-Angulo H, Rudas A, Salamão R, Silva N, Terborgh J and Torres-Lezama A (2009) Drought sensitivity of the Amazon rainforest. *Science* **323** 1344–7

Potter C (2003) Continental-scale comparisons of terrestrial carbon sinks estimated from satellite data and ecosystem modeling 1982–1998 *Glob. Planet. Change* **39** 201–13

Restrepo-Coupe N, da Rocha H R, Hutyra L R, da Araujo A C, Borma L S, Christoffersen B, Cabral O M R, de Camargo P B, Cardoso F L, da Costa A C L, Fitzjarrald D R, Goulden M L, Kruijt B, Maia J M F, Malhi Y S, Manzi A O, Miller S D, Nobre A D, von Randow C, Sá L D A, Sakai R K, Tota J, Wofsy S C, Zanchi F B and Saleska S R (2013) What drives the seasonality of photosynthesis across the Amazon basin? A cross-site analysis of eddy flux tower measurements from the Brasil flux network *Agric. For. Meteorol.* **182-183** 128–44

Rice A, Pyle E and Saleska S (2004) Carbon balance and vegetation dynamics in an old-growth Amazonian forest *Ecol. Appl.* **14** S55–S71

Rocha H Da and Goulden M (2004) Seasonality of water and heat fluxes over a tropical forest in eastern Amazonia *Ecol. Appl.* **14** 22–32

Rowland L, Hill T C, Stahl C, Siebicke L, Burban B, Zaragoza-Castells J, Ponton S, Bonal D, Meir P and Williams M (2014) Evidence for strong seasonality in the carbon storage and carbon use efficiency of an Amazonian forest. *Glob. Chang. Biol.* **20** 979–91

Saatchi S S, Harris N L, Brown S, Lefsky M, Mitchard E T a, Salas W, Zutta B R, Buermann W, Lewis S L, Hagen S, Petrova S, White L, Silman M and Morel A (2011) Benchmark map of forest carbon stocks in tropical regions across three continents. *Proc. Natl. Acad. Sci. U. S. A.* **108** 9899–904

Salazar L F, Nobre C a. and Oyama M D (2007) Climate change consequences on the biome distribution in tropical South America *Geophys. Res. Lett.* **34**

Saleska S R, Miller S D, Matross D M, Goulden M L, Wofsy S C, da Rocha H R, de Camargo P B, Crill P, Daube B C, de Freitas H C, Hutyra L, Keller M, Kirchhoff V, Menton M, Munger J W, Pyle E H, Rice A H and Silva H 2003 Carbon in Amazon forests: unexpected seasonal fluxes and disturbance-induced losses. *Science* **302** 1554–7

Samanta A, Knyazikhin Y, Xu L, Dickinson R E, Fu R, Costa M H, Saatchi S S, Nemani R R and Myneni R B (2012) Seasonal changes in leaf area of Amazon forests from leaf flushing and abscission *J. Geophys. Res.* **117** 1–13

Silva F B, Shimabukuro Y E, Aragão L E O C, Anderson L O, Pereira G, Cardozo F and Arai E (2013) Corrigendum: Large-scale heterogeneity of Amazonian phenology revealed from 26-year long AVHRR/NDVI time-series *Environ. Res. Lett.* **8** 029502

Swenson S C and Wahr J (2006) Post-processing removal of correlated errors in GRACE data, *Geophys. Res. Lett*., **33**, L08402

Thomas A and Reager J (2014) A GRACE-based water storage deficit approach for hydrological drought characterization *Geophys. Res. Lett.* 1537–45

Valladares F, García Plazaola J I, Morales F, Niinemets U (2012) Photosynthetic responses to radiation. In: Flexas J, Loreto F, Medrano H (eds) Terrestrial photosynthesis in a changing environment. A molecular, physiological, and ecological approach. Cambridge University Press, Cambridge, pp 239–256

Van De Griend A A and Wigneron J (2004) On the Measurement of Microwave Vegetation Properties: Some Guidelines for a Protocol *IEEE Trans. Geosci. Remote Sens*. 42 2277–89

Schaik C van, Terborgh J and Wright S (1993) The phenology of tropical forests: adaptive significance and consequences for primary consumers *Annu. Rev. Ecol*. 24 353–77

Wielicki B, Barkstrom B, Harrison E, Lee III R, Smith G, Cooper J (1996) Clouds and the Earth's Radiant Energy System (CERES): An earth observing system experiment *Bull. Am. Meteorol. Soc*. **77** 853–68

White M A, Thornton P E, Running S W and Nemani R R (2000) Parameterization and Sensitivity Analysis of the BIOME – BGC Terrestrial Ecosystem Model : Net Primary Production Controls *Earth Interact.* **4**

Wright S J and Schaik C Van (1994) Light and the phenology of tropical trees *Am. Nat.* **143** 192–9

Wright S J (1996) Phenological Responses to Seasonality in Tropical Forest Plants, Tropical Forest Plant Ecophysiology SE - 15 Eds. S Mulkey, R Chazdon and A Smith (Springer US) pp 440–60

Xiao X, Zhang Q, Saleska S, Hutyra L, De Camargo P, Wofsy S, Frolking S, Boles S, Keller M and Moore B (2005) Satellite-based modeling of gross primary production in a seasonally moist tropical evergreen forest *Remote Sens. Environ.* **94** 105–22

Xu L, Samanta A, Costa M H, Ganguly S, Nemani R R and Myneni R B (2011) Widespread decline in greenness of Amazonian vegetation due to the 2010 drought *Geophys. Res. Lett.* **38** 2–5

Chapter 6. Development of Climate Indicators for National Climate Assessments

The work presented in this chapter outlines a set of Vegetation Health Climate Indicators for inclusion in the National Climate Assessment (NCA) Indicator System that will be relevant to land managers, policy makers and the public across a wide range of sectors. The NCA, mandated by Congressional Legislation with the Global Change Research Act of 1990, and carried out by the US Global Change Research Program (USGCRP), is working to develop a sustainable Climate Indicator System that is scientifically vetted, continually updated, and enhanced at each iteration. The National Climate Indicators are meant to be easily interpretable, highly policy relevant indicators of key measurements of physical, ecological and societal metrics of the nation's condition.

In September of 2013, the National Climate Assessment Development Advisory Committee (NCADAC) published the "*Report on Preparing the Nation for Change: Building on Sustained National Climate Assessment Reports*" (Janetos, et al., 2012). In that report the NCADAC called for the creation of an indicator system to more coherently assess climate changes, impacts, vulnerabilities, opportunities, and preparedness that will allow; better evaluation of changes from an established baseline over time, inter-comparison of changes between different regions and environments, improved scientific understanding of thresholds and tipping points, and expanded access to easily-interpretable, decision-relevant information. The indicators developed for this portion of the dissertation meet the components outlined in that report by providing: deviations from a "normal" or baseline historical state; wall-to-wall national maps at high spatial resolution to allow for inter-comparisons at national, regional, and local scales; and easily-interpretable maps and graphs with intuitive common color palettes that provide information on the health of ecosystems relevant to public interests and decision makers.

More recently (February 2014), the NCADAC released the "*National Climate Indicators System Report*" (Kenney et al., 2014) that outlines the system or sector topics for the development of Indicators, and the criteria for the selection of Indicators for inclusion in sustained NCAs. The Indicators detailed here are directly applicable to many of the system and sector topics outlined including; Agriculture, Forests, Grasslands-Rangelands-Pastures, Seasonal

Timing and Phenology, and Water Cycle and Management. The Indicators also meet all the selection criteria as they are scientifically defensible, scalable, directly related to climate, nationally important, built on existing agency efforts, and linked to the conceptual framework as originally proposed in the "*Indicators System Technical Input Report to the National Climate Assessment*" (Buizer et al., 2013).

6.1 Approach and Methods

The Indicators focus on three primary components responsive to the climate system; carbon sink/source dynamics, vegetation health, and water balance. The carbon and vegetation health indicators implement annual and seasonal ecosystem productivity from the MODIS Net and Gross Primary Productivity (NPP, GPP) products (Running et al., 2004; Zhao et al., 2005; Zhao & Running, 2010). The water flux indicator is derived from the MODIS Evapotranspiration (ET) product (Mu et al., 2007; Mu et al., 2011). All of the indicators are based on science algorithms and global data records developed and refined by the Numerical Terradynamic Simulation Group (NTSG) at the University of Montana in partnership with NASA. Implementation of the data records will include the documented estimates of precision and uncertainty for each data set, which will be carried forward into Indicator algorithm development. These estimates of precision and uncertainty, and how they are implemented in the Indicator algorithm, will be provided in the corresponding metadata and documentation to allow for traceability of each Indicator to its native data product(s). Together, these indicators represent an overall assessment of ecosystem and vegetation health based on tangible concepts of short- and long-term vegetation health and growth, and water balance. Concepts that decision makers and users at all levels can understand.

This work utilizes the ongoing 14+ year MODIS record to build nationally complete and geo-spatially accurate annual anomaly maps in identical format from this suite of scientifically vetted, freely available products that are scheduled for continual production. All indicators are calculated on a pixel-wise basis at the native resolution of the data product ($1km^2$). Although some of the resulting maps presented here focus on the contiguous U.S., the Indicators include Alaska, Hawaii, Puerto Rico, and the Virgin Islands. The input products are listed in Table 1,

including planned products from the recently launched VIIRS sensor that will allow for future production of the proposed indicators.

Table 6.1. Input products for the creation of the proposed Indicators; inclusive of planned VIIRS products that would allow for future production of the Indicator suite.

Data Product	Sensors	Time Span
Gross Primary Productivity	MODIS	2000-present
	VIIRS	2011-present
Net Primary Productivity	MODIS	2000-present
	VIIRS	2011-present
Evapotranspiration	MODIS	2000-present
	VIIRS	2011-present

The Indicators also have direct connections to the third NCA, the Pilot National Climate Indicator System (due for release in June 2015) and Indicator development projects funded by the ROSES 2012 A.47 NASA program, which will allow for integration and collaboration across projects to help create a comprehensive and coherent Indicators system. After the description of each Indicator, connections to the NCA Pilot and NASA Indicators are provided. The Indicators also address potential gaps in the current NCA Pilot Indicators System. The system currently provides two indicators on vegetation productivity, a Forest Growth/Productivity Indicator and a Crop Production Indicator, which obviously neglect grassland, shrubland, savanna and woody savanna systems and does not provide a means to compare vegetation responses to climate across land covers and on a national scale. The GPP and NPP Indicators, presented as wall-to-wall national maps (inclusive of Alaska, Hawaii, Puerto Rico, and the Virgin Islands), fill this gap. The current Pilot System also lacks an intra-seasonal national scale indicator related to vegetation or ecosystem health. While the NPP indicator provides a proxy for this, the seasonal status of vegetation may not be discernable through a measure of its yearly NPP; a system in steady-state may display no gain or loss in productivity. The GPP indicator alternatively provides a more direct measure of the seasonal status of vegetation (at 8-day intervals) and its intra-annual variability.

6.2 Carbon and Vegetation Health Indicators of Net and Gross Primary Productivity

Net Primary Production (NPP) is the annual growth of all plant material on a unit of land. Both NPP and GPP are key carbon indicators of environmental health and ecosystem services, including food, fiber, and fuels supporting national economies, human sustainability and quality of life. A global annual calculation of terrestrial NPP is being continuously produced since 2000 by the NASA Earth Observing System MODIS Land Science team (Running et al., 2004; Zhao et al., 2005; Zhao & Running, 2010). The algorithm combines MODIS vegetation data with daily global meteorology to map NPP at 1km^2 resolution. The NPP product provides global estimates of carbon source/sink dynamics and vegetation response to climate. This indicator is calculated on an annual basis (coincident with the production of the NPP product), as pixel-wise anomalies from each pixel's long-term data record mean.

$$\text{NPPAnomaly}_{\text{annual}} = \text{NPP}_{\text{current year}} - \text{NPP}_{\text{data record mean}} \quad (1)$$

Results of this indicator highlight the spatial resolution and variability of vegetation productivity at a national scale (Figure 6.1). The indicator fits particularly well into the regional views format provided by the current NCA and Pilot Indicators System, displaying how changes in climate can have dramatic effects within and across regions.

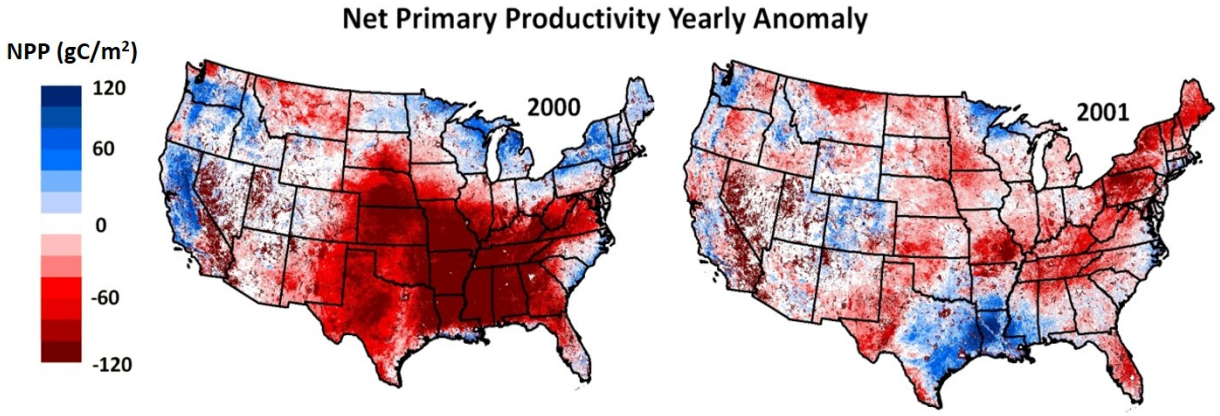

Figure 6.1. Yearly maps of the Net Primary Productivity Indicator for years 2000 and 2001. The NPP anomaly is calculated as the given year's difference from the full data record (2000-2013) mean.

In addition to maps, national and regional summary plots of the NPP Indicator are provided. Figure 6.2 displays a sample of a national summary plot showing the percentage of area above or below the long-term mean and the sum of national NPP by year. Providing the indicators in both geographic and summary plot formats is essential. The maps allow for local and regional assessments necessary to specific end users (land managers, agricultural interests, etc.) and the summary plots provide a broad overview useful to national scale policy makers.

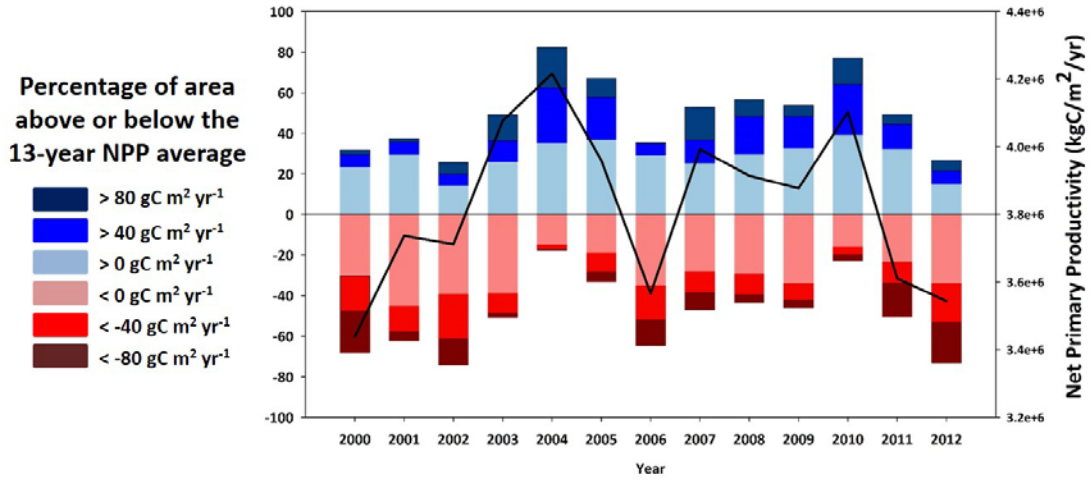

Figure 6.2. Summary plot of the NPP Anomaly displaying the percent of area (bars) in the contiguous U.S. above or below the long-term mean, in 20gC m^{-2} increments. Included is the sum of national NPP (black line) by year.

NPP Indicator – Connection to NASA Indicators (NI) and NCA Pilot Indicators (PI): The NPP Indicator is relevant to a wide array of NIs and PIs and can enhance Indicator development and application. As a measure of net CO_2 source or sink strength of the vegetated land surface it can inform Global Atmospheric Concentrations of CO_2, Annual Terrestrial Net CO_2 Emissions, Forest Growth and Productivity PIs, and be coupled with Drought Indicators (the PDSI PI and the Resilience to Extreme Climate Events NI) to monitor drought impacts on growth. It can also be used in concert with the Forest Area Extent and Grassland, Rangeland, Pastureland Extent PIs, and the Land Cover Indicators NI, as changes in land cover and the spatial extent of specific biome types have direct impacts on productivity. NPP also has direct connections to the Crop

Condition, Progress, and Production PI, and the Agricultural Productivity Indicator Analysis System NI.

Gross Primary Production (GPP) of vegetation is the amount of C fixed during photosynthesis, which is directly affected by climatic factors (temperature, light and water availability) and disturbance regimes (wildfire, drought, landslides, etc.). The high temporal (8-day) and spatial ($1km^2$) resolution of the MODIS GPP product (Running et al., 2004; Zhao et al., 2005) provides a near real time measure of vegetation response to local climate conditions and a proxy for ecosystem health. This indicator is calculated every 8 days (coincident with the production of the GPP product), as pixel-wise anomalies from the long-term pixel mean of the same 8-day period across the entire data record.

$$GPPAnomaly_{\text{8-day period}} = GPP_{\text{8-day period}} - GPP_{\text{8-day period data record mean}} \quad (2)$$

Results provide insight on the value of these data as a tool for near-real time monitoring of vegetation status in response to climate and extreme events including wildfire or drought. Figure 6.3 displays the GPP Indicator for an 8-day period in 2004 over Alaska, including documented wildfire perimeters that burned in 2004 (Jones et al., 2013). The GPP anomalies in the years following fire provide estimates of vegetation productivity recovery to pre-fire levels and also highlight intra-seasonal variability. These anomalies can also aid land managers and agricultural interests in addressing specific questions such as; is this year's spring growth comparable to previous years? Are negative autumn anomalies indicating drought conditions for vegetation?

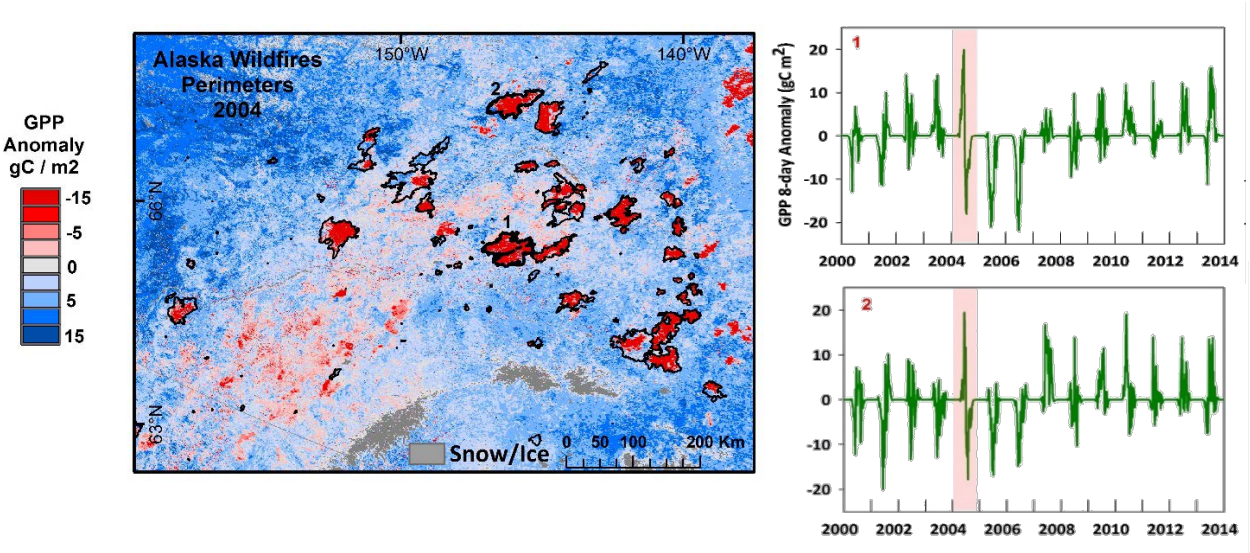

Figure 6.3. Map of the MODIS GPP Anomaly for the July 20-27, 2004 period with year 2004 Alaska fire perimeters (black polygons). Time series (8-day) plots of GPP Anomaly means from 2000 to 2013 within the two labeled fire perimeters (1,2). Pink bar is year of fire.

GPP Indicator – Connection to NASA Indicators (NI) and NCA Pilot Indicators (PI): The GPP Indicator can help to inform the Wildfire Effects-Burned Area PI (as demonstrated above) and both the Forest Growth and Productivity PI and Agricultural PIs and NIs by providing essential information on the seasonal peaks and troughs in productivity which can inform land management decisions and crop planting and harvest timing.

6.3 Water Focused Evapotranspiration Indicator

Terrestrial ET includes evaporation from wet and moist soil, from rain water intercepted by the canopy, and transpiration through stomata on plant leaves and stems. The MODIS ET product (Mu et al., 2007; Mu et al., 2011) can be used to calculate regional water and energy balance, and soil water status providing key information for water resource management. With long-term ET data, the effects of changes in climate, land use, and ecosystem disturbances (e.g. wildfires and insect outbreaks) on regional water resources and land surface energy change can be quantified. The ET indicator will be calculated on an annual basis (coincident with the production of the annual MODIS ET product), as pixel-wise anomalies from the long-term pixel's data record mean.

$$ETAnomaly_{annual} = ET_{current\ year} - ET_{data\ record\ mean} \quad (3)$$

Initial production of this indicator over North America is shown in Figure 6.4 demonstrating its applicability for both national assessments of water status and drought conditions (e.g. 2002) and examination of regional variability.

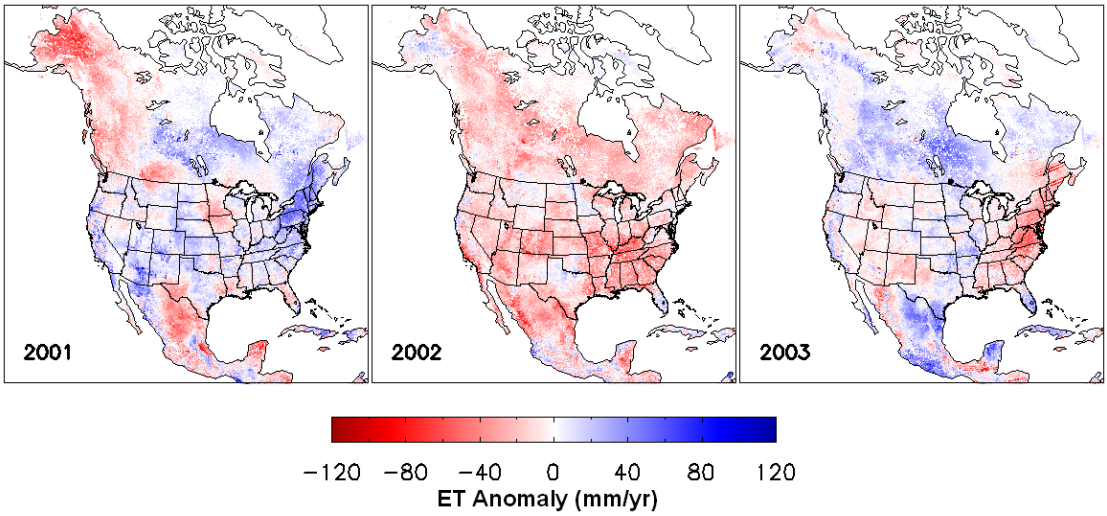

Figure 6.4. North America annual ET anomalies (2001, 2002, 2003) relative to a six year (2001-2006) average.

ET Indicator – Connection to NASA Indicators (NI) and NCA Pilot Indicators (PI)*:* The ET Indicator provides a broad summary of ecosystem scale water fluxes with direct connections to the Water Cycle and Management PIs of Precipitation and Streamflow. It could also be closely coupled to water based NIs such as the Water Cycle Intensification Indicator, Land Surface Water State Indicator, and Regional Resilience to Extreme Climate Events Indicator. The underlying satellite data and daily surface meteorology used for ET production is also fully consistent with the proposed national Carbon Indicators for GPP and NPP.

6.4 Planned Production of Indicators

The work detailed in the previous sections was conducted in response to a funded project entitled “Translating EOS datasets into National Ecosystem Biophysical Indicators” as part of the NASA ROSES 2012 A.47 “Development and Testing of Potential Indicators for the National Climate Assessment” program. The results demonstrated a successful ‘proof of

concept' to NASA program managers and the NCADAC. In April 2015, the NCADAC selected the GPP and NPP Indicators for inclusion in the Pilot Indicators system with possible inclusion in future NCAs. In response to this selection we are developing a production work plan that will capitalize on a partnership with the NASA Earth Exchange (NEX) and incorporate end-user feedback. Step-by-step processes for the creation of Indicators will also be provided to the NCADAC to allow for independent production of the Indicators.

The workflow will exploit Enabling Tools provided by NEX. Following the initial development and production of Indicators, the algorithms and operational code will be transferred to and implemented within NEX for sustained future production of the Indicators and for access by the user community. NEX provides an ideal platform for engaging the NCA community, disseminating results to a broader audience, and a complete work environment in which users can explore and analyze large Earth science data sets, run modeling codes, and collaborate on projects. Including our proposed Indicators work as a NEX Project will allow multiple user communities to capitalize on the NEX analytical tools and data stores to both explore the Indicators in detail and build upon our work to derive their own indicators to suit specific needs or applications.

The goal of the work plan is to develop a fully automated processing stream utilizing the data and computing resources on NEX. The flowchart (Figure 6.5) displays the workflow. The initial work of data quality control, algorithm development and refinement, mosaic and masking techniques, and test outputs of mapped indicators and plots will be conducted within the Numerical Terradynamic Simulation Group at the University of Montana. The algorithms for each Indicator will be developed independently in this initial stage by iterating on data quality control applications, algorithm development, and product development. The test products will be evaluated and provided to end users for feedback, specifically Regional and State Climate Centers and Offices (see Section 6.5). Based on this feedback, refinements on the algorithms and end products will be incorporated until a final processing stream is established. After this initial phase, the algorithms will be transferred to the NEX where they will be refined into an operational status to ingest the MODIS data products and produce the mapped Indicators. We will also develop and iterate on different versions of summary statistics and

plots. We will seek input from data presentation specialists and interested users to determine the best format for these plots that will most easily convey information to land managers, policy makers, and the general public.

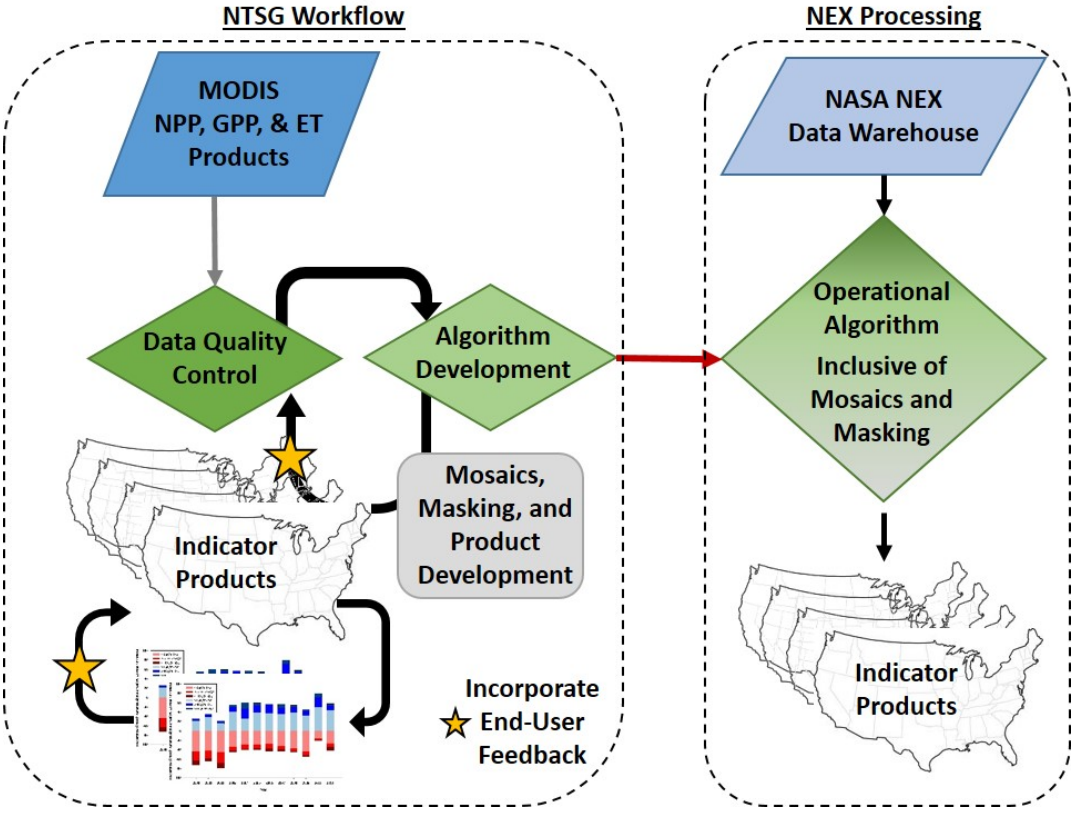

Figure 6.5. Workflow diagram for production of Indictors. Iterative algorithm development and product creation will take place at NTSG at the University of Montana. Initial products will be distributed to end-users for feedback which will be incorporated throughout the iterative process. The operational algorithm will then be transferred to NEX for automated processing.

6.5 Incorporating End-User Feedback

This suite of Indicators provides critical information on hydrologic and vegetation responses to a changing climate and are therefore applicable to decision makers across a wide range of sectors and environments. We anticipate a host of end-users across Federal Agencies (e.g. USFS, USDA, BLM), state and local governments, and many of the sectors defined in the National Climate Assessment (Water; Energy; Agriculture; Forests; Ecosystems; Energy, Water, and Land; Land Use and Land Cover Change; Biogeochemical Cycles). It is therefore difficult to pinpoint which user communities and sectors will find these Indicators most valuable and

applicable to their needs, which is why we plan to incorporate feedback from a wide array of user-communities in the development of the final products. We will capitalize on the well-established network of regional and state level Climate Centers and Offices. These Centers and Offices shape and coordinate their data distribution efforts to meet the needs most applicable to their regional and local interests; such as agricultural interests in regions where crops are a dominant part of the economy, or forestry interests in states where the development of policy in regards to logging procedures or wildfire prevalence is of greatest concern. We will first work with the Montana Climate Office, located at the University of Montana, to gain insight into the data formats and presentation styles most useful to a Climate Office and community stakeholders. The first iteration of Indicators will then be provided to Regional and State Climate Centers and Offices through The American Association of State Climatologists. We will request feedback on which Indicators are most applicable to end-users within each region and state, and then incorporate this feedback in the iterative process of algorithm and product refinement. This method of distribution and collection of feedback will allow us to refine the Indicators to meet the needs of specific end-users, as we cannot presume that one size fits all.

6.6 Summary

The established and well-vetted long term NASA EOS MODIS science data products of NPP, GPP, and ET, provide an ideal dataset for the creation of Indicators for the National Climate Indicator System. The work presented here and resulting GPP and NPP Indicators were recently (March 2015) selected by the NCADAC to be part of the NCA Pilot Indicator System. Work on this project is therefore ongoing and detailed step-by-step instructions for the creation of Indicators will be provided to the NCADAC in the coming months.

6.7 Development of Alternative Indicator Visualizations

Developing innovative methods to display the Climate Indicators was, initially, a primary component of the Indicator development process. The goal was to provide graphic representations of the Indicators that were easily interpretable by policy makers and the general public, with an emphasis to avoid the standard plots and maps that are common to scientific publications. I therefore developed multiple methods to display the information,

ranging from relatively standard maps and plots to more unconventional versions. Below is a collection of those visualizations along with explanations of the aims and approach that drove their creation. Note: Some of the visuals include Indicators beyond the GPP, NPP, and ET Indicators described above and were included to establish that a common visualization could be used across a range of data products.

First, plots and maps were developed to highlight the variability of NPP across geographic regions while maintaining a national view. Figure 6.6 displays the yearly time series of NPP anomalies for both the U.S. (filled area) and the contribution of each region (gray bars).

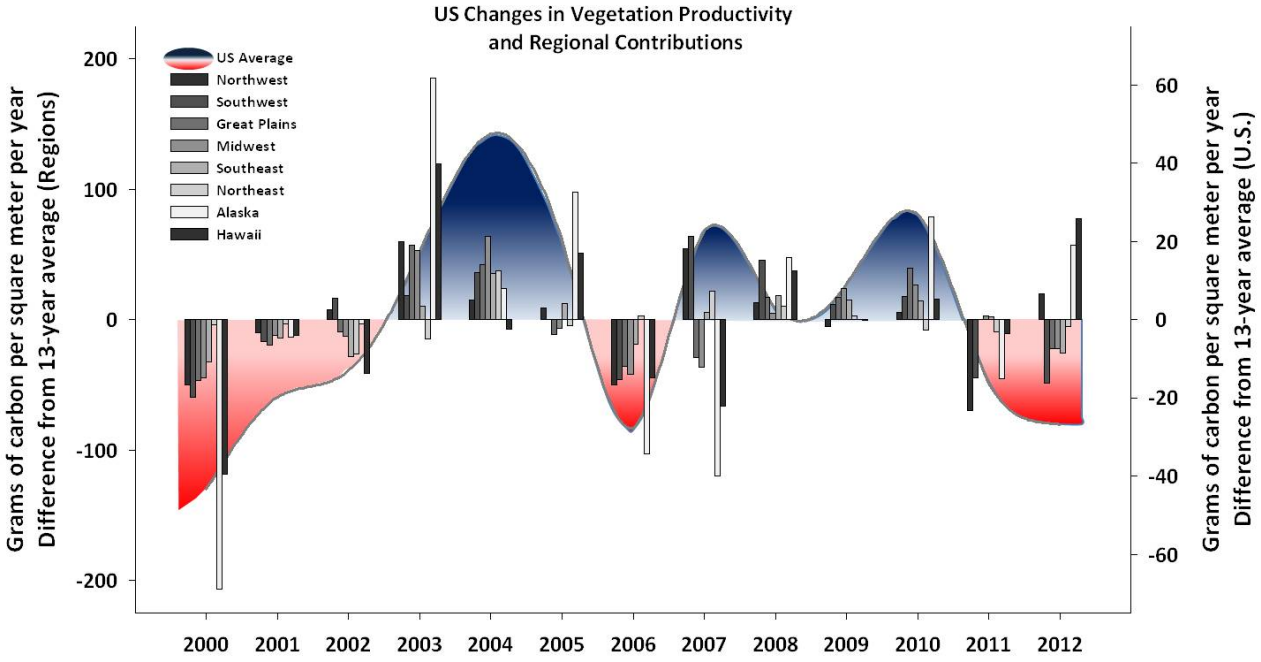

Figure 6.6. Yearly NPP anomalies from the long-term mean for both the total U.S. (filled areas) and by regions (bars), providing a proxy to determine regional contributions to the overall U.S. NPP anomaly.

The same approach was then applied to a map format that incorporates region specific plots. Figure 6.7 provides time series area plots, both of the entire U.S. and also by region. The area plots are simplified (no units displayed) whereby the reference lines of 50 gC/m^2 and -50 gC/m^2 (displayed in the U.S. plot) are maintained across each plot allowing for a quick reference as to how each specific region compares to the U.S. average. Figure 6.8 provides a similar approach, but each year is depicted as an incremental bar, colored either red (a decrease as compared to

the previous year) or green (an increase from the previous year). In this format, NPP is cumulative through time, whereby even though a specific year (bar) may indicate a positive anomaly (green color) relative to the previous year, it may still lie below the reference line. This method provides a proxy of vegetated land surface C depletion or accumulation through time.

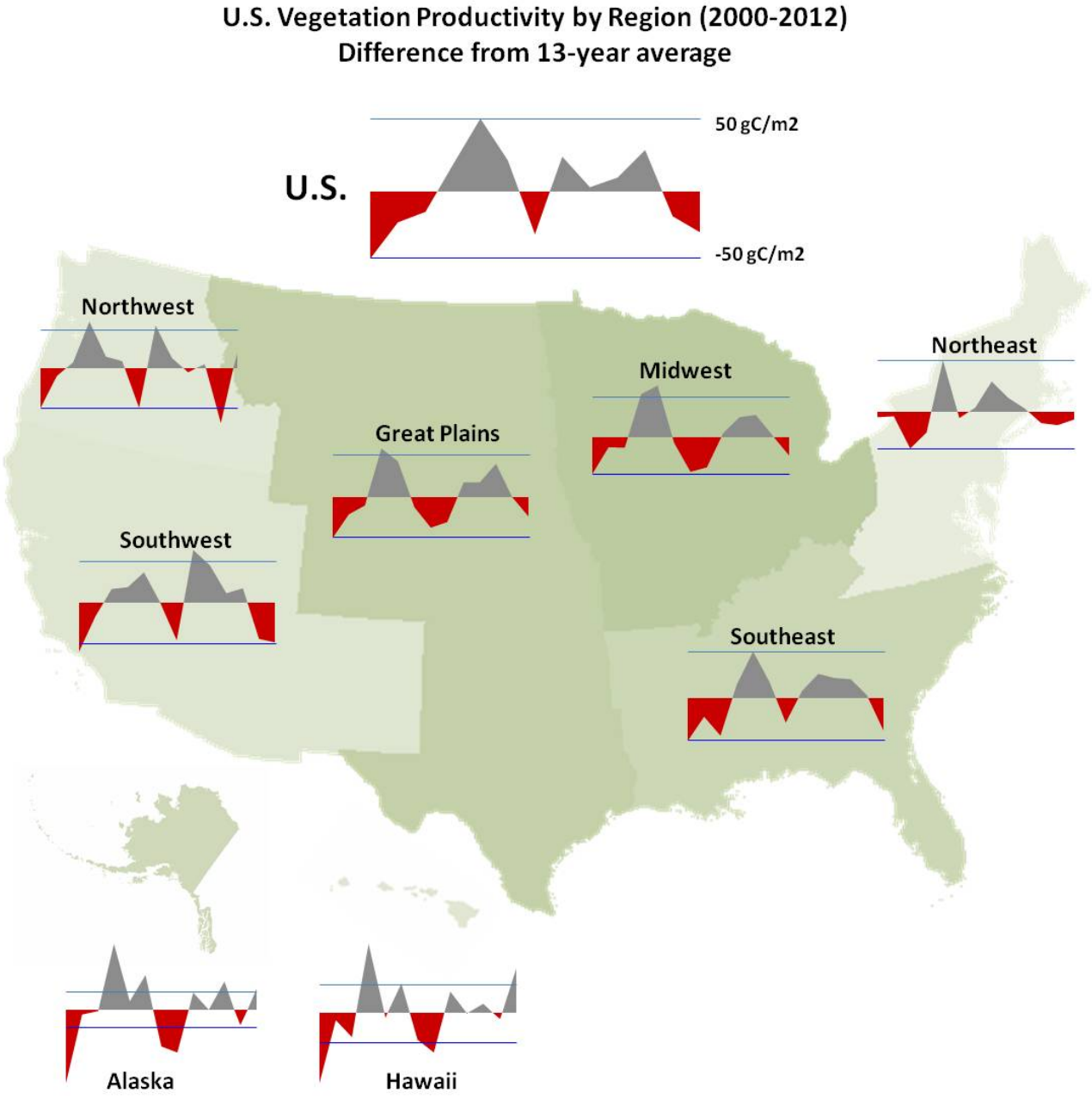

Figure 6.7. Yearly NPP anomalies from the long-term mean for both the total U.S. and by region. The 50 gC/m^2 and -50 gC/m^2 reference lines (displayed in the U.S. plot) are maintained across each plot.

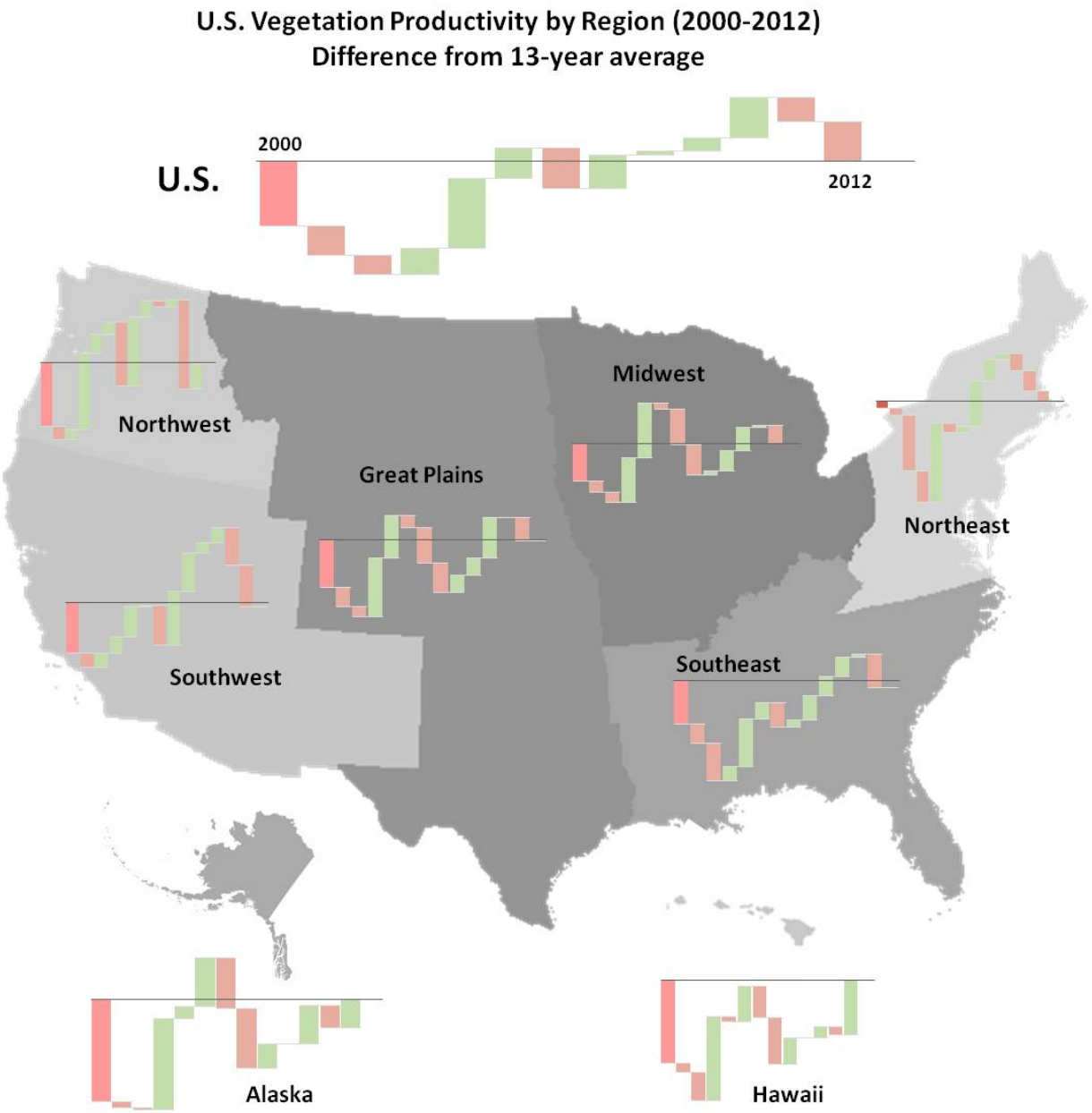

Figure 6.8 Yearly NPP anomalies from the long-term mean for both the total U.S. and by region displayed as cascade plots representing accumulation or depletion of NPP through time.

The next set of visualizations attempted to move away from any standard scientific map or plot to provide a quick reference of the status of the Indicator, along with some detailed data information. These were constructed to fit within the column of a newspaper and resemble common financial indicators (e.g. stock market trends or commodity prices).

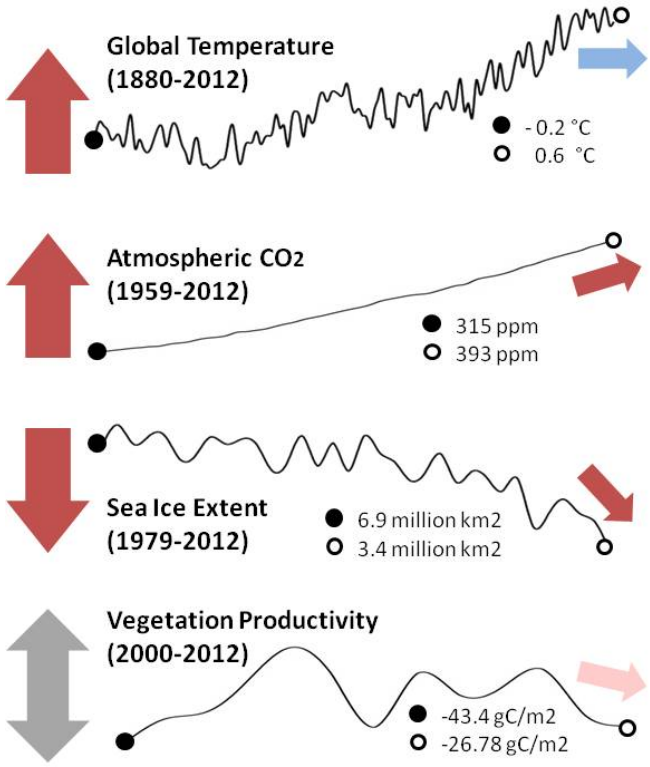

Figure 6.9. Experimental summary figure of four Climate Indicators (Global Temperature, Atmospheric CO2, Sea Ice Extent, Vegetation Productivity). The figure aims to provide a synopsis of long (large arrows) and short (small arrows) term trends, the degree of concern related to those trends (arrow color), the first and most current measures, and the time series. The condensed figure is formatted to fit in a newspaper column or on the borders of a webpage and resemble common financial indicators (e.g. stock market trends, commodity prices).

Bold arrows at left indicate overall trend in the indicator and the color represents the level of concern from a climate change perspective (red = high concern; grey = minimal concern; blue = no concern or conditions are improving). Lines represent the data record through time with the past first recorded and current year values indicated by the closed and open circles (respectively). Small arrows represent the recent short-term (5-year) trend which are also colored based on the red to blue level of concern from a climate change perspective. Once the reader becomes familiar with this format, they can ingest it quickly focusing on three elements (large arrow, name of indicator, small arrow) providing a quick synopsis of the status. A problem with this however is that the large arrow is based on long-term data and is not likely

to change within the next 5-10 years. It will begin to look very static over time as though no real significant change is taking place.

The visualization in Figure 6.9 was then distilled even further to provide only essential information on the Indicator (Figure 6.10) with equal visual weighting to the long-term trend, the 5-year trend and the current year's status. Bold arrows provide the long, short and near-term status of the Indicator; arrow direction indicates if the variable is increasing or decreasing and color represents the level of concern. Lines provide the actual data through time, but no values or units are provided. The percent change from the previous year is the only number provided.

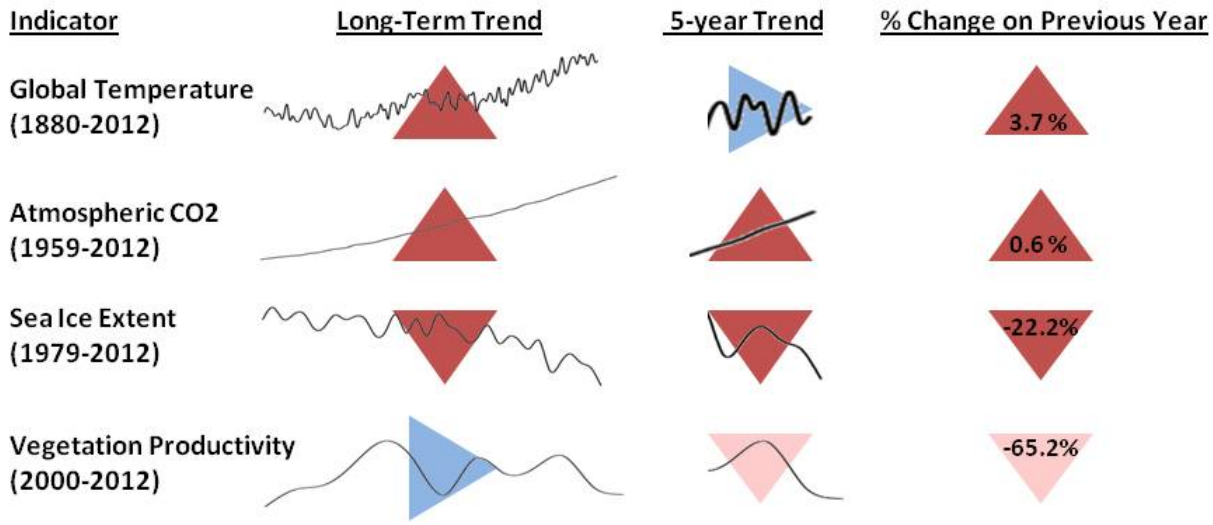

Figure 6.10 A further distillation of the information from four Climate Indicators (Global Temperature, Atmospheric CO2, Sea Ice Extent, Vegetation Productivity) provided in Figure 6.9, with an emphasis on long-term trend (first column), 5-year trend (second column), and change from the previous year (third column).

The final visualization attempted to maintain a minimalist approach while retaining and displaying all of the information/data inherent to the Indicator (Figure 6.11). Each bar encapsulates the full range of the record, proving both the minimum and maximum recorded values and their year of measure. The change over a recent period is shown; large white circle (current year's value) and small grey circle (past value - for NPP and Sea Ice Extent 3 years and for Temperature 5 years) and arrow to display direction of change. The color gradient is a histogram of the number of years within the range; i.e. dark colors represent more years within

those values and give the viewer an immediate reference as to what value represents “normal” conditions and how far the Indicator has departed from normal. It also provides more enhanced information for professionals or scientists (is this a uniform, bi-modal, or skewed distribution?).

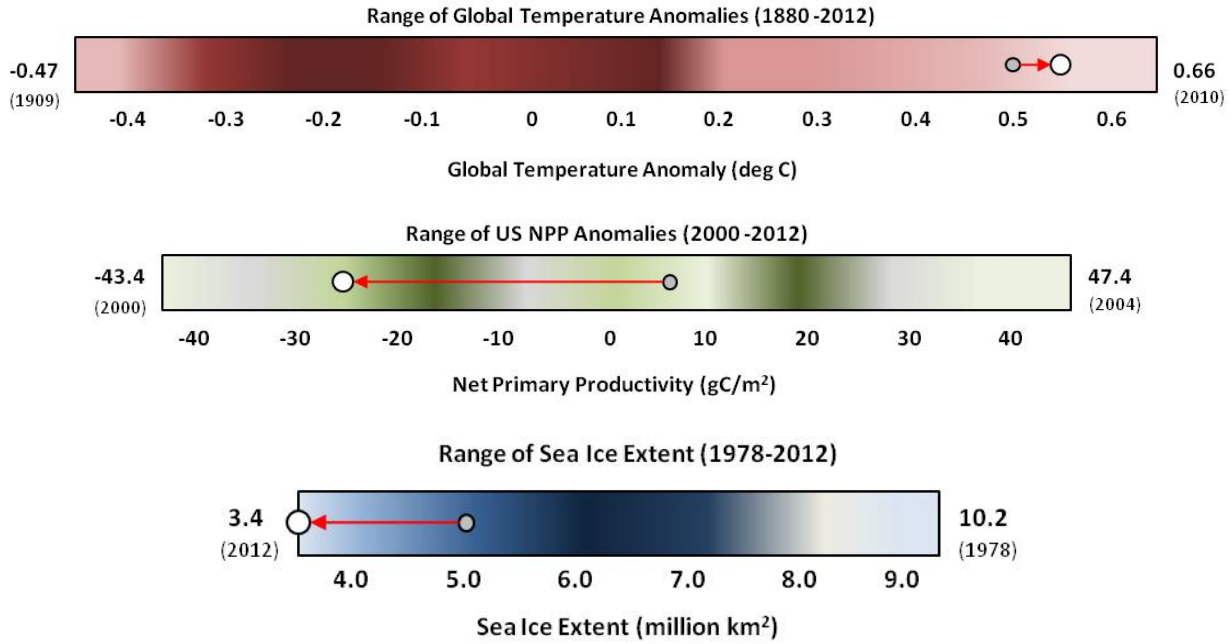

Figure 6.11. Visuals of Global Temperature Anomalies, Net Primary Productivity Anomalies, and Sea Ice Extent data records. Numbers to left and right of each bar display the minima and maxima of the data records, and year of occurrence in parentheses. Change over a recent period is shown; large white circle (current year’s value) and small grey circle (past value - for NPP and Sea Ice Extent 3 years and for Temperature 5 years) and red arrow to displays direction of change. The color gradient is a histogram of the number of years within the range; i.e. dark colors represent peaks in histograms and highlights the distribution (e.g. uniform, bi-modal, skewed) of the data records.

This collection of visualizations was provided to the NCADAC and Climate Indicators working groups. The currently selected Indicators and visualizations however have not adapted any methods shown here. Currently the NCA Indicators are presented using conventional maps and line or bar plots. The final visual format of each Indicator will be determined by the NCADAC and hopefully will consider alternative formats, such as those presented here.

6.8 References Cited

Buizer, J. L., P. Fleming, S. L. Hays, K. Dow, C. B. Field, D. Gustafson, A. Luers, and R. H. Moss (2013) Report on Preparing the Nation for Change: Building a Sustained National Climate Assessment Process, National Climate Assessment and Development Advisory Committee, 2013.

Janetos, A.C., R.S. Chen, D. Arndt, M.A. Kenney (2012) National Climate Assessment indicators: Background, development, & examples, Feb. 2012. http://downloads.usgcrp.gov/NCA/Activities/NCA-Indicators-Technical-Input-Report-FINAL--3-1-12.pdf

Jones, M. O., Kimball, J. S., Jones, L.A. (2013) Satellite Microwave Detection of Boreal Forest Recovery from the Extreme 2004 Wildfires in Alaska and Canada. *Global Change Biology*

Kenney, M.A, Janetos, A.C, et. al, (2014) National Climate Indicators System Report, National Climate Assessment and Development Advisory Committee, 2014.

Mu, Q., F. A. Heinsch, M. Zhao, S. W. Running (2007) Development of a global evapotranspiration algorithm based on MODIS and global meteorology data. *Remote Sensing of Environment* **111**: 519-536

Mu, Q., M. Zhao, S. W. Running (2011) Improvements to a MODIS Global Terrestrial Evapotranspiration Algorithm. *Remote Sensing of Environment*, **115**: 1781-1800

Running, S.R., R. Nemani, F. A. Heinsch, M. Zhao, M. Reeves, and H. Hashimoto (2004) A continuous satellite-derived measure of global terrestrial primary production, *BioScience* **54**(6): 547-560.

Zhao, M. and S. W. Running (2010) Drought-induced reduction in global terrestrial net primary production from 2000 through 2009. *Science* **329**: 940-943.

Zhao, M., F. A. Heinsch, R. R. Nemani, and S. W. Running (2005) Improvements of the MODIS terrestrial gross and net primary production global data set. *Remote Sensing of Environment* **95**: 164–176.

7.0 Conclusions and Future Research

The research and results detailed in this dissertation demonstrate the benefits of incorporating microwave vegetation optical depth (VOD) for measuring and monitoring land surface phenology from local to global scales. VOD sensitivity to changes in canopy biomass and water content provides a measure that first, advances our knowledge of vegetation phenological response to the climatic constraints of water, temperature and solar irradiance, as well as biomass recovery following wildfire, and second, serves as an independent remote measure of vegetation that compliments more traditional optical-infrared satellite measures responsive primarily to the reflective properties of vegetation and the land surface. Although of coarse spatial resolution, the VOD parameter provides near-daily global coverage, minimally affected by clouds or atmospheric constraints, and is therefore ideally suited for global vegetation phenology monitoring and modeling.

Chapter 2 detailed the first comprehensive application of this specific VOD dataset to monitoring vegetation phenology. The introduction of any new remote sensing algorithm and dataset to the scientific community requires a wide array of scientific inquiry and well-vetted results to establish the data as first, scientifically defensible, and second, useful across a range of applications. This dissertation met its objectives (Section 1.6) and achieved both of those goals by; providing detailed documentation and application of the VOD algorithm (Chapter 2); its comparison to independent measures of vegetation phenology across spatial and temporal scales and anticipated variation in phenological response to climatic constraints as compared to optical-infrared and other microwave measures (Chapters 1, 2 and 3); its application for monitoring vegetation biomass recovery following wildfire (Chapter 4); and how it can be used to improve representation of vegetation phenology within global land surface models (Chapter 5). All results of this work have been published in peer-reviewed scientific journals (Jones et al., 2011; 2012; 2013a; 2013b; 2014).

7.1 Dissertation Hypotheses

Four hypotheses, outlined in section 1.6, were tested in this dissertation research. Generally, each of the four hypotheses were confirmed, but conclusions are constrained by the

scope of each study and highlight the need for continued research. The first hypothesis stated; through its sensitivity to changes in vegetation water content and biomass, the seasonality of microwave VOD and associated phenology metrics will lag or lead optical-infrared derived phenology metrics based on specific land cover responses to climatic constraints on vegetation growth. The calculation of phenology metrics (Chapter 1), visual assessment and time series analysis (Chapters 1 through 5), and assessments of phase shifts across time series (Chapter 5), demonstrated that VOD time series lag and/or lead optical-infrared satellite measures based on climatic constraints and land cover type.

The second hypothesis: Vegetation water content changes inferred from GPS Normalized Microwave Reflection Index (NMRI) data provide validation of VOD response to changes in vegetation water content over the western continental USA and Alaska. Results of this research highlighted both the applicability of using GPS NMRI to validate VOD measures as well as limitations. First, the large number of significant correlations (276 of 305 sites) between the small footprint (stand or patch scale) NMRI and the coarse resolution (25km^2) VOD indicated broad regional agreement between these two microwave measures. Also, the sign and magnitude of NMRI and VOD temporal anomalies were generally coincident with variability in the monthly vapor pressure deficit (a surrogate indicator of plant-available moisture controls on vegetation activity), indicating similar climate sensitivity of both vegetation water content metrics despite differences in the microwave frequency and spatial scale of the retrievals. However, the difference in start of season metrics calculated from each dataset and heterogeneity of multiple NMRI time series within a single VOD pixel highlight the inherent limitations in comparing two remotely sensed datasets with a large difference in spatial resolutions. Although the incorporation of moderate resolution MODIS NDVI data provided insight regarding the relative contribution of each land cover type to the aggregate VOD pixel, future research is needed to develop proper weighting schemes by land cover contributing to the VOD retrieval. NMRI site records are also limited to primarily grassland and shrubland conditions with minimal coverage of higher biomass areas (forests), constraining application of this VOD validation assessment. Expansion of the NMRI network to forested areas is underway however and is discussed in the future research section (7.2).

The third hypothesis: The satellite microwave VOD signature will display an alternate vegetation recovery response related to canopy foliar and woody biomass regeneration following large scale fire events versus the canopy greenness recovery inferred from the optical-infrared satellite record, and the variation in response will be dependent on the proportion of woody vegetation loss within fire perimeters. The results of this study confirmed both an alternate vegetation recovery inferred from VOD and variation in that recovery dependent on woody vegetation loss. These results however are based on a relatively short time series (years 2003 to 2010) and restrict the relevancy of our findings to short-term biomass recovery. Further analysis is necessary, incorporating longer time series records over a larger sample of fires. Nonetheless, the results demonstrated that synergistic use of pre- and post-fire optical-infrared and microwave measures can improve our understanding of the variation in biomass recovery; where optical-infrared vegetation indices can provide a proxy of the photosynthetic capacity of a recovering land surface while VOD retrievals provide an estimate of the above ground biomass resulting from that capacity.

The fourth hypothesis: Equatorial Amazon forests exhibit a distinctive seasonal signal whereby the seasonal timing of water availability, canopy biomass growth, and net leaf flush are responsive to seasonal disparities in both water and solar radiation availability. By incorporating six satellite remote sensing datasets, flux tower data, and field data, we confirmed that equatorial Amazon forests do exhibit a seasonal signal responsive to both water and solar radiation availability. The results provide a new method for modeling tropical vegetation phenology based on the number of dry months experienced by a given pixel or region. The modeled onset of woody or leaf growth can be triggered by either increases in direct PAR or increases in water availability (or a combination of both) dependent on the length of the dry season. This method was presented to the Terrestrial Sciences Section of the National Center for Atmospheric Research, the group responsible for developing and advancing the Community Land Model. The scientists welcomed the testing of this methodology within the model and it is my aim to continue this endeavor in coordination with NCAR scientists. Results of this study however are limited to the southern equatorial Amazon. Northern Amazon forests, particularly northwest forests, experience a very limited dry season if at all.

And we cannot speculate on results of this method for tropical forests on a global scale. Future research is clearly necessary to determine the applicability of this method beyond the scope of the forests used in this study.

7.2 Future Research

Future research will focus on four main components. First, as of October 2011 the AMSR-E instrument stopped producing data due to a rotational problem with the antenna. This limited application of the VOD parameter for longer time series studies. However, an effort is underway to produce the VOD parameter from data collected by AMSR2, a satellite microwave sensor with near identical frequency channel specifications to AMSR-E, and became operational in July of 2012. The resulting VOD products are being inter-calibrated using overlapping data from the Microwave Radiation Imager (MWRI) onboard the FengYun (FYJ-3A/B) satellite to bridge the temporal gap between AMSR-E and AMSR2 (Du et al., 2014). Initial studies are being conducted to compare the two data records, and ideally will provide a continuous record for application to the components of the future work proposed below.

Second, the NMRI data records are currently limited to grassland and shrubland vegetation types. The PBO H20 group responsible for this data are experimenting with GPS antennas mounted on towers above forested canopies. Data retrieval at these sites has been hindered by multiple hardware and environmental issues (e.g. lightning strikes, high winds, etc.) Initial results are promising however. Figure 7.1 displays NMRI retrievals over the Harvard Forest study site plotted with coincident VOD data produced from AMSR2. The two time series display similar season onset and offset slopes, and a midseason trough. However, a large temporal offset is present; the NMRI displays a later onset and earlier offset which may be attributable to the large difference in spatial resolution of the two measures. As more NMRI data over forested systems becomes available we will work closely with the PBO H2O group to compare these time series to VOD retrievals to pursue further validation efforts.

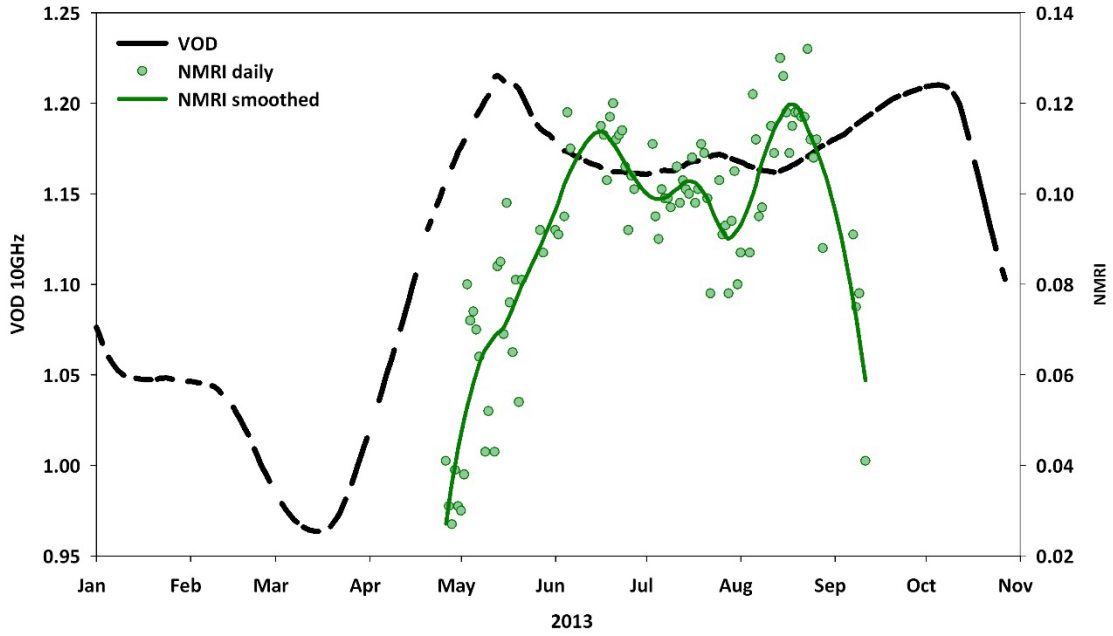

Figure 7.1. VOD time series (black line) derived from the AMSR2 sensor plotted with daily (green dots) and a smoothed (7-day running mean) NMRI retrievals over the Harvard Forest Tower site.

Third, the study estimating forest biomass recovery following wildfires should be revisited. The end of AMSR-E data collection prevented a longer time series assessment of VOD data. The newly available temporally contiguous AMSR-E/AMSR2 VOD record should be analyzed over the fire perimeters, along with the MODIS NDVI record. First to determine whether VOD trajectories are maintained and reflect the recruitment and growth of woody species and second, to determine whether NDVI records maintain the plateau found after ~2 years or whether future years reflect a secondary growth stage as woody vegetation establishes. The sub-pixel sensitivity of the VOD measure also allows for the inclusion of more fire perimeters, providing a far greater sample size for statistical analysis and the calculation of recovery trajectories. This also allows for a sensitivity study to determine a minimum fire area or woody tree cover loss detectable within a 25km^2 VOD retrieval.

Fourth, the application of VOD for tropical phenology monitoring and modeling needs to be extended across global tropical forests. The contiguous AMSR-E/AMSR2 record can be applied to assess whether phase shift differences between the multiple measures are consistent across forests and whether the dependence on dry season length is maintained. This

extension to global tropical forests would provide the first necessary step prior to applying these methods to the phenology sub-model within the Community Land Model. This work would also benefit from the incorporation of satellite derived sun-induced fluorescence (SIF) data, a proxy for photosynthetic activity. We might hypothesize that SIF time series will lag the VOD and LAI time series over light adapted systems, as peaks in photosynthesis would occur during periods of solar irradiance peaks and shortly after peaks in leaf area.

7.3 Conclusion

A principal aim of this work was to establish the VOD parameter as a scientifically defensible and valuable tool for monitoring vegetation from regional to global scales. This has been demonstrated through the multiple applications presented and resulting peer-reviewed manuscripts. In order to develop a more comprehensive understanding of vegetation response to a changing climate it is essential that multiple measures responsive to distinct characteristics be analyzed synergistically. This work has advanced that scientific endeavor by incorporating remote sensing measures across wavelengths and spatial scales, in conjunction with field and flux tower data, to further our understanding of vegetation response to climatic factors and extreme events.

The accuracy of land surface model projections of vegetation carbon sequestration and vegetation feedbacks to the soil and atmosphere is dependent on proper characterization of vegetation phenology, inclusive of changes in leaf area and photosynthetic capacity as well as changes in biomass and vegetation water content. Mischaracterization of the timing of these process can result in insufficient coupling of the water, energy, and carbon fluxes along the soil-plant-atmosphere continuum, with cascading effects on weather patterns and global circulation processes (Richardson et al. 2012; Levis and Bonan, 2004). This dissertation has aided in clarifying the temporal asynchrony that can occur across multiple vegetation phenological processes and their dependence on climatic drivers and land cover type. This information can be incorporated in future model iterations and ideally provide a broader understanding of ecosystem functioning and its response to a changing climate.

7.4 References Cited

Du J, Kimball JS, Shi JC, Jones LA, Wu SL, Sun RJ, Yang H, (2014) Inter-calibration of satellite passive microwave land observations from AMSR-E and AMSR2 using overlapping FY3B-MWRI sensor measurements. *Remote Sensing* **6**, 8594-8616.

Jones MO, Jones LA, Kimball JS, McDonald KC (2011) Satellite passive microwave remote sensing for monitoring global land surface phenology. *Remote Sensing of Environment*, **115**, 1102–1114.

Jones MO, Kimball JS, Jones LA, McDonald KC (2012) Satellite passive microwave detection of North America start of season. *Remote Sensing of Environment*, **123**, 324–333.

Jones, MO, Kimball JS, Jones LA (2013a) Satellite Microwave Detection of Boreal Forest Recovery from the Extreme 2004 Wildfires in Alaska and Canada. *Global Change Biology*

Jones, MO, Kimball JS, Small EE, Larson KM (2013b) Comparing Land Surface Phenology Derived from Satellite and GPS Network Microwave Remote Sensing. *International Journal of Biometeorology*

Jones, MO, Kimball JS, Nemani RR (2014) Asynchronous Amazon forest canopy phenology indicates adaptation to both water and light availability. *Environmental Research Letters*

Levis S, Bonan GB (2004) Simulating springtime temperature patterns in the community atmosphere model coupled to the community land model using prognostic leaf area. *Journal of Climate*, **17**, 4531–4540.

Richardson AD, Anderson RS, Arain MA, et al. (2012) Terrestrial biosphere models need better representation of vegetation phenology: results from the North American Carbon Program Site Synthesis. *Global Change Biology*, **18**, 566–584.

Appendix A

The following is a Brief Communications Arising (BCA) response to "Amazon forests maintain consistent canopy structure and greenness during the dry season", a research article published in the journal *Nature* (Morton et al., 2013). The BCA is presented here in its entirety inclusive of a letter submitted to the Nature editors describing, in detail, our critique of the methods used in that article. My co-authors on this work were John S. Kimball and Ramakrishna R. Nemani.

A.1 Amazon forests show canopy structure seasonality

Previous analysis[1] of AMSR-E (Advanced Microwave Scanning Radiometer for EOS) vegetation optical depth (VOD) retrievals spanning a multi-year (2003-2008) record document recurring seasonal changes in canopy biomass structure over Amazon forests and contradict the idea of unchanging canopy properties and Amazon forest structure stability as published in this journal[2].

Morton et al.[2] claim "*no evidence for consistent seasonal changes in canopy structure or reflectance properties of southern Amazon forests from satellite lidar and optical remote sensing observations*". Morton et al. also indicate that apparent seasonal increases in MODIS EVI or LAI are artifacts of sun-sensor geometry on NIR reflectance, yet the LAI retrieval algorithm accounts for uncertainties in surface reflectance and sun and view geometry[3]. Contrary to the findings of Morton et al., the AMSR-E VOD record demonstrates marked seasonality in canopy biomass structure over Amazon forests[1] that shows a temporally lagged correlation with MODIS LAI (Figure 1a,b). Unlike passive optical and lidar sensors, the VOD signal from satellite microwave remote sensing is independent of sun-sensor geometry and relatively insensitive to atmospheric effects.

The VOD parameter defines the frequency dependent extinction of land surface microwave emissions by the intervening vegetation layer[4,5] and is sensitive to changes in canopy water content of both photosynthetic and woody biomass. The satellite microwave VOD record also provides near-daily observations of the land surface, albeit at coarse (25-km) spatial resolution[1]. The VOD retrieval algorithm minimizes the potential influence of

atmosphere precipitable water vapor, temperature, surface inundation and soil moisture effects[1]. The higher frequency (18.7 GHz) AMSR-E VOD signal approaches theoretical saturation over Amazon forests and likely reflects the status of emergent leaves and branches over a semi-infinite canopy layer[1].

The VOD and LAI both exhibit seasonality of Amazon forests contrary to Morton et al. claims of a consistent canopy structure. An apparent temporal phase difference in VOD and LAI seasonality (Figure 1b) follows well demonstrated physiological mechanisms and field level studies of canopy seasonality. An initial water content increase is required for cell expansion and new leaf formation[7] (Apr-Jul). Leaf area is maintained through the first half of the dry season (Jul-Aug) as trees maintain above average canopy biomass water content (VOD) via deep tap roots[8] and hydraulic redistribution[9], even with less precipitation and dry season increases in evapotranspiration[10]. Leaf senescence and abscission peak (Aug-Nov) as vegetation water content declines and reaches minimum values. The timing of leaf flush and litterfall indicated by the VOD and LAI seasonal signatures is supported by published field observations (Figure 1b)[11-13].

It is unclear why Morton et al.[2] assumed the LAI algorithm did not account for changes in view and illumination conditions when the algorithm documentation states otherwise[3,14]. In past work[1] and detailed here, we rebut the claim of Morton et al. by demonstrating a distinct Amazon forest seasonality from satellite microwave data that is independent of sun-sensor geometry yet coincident with MODIS LAI seasonality and evidence from field studies. These apparent inconsistencies also point out the need for more comprehensive studies of the tropics involving coordinated field observations and multiple satellite perspectives, including microwave and optical sensors that can provide synergistic information, while offsetting limitations from any single technology.

A.1.1 Data and Methods

For the application in Figure 1, a near-daily AMSR-E VOD record from 2003-2010[6] was aggregated to a monthly mean climatology over evergreen broadleaf forest (EBF) dominant (>80%) 25km pixels in the Amazon region. The normalized VOD seasonal amplitude was

calculated from the monthly time series for each grid cell [(maximum-minimum)/annual mean] across the 8-year record (Figure 1a). The VOD and MODIS LAI monthly climatology (normalized by annual means) and monthly average precipitation (TRMM) from 2003-2010 (Figure 1b) were calculated for all EBF dominant 25km pixels having >5% VOD seasonal amplitude and located within the southern Amazon domain investigated by Morton et al.[2] (black box Figure 1a).

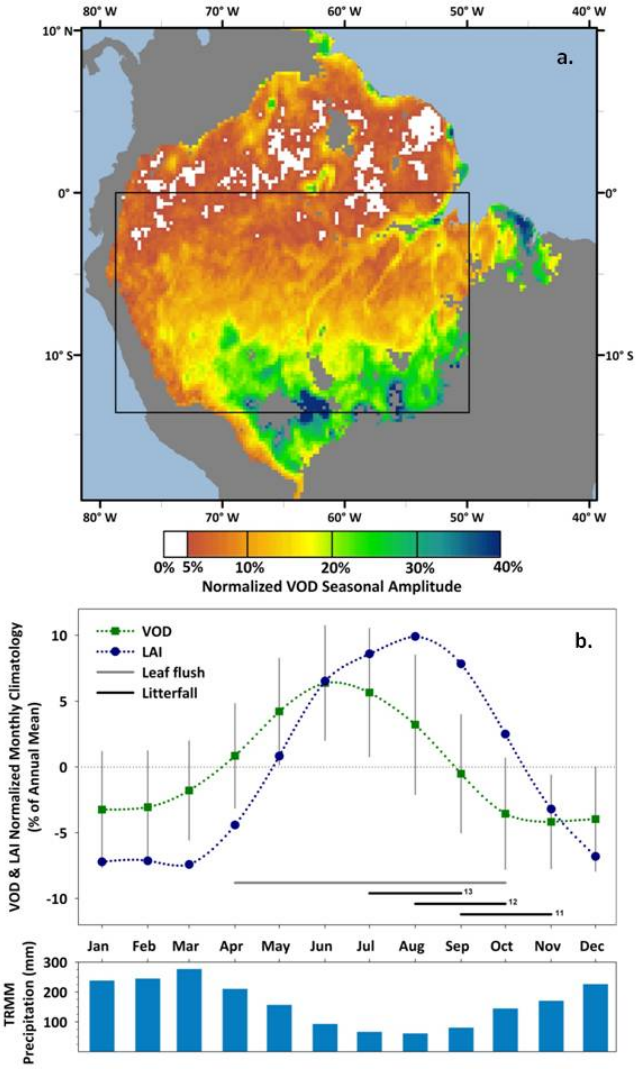

Figure 1. (a) Normalized VOD seasonal amplitude for all evergreen broadleaf forest (EBF) dominant (>80%) 25km pixels calculated from the monthly time series for each grid cell [(maximum-minimum)/annual mean] for the 2003-2010 record. (b) VOD and MODIS LAI monthly climatology (normalized by annual means) and monthly average precipitation (TRMM) from 2003-2010 for all EBF dominant 25km pixels having >5% VOD seasonal amplitude and located within the southern Amazon domain investigated by Morton et al.[2] (black box in (a)). Grey vertical bars are VOD monthly climatology standard deviation. Grey and black horizontal

bars denote respective months of increasing individuals with new leaves[11] and months of peak litterfall from available field studies[11-13].

A.2 References

1. Jones, M. O., Jones, L. A., Kimball, J. S. & McDonald, K. C. Satellite passive microwave remote sensing for monitoring global land surface phenology. *Remote Sens. Environ.* **115,** 1102–1114 (2011).
2. Morton, D. C. *et al.* Amazon forests maintain consistent canopy structure and greenness during the dry season. *Nature* **506,** 221–4 (2014).
3. Knyazikhin, Y., Martonchik, J. V., Myneni, R. B., Diner, D. J. & Running, S. W. Synergistic algorithm for estimating vegetation canopy leaf area index and fraction of absorbed photosynthetically active radiation from MODIS and MISR data. *J. Geophys. Res.* **103,** 32,257-32,276 (1998).
4. Jackson, T. J., & Schmugge, T. J. Vegetation Effects On The Microwave Emission Of Soils. *Remote Sens. Environ.,* **36**, 203-212 (1991).
5. van de Griend, A. A., & Wigneron, J. On the Measurement of Microwave Vegetation Properties: Some Guidelines for a Protocol. *IEEE Trans. Geosci. Remote Sens.* **42,** 2277–2289 (2004).
6. Jones L. A. & Kimball J. S. Daily Global Land Surface Parameters Derived from AMSR-E. Boulder, Colorado USA: National Snow and Ice Data Center. Digital media (http://nsidc.org/data/nsidc-0451.html) (2011)
7. Pantin, F., Simonneau, T. & Muller, B. Coming of leaf age: control of growth by hydraulics and metabolics during leaf ontogeny. *New Phytologist Tansley Reviews* **196**, 349–366 (2012).
8. Nepstad, D. C., *et al.* The role of deep roots in the hydrological and carbon cycles of Amazonian forests and pastures, Nature, **372**, 666–669. (1994)
9. da Rocha, H. R., *et al*. Seasonality of water and heat fluxes over a tropical forest in eastern Amazonia, Ecol. Appl., **14**(4), S22–S32. (2004),
10. Hutyra, L. R, *et al*. Climatic variability and vegetation vulnerability in Amazonia, *Geophys. Res. Lett*., **32**, L24712 (2005).
11. Brando, P. M. *et al.* Seasonal and interannual variability of climate and vegetation indices across the Amazon. *Proc. Natl. Acad. Sci. U.S.A.* **107,** 14685–90 (2010).
12. Rice, A. H., et al. Carbon balance and vegetation dynamics in an old-growth Amazonian forest, Ecol. Appl., 14(4), s55–s71. (2004)
13. Goulden, M. L., *et al.* Diel and seasonal patterns of tropical forest CO2 exchange, *Ecol. Appl.*, **14**(4), S43–S54. (2004).
14. Samanta, A. *et al.* Seasonal changes in leaf area of Amazon forests from leaf flushing and abscission. J. *Geophys. Res*. 117, G01015 (2012).

A.3 Letter to Nature Editors

Dear *Nature* Editors,

This Brief Communications Arising (BCA) submission is in response to the *Nature* Research Letter "Amazon forests maintain consistent canopy structure and greenness during the dry season" (Morton et al., 2014; **506**, 221-224) and contests the claim of Morton et al. that there is "*no evidence for consistent seasonal changes in canopy structure or reflectance properties of southern Amazon forests from lidar and optical remote sensing observations*". In accordance with BCA guidelines, we first sent our rebuttal to the primary author and received a response. All communications are included with this submission.

Previous analysis of MODIS Leaf Area Index (LAI) and AMSR-E (Advanced Microwave Scanning Radiometer for EOS) vegetation optical depth (VOD) retrievals spanning a multi-year (2003-2008) record document recurring seasonal changes in canopy biomass structure over Amazon forests and contradict the idea of unchanging canopy properties and Amazon forest structure stability. An updated analysis was conducted covering the same geographic domain used by Morton et al., but employing AMSR-E VOD and MODIS LAI data records extending from 2003-2010. The VOD and LAI both exhibit Amazon forest seasonality that follows well demonstrated physiological mechanisms and published field observations of canopy seasonality.

The response by Morton et al. relies on model simulations and GLAS data to rebut the major findings of our study regarding observed seasonal changes in LAI that are consistent with leaf flushing and litterfall from field studies, and the sensitivity of VOD to canopy scale changes. First, the authors do not implement the MODIS LAI product but claim their findings affect LAI retrievals. They discount evidence for seasonal changes in LAI by reiterating unwarranted claims that the LAI algorithm does not properly account for changes in sun-sensor geometry, yet the algorithm documentation and associated peer-reviewed publications clearly state otherwise. For example, the MODIS LAI and FPAR Algorithm Theoretical Basis Document explicitly discusses the principal plane effects (e.g., Sections 2.4.1, 2.7) that Morton et al. rediscover in their paper. Also, although the authors did not include field observations in their analysis, they agree that documented field studies report seasonal changes in LAI, but that

these changes are “small”. The remote sensing and field studies cited in the authors Letter and response display LAI changes on the order of 0.4-1.4, yet they set their model threshold of “large” change detection at 2.0 and then conclude that the GLAS lidar does not detect consistent changes in LAI. Ultimately, the LAI and VOD results are temporally coincident with field observations while the results of Morton et al. are not.

The authors also dispute our documented changes in LAI by assuming, through model simulations, that large changes in LAI will be detected through changes in the GLAS WCRH values. However, the GLAS analysis of Morton et al. suffers from several critical limitations. First, GLAS suffers from atmosphere cloud/smoke/aerosol contamination constraints similar to other optical sensors, resulting in geographically sparse and temporally inconsistent data, but the authors do not provide any information on retrieval uncertainty or sampling error from the GLAS data. Second, the sparse GLAS “pairings” used to interpret changing WCRH are taken from different years; May and June data from 2005 and 2006 are compared to October data from 2004 and 2007. Third, the “pairings” are also based on a 0.02 degree search radius, implying that a “pair” of 55m lidar footprints may be up to 2km apart. And finally, the extended data figure 5 from Morton et al. displays spatially proximal, highly positive and negative seasonal differences in WCRH that, according to their model, would equate to LAI changes on the order of 1.0-2.0. Supposing these changes occur across a single season (which they do not) implies large LAI seasonal variations contrary to a consistent canopy structure, and changes that are nearly independent of local meteorological or edaphic conditions, which conflicts with evidence for recurring LAI seasonality and associated environmental triggers from published field studies. The lack of evidence for consistent seasonal changes in canopy structure from the GLAS data indicated by Morton et al. is likely an artifact of large lidar sampling error and associated retrieval uncertainty from the sparse GLAS WCRH “pairings”.

In regards to our VOD analysis, the authors state that it is unclear how VOD seasonality is independent of rainfall seasonality and moisture status. The VOD is a spatially integrated measure of canopy biomass structure and associated water content. The AMSR-E VOD record is publicly available and derived from a peer-reviewed published algorithm with documented accuracy and well-defined retrieval uncertainty. The algorithm screens out active precipitation

and minimizes the potential influence of atmosphere precipitable water vapor, temperature, surface inundation and soil moisture effects. If VOD was responsive solely to precipitation it would be seasonally coincident with rainfall (increasing in the wet season and decreasing in the dry season), yet the data record shows otherwise. Assuming the authors are referring to vegetation canopy biomass water content in regards to the term "moisture status", the VOD is not "isolated" from this parameter, but is in fact a VOD retrieval attribute and critical element of canopy seasonality. The VOD response to canopy "moisture status" and associated biomass changes displays seasonality that follows well documented vegetation physiological mechanisms associated with leaf flush and senescence, and is coincident with the LAI record and published field studies.

Finally, the statement that "the pattern of VOD seasonal amplitude is opposite to the spatial pattern of seasonal changes in LAI in previous studies" is simply not true. First, the LAI studies cited by Morton et al. use a different spatial and temporal compositing method than our analysis of VOD amplitude and are therefore not directly comparable. Second, the statement has no bearing on the argument being addressed; both LAI and VOD records indicate recurring seasonal changes in canopy structure of southern Amazon forests that are consistent with observed canopy seasonality and physiological attributes documented from published field studies. The major finding of no evidence for consistent seasonal changes in canopy structure from Morton et al. is contrary to the weight of evidence from our VOD and LAI analysis, and prior studies. This apparent contradiction may reflect large uncertainties in the model simulations and GLAS WCRH data used in the Morton et al. study.

The authors of the BCA submission request that this letter to the *Nature* editors be included with the submission if it is sent to independent referees. The authors of the Brief Communications Arising submission have no competing interests as defined by Nature Publishing Group, or other interests that might be perceived to influence the results and/or discussion reported in this article.

Sincerely,

Matthew O. Jones
John S. Kimball
Ramakrishna R. Nemani

Appendix B.

B.1 Sinusoidal Model Results

Sinusoidal model [$y_t = y_0 + a\sin(2\pi x/b+c)$] results for GRACE TWS, AMSR-E VOD, and MODIS LAI using monthly ecoregion means from 2003 to 2011 (VOD, Jan. 2003 – Sept. 2011). *p<0.001

Ucayali	**r^2**	**Parameter**	**Coefficient**	**Std. Error**	**p**
TWS	0.830*	a	14.31	0.646	<0.0001
		b	12.037	0.035	<0.0001
		c	6.172	0.091	<0.0001
		y_0	-0.327	0.458	0.4771
VOD	0.454*	a	0.091	0.010	<0.0001
		b	11.940	0.080	<0.0001
		c	4.724	0.216	<0.0001
		y_0	1.976	0.007	<0.0001
LAI	0.585*	a	0.242	0.02	<0.0001
		b	12.003	0.061	<0.0001
		c	3.619	0.169	<0.0001
		y_0	2.925	0.014	<0.0001

Southwest Amazon	**r^2**	**Parameter**	**Coefficient**	**Std. Error**	**p**
TWS	0.903*	a	21.139	0.691	<0.0001
		b	12.02	0.025	<0.0001
		c	6.037	0.066	<0.0001
		y_0	-0.6	0.489	0.2222
VOD	0.742*	a	0.169	0.010	<0.0001
		b	12.020	0.044	<0.0001
		c	4.608	0.117	<0.0001
		y_0	1.996	0.007	<0.0001
LAI	0.739*	a	0.403	0.024	<0.0001
		b	11.954	0.043	<0.0001
		c	3.613	0.119	<0.0001
		y_0	3.256	0.017	<0.0001

Jurua-Purus	**r^2**	**Parameter**	**Coefficient**	**Std. Error**	**p**
TWS	0.880*	a	27.033	0.992	<0.0001
		b	12.003	0.027	<0.0001
		c	5.656	0.072	<0.0001
		y_0	-0.903	0.698	0.1988
VOD	0.616*	a	0.089	0.007	<0.0001
		b	12.060	0.060	<0.0001
		c	4.590	0.158	<0.0001
		y_0	1.853	0.005	<0.0001

LAI	0.750*	a	0.469	0.027	<0.0001
		b	11.987	0.042	<0.0001
		c	3.611	0.116	<0.0001
		y_0	3.37	0.019	<0.0001

Purus-Madeira	**r^2**	**Parameter**	**Coefficient**	**Std. Error**	**p**
TWS	0.913*	a	46.794	1.434	<0.0001
		b	12.002	0.023	<0.0001
		c	5.562	0.06	<0.0001
		y_0	-1.728	1.008	0.0897
VOD	0.747*	a	0.107	0.006	<0.0001
		b	12.020	0.044	<0.0001
		c	4.500	0.117	<0.0001
		y_0	1.793	0.004	<0.0001
LAI	0.691*	a	0.387	0.025	<0.0001
		b	11.968	0.048	<0.0001
		c	3.851	0.134	<0.0001
		y_0	3.168	0.018	<0.0001

Madeira-Tapajós	**r^2**	**Parameter**	**Coefficient**	**Std. Error**	**p**
TWS	0.937*	a	35.273	0.913	<0.0001
		b	11.998	0.019	<0.0001
		c	5.695	0.051	<0.0001
		y_0	-1.385	0.643	0.0335
VOD	0.814*	a	0.146	0.007	<0.0001
		b	12.000	0.036	<0.0001
		c	4.590	0.095	<0.0001
		y_0	1.812	0.005	<0.0001
LAI	0.738*	a	0.325	0.019	<0.0001
		b	11.951	0.043	<0.0001
		c	3.71	0.12	<0.0001
		y_0	3.101	0.013	<0.0001

Tapajos-Xingu	**r^2**	**Parameter**	**Coefficient**	**Std. Error**	**p**
TWS	0.917*	a	26.191	0.786	<0.0001
		b	12	0.022	<0.0001
		c	5.583	0.059	<0.0001
		y_0	-1.096	0.553	0.0502
VOD	0.662*	a	0.119	0.008	<0.0001
		b	12.010	0.053	<0.0001
		c	4.683	0.142	<0.0001
		y_0	1.915	0.006	<0.0001
LAI	0.791*	a	0.466	0.024	<0.0001
		b	12.047	0.037	<0.0001
		c	4.257	0.102	<0.0001
		y_0	3.065	0.017	<0.0001

Xingu-Tocantins-Araguaia	r^2	Parameter	Coefficient	Std. Error	p
TWS	0.881*	a	33.27	1.219	<0.0001
		b	12	0.027	<0.0001
		c	5.474	0.072	<0.0001
		y_0	-0.982	0.856	0.2541
VOD	0.628*	a	0.108	0.008	<0.0001
		b	12.000	0.056	<0.0001
		c	4.869	0.151	<0.0001
		y_0	1.812	0.006	<0.0001
LAI	0.632*	a	0.295	0.022	<0.0001
		b	12.053	0.055	<0.0001
		c	4.869	0.149	<0.0001
		y_0	2.472	0.016	<0.0001

Tocantins Pindare	r^2	Parameter	Coefficient	Std. Error	p
TWS	0.831*	a	21.653	0.971	<0.0001
		b	11.997	0.033	<0.0001
		c	5.17	0.087	<0.0001
		y_0	0.139	0.681	0.8391
VOD	0.804*	a	0.145	0.007	<0.0001
		b	11.990	0.037	<0.0001
		c	4.326	0.100	<0.0001
		y_0	1.735	0.005	<0.0001
LAI	0.752*	a	0.352	0.02	<0.0001
		b	12.041	0.042	<0.0001
		c	4.723	0.113	<0.0001
		y_0	2.25	0.014	<0.0001

Maranhao Babacu	r^2	Parameter	Coefficient	Std. Error	p
TWS	0.720*	a	18.746	1.162	<0.0001
		b	12.026	0.045	<0.0001
		c	5.286	0.121	<0.0001
		y_0	0.504	0.815	0.5376
VOD	0.814*	a	0.146	0.007	<0.0001
		b	12.000	0.036	<0.0001
		c	4.590	0.095	<0.0001
		y_0	1.812	0.005	<0.0001
LAI	0.760*	a	0.385	0.021	<0.0001
		b	11.973	0.041	<0.0001
		c	4.944	0.11	<0.0001
		y_0	2.134	0.015	<0.0001

Appendix C.

C.1 Pairwise Bispectral Analysis

As the sinusoidal model results in a generalized monthly climatology, we also conducted a more robust pairwise bispectral analysis between the three primary time series used in the analysis (TWS, VOD, and LAI) to confirm that the results did not significantly differ between these two methods. The pairwise bispectral analysis (see Shumway and Stoffer 2011; Bendat and Piersol 2012) provides the coherence, a linear correlation between two series indexed by frequency, and the phase lag, or the average delay between the two series as a function of Fourier frequency. In all cases the frequency of maximum coherence was equivalent to a 12 month cycle and the lag at the maximum coherence was similar to that derived from the sinusoidal model method. The bispectral analysis resulted in some improvement in the linear regressions of mean dry season length with the lag of the TWS-LAI time series (r^2 increase from 0.67 to 0.82) and the TWS-LAI time series (r^2 increase from 0.73 to 0.78), but a decrease with the VOD-LAI (r^2 decrease from 0.69 to 0.62). A table of the results, as well as plots and regressions from this analysis, are shown below.

	GRACE-VOD		**VOD-LAI**		**GRACE-LAI**	
Ecoregion	**Coherence**	**lag (months)**	**coherence**	**lag (months)**	**coherence**	**lag (months)**
Ucayali	0.87	2.27	0.89	2.46	0.93	4.75
Southwest Amazon	0.97	2.59	0.96	1.77	0.99	4.36
Jurua-Purus	0.91	2.63	0.91	1.26	0.99	3.92
Purus-Madeira	0.94	2.35	0.93	0.80	0.98	3.17
Madeira-Tapajós	0.97	2.17	0.95	1.45	0.99	3.62
Tapajos-Xingu	0.95	1.97	0.94	0.76	0.99	2.76
Xingu-Tocantins-Araguaia	0.94	1.26	0.90	0.00	0.95	1.32
Tocantins/Pindare	0.98	1.75	0.97	-0.77	0.98	0.99
Maranhao Babacu	0.99	0.85	0.98	-0.41	0.97	0.45

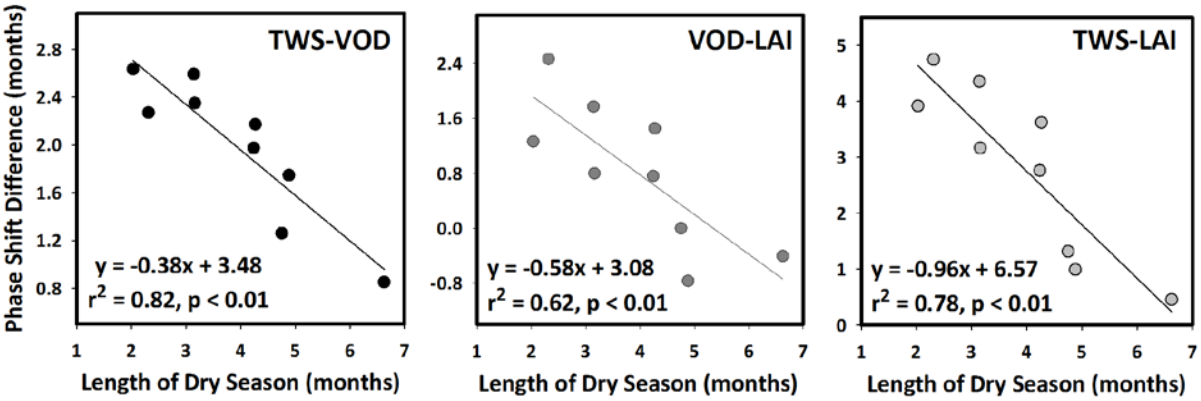

C.2 References

Shumway R H and Stoffer D S 2011 *Time Series Analysis and Its Applications: With R Examples*, Third Edition, Springer New York. DOI 10.1007/978-1-4419-7865-3

Bendat J S and Piersol A G 2012 *Random Data: Analysis and Measurement Procedures*, Fourth Edition, Wiley Online Library. DOI: 10.1002/9781118032428